Photonic Applications and Hybrid Integration of Single Nitrogen Vacancy Centres in Nanodiamond

D I S S E R T A T I O N

zur Erlangung des akademischen Grades

Dr. Rer. Nat
im Fach Physik

eingereicht an der
Mathematisch-Naturwissenschaftlichen Fakultät
Humboldt-Universität zu Berlin

von
Dipl.-Phys. **Andreas Wolfgang Schell**

Präsident der Humboldt-Universität zu Berlin:
Prof. Dr. Jan-Hendrik Olbertz

Dekan der Mathematisch-Naturwissenschaftlichen Fakultät:
Prof. Dr. Elmar Kulke

Gutachter:
1. Prof. Dr. Oliver Benson
2. Prof. Achim Peters, PhD
3. Prof. Dr. Rudolf Bratschitsch

Tag der mündlichen Prüfung: 15.12.2014

Abstract

For the future of optical technology as well as for fundamental physics experiments, it is increasingly important to make use of quantum effects. One of the most fundamental manifestations of quantum effects in optics is the existence of single photons, i.e., single particles of light. While any stream of light consists of photons, the creation of a regulated photon stream with a defined discrete number of quanta is highly demanding. A specific case is the generation of a stream of single photons by single quantum emitters.

In this thesis, one of such single photon emitters, the nitrogen vacancy centre (NV centre) in diamond, will be examined. A special challenge for working with defect centres in diamond is addressing them and their controlled coupling to photonic structures. Here, by using different hybrid approaches, NV centres in diamond nanoparticles are integrated into photonic structures. Firstly, using a pick-and-place nanomanipulation technique with an atomic force microscope, a single NV centre is coupled to a photonic crystal cavity and an optical fibre. Coupling to the photonic crystal cavity results in an enhancement of the NV centre's zero phonon line by a factor of 12.1 and coupling to the fibre yields a directly coupled single photon source with an effective numerical aperture of 0.82. By coupling to plasmonic waveguides, the signature of single surface plasmon polaritons is found. Secondly, by development of a hybrid material, another approach is pursed. Here, instead of placing the nanodiamonds on the structures of interest, they are inside the material from which the structures are built. With the technique of two-photon direct laser writing, on-chip integration and combination of waveguides, resonators, and single photon emitters is demonstrated.

To guide the way to more efficient extraction of photons from such structures, numerical calculations on elliptical solid immersion lenses and of a photon to plasmon coupler are performed. For the same purpose, parabolic microantennas are employed resulting in collected photon rates of about two million photons per second from a single NV centre.

In order to learn more on the dynamics of NV centre in nanodiamonds and find ways for improvements, the dynamics of the ultra-fast spectral diffusion of the NV centre's zero phonon line are investigated using a photon correlation interferometer

In addition to techniques for the fabrication of photonic and plasmonic structures, also methods for their characterisation are needed. For this, it can be exploited that the NV centre also is not only a single photon emitter, but can also be employed as a sensor. Here, the NV centre is used to measure the local density of optical states in a scanning probe experiment, establishing the technique of three-dimensional quantum emitter fluorescence lifetime imaging.

Zusammenfassung

Sowohl für die Zukunft optischer Technologien als auch für physikalische Grundlagenexperimente ist es zunehmend wichtig, Quanteneffekte zu benutzen. Einer der fundamentalsten Quanteneffekte in der Optik ist die Existenz des Photons, das heißt, eines einzelnen Lichtpartikels. Während alles Licht aus Photonen besteht, ist es überaus fordernd einen geregelten Fluss von Photonen mit einer definierten und diskreten Photonenzahl herzustellen. Ein Spezialfall ist die Herstellung eines Flusses aus einzelnen Photonen durch Einzelphotonenemitter. In dieser Arbeit wird das Stickstoff-Fehlstellenzentrum (NV Zentrum) in Diamant als ein solcher Einzelphotonenemitter untersucht. Eine besondere Herausforderung beim Arbeiten mit Defektzentren in Diamantnanopartikeln ist ihre Adressierung und ihre kontrollierte Kopplung an photonische Strukturen. Durch Benutzung eines hybriden Ansatzes werden hier NV Zentren in Diamantnanopartikeln in photonische Strukturen integriert. Zuerst wird eine aufnehmen-und-ablegen-Nanomanipulationstechnik mittels eines Rasterkraftmikroskops verwendet um einzelne NV Zentren an eine photonische Kristallkavität und eine optische Faser zu koppeln. Durch Kopplung an die photonische Kristallkavität wird die Emission der Nullphononenlinie des NV Zentrums um den Faktor 12.1 erhöht und durch Kopplung an die optische Faser entsteht eine direkt gekoppelte Einzelphotonenquelle mit einer effektiven numerischen Apertur von 0.82. Durch Kopplung an plamonische Wellenleiter können einzelne Oberflächenplasmon-Polaritonen nachgewiesen werden. Zweitens wird ein anderer Ansatz, die Entwicklung eines hybriden Materials, verfolgt. Hier sind die Nanodiamanten, anstatt sie auf die Strukturen von Interesse zu legen, von Anfang in dem Material enthalten, aus dem die Strukturen hergestellt werden. Mittels direktem Zweiphotonen-Laserschreiben ist es dann möglich, Kombinationen aus chipintegrierten Wellenleitern, Resonatoren und Einzelphotonenemittern zu zeigen.

Um Wege zur effizienteren Extraktion von Photonen aus solchen Strukturen aufzuzeigen, wurden numerische Berechnungen von elliptischen Festkörperimmersionlinsen und eines Photonik-zu-Plamonik- Konverters ausgeführt. Zum selben Zweck werden auch parabolische Mikroantennen verwendet, was zu Photonenraten von circa zwei Millionen pro Sekunde von einzelnen NV Zentren führt.

Um mehr über die Dynamik von NV Zentren in Nanodiamant zu erfahren und Wege zu ihrer Verbesserung zu finden, wird die Dynamik der Nullphononenlinie des NV Zentrums mittels eines Photonenkorrelationsinterferometers untersucht.

Zusätzlich zu Techniken zur Herstellung photonischer und plasmonischer Strukturen werden auch Methoden zu ihrer Charakterisierung benötigt. Hier für kann es ausgenutzt werden, dass das NV Zentrum weiter nicht nur ein Einzelphotonenemitters ist, sondern es ebenso als Sensor verwendet werden kann. Das NV Zentrum wird hier verwendet, um die lokale optische Zustandsdichte

in einem Rastersondenverfahren zu messen, was die Technik der dreidimensionalen Quantenemitter Fluoreszenzlebensdauermikroskopie einführt.

Contents

1. Introduction

At the latest with the invention of the transistor, electronic devices began to enter basically all areas of science, industry, and daily life. Today, technology is heavily based on electronics, but over the last decades devices employing optics along with electronics or even working purely optical are increasingly developed and used. This is mainly due to the following advantages optics has: Light is a versatile carrier of information, which can be generated, modulated, and detected fast and efficiently. The electromagnetic spectrum offers a great bandwidth which can be used. Furthermore, optical devices have the potential to work more power efficient than their electronic counterparts.

Nearly all of this successful technology is based on – and also limited by – the laws of classical physics. In principle, a much larger variety of physical phenomena can be exploited when leaving the realm of classical physics and entering the world of quantum mechanics. This offers great advantages, but is also very challenging. Existing techniques have to be improved and new ones need to be developed when trying to deal with fragile quantum states in a controlled way. Usually, when the size of objects get bigger, they tend to follow the laws of classical physics, so quantum mechanical objects typically have very small sizes on the nanometre scale. Recent progress in nanotechnology enables working with such tiny objects. Nanotechnology makes it possible to efficiently address these quantum objects using electronics or light, so that first quantum devices can be built and used.

The main promises of quantum – and especially quantum optical – technology lie in the following fields:

In the field of **Quantum Information Processing** [1], the laws of quantum mechanics are employed for the purpose of communication and computation. Quantum communication is a promising way of exchanging secret information without any possibilities for an eavesdropper to successfully read the message undetected [2]. This security comes directly from the laws of quantum mechanics – the no cloning theorem [3, 4] hinders an eavesdropper to read out data without altering the information. In quantum computing [5, 6], an advantage over classical computing can be gained by working with quantum mechanical systems. This can be achieved using so-called qbits (quantum bits), two state systems which, in contrast to classical bits, can be in quantum superposition states. A promising implementation for

this is to use photons as qbits [7]. The main experimental challenges in this field lie in the reliable generation, read-out, and protection against decoherence of the quantum states used.

In the field of **Quantum Metrology**, quantum mechanics is used to measure signals with a precision beyond the limits set to classical physics [8–10]. To achieve this, states which are not existing in classical physics, such as squeezed states [11, 12] or NOON-states [13], are used in the sensing apparatus. Today, besides proof of principle demonstrations in laboratory [14], quantum sensing is successfully used to enhance the precision of metrology experiments, such as interferometers for the search for gravitational waves [15]. The experimental challenges here are again, as in the case of quantum information processing, reliable generation, read-out, and protection against decoherence.

The field of **Quantum Engineering** [16], which is understood here as engineering of coherent quantum systems, includes, but is not limited to the two above fields. Quantum effects can be used to enhance the efficiency of numerous devices with respect to their purely classical counterparts, like solar cells [17]. Also, quantum systems can be used in another way: They can be used to obtain (quantum and classical) information about their environment, what can be used in scanning probe approaches to understand and improve devices even on the quantum level. This makes understanding and applying of quantum mechanics increasingly important in engineering.

This thesis deals with different aspects applicable in the above fields, such as single photon generation in single photon sources, on-chip integration of quantum networks, characterisation of quantum emitters and scanning probe microscopy using quantum systems. New technologies and devices for quantum science are developed and applied. In particular, the nitrogen vacancy centre in diamond, which can serve as a solid-state artificial atom, is employed as a model system to demonstrate these technologies.

The contents of this thesis' chapters are:

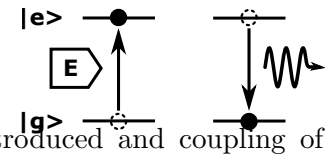

In **Chapter 2**, the concept of photons in a quantum mechanical sense, as it will be used in the other chapters, is introduced and some of the photons' properties are explained. Then, photon indistinguishability is introduced and coupling of light and matter is examined in the framework of quantum cavity electrodynamics. For practical experiments with single photons, techniques for their detection and preparation, i.e., single photon emitters and detection schemes, are shown.

Chapter 3 deals with the nitrogen vacancy centre (NV centre) in diamond. The NV centre is an optical emitter capable of emitting single photons and will be used throughout this thesis. Its optical as well as its spin properties are outlined and special attention is paid on the case of NV centres in nanodiamonds. These are well suited for integration into other nanoscale structures, however, their optical properties are degraded compared to bulk diamond. Hence, the behaviour of their zero phonon line is studied in an experiment on its ultra-fast spectral diffusion.

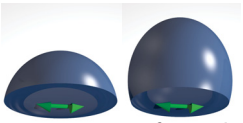

In **Chapter 4**, the problem of single photon collection is investigated. Collecting light from and optically addressing of single photon emitters like the NV centre requires microscopy, whose basic ideas and techniques are introduced. An important property of single photon sources is that they ideally always emit a stream of single photons without gaps, which leads to the requirement of having a high photon collection efficiency. Ways to improve this efficiency are shown with a special focus on a novel device for this task: elliptical solid immersion lenses.

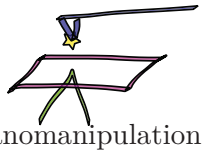

Chapter 5 introduces the atomic force microscope (AFM) and its application in fabrication of quantum systems from nanoparticles. An AFM can be used not only to measure topography, but also to manipulate the position of nanoparticles in so called nanomanipulation processes. Besides pushing the particles with the microscope, it is reported on a technique of picking up pre-characterised nanoparticles and placing them on micro- and nanostructures in a controlled way.

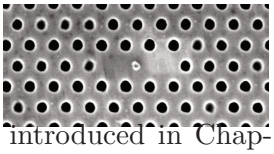

Chapter 6 deals with precisely fabricated hybrid systems, i.e., systems made from different material systems in order to get enhanced functionality. The hybrid systems shown here are assembled using the pick-and-place method introduced in Chapter 5. The first structure reported on is a nanodiamond with single NV centre coupled to a photonic crystal cavity in order to enhance its zero phonon line. The second system reported on is a directly fibre integrated single photon source made from a nanodiamond placed on a photonic crystal fibre.

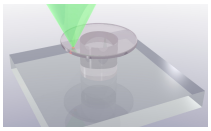

In **Chapter 7**, another approach with different properties to build hybrid systems is shown. Instead of nanoassembling the systems like in Chapter 6, the systems are built from a composite material. This material already consists of the structures' constituents from the start. By developing a hybrid material made from nanodiamonds and a photoresist, three-dimensional hybrid structures of nearly arbitrary shape can be built by two-photon direct laser-writing. Using this material, on-chip photonic circuits are built. These circuits are capable of generating single photons and guiding of light. Optical resonators for enhanced light matter interaction and resonant filtering can be integrated. Also, the single photon collection problem of Chapter 4 is tackled with the hybrid material by building parabolic antennas to redirect emitted photons.

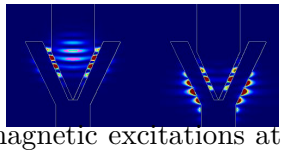

In **Chapter 8**, surface plasmon polaritons (SPPs) and their properties are introduced theoretically and investigated experimentally. SPPs are promising candidates to enhance light matter interaction and for guiding of electromagnetic excitations at the nanoscale. The generation of single propagating SPPs is shown and a coupler from a dielectric waveguide to SPPs is designed and numerically investigated.

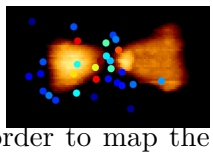

Chapter 9 introduces a way to measure the electromagnetic properties of structures on the nanoscale using single quantum emitters as probes. After theoretical pre-considerations, an experiment of manipulating the position of a single NV centre in order to map the local density of optical states (LDOS) at a plasmonic nanoantenna is demonstrated. Then, the technique of quantum emitter fluorescence lifetime imaging (QEFLIM) is introduced. QEFLIM, as a three-dimensional scanning probe technique, is used to map the LDOS in the vicinity of silver nanowires.

In the last chapter, **Chapter 10**, the experiments and techniques introduced here are reviewed in a summary and an outlook is given.

2. Single Photons

Single photons and especially single photon emitters are a central topic of this thesis. Hence, in this chapter, a short introduction to theory and experimental aspects of single photons is given. After introducing the general concept of a photon in Section 2.1, the theory of light matter interaction in the sense of cavity electrodynamics is introduced in Section 2.2. In Section 2.4, central aspects of single photon detection are discussed before in Section 2.5 emitters of single photons are introduced.

2.1. Photons and Non-Classical Light

In this section, the concept of a photon is introduced and the electromagnetic field is quantised. A part of this section deals with photon statistics, which is a very important property of light fields that will be used in many instances in this thesis.

2.1.1. The Photon

After the derivation of a formula describing black body radiation by Planck in the year 1900 [18] and the explanation of the photoelectric effect by Einstein in 1905 [19], both making use of quantisation, it was Lewis in 1926 [20] who coined the word photon. Even though its original meaning was slightly different, today photons are understood as the quanta of excitation of the quantised electromagnetic field with an energy E of

$$E = h\nu, \tag{2.1}$$

where h is Planck's constant and ν is the photon's frequency [21]. Although many phenomena in electrodynamics can be explained using classical Maxwell's equations, the concept of the photon can be used for their description, either for didactic reasons or for simplicity. In contrast, other important phenomena, like photon antibunching (see Section 2.1.3), cannot be described classically and the concept of a photon is mandatory for their description. A short derivation on how the electromagnetic fields can be quantised is given in the following.

2.1.2. Quantisation of Electromagnetic Fields

Here, for quantising the electromagnetic field, an approach using directly the energy of the electromagnetic field is used [13, 22]. The energy confined in an electromagnetic field is given by [23]:

$$W = H = \frac{C}{2} \times (\mathbf{E}^2 + c^2\mathbf{B}^2), \tag{2.2}$$

with $C = V\epsilon_0$ being a constant, ϵ_0 the permittivity of vacuum, and V an arbitrary Volume. This is a representation of the classical Hamiltonian H.

Assuming a complete set of eigenmodes in the volume, H can be written as:

$$H = \frac{C}{2} \sum_i c_i(\mathbf{E}_i^2 + c^2\mathbf{B}_i^2), \tag{2.3}$$

with the summation running over all modes and polarisations and the expansion coefficients c_i . For simplicity, in the following only one mode is considered:

$$H = \frac{C}{2}(E^2 + c^2B^2) \tag{2.4}$$

and time harmonic fields as given from the wave solutions of the Maxwell's equations, are assumed:

$$E = E_0 cos(\omega t + \phi), \tag{2.5}$$

$$B = cB_0 sin(\omega t + \phi) = E_0 sin(\omega t + \phi), \tag{2.6}$$

where ω is the frequency, ϕ is the phase, and the equal distribution of energy between electric and magnetic field has been used [23].

Now E and B are identified with the canonical variables P and Q in the following way:

$$Q = \sqrt{\frac{C}{\omega}}E;\ P = \sqrt{\frac{C}{\omega}}B. \tag{2.7}$$

This leads to a Hamiltonian of Form

$$H = \frac{\omega}{2}(P^2 + Q^2), \tag{2.8}$$

where the canonical variables Q and P fulfil the canonical Hamiltonian equations [24]:

$$\dot{Q} = \frac{\partial H}{\partial P} = \omega P,\ \dot{P} = -\frac{\partial H}{\partial Q} = -\omega Q, \tag{2.9}$$

which can be easily seen from Equations 2.5, 2.6 and 2.7.

Direct canonical quantisation by substitution of the of the Poisson brackets

$$\{f, g\} := \sum_{k=1}^{s} \left(\frac{\partial f}{\partial q_k} \frac{\partial g}{\partial p_k} - \frac{\partial f}{\partial p_k} \frac{\partial g}{\partial q_k} \right) \tag{2.10}$$

by the commutator times $-i/\hbar$ yields the operators $\hat{Q}$ and $\hat{P}$ with the commutation relation

$$[\hat{Q}, \hat{P}] = i\hbar. \tag{2.11}$$

Introduction of ladder operators $\hat{a}$ and $\hat{a}^\dagger$ following

$$\hat{a} = \frac{1}{\sqrt{2\hbar}}(\hat{Q} + i\hat{P});\ \hat{a}^\dagger = \frac{1}{\sqrt{2\hbar}}(\hat{Q} - i\hat{P}) \tag{2.12}$$

leads to a new representation of the Hamiltonian:

$$\hat{H} = \hbar\omega(\hat{a}^\dagger\hat{a} + \tfrac{1}{2}). \tag{2.13}$$

In this representation, it is obvious that the Hamiltonian of quantised fields is equivalent to a quantum mechanical harmonic oscillator [25] and all of its known results can be applied. The energy eigenstates to Equation 2.13 are so called number states or Fock states $|n\rangle$ satisfying [26]

$$\hat{a}^\dagger\hat{a}\,|n\rangle = n\,|n\rangle\,. \tag{2.14}$$

More information on the properties and consequences of Equation 2.13 can for example be found in Walls and Milburn [26]. From all these properties, the photon statistics, which is a central part of this thesis, is presented in the next subsection.

2.1.3. Photon Statistics

Light, i.e., a stream of photons, is not only characterised by an overall intensity, but also by its temporal fluctuations. These fluctuations can be described by looking at the temporal statistics of the arrival times of the photons. Figure 2.1 shows the distribution of the photon numbers in a given time interval for three kinds of light sources: a thermal light source like an incandescent light bulb in (a), a coherent light source like a laser in (b) and a perfect single photon source in (c). For a given average photon number $\bar{n}$, the probabilities P_n to find n photons in a measurement

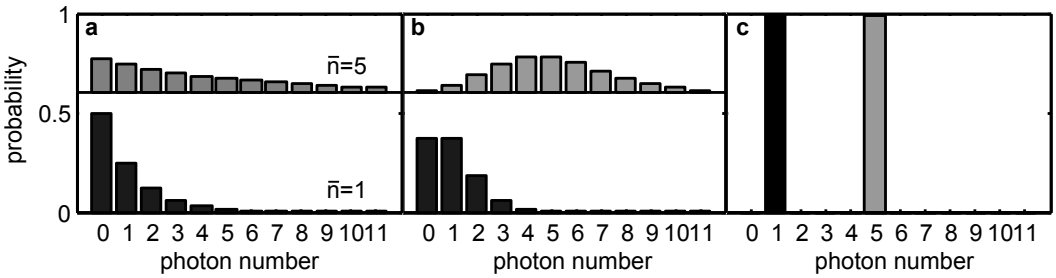

Figure 2.1.: Photon number distributions. For an average photon number $\bar{n} = 1$ (black) and $\bar{n} = 5$ (grey) the probability to find a certain photon number in a measurement is shown. In (a) for thermal light, in (b) for a Poissonian source like a laser and in (c) for a single photon source. The curves for $\bar{n} = 5$ are, except in (c), offset by a value of 0.6.

are [26]:

$$P_n = \begin{cases} \frac{\bar{n}^n}{1+\bar{n}^{n+1}}, & \text{for thermal light,} \\ e^{-\bar{n}}\frac{\bar{n}^n}{n!}, & \text{for coherent light,} \\ 0 \text{ for } n \neq \bar{n} & \text{for a number state.} \\ 1 \text{ for } n = \bar{n} & \end{cases} \tag{2.15}$$

As can be seen in Equation 2.15, the photon numbers of thermal light sources are described by a Bose-Einstein distribution and for coherent light sources by a Poissonian distribution. Both of these distributions can be derived using classical arguments [21]. In contrast, there is no classical derivation for the case of single photon sources, hence, they emit so called non-classical light.

One way to distinguish what kind statistics is present is to evaluate the intensity autocorrelation function (second order autocorrelation function of the electric field) $g^{(2)}(\tau)$ of the emitted light. This function is defined as:

$$g^{(2)}(\tau) := \frac{\left\langle : \hat{I}(t)\hat{I}(t+\tau) : \right\rangle}{\left\langle \hat{I}(t) \right\rangle^2} = \frac{\left\langle \hat{a}^\dagger(t)\hat{a}^\dagger(t+\tau)\hat{a}(t+\tau)\hat{a}(t) \right\rangle}{\left\langle \hat{a}^\dagger(t)\hat{a}(t) \right\rangle^2}, \tag{2.16}$$

with the intensity operator $\hat{I}(t) = \hat{a}^\dagger\hat{a}$, the time difference τ, :: indicating normal ordering of the operators, and $\langle ... \rangle$ indicating time averaging [27]. Evaluation of

Equation 2.16 for a time difference of $\tau = 0$ leads to

$$g^{(2)}(0) = \begin{cases} 2, & \text{for thermal light,} \\ 1, & \text{for coherent light,} \\ 1 - \frac{1}{n}, & \text{for a n-photon number state,} \end{cases} \tag{2.17}$$

what can be used as a criterion for determining the source type. The actual interpretation of this value is that if $g^{(2)}(0) > 1$, there is an increased probability of detecting a second photon directly after the first detection event, so called photon bunching. For $g^{(2)}(0) = 1$ the probability for detecting a second photon is independent on the time difference to previous events and for $g^{(2)}(0) < 1$ the probability for photon detection after a first event is reduced, what is called antibunching.

2.2. Cavity Electrodynamics

In this section, basic properties of the interaction between emitters of light and optical cavities will be discussed. This interaction leads to a variety of phenomena which can be exploited in order to tailor the properties of the emitter and the light it sends out. More detailed descriptions can be found for example in [28] and [13].

2.2.1. Pseudo-Spin Description of a Two Level System

A two level system can be described in analogy to a spin $\frac{1}{2}$ particle in a magnetic field [26]. The two states of the spins are then in a one-to-one correspondence with the two states of the two level system. This makes it convenient to describe the system by the Pauli spin matrices [26]:

$$\hat{\sigma}_x = \begin{pmatrix} 0 & 1 \\ 1 & 0 \end{pmatrix}, \quad \hat{\sigma}_y = \begin{pmatrix} 0 & -i \\ i & 0 \end{pmatrix}, \quad \hat{\sigma}_z = \begin{pmatrix} 1 & 0 \\ 0 & -1 \end{pmatrix}, \tag{2.18}$$

which leads to raising and lowering operators $\hat{\sigma}^+$ and $\hat{\sigma}^-$ given by:

$$\hat{\sigma}^+ = \hat{\sigma}_x + i\hat{\sigma}_y, \quad \hat{\sigma}^- = \hat{\sigma}_x - i\hat{\sigma}_y. \tag{2.19}$$

This is in analogy to the ladder operators introduced earlier in Equation 2.12. The Hamiltonian of the two level system is then given by [26]:

$$\hat{H}_E = \frac{1}{2}\hbar\omega_0\hat{\sigma}_z, \tag{2.20}$$

with $\hbar\omega_0$ being the energy difference of the two levels.

2.2.2. Jaynes-Cummings Model

To describe interaction between an emitter and a light field, the emitter is modelled as a two level system and the light field is treated as a quantum mechanical harmonic oscillator (cf. Equation 2.13). The interaction of emitter and field is given by [13]:

$$\hat{H}_I = \hbar\lambda(\hat{\sigma}^+ + \hat{\sigma}^-)(\hat{a} + \hat{a}^\dagger), \tag{2.21}$$

with λ being the coupling constant. with a light field of frequency ω, this leads to a full Hamiltonian of:

$$\hat{H} = \frac{1}{2}\hbar\omega_0\hat{\sigma}_z + \hbar\omega\hat{\sigma}_z + \hbar\lambda(\hat{\sigma}^+ + \hat{\sigma}^-)(\hat{a} + \hat{a}^\dagger). \tag{2.22}$$

Application of the so called rotating wave approximation (RWA), where operator products oscillating with $\omega_0 + \omega$ are assumed to average out and only keeping the difference terms leads to the Jaynes-Cummings Hamiltonian $\hat{H}_{JC}$ [13]:

$$\hat{H}_{JC} = \frac{1}{2}\hbar\omega_0\hat{\sigma}_z + \hbar\omega\hat{\sigma}_z + \hbar\lambda(\hat{\sigma}^+\hat{a} + \hat{\sigma}^-\hat{a}^\dagger). \tag{2.23}$$

2.2.3. Cavity-Emitter Coupling

Knowing the interaction Hamiltonian $\hat{H}_I$ of emitter and light field, the coupled system of emitter and cavity can be investigated. With a single excitation, the system can be in the states $|1\rangle = |e\rangle|0\rangle$ and $|2\rangle = |g\rangle|1\rangle$, where on the right hand side the first ket notes the emitters ground $|g\rangle$ and excited state $|e\rangle$ and the second ket the state of the cavity being empty $|0\rangle$ and occupied by a photon $|1\rangle$. To allow the excitation to leave the system, a third state $|3\rangle = |g\rangle|0\rangle$ is needed. For this situation, the master equation for the evolution of the density operator $\hat{\rho}$ reads (for details see [13]):

$$\frac{d}{dt}\hat{\rho} = -\frac{i}{\hbar}[\hat{H}_I, \hat{\rho}] - \frac{\kappa}{2}(\hat{a}^\dagger\hat{a}\hat{\rho} + \hat{\rho}\hat{a}^\dagger\hat{a}) + \kappa\hat{a}\hat{\rho}\hat{a}^\dagger, \tag{2.24}$$

where $\kappa = \omega_0/Q$ with the quality factor of the cavity Q. The quality factor is the ratio of the cavity's resonance frequency and its linewidth. On resonance ($\omega_0 = \omega$), for the elements of the density operator $\rho_{ij} = \langle i|\hat{\rho}|j\rangle$ this is equivalent to the following differential equations, the so called one photon Bloch equations [13]:

$$\dot{\rho}_{11} = \frac{i}{2}\Omega_0(\rho_{12} - \rho_{21}), \tag{2.25}$$

$$\dot{\rho}_{22} = -\frac{\omega_0}{Q}\rho_{22} - \frac{i}{2}\Omega_0(\rho_{12} - \rho_{21}), \tag{2.26}$$

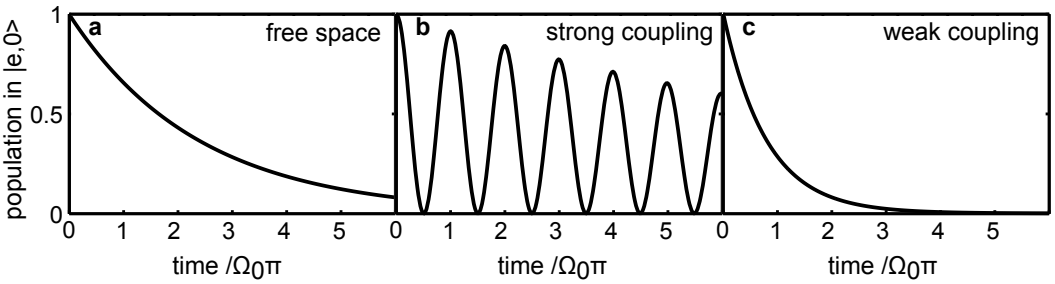

Figure 2.2.: Regimes of cavity quantum electrodynamics. In (a) the temporal evolution of the population of an initially exited emitter in free space is sketched. (b) shows the curve for strong coupling of the emitter to a cavity and (c) shows the case of weak coupling. In the weak coupling regime, the curve is an exponential, but with a higher decay rate than in the free space case.

$$\dot{\rho}_{12} - \dot{\rho}_{21} = i\Omega_0(\rho_{11} - \rho_{22}) - \frac{1}{2}\frac{\omega_0}{Q}(\rho_{12} - \rho_{21}). \tag{2.27}$$

$$\dot{\rho}_{33} = \frac{\omega_0}{Q}\rho_{22}, \tag{2.28}$$

with $\Omega_0 = 2\lambda$ being the vacuum Rabi frequency. As an additional constraint, the trace of the density matrix has to be one:

$$\rho_{11} + \rho_{22} + \rho_{33} = 1. \tag{2.29}$$

With the initial condition $\rho_{11}(0) = 1$, i.e., an initial excitation of the emitter, solving the system yields for ρ_{11} [29]:

$$\rho_{11}(t) = e^{-\frac{\kappa t}{2}}\left[\cosh\left(\frac{At}{2}\right) + \frac{\kappa}{A}\sinh\left(\frac{At}{2}\right) - \frac{2\Omega_0^2}{A^2}\right], \tag{2.30}$$

with A as an abbreviation for $\sqrt{\kappa^2 - 4\Omega_0^2}$.

2.2.4. Coupling Regimes

Equation 2.30 can be simplified by approximating for different ratios of damping κ and strength of the coherent dynamics expressed in terms of the vacuum Rabi frequency Ω_0. Two regimes are found:

- For $\kappa \ll \Omega_0/2$ the system is in the **strong coupling** regime. The coherent dynamics is much stronger than the damping, leading to (damped) oscillations

of the population of ρ_{11} [29]:

$$\rho_{11}(t) = \frac{1}{2} e^{-\frac{\kappa t}{2}} \left[1 + \cos(\Omega_0 t)\right]. \tag{2.31}$$

The oscillations can be interpreted as a photon being repeatedly emitted into the cavity and subsequently getting absorbed by the emitter, which is after emission in its ground state. Due to small, but present, damping the amplitude of the oscillations gets smaller over time.

- For $\kappa \gg \Omega_0/2$ the system is in the **weak coupling** regime. For ρ_{11} this leads to [29]:

$$\rho_{11} = e^{-\frac{\Omega_0^2}{\kappa t}}. \tag{2.32}$$

This is an exponential decay, analogous to the case without a cavity, but faster. The factor, by which the the decay is faster than the free space case, is called the Purcell factor F [30]. It is given by [29]:

$$F = \mathbf{F}(\mathbf{r}) \cdot \mathbf{e}_D \frac{\lambda_c^3}{4\pi^2} \frac{Q}{V_{eff}}, \tag{2.33}$$

where λ_c is the cavity's resonance wavelength, $\mathbf{F}(\mathbf{r})$ is a form factor accounting for the emitters positions, V_{eff} is the effective mode volume, and $\mathbf{e}_D$ is the unit vector in the emitter's dipole's direction.

Figure 2.2 shows the different regimes in comparison to the free space decay of the emitter. In this thesis, all experiments are carried out in the weak coupling regime.

2.3. Photon Indistinguishability

In the previous section, the interaction of light and matter was examined. Another important interaction in quantum optics is the interaction of two photons. This interaction can either be mediated by matter or, in contradiction to everyday life's experience, take place between the photons directly. While two classical macroscopic beams of light can cross another, this is not necessarily the case in quantum optics. In quantum optics, due to quantum interference, photon-photon interaction is possible [31]. The most prominent example of such an interaction is the Hong-Ou-Mandel (HOM) effect [32], where two indistinguishable photons interact at a beamsplitter in such a way, that they always exit one of the output ports bunched together.

The underlying reason for this bunching behaviour is explained in the following. For the description of a beamsplitter, firstly an equation which describes the

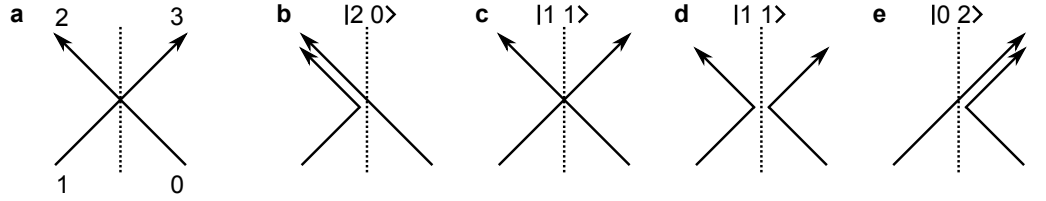

Figure 2.3.: Hong-Ou-Mandel effect. In (a), a sketch of a beamsplitter (dotted) and its input and output modes (1-4) is shown. (b-e) show four different situations for photons being reflected and/or transmitted. The situations in (c) and (d) interfere destructively, as can be seen from Equation 2.36. This leads to a bunching behaviour of two single input photons after the beamsplitter.

transformation of the two incoming modes (denoted as [0,1]) to the output modes (denoted as [2,3]) is needed. Note that a beamsplitter in quantum optics always needs to be described having two input ports [13]. For a beamsplitter consisting of a single dielectric layer, these equations read [13]:

$$\hat{a}_2 = \frac{1}{\sqrt{2}}(\hat{a}_0 + i\hat{a}_1), \tag{2.34}$$

$$\hat{a}_3 = \frac{1}{\sqrt{2}}(i\hat{a}_0 + \hat{a}_1), \tag{2.35}$$

where $\hat{a}_k$ denotes the annihilation operator of mode k. For the HOM effect, where the photons enter the beamsplitter through different ports, the input state at the beamsplitter is $|1\rangle_0 |1\rangle_1$, what is equivalent to $\hat{a}_0^\dagger \hat{a}_1^\dagger |0\rangle_0 |0\rangle_1$. After the action of the beamsplitter, the operators for modes 0 and 1 are replaced by the operators for modes 2 and 3 according to Equations 2.34 and 2.35. This yields:

$$|1\rangle_0 |1\rangle_1 \rightarrow \frac{1}{2}(i\hat{a}_2^\dagger \hat{a}_2^\dagger - \hat{a}_2^\dagger \hat{a}_3^\dagger + \hat{a}_2^\dagger \hat{a}_3^\dagger + i\hat{a}_3^\dagger \hat{a}_3^\dagger) |0\rangle_2 |0\rangle_3 . \tag{2.36}$$

As can be seen, the $\hat{a}_2^\dagger \hat{a}_3^\dagger$ terms, which would lead to one photon in each output mode have different signs and thus cancel out, what leads to:

$$|1\rangle_0 |1\rangle_1 \rightarrow \frac{i}{2}(|2\rangle_2 |0\rangle_3 + |0\rangle_2 |2\rangle_3). \tag{2.37}$$

Only states where the two photons are in the same mode exit the beamsplitter. Figure 2.3 shows the four terms in Equation 2.36. In the HOM effect, the situations in (c) and (d) interfere destructively.

The HOM effect is one of the main pillars in linear optics quantum computing

(LOQC) [33]. It forms the basis for the Knill-Laflamme-Milburn scheme, a quantum computing scheme which only needs linear optics, single photons, and photon detectors [34]. Using the HOM effect, entanglement has been demonstrated between two remote nitrogen vacancy centres in diamond (see Chapter 3) [35]. These possibilities have lead to a huge interest in achieving two-photon quantum interference and have triggered many works aiming at providing photon sources for this.

For the HOM effect to show up, besides temporal and spatial mode matching, which can easily be achieved by spatial filtering and optical delay lines, the main requirement is photon indistinguishability, i.e., that an exchange of the two photons does not alter the state. Therefore, production of a defined number of indistinguishable photons is a very important task for quantum optical photon sources.

In Section 2.5, different emitters of single photons are introduced. The degree of indistinguishability of the photons they emit depends on many different parameters, and effects like spectral diffusion (see Section 3.6) can even destroy the indistinguishability of subsequent photons from the same emitter. Another source of indistinguishable photons are photon pair sources based on parametric fluorescence [36], which can be able to produce two photons at the same time, which have exactly the same properties [32, 37].

When thinking of future extended quantum communications networks [38], compatibility of different kinds of sources becomes an issue. For this, quantum interference of photons from dissimilar sources in need. Semonstrations of this can be found in [39, 40]. dissimilar sources in need. Semonstrations of this can be found in [39, 40].

2.4. Measurement of Single Photons

In working with single photons, techniques to not only detect photons, but also to measure their temporal behaviour are essential. Here, some of these techniques, i.e., time correlated single photon counting and correlation measurements, are introduced. An overview of single photon detectors for quantum photonics, which are not covered here, can be found in Reference [41].

2.4.1. Time Correlated Single Photon Counting

One technique to measure the temporal properties of photon emitters is time correlated single photon counting (TCSPC) [42]. It uses single photon detectors and fast time measurement electronics to measure the arrival time of photons down to the picosecond timescale. A pulsed source excites the emitter and the arrival time of the subsequently emitted photons relative to the excitation pulses is measured. Since single photon counters are used and the electronics normally can only detect one event per cycle, care has to be taken that the probability of having two photons

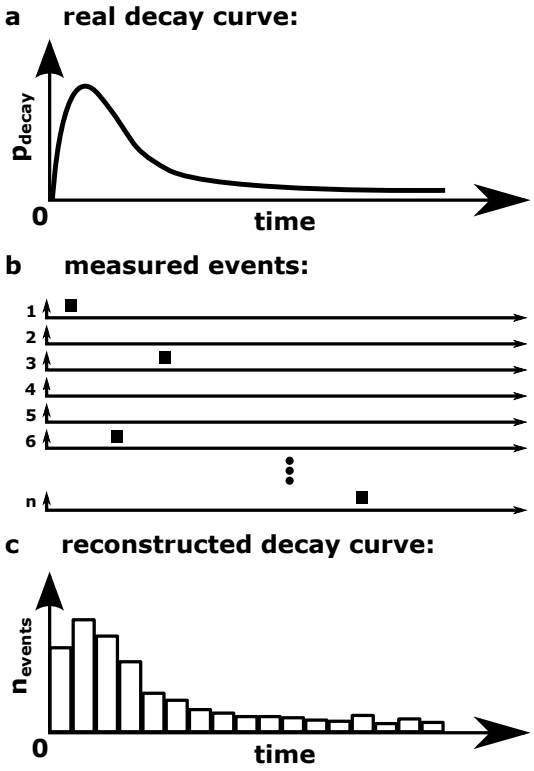

Figure 2.4.: Time correlated single photon counting. (a) shows the real decay curve of an emitter. (b) shows the distribution of events for the periods 1 to n and (c) shows the reconstructed decay curve, i.e., a histogram of this events.

in one cycle is practically zero, because a second photon can not be detected, what introduces an error. Modern electronics can circumvent this problem by having very short dead times and the ability to detect multiple events per cycle. A histogram of the inter-period arrival times of the individual photons now gives the overall decay behaviour of the emitter (see Figure 2.4).

An extension of this is the time tagged time correlated single photon counting (TTTCSPC, also called time tagged time resolved, TTTR) where for each individual photon not only the arrival time relative to the excitation pulses is stored, but the absolute arrival time with respect to the start of the measurement. This allows for more comprehensive analysis of the data obtained, for example time gating in post processing, as used in Section 3.6 or even techniques using gating and additional event markers as in Section 9.3.

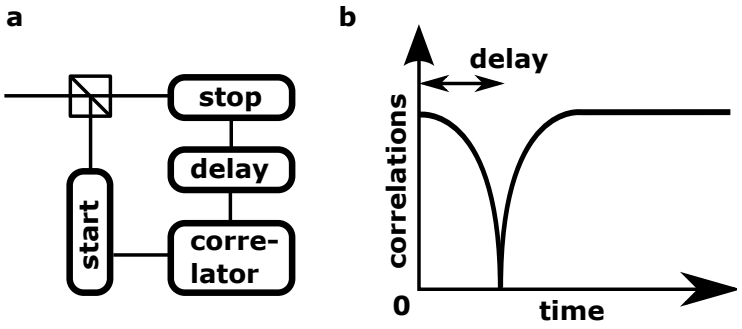

Figure 2.5.: Autocorrelation measurement. (a) shows a Hanbury Brown and Twiss setup. (b) is a sketch of an antibunched signal electronically delayed to compensate for dead times in the setup.

2.4.2. Measurement of $g^{(2)}(\tau)$

For the experimental determination of the second order correlation function $g^{(2)}(\tau)$, in principle one has to measure all the arrival times of the incoming photons and calculate their autocorrelation function. However, this is a very demanding task. With commonly used photodetectors, like avalanche photo diodes (APDs) or photomultiplier tubes (PMTs), the main limitation is the dead time of either the detector itself or of the timing electronics. Therefore, a so called Hanbury Brown and Twiss (HBT) setup [43] is used. A sketch of this setup can be found in Figure 2.5 (a). In this setup, the beam is split by a beamsplitter and sent to two detectors in order to circumvent the detector dead time. One detector is used to start and one is used to stop the time measurement. Further, a delay in the electronic signal of the detector connected to the stop compensates the electronics's dead time by shifting the zero delay time of the optical part towards the positive time axis of the electronic part (see Figure 2.5 (b)). It should be noted that an HBT setup only approximates the real $g^{(2)}(\tau)$ because only photon pairs hitting the start detector with one photon and the stop directly afterwards are recorded leading to a loss of 3/4 of the events and an error for longer correlation times. Also, this approximation is only valid when the probability to detect the individual photons is low. Then, correlations among the photons do not influence the measurement in an unwanted way, since their contribution to the detection probability is negligible.

2.5. Single Photon Emitters

Classical light, such as light from incandescent light bulbs (thermal light, Figure 2.1 (a)) and lasers (coherent light, Figure 2.1 (b)), is easily available and used in everyday life. For non-classical light this is not the case, since the required

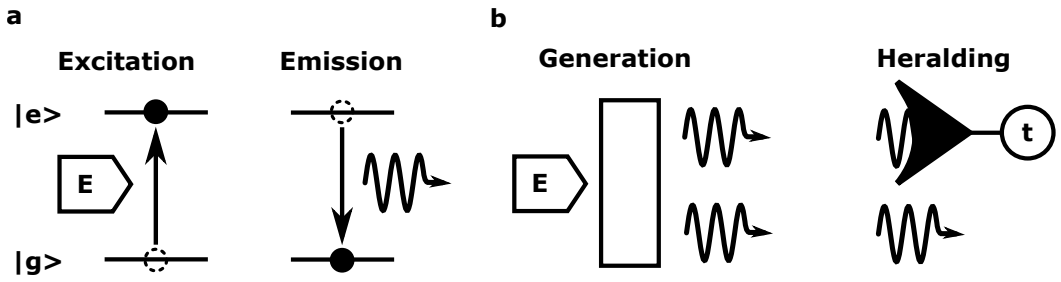

Figure 2.6.: Single photon emission. (a) Sketch of a deterministic single photon emitter. It is excited, what, for example due to Coulomb interaction or the Pauli principle [45], leads to one single excitation in the system. This excitation subsequently spontaneously decays and a single photon is emitted. (b) Sketch of a probabilistic source. A correlated photon pair is generated, e.g., by parametric fluorescence [36]. One of the photons is detected to herald the remaining single photon.

technology is still in its infancy. Also, generation (and measurement) of single photons today often requires special equipment and is in most cases only feasible in a laboratory environment. Figure 2.6 sketches the basic working principle of single photon sources. Either a single excitation is used to create a single photon (Figure 2.6 (a)) or correlated photons are created, with one being detected to herald the other (Figure 2.6 (b)) [44]. Note that the so called heralded single photons are not single photons in a strict sense, since they are never in the corresponding pure Fock state.

In the following, an overview of the most common single photon emitters is given. More detailed description of single photon emitters are given by Lounis et al. [46] and Eisaman et al. [47].

2.5.1. Atoms

Neutral atoms can be used as single photon emitters [48, 49] and antibunching has been observed for the first time on a beam of Na atoms [48]. In more advanced schemes aiming at high rates of single photon generation, the atoms are cooled by a laser [50, 51] in a magneto optical trap [52]. Subsequently they fall through a high finesse cavity so one can get single photons out, but only when there is exactly one atom inside the cavity. This is a statistical process resulting in time spans with single photon emission (one atom present), without emission (no atom present) or multiphoton emission (more than one atom). This can be overcome by trapping a single atom in a dipole trap [53–55], where it is possible to hold the atom on the timescale of several seconds.

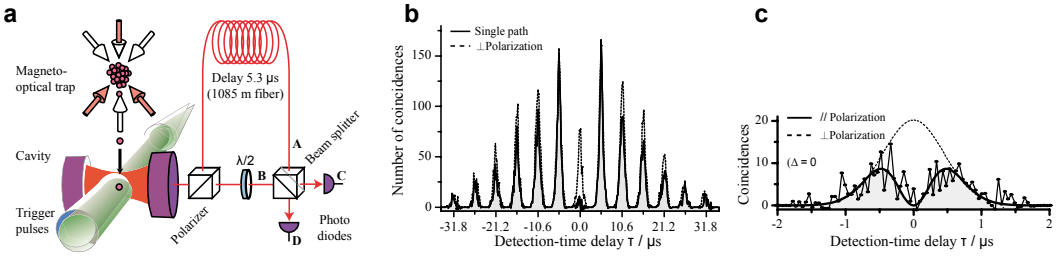

Figure 2.7.: Indistinguishable photons from atoms. (a) shows the setup used by Legero *et al.* [56] to produce and analyse indistinguishable photons from atoms. Atoms are first trapped in a magneto optical trap. Then, they fall through an optical cavity, where laser light triggers the emission of single photons, if there is only one atom in the cavity. Subsequently, the single photons are sent through an interferometer with single photon detectors at both output ports. (b) shows the measured coincidences with one interferometer arm blocked (solid line), where a pronounced antibunching dip is visible. If the arm is open, but the arms are polarised differently (dotted line), the depth of the dip is reduced to about 0.5 (cf. Equation 2.17). (c) shows the coincidences for both arms open for parallel and perpendicular polarisations. For parallel polarization, the coincidences are suppressed at zero time delay due to the Hong-Ou-Mandel effect (see Section 2.3). (adapted from [56])

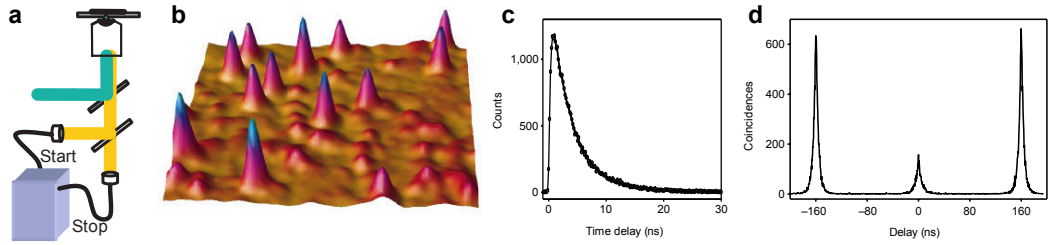

Figure 2.8.: Single photons from molecules. (a) setup used by Lounis *et al.* [59] to measure single photon emission from molecules at room temperature. A confocal microscope (see Section 4.1) is used to excite the molecules and collect the light, which is analysed by a HBT correlator. (b) is a 10 µm by 10 µm confocal micrograph of single terrylene molecules. (c) shows a lifetime histogram of such a molecule acquired by TCSPC. In (d), the autocorrelation function as acquired with the HBT correlator is shown. The peak at zero time delay is heavily suppressed, indicating single photon emission from the molecule. (adapted from [59])

Ionised atoms have the advantage that they can be held in radio frequency traps due to their charge [57]. In this way, it can be assured that there is always one single ion emitting single photons. Also, it is possible to implement various miniaturised ion traps on a semiconductor chip [58]. With today's semiconductor fabrication techniques, this could open a way for implementing many (interacting) single photon emitters in a small volume.

Photons emitted by atoms usually have small linewidths and are indistinguishable [56] – very useful features for most quantum optics applications. A measurement on the indistinguishability of photons emitted by atoms is shown in Figure 2.7. Major disadvantaged of atoms as single photon emitters are the complicated laser systems and ultra-high vacuum apparatuses needed, which easily can fill up a whole laboratory. Also, for many ions the optical transitions lie in the ultraviolet spectral range [47]. This makes the optical elements expensive and hinders effective use of optical fibres due to their high absorption at these wavelengths.

2.5.2. Molecules

Single molecules are capable of emitting single photons at cryogenic temperatures [60] as well as at room temperature [59, 61]. Single photon emission was first demonstrated by molecules embedded in a solid [60], but is also possible for molecules in solution [62]. An optical measurement of single terrylene molecules is shown in Figure 2.8. The level structure of fluorescent molecules can be described by a three level system with a singlet ground state $|S_0\rangle$, an exited singlet state $|S_1\rangle$, and an intermediate triplet state $|T_1\rangle$. Single photons are emitted when the

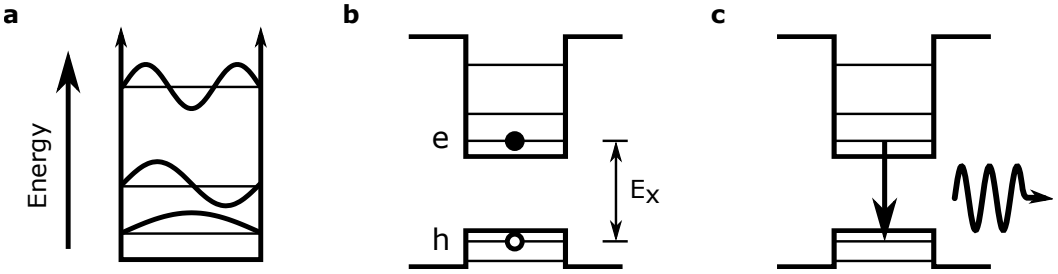

Figure 2.9.: Quantum dot level structure. (a) shows a particle in an infinite potential well. Discrete energy levels (vertical lines) arise from the confinement. Also, the corresponding wave functions are indicated. (b) shows the level structure of a quantum dot. Electron e and hole h are separated by the energy difference E_x. (c) shows the recombination of electron and hole, which leads to emission of a single photon.

molecule is pumped from $|S_0\rangle$ to $|S_1\rangle$ and then relaxes to $|S_0\rangle$. With a small probability it can also enter the triplet state $|T_1\rangle$, which is a dark state, i.e., no photon is emitted [47].

Besides many advantages of single molecules as single photon emitters like narrow, at cryogenic temperatures even Fourier limited, zero phonon lines (ZPLs) [63], their main drawback is their lack of stability. They show a blinking behaviour and there is always a chance of destroying the molecule irreversibly via photo bleaching [64].

2.5.3. Quantum Dots

Quantum dots are semiconductor structures so small, that their radius a becomes comparable to the exciton Bohr radius a_b [65]. In the case $a \ll a_b$, the so called strong confinement regime, electron and hole behave like particles in a box, and therefore have discrete energies (see Figure 2.9 (a)) [66]. Because of this, the energy of an electron hole pair inside the quantum dot is also discretised (Figure 2.9 (b)). When electron and hole recombine, this energy can be released as a single photon (Figure 2.9 (c)). Coulomb interaction between electron and hole gives rise to additional terms when calculating the energy. Further corrections are introduced when dealing with more complicated states like the biexciton (a state of two excitons [67]) or the trion (a state of an exciton together with an additional electron or hole [68]). A measurement indicating single photon emission from colloidal CdSe/ZnS quantum dots is shown in Figure 2.10 [69]. Besides single photon emission, a pronounced blinking behaviour is visible.

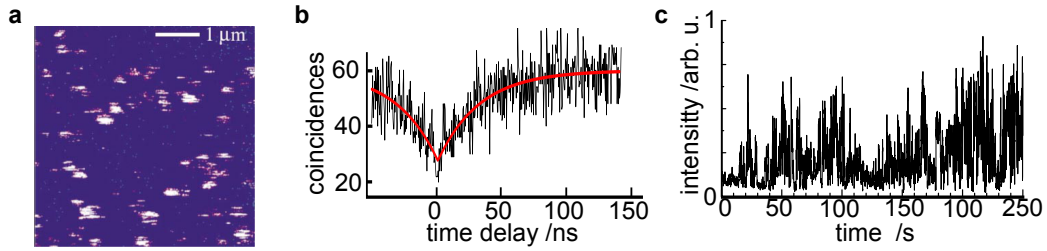

Figure 2.10.: Single photons from CdSe/ZnS quantum dots. (a) shows a confocal microscopy image of CdSe/ZnS quantum dots on glass as measured by Michler *et al.* [69]. Blinking of the quantum dots is visible as bright or dark lines along the scanning direction. (b) is an antibunching measurement from a single quantum dot indicating single photon emission. The red line is a fit to the data. (c) shows the blinking behaviour of a CdSe/ZnS quantum dot. The quantum dot switches from bright states to dark states and vice versa. (adapted from [69])

2.5.4. Defect Centres in Wide Band Gap Semiconductors

Defect centres in wide band gap semiconductors have attracted much attention as single photon emitters. However, there is only a small number of single photon emitting defect centres known, for example in zinc oxide [70], in silicon carbide [71] or in diamond [72], but it is likely that more are about to be discovered. In diamond alone, more than 500 centres have been discovered [73], which by far not all have been explored in detail. The centres consist of impurities and/or vacancies in the semiconductor's crystal lattice, leading to additional energy levels inside the band gap.

Defect centres in diamond are the best studied ones and single photon emission has been proven for the nitrogen-vacancy centre (NV centre) [74], the nickel-nitrogen complex (NE8) centre [75], the silicon-vacancy centre (SiV centre) [76] and a chromium related centre [77]. In addition to naturally occurring defect centres or ones generated during artificial crystal growth, defect centres can be created via ion implantation [78]. In this way, it is possible to have centres at pre-defined sites [79].

The size of the defect centre's host crystal can be on the order of 10 nm [80]. Optically active SiV centres have been found in crystals that did only contain about 400 Carbon atoms, corresponding to a size of 1.6 nm [81]. These so called nanocrystals can be moved via nanomanipulation techniques, which allows for robust controlled coupling of single photon emitters to photonic structures (see Section 5.2).

Throughout this thesis, the NV centre will be used as a single photon emitter, hence this centre is introduced in detail in Chapter 3.

Chapter Summary: Single Photons

In this chapter, the concept of single photons and some of their important statistical properties were introduced. Coupling of light and matter was discussed in the framework of cavity electrodynamics and two-photon quantum interference was introduced. Methods for measuring single photons as well as the emitters of single photons were shown. Measurement and generation of single photons are an integral part of the experiments reported in this thesis, what makes the concepts and methods shown here indispensable for all the other chapters. While here a broad overview of single photon emitters was given, in the remainder of this thesis mostly the NV centre in nanodiamond will be used. In the next chapter, the NV centre as a single photon emitter will be explained in detail.

3. The Nitrogen Vacancy Centre

In this chapter, the nitrogen vacancy centre (NV centre) in diamond is introduced. It will serve as a single photon emitter throughout this thesis. The NV centre is the most prominent defect centre in diamond and the most intensively studied one [80].

After showing the NV centre's structure in Section 3.1, its optical and spin properties will be examined in Sections 3.2 and 3.3, respectively. A special case are NV centres in diamond nanoparticles, whose properties are introduced in Section 3.4. Applications of NV centres are reviewed in Section 3.5, before concluding by showing an experimental work on measuring the ultra-fast spectral diffusion which can be encountered for NV centres in nanodiamonds in Section 3.6. The experiment on the measurement of the ultra-fast spectral diffusion is also featured in the publication *Measurement of the Ultrafast Spectral Diffusion of the Optical Transition of Nitrogen Vacancy Centers in Nano-Size Diamond Using Correlation Interferometry* published in *Physical Review Letters* [82].

3.1. Diamond and the NV Centre

Diamond is a material with a number of extraordinary properties. These properties, some of which will be highlighted here, make diamond a valuable gem stone and also lead to a large variety of technical applications [83]. Diamond is a crystal consisting of carbon atoms in a face centred cubic (fcc) lattice with a lattice constant of 3.56 Å and a two atom basis [84]. It can be found occurring naturally as a mineral or can be grown artificially [85].

In today's industrial applications, the most important property of diamond is its extraordinary hardness (10 on the Mohs scale and 45.3 on the Vickers scale [84]). But especially for quantum applications, the following properties can be also very important [80]:

- **Band gap:** A wide band gap of 5.5 eV [80] leads to a large transparency window from the ultra-violet to the infra-red.
- **Refractive index:** An index of refraction of 2.4 enables for tight confinement and guiding of light.
- **Thermal conductivity:** Diamond has one of the highest thermal conductivities known [86]. This can be used to guide away heat produced in the

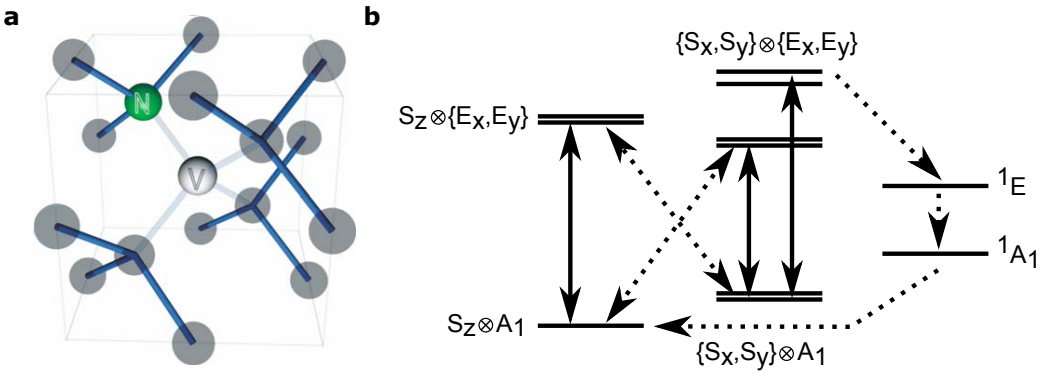

Figure 3.1.: Atomic and level structure of the NV centre. (a) shows the NV centre. A nitrogen atom (N) is substituted for a carbon atom adjacent to a vacancy (V) in the diamond lattice. (b) shows the level structure of the NV^- centre without strain or external fields applied and the associated transitions indicated by arrows for optical transitions and dotted arrows for other relaxation paths. Strain can alter the level structure, as can be seen in 3.3 (b). (For details and a derivation see [88]). ((a) from [89], (b) after [88])

quantum device or to more easily reach low temperatures, as required for some applications.

- **Breakdown voltage:** A high breakdown voltage, as the one of diamond, is useful for electrical devices such as diodes, since higher fields can be applied to the material without destroying the device.

Besides these properties, what makes diamond an ideally suited quantum optical material, is the existence of defects in the diamond lattice, such as the nitrogen vacancy centre – one of the so called colour centres in diamond. Their name stems from the fact that these centres are optically active, giving the otherwise transparent diamond a colour.

In natural diamond, the NV centre is the most abundant colour centre. Besides its natural occurrence, it is also found in artificial diamonds and can furthermore be produced by radiation damage due to irradiation and subsequent post annealing or by direct implantation of nitrogen [87].

The centre consists of a vacancy in the diamond lattice with an adjacent substitutional nitrogen atom, as shown in Figure 3.1. It therefore belongs to the $C_{3\nu}$ symmetry group. From this symmetry, information on the optical properties, which will be discussed in the next section from a more phenomenological point of view, can be obtained [88].

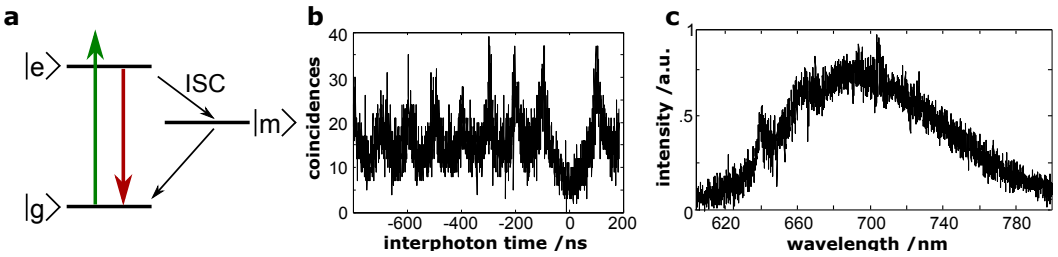

Figure 3.2.: Optical properties of the NV$^-$ centre. (a) Simplified level scheme of the NV$^-$ centre. The system can be pumped off-resonantly from the ground state $|g\rangle$ in the excited state $|e\rangle$, from where it decays under photon emission back to the ground state or, with a smaller probability, undergoes inter-system-crossing to a metastalbe state $|m\rangle$. (b) Autocorrelation function of photons emitted by a NV$^-$ centre in nanodiamond under pulsed excitation (repetition rate 10 MHz). Clearly, the peak at zero time delay is missing, indicating single photon emission. (c) Room temperature fluorescence spectrum of the same NV$^-$ centre. A low temperature spectrum of another NV centre can be found in Figure 3.5. (Data also published in: [91])

3.2. Optical Properties

The optical properties of the NV centre are remarkable. It is the first defect centre where single photon emission was proven [74] and, like many defect centres in diamond, it is photostable and able to emit single photons even at room temperature [74].

The most common charge states of the NV centre are the neutral NV^0 and the negatively charged NV$^-$ [90]. Their zero phonon lines (ZPLs) are at 575 nm and 637 nm, respectively [72]. Broad phonon sidebands accompany the ZPLs even at low temperatures. The Debeye-Waller factor – a measure for the share of zero phonon line and sidebands – is very small (0.04) [72].

The NV$^-$ level structure can be approximated by a three level system with a triplet ground state $|g\rangle$, a triplet excited state $|e\rangle$, and a single metastable state $|m\rangle$ [89]. This approximation, though very simple, is good enough to explain all the effects encountered in the experiments shown throughout this thesis. Other effects, like the possibility to address the NV centres spin (see Section 3.3), need a more complicated scheme. More detailed level schemes of the NV$^-$ centre and transition rates can be found in [88, 92, 93]. The system can be optically pumped from the ground state $|g\rangle$ in the excited state $|e\rangle$, from where it decays under photon emission back to the ground state or, with a smaller probability, undergoes inter-system-crossing (ISC) to a metastalbe state $|m\rangle$ (see Figure 3.2). The excited state lifetime at room temperature is circa 12 ns in bulk diamond [88]. In the NV

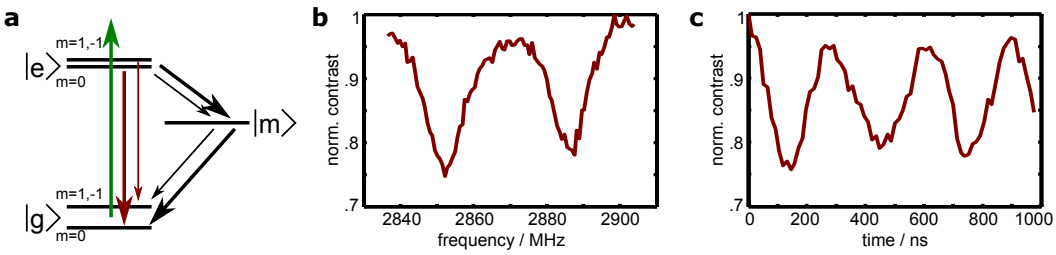

Figure 3.3.: Spin physics of the NV$^-$ centre. (a) is a simplified level scheme of the NV$^-$ centre (*cf.* Figure 3.2) including the relevant spin sublevels of ground and excited state. The thickness of the arrows indicates the strength of the transitions. This level scheme enables for optical detection of the magnetic resonance of the spin (for details see text). (b) shows the measured contrast in fluorescence signal versus the frequency of microwaves applied to a NV centre. Two dips can be seen at the positions, when the frequency corresponds to the transitions $m = 0 \rightarrow m = 1$ and $m = 0 \rightarrow m = -1$. The degeneracy of the $m = 1$ and $m = -1$ levels is lifted due to strain in the crystal and a magnetic field. (c) shows optically detected Rabi oscillation of the spin of a single NV centre. [98]

centre, due to its symmetry, emission occurs via two perpendicular dipoles [88]. For the polarisation if the emission this results in a pattern corresponding to the two dipoles – a pattern which is less directional than the one corresponding to a single dipole. This may lead to reduced efficiencies when coupling to cavities in cavity quantum electrodynamics (see Section 2.2). Tuning of the emission wavelength is possible via the Stark effect [94].

3.3. Spin properties

Besides its optical properties, the NV$^-$ centre also possesses useful electron spin properties, which make it a nearly ideal model system to study the behaviour of a single spin.

The NV centre's ground state is split by spin-spin-interaction into sublevels $|e\rangle_{m=0}$ and $|e\rangle_{m\pm1}$, which are separated by 2.88 GHz [95]. It is possible to read out the spin of the ground state optically [96] even at the single centre level [97]. The reason for this process called optically detected magnetic resonance (ODMR) can be seen when looking at the level scheme in Figure 3.3 (a). On excitation, which is spin conserving, the excited state has different decay channels depending its current spin state. For the $m = 0$ state, the probability of decaying into the ground state is higher than for the $m = \pm1$ states, which have a higher probability of decaying into the metastable state than the $m = 0$ state. Since the metastable

state has a relatively long lifetime on the 100 ns time-scale [99] and a non-radiative decay, this makes fluorescence from the $m = 0$ measurably brighter. Hence, just by comparing the fluorescence intensities, the spin state can be read out. The decay channel through the metastable state is not spin conserving, so by decaying through the metastable state, there is a chance that the information on the initial spin state is lost [100]. At first sight, this seems to be a drawback, but in fact, this can be used to spin polarise the NV centre: the decay from the metastable state preferentially occurs into the $m = 0$ state, so after a few cycles, the NV centre will be polarised in the $m = 0$ state [100].

By applying microwave radiation resonant with the ground states level splitting, the electronic spin of the centre can be manipulated directly. In Figure 3.3 (b), the measured fluorescence signal versus the frequency of microwaves applied to a NV centre is shown. When the microwave is resonant with the ground state splitting, the fluorescence is decreased because the the NV centre spends more time in the darker $m = \pm 1$ state. In Figure 3.3 (b) two of these dips can be seen because of strain in the diamonds crystal and an additional magnetic field, which shift the levels $m = 1$ and $m = -1$ differently.

This control of the spin state via application of microwaves can be used to do spin manipulation with a single spin in the solid state. For example, as it is shown in Figure 3.3 (c), it is possible to drive Rabi oscillations [101]. The coherence time (T_2) of the NV centre's spin can reach values of nearly 1 s – a value very large for optically addressable solid-state systems [102]. Using the NV centre to optically address nearby nuclear spins, whose coherence times are usually longer than electronic ones [103], even longer coherence times for a spin qbit of over 1 s can be achieved [104]. These excellent spin properties are one of the main driving forces behind applications of NV centres (see Section 3.5) and the interest in their integration into photonic structures (see Chapters 6 and 7).

3.4. Nanodiamonds

When diamond crystals are very small (usually smaller than circa 100 nm), they are called nanodiamonds. Their main applications are grinding and polishing processes in industry, which are making use of diamonds hardness without using its optical properties. To produce nanodiamonds, two main processes have emerged: detonation derived samples (detonation diamonds) and high-pressure high-temperature (HPHT) synthesised samples [105]. On much smaller scales, there exist more techniques to produce nanodiamonds, for example bead assisted sonic disintegration (BASD) [106], where nanodiamonds are produced from bulk diamond. Besides this, nanodiamonds can be found naturally in meteorites [107]. All these kinds of nanodiamonds have different properties such as purity and therefore abundance of

defects.

Optically active defect centres have been found in nanodiamonds only consisting of about 400 carbon atoms, corresponding to a size of only 1.6 nm [81]. What makes defect centres nanodiamonds especially interesting, is that they can be integrated into photonic structures made from other material systems in a so-called hybrid approach (see Chapters 6 and 7) [108]. In this approach, due to the combination of different materials, it is possible to use particular strengths of the individual material systems while avoiding their weaknesses.

For defect centres in nanodiamond, this flexibility comes at a cost. The optical as well as the spin properties of defect centres nanodiamonds are inferior the properties in bulk diamonds. For example, the quantum efficiency of the nitrogen vacancy centre in nanodiamonds varies widely from 10 % to 90 % [109] and blinking of the in diamond stable centre can be observed [110]. While there is still no satisfactory explanation on the details, it seems that the main reasons for this are strain in the nanodiamonds lattice, impurities (compared to ultra-clean artificial bulk diamond), and the crystals surface, which in nanoparticles always is very close to the defect centre [111]. One phenomenon, which can be found in NV centres in nanodiamonds, is ultra-fast spectral diffusion [82]. To understand and prevent this would enable for coupling of different NV centres in nanodiamond optically, what would immediately lead to a vast amount of new applications of the techniques described in this thesis. A detailed discussion of the ultra-fast spectral diffusion is shown in Section 3.6.

3.5. Applications

Being a photostable single photon emitter even at room temperature, an obvious application for the NV centre is as a single photon source. Compared to most other single photon emitters introduced in Section 2.5, which often need cryogenic cooling (self assembled quantum dots), complicated trapping (atoms/ions) or have problems with photostability (colloidal quantum dots/molecules), the NV centre can be easily integrated and used. In Section 6.2, an example of a single photon source based on a directly fibre coupled NV centre is shown. Other implementations include approaches to miniaturise confocal microscopes [112], direct coupling to tapered fibres [113, 114] or even electrically pumped light emitting diodes [115, 116]. First experiments using single photons generated by NV centres in conventional microscopes as well as from more sophisticated sources have been carried out, e.g., in quantum key distribution [112, 117].

Besides just providing photons for experiments, the possibility of addressing single electron spins provided by NV centres enables for experiments in fundamental physics. Recently, the quantum Zeno effect on a single solid state system has been demonstrated [118], quantum nonlocality has been investigated by performing Bell

tests [119], and quantum contextuality was examined [120].

In the field of quantum information science [1], the high degree of control that can be achieved over NV centres' quantum states makes them particularly useful as qbits [121, 122]. Experimentally, entanglement of distant NV centres [35] and quantum teleportation [123] have been successfully demonstrated, paving the road to more complex experiments.

Another application for NV centres is to use them in sensing [124]. In Chapter 9, the optical transition of the NV centre is used to acquire information on the local density of optical states at the nanoscale. Other sensing methods make use of the NV centre's spin properties, like magnetic field sensing [125, 126], electric field sensing [127], and measuring temperature [128–130]. Here, one of the advantages of the NV centre is that it is easily read out and it is also a small nanoscale object. Hence, it can be used as a very small local probe. Proposals exist also for sensing of other quantities like gravitation [131] or rotations [132].

Like other nanoscale photon emitters, nanodiamonds containing NV centres can also be used as a biomarkers [133]. They are not cytotoxic and, if irradiated nanodiamonds with many centres are used, very bright biomarkers whose surface furthermore can be functionalised easily [133]. Its applications in biology are not limited to optical microscopy: their spin properties can be used for tracking of individual nanodiamonds inside living cells [134] or for magnetic imaging of cells [135].

3.6. Measurement of Ultra-Fast Spectral Diffusion

As shown in Section 3.4, working with NV centres in nanodiamonds has many advantages, but also introduces some difficulties. One main difficulty with NV centres in nanodiamond is spectral diffusion of the zero photon line. Spectral diffusion is a phenomenon often encountered in solid state single photon emitters for example in quantum dots [136], molecules [137], and defect centres [95]. The zero phonon line of the emitter is shifting spectrally over time. This is an unwanted behaviour for single photon sources in most applications in quantum information science, since it destroys the photon indistinguishability required for two-photon interference [31] and makes resonant addressing of the emitter difficult (see Section 2.3). Spectral diffusion hence hampers scaling up quantum optical systems from systems with one single photon emitter to systems with multiple interacting single photon emitters at multiple locations.

To counteract the unwanted process of spectral diffusion, active stabilisation schemes can be employed. For example, locking of the resonance frequency of a quantum dot to optical transitions in a Rubidium gas has been demonstrated [138] and an active stabilisation of nitrogen vacancy centres in bulk diamond has been achieved [139]. One requirement for these active stabilisation schemes is that the

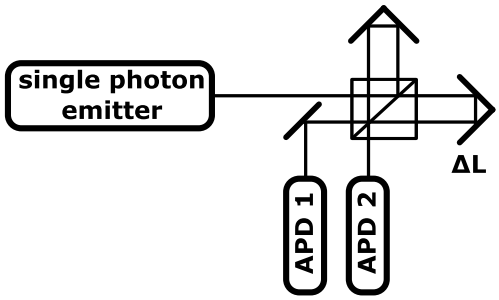

Figure 3.4.: Spectral diffusion measurement scheme. The spectral position of a single photon emitter is converted to intensity fluctuations in a Mach-Zehnder interferometer and read out using two APDs. The interferometer arms are unbalanced with a path length difference of $2\Delta L$.

spectral diffusion is sufficiently slow to allow for detection of the current position of the line. It is therefore important to understand the underlying processes in order to engineer the properties of spectral diffusion, and, in the best case, completely inhibit it.

3.6.1. Measurement Scheme

It is straightforward to measure spectral diffusion by simply looking at the behaviour of the emission line with a spectrometer's camera [140], however, for high time resolutions other techniques have to be employed. For quantum dots, it has been shown that using two monochromators and avalanche photo diodes subnanosecond time resolutions for the measurement of spectral diffusion can be achieved, which is considerably faster than the time resolutions on the millisecond scale achievable with cameras [141]. Another technique to measure spectral diffusion on fast timescales is to convert the spectral fluctuations of the emitter to intensity fluctuations via changing the path length in an interferometer, as used in References [142, 143]. Both approaches have certain limitations, for the first its the bulky setup employing two independent monochromators and the second need moving parts, which effectively limits its time resolution to the order of approximately 100 µs.

To overcome this, here, a way to measure the rate of spectral diffusion interferometrically without any moving parts is introduced [82]. With an unbalanced Mach-Zehnder interferometer, spectral jumps of a single photon stream are converted into intensity fluctuations, which are being detected at the interferometer's two output ports with single photon counting avalanche photo diodes (see Figure 3.4).

The photon detection rate for the symmetric (asymmetric) port $\langle \hat{I}_{S/A,\lambda}(t) \rangle_t$ is

given by time averaging the intensity operator:

$$\hat{I}_{S/A,\lambda}(t) = \eta_{S/A,\lambda}\, \hat{n}(t)\, m_{S/A\,\lambda}(t), \tag{3.1}$$

with the detection quantum efficiency $\eta_{S/A,\lambda}$, the modulation introduced by the interferometer $m_{S/A,\lambda}(t)$, and the photon number operator $\hat{n}(t) = \hat{a}^\dagger \hat{a}$. The wavelength dependence in the indices will be suppressed in the following calculations. The modulation term for a Mach-Zehnder interferometer is given by:

$$m_{S/A}(t) = 1 \pm c \sin\left(\frac{2\pi x}{\lambda(t)}\right), \tag{3.2}$$

with the path length difference $\Delta L = x$ and the contrast of the interference fringes c. Plus and minus sign correspond to symmetric and asymmetric port, respectively. The cross-correlation function $g^{(2)}_{SA}(\tau)$ between the arm is given by:

$$g^{(2)}_{SA}(\tau) = \frac{\left\langle : \hat{I}_S(t)\hat{I}_A(t+\tau) : \right\rangle_t}{\left\langle \hat{I}_A(t) \right\rangle_t \left\langle \hat{I}_S(t) \right\rangle_t}, \tag{3.3}$$

$$g^{(2)}_{SA}(\tau) = g^{(2)}(\tau) \langle m_S(t) m_A(t+\tau) \rangle_t, \tag{3.4}$$

where for the second equation the definition of the second order autocorrelation function $g^{(2)}(\tau)$ in Equation 2.16 is used. At this point, some assumptions on the emitter under investigation and the interferometer have to be made. Firstly, the emitter jumps in between random positions under a broad envelope. Broad here means broader than the emission's linewidth. Secondly, the jumps lead to a significant changes in the intensities at the interferometer outputs and several interferometer fringes lie in this envelope, what can be achieved by choosing a suited arm length difference ΔL.

The information on spectral jumps is now contained in the term $\langle m_S(t) m_A(t+\tau) \rangle_t$. It can be evaluated by introducing the probability $p(\tau)$ that the signal is unchanged after a time interval τ:

$$\langle m_S(t) m_A(t+\tau) \rangle_t = p(\tau) \langle m_S(t) m_A(t) \rangle_t + (1 - p(\tau)) \cdot \langle m_S(t) m_A(t') \rangle_{t,t'}. \tag{3.5}$$

Now, Equation 3.2 is used to evaluate the first and second part of the sum in Equation 3.5, i.e.:

$$\langle m_S(t) m_A(t) \rangle_t = 1 - \frac{c^2}{2}, \tag{3.6}$$

$$\langle m_S(t) m_A(t') \rangle_{t,t'} = 1, \tag{3.7}$$

where in the second equation the fact was used, that for several interferometer fringes and random jumps the sine terms average out. Furthermore, the same is true for instabilities of the interferometer, as long as they are on timescales longer than the spectral diffusion. Putting everything back in Equation 3.4 yields:

$$g^{(2)}_{SA}(\tau) = g^{(2)}(\tau)\left(1 - \left(\frac{c^2}{2}\right)p(\tau)\right). \tag{3.8}$$

This can be solved for the probability that a jump has occurred $p(\tau)$:

$$p(\tau) = \frac{2}{c^2}\left(1 - \frac{g^{(2)}_{SA}(\tau)}{g^{(2)}(\tau)}\right). \tag{3.9}$$

Amazingly, this result only depends on two correlation functions, the second order autocorrelation function of the bare emitter and the cross correlation between the interferometer arms.

3.6.2. Measurement of the Spectral Diffusion in Nanodiamonds

The setup for measuring the spectral diffusion of the zero phonon line of NV centres in nanodiamonds consists of the Mach-Zehnder interferometer shown in Figure 3.4 and a NV centre as single photon source. The NV centres used are hosted in nanodiamonds (type Ib bulk diamond milled to a size between 30 nm and 100 nm) which are deposited on a zirconium dioxide solid immersion lens (SIL) for improved collection efficiency (see Section 4.2.1 and Reference [144]). The SIL is mounted in a liquid Helium flow cryostat and the photons are collected with a high numerical aperture objective (NA=0.9) mounted inside the isolation vacuum. The NV centre is excited with a picosecond 531 nm laser or a 10 nm broad part of the spectrum of a supercontinuum source. The excitation laser is filtered out by longpass filters. An additional removable bandpass centred at 637 nm with a width of 7 nm is used in order to selectively collect the zero phonon line (see Figure 3.5 (a)). A time tagging electronic is used to collect signals (see Section 2.4.1).

With this setup, the correlation functions $g^{(2)}(\tau)$ and $g^{(2)}(\tau)_{AS}$ are measured. Photon collection took typical times of 30 minutes, depending on the actual count rate of the NV centre. An example of such a dataset is shown in Figure 3.5 (b). Already in the bare curves differences are visible. Together with Equation 3.9 and the definition that the time on which spectral diffusion occurs τ_d is the 1/e time, these data can be plotted as in Figure 3.6 (a). The value of $p(\tau)$ is shown. It follows an exponential behaviour with a spectral diffusion time of $\tau_d = 4.6 \pm 0.6$ µs. Also the interferometer contrast c in Equation 3.9 is calculated to be 35 % – a value below the 90 % that were independently measured with a laser beam. This is attributed

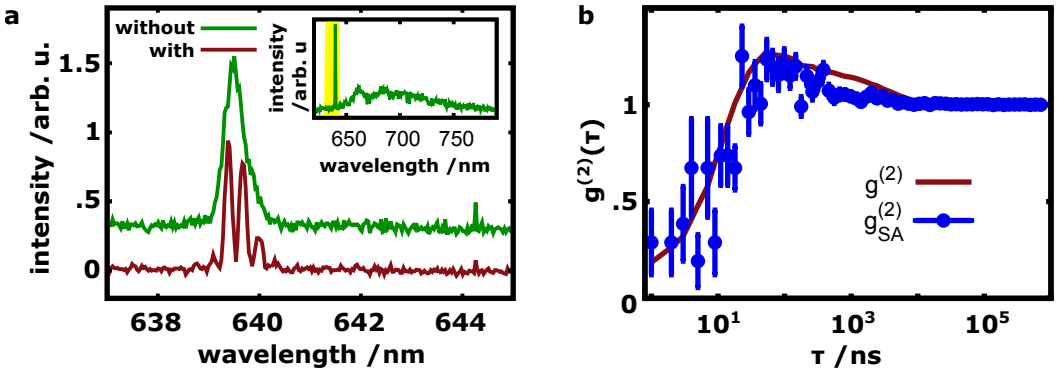

Figure 3.5.: NV centre spectrum and correlation functions. In (a), a spectrum of the zero phonon line of a NV at liquid helium temperature is shown. Green is the filtered ZPL without the interferometer and red one output of the interferometer. An offset is added for visibility. The inset shows the unfiltered spectrum with its phonon sidebands. The region transmitted by the narrowest bandpass marked in yellow. (b) shows the correlation functions $g^{(2)}(\tau)$ and $g^{(2)}(\tau)_{AS}$. Differences due to spectral diffusion are visible. (Adapted from [82])

to two main reasons: firstly there always is some fluorescence background present in the measurements (see the non-vanishing $g^{(2)}(0)$ in Figure 3.5 (b)), and secondly, the NV centre posses two dipole transitions, which need not to be degenerate (see Section 3.2) [139].

With a working technique of studying the spectral diffusion at fast timescales, the influence of the excitation laser on the properties of spectral diffusion is now studied.

In a first experiment, the power of the excitation laser (wavelength $\lambda = 531$ nm) is varied well below saturation in the linear regime and the spectral diffusion rate is measured. The corresponding data are shown in Figure 3.6 (c,d) for two different NV centres. A linear dependency of the jump rate on the excitation power is found. The two red dots in Figure 3.6 (d) were not used, as a closer evaluation of the data revealed a increased count rate compared to the normal power dependence. This is a clear indication of an experimental error, probably due to the adhesion of dirt from the vacuum system in the strongly focussed laser beam over time. As shown in Figure 3.6 (c), a quadratic power dependence can be excluded. Therefore, no two-photon process, like photo induced charge conversion [145], is the main course of the observed spectral diffusion.

In a second experiment, the dependence on the wavelength of the spectral diffusion is studied. With 10 nm wide bandpass filters, parts of the spectrum of a supercontinuum source are cut out and used for excitation, while the count rate

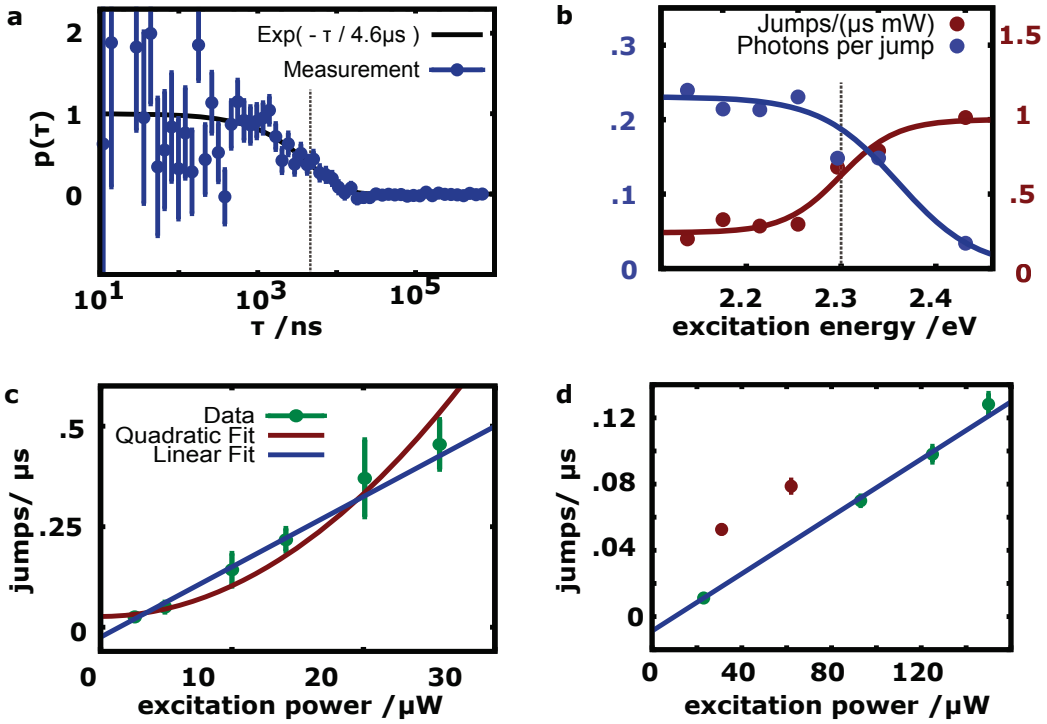

Figure 3.6.: Measurement of spectral diffusion. (a) shows the probability $p(\tau)$ that no spectral jump occurred in the time interval τ, as it is calculated from the correlation function shown in Figure 3.5. The black curve is an exponential fit to the data and the dotted line indicated the 1/e value τ_d. (b) shows the dependence of the spectral diffusion rate (right axis) and collected photons per jump (left axis) as function of excitation photon energy. The behaviour changes around 2.3 eV as indicated by the dotted line. In (c) and (d), the excitation power is varied at a wavelength of $\lambda = 531$ nm (equivalent to an energy of 2.34 eV). A clear linear behaviour is visible. The two red data points were not used in the linear fit as explained in the text. (Adapted from [82])

is kept constant at 1.4 ± 0.2 kcts/s. The corresponding data are shown in Figure 3.6 (b). The curves for the photons per jump as well as the jump rate per excitation power change at 2.3 eV. Note that with the technique used here, it is even possible to measure the jump rate when there is less than one photon per jump.

In a third experiment, the temperature dependence of τ_d is investigated, but in the range from $5 - 20$ K no such dependence is found.

From these experiments, the following conclusions are made:

- The excitation laser is the source of the spectral diffusion observed, since the rate scales linearly with laser power and a linear fit reveals that spectral diffusion would be absent without an excitation laser.
- Because of the linear dependency of jump rate and laser power, it is not possible to get more photons per jump by reducing the laser power.
- Changing the temperature will not allow more photons to be extracted in between jumps.
- By reducing the excitation laser photon energy below 2.3 eV, it is possible reduce the rate of spectral diffusion and hence get more photons out.

All these findings are compatible with a charge trap model (see Reference [82] for details), but a more detailed investigation has to be carried out in the future. Also it is unclear what the cause reduction in the diffusion rate at 2.3 eV photon energy is, since the main impurity is nitrogen, which forms a charge trap at 1.7 eV [146, 147] and therefore gets ionised in any case. An important consequence of these conclusions is, that it will be extremely demanding (if not impossible) to stabilise the emission line of nanodiamonds and to show quantum effects like the Hong-Ou-Mandel effect with photons from different NV centres in nanodiamonds. This is caused by the low number of photons that can be extracted (and therefore used for stabilisation) before the line jumps. What is possible, is to use photons from one the same NV centre, because the jump rate is still much smaller than the emission rate, so that consecutive photons are most likely from the same line. The big disadvantage of this approach is the loss of scalability. In order to be able to use nanodiamonds in a scalable approach, the timescales of spectral diffusion have to be changed, either by material science or by implementing resonant excitation [148].

Chapter Summary: The Nitrogen Vacancy Centre

In this chapter, the nitrogen vacancy centre in diamond and some of its properties were introduced. In particular, its optical and spin properties were reviewed. For

the special case of nanodiamonds, the NV centre's properties are slightly changed, what leads to effects like spectral diffusion of the centre's zero phonon line. After highlighting some of the application of NV centres, a measurement of the ultra-fast spectral diffusion in nanodiamonds was shown. Spectral diffusion is one of the main obstacle for interactions of two different NV centre's in nanodiamond, so understanding it is of great importance. Solutions for two of the other challenges in working with NV centres in nanodiamonds, i.e., to efficiently collect emitted photons and integration of the centres in photonic structures, will be treated in the following chapters. While the NV centre in nanodiamonds is the emitter used in all the experiments shown, the next chapter is on efficient collection of single photons from quantum emitters, which do not necessarily have to be NV centres.

4. Collecting Photons

When working with low light levels, like with single photons, it is important to work efficiently, i.e., not to waste photons due to loss or low photon collection. Many single photon emitters, as introduced in Section 2.5, are nanoscopic optical systems. Therefore, two main things are needed: First, the emitter needs to be addressed. Hence, in Section 4.1 the optical microscope is introduced. Second, the collection efficiency has to be as high as possible. Ways to improve the collection efficiency are presented in Sections 4.2and 4.3 . Parts of Sections 4.2 and 4.3 have been published in *Optics Letters* with the title *Numerical analysis of efficient light extraction with an elliptical solid immersion lens* [149].

4.1. Optical Microscopy

In many areas of natural sciences, optical microscopes play a major role. Their ability of magnification and therefore to allow for looking at very small things and seeing details that are not visible with the naked eye makes them an indispensable tool for scientists. They are used so often, that they became a symbol of scientific research [150]. Here, an overview on the basic operation principle and properties of optical microscopes is given.

The easiest way to achieve magnification is to use a simple magnifying glass. It increases the angle α under which light from different points of an object hits the eye, what forms a virtual enlarged image as shown in Figure 4.1 (a,b) [151]. In contrast to a magnifying glass (or more complicated variants thereof, which may involve more elements), a compound microscope consists of two distinct parts: an objective and an eyepiece. The objective is used to collect the light from a sample and form a real intermediate image inside the microscope, which is in turn imaged by the eyepiece. A sketch of this is shown in Figure 4.1 (c).

4.1.1. The Microscope Objective

In this thesis, mostly other variants of microscopes, like a confocal microscope (see Section 4.1.3), are used which have no eyepieces and direct the light they collect directly onto a detector. In any case, the most important component is the first lens system, the microscope objective. It directly determines which fraction of light is collected and how good the quality of an image can be. Modern microscopes

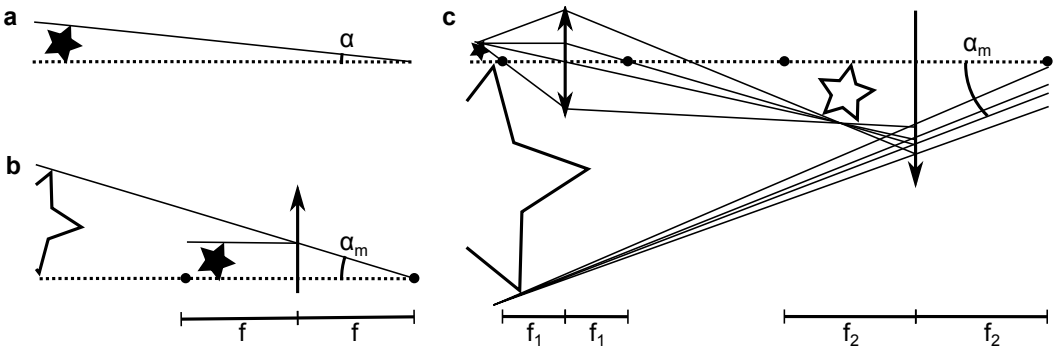

Figure 4.1.: Magnifying glass and microscope. In (a) an observer at the right is looking at an object without additional optics. The angle α between rays from different point of the object is a measure for how big the object looks. In (b) a magnifying glass is applied. Light from the object is refracted what leads to a larger, magnified α_m. In (c) the principle of a microscope is sketched. A first lens (objective) collects light from the object and forms a real image, which is then images by a second lens (ocular) forming an enlarged virtual image.

usually use so called infinity corrected systems in which the microscope objective, as introduced in Figure 4.1 (c), is split in two parts: One part collecting the light and sending out a collimated beam (i.e., focussed to infinity) which is still called objective and another part, the tube lens, which forms the intermediate image. In this thesis, only this system is used due to the great advantage in flexibility it offers. A selection of the important properties of microscope objectives in this sense is reviewed in the following.

- **Numerical aperture.** The numerical aperture (NA) is given by [152]:

$$NA = n \sin \alpha, \tag{4.1}$$

  with n being the refractive index of the surrounding medium ($n = 1$ for air objectives and $n > 1$ for immersion type objectives) and α being the maximum angle with the optical axis, that light stemming from the focal point can have while still being collected. An increased angle α leads to increased photon collection, therefore, to collect many photons, the NA for a fixed immersion medium should be as high as possible. Typically, for air objectives, NAs as high as 0.95 are commercially available. Using them, about one third of the full solid angle is covered.

- **Magnification.** For an infinity corrected objective, the quantity magnification only makes sense with the corresponding tube lens, since the objective

alone does not form an image. What can lead to confusion is that different companies use different focal lengths for the tube lenses in their microscopes. Hence, a more useful quantity is the objective's focal length. It can be calculated by treating the system as telescope. Using the equation for a telescope's magnification [151] leads to:

$$f_{objective} = f_{tube}/M, \tag{4.2}$$

with $f_{objective}$ as the objectives focal length, f_{tube} the tube lens' focal length as intended by the manufacturer and the M the nominal magnification of the objective.

- **Point spread function.** The point spread function (PSF) is the pattern, which is illuminated or observed by a lens (or system of lenses) at its focal plane, provided there is an incident collimated beam or a point emitter, respectively [153]. This generally three-dimensional function is often approximated in two dimensions as an Airy function, the so called Airy disk. This is only a a valid approximation in the paraxial case where the NA is small (see [152] and [153] for details). For ideal imaging systems, the PSF only is dependent on the NA and the wavelength. If this is the case in good approximation, a system is called diffraction limited, since the limit in size is the diffraction taking place due to the finite NA. To achieve diffraction limited PSFs for high NA objectives at different wavelengths and for large fields of view, corrections for chromatic and spherical aberrations are applied, leading to a large variety of different objective types with different properties. To describe them would go beyond the scope of this description of the parameters most important for this thesis.

- **Back aperture size.** A property of an objective, which is very important when light is coupled in or out of the objective, is the size of the microscopes back aperture. This aperture determines which diameter D an outcoming beam from a point source has or which diameter D an ingoing beam has to have ideally. It can be calculated as follows [154]:

$$D = 2 \cdot f \cdot NA. \tag{4.3}$$

This looks like what is expected for paraxial approximation only, but for most microscope objectives (so called aplantic objectives) it is also true for high NAs. The reason for this lies in the fact that in order to get a good image also for points not exactly on the optical axis, an optical system has to obey Abbe's sine condition (see [151] for more information).

4.1.2. Resolution

Resolution is the ability of a microscope to resolve light stemming from adjacent points. Clearly, this is given by the size of the PSF. When the PSF gets larger, it will get harder to resolve distinct points. Traditionally, there are different criteria on how to judge if two points are considered as resolved. The most common criteria are the Rayleigh and Sparrow criteria. In the Rayleigh criterion, two equally bright points are resolved when the intensity maximum of one point coincides with the first intensity minimum of the other, while the Sparrow criterion states that two equally bright points are resolved when their combined intensity yields a local minimum or a flat top instead of a peak [155]. Assuming an Airy function for the lateral PSF, for the Rayleigh criterion this leads to [152]:

$$d_{lateral,R} = 0.61\frac{\lambda}{NA}, \tag{4.4}$$

while it is [156]:

$$d_{lateral,S} = 0.51\frac{\lambda}{NA} \tag{4.5}$$

for the Sparrow criterion. Note that these criteria used for resolution are defined for practical reasons: If one would consider a completely noiseless case or has some additional information on the sample to be measured, even much closer objects could be measured, e.g., by deconvolving with the PSF. As an easy example, if it is known that there is just a single emitter, it is easily possible to localise it better than the resolution limit just by looking for the centre of the measured signal. Many advanced superresolution microscopy schemes employ a similar approach in order to localise many emitters [157].

4.1.3. Confocal Microscopy

In contrast to standard optical microscopy, in confocal microscopy only one point is illuminated at a time and also detection of the signal only takes place for this point. The basic principle can be seen in Figure 4.2 (a). A light source, commonly a laser, is focused by an objective lens and detection happens by imaging the focal point on a pinhole. As Figure 4.2 (b) and (c) show, light that is not stemming from the illuminated point is suppressed by the detection pinhole. Even more, these points are also not illuminated. Mathematically this can be expressed by multiplying the PSF of the excitation light with the PSF of the detection pinhole. This is called the confocal PSF. For a suitable small pinhole size, the confocal PSF is the original PSF squared, what slightly increases the resolution of the microscope. Note that this is only the case for the Sparrow criterion, since the minima used in the Rayleigh criterion do not shift for a squared PSF. However, more important than

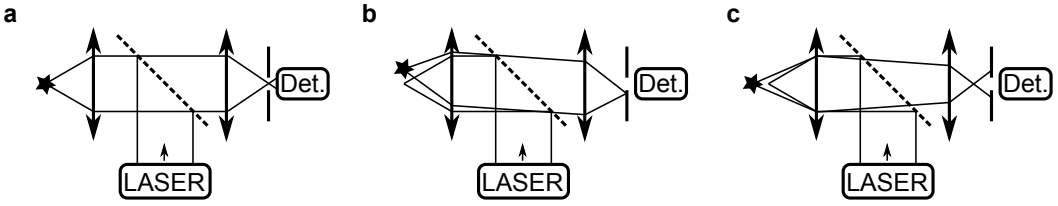

Figure 4.2.: Confocal microscope. In (a) the working principle of a confocal microscope is shown. A light source is focused on a single point of the sample and the detected light coming back from this point is spatially filtered by a pinhole. As (b) and (c) show, in this way background light from adjacent points gets suppressed.

the increased resolution is the increased signal to noise ratio achieved in confocal microscopy. Squaring the original PSF heavily reduces unwanted side-lobes.

The confocal microscope described so far only gets information from one point. In order to form an image, the sample has to scanned, either by moving the sample or by moving the excitation and detection spot. Often, confocal microscopy is implemented as fluorescence confocal microscopy, where a laser is used to excite fluorescing molecules (or other emitters) and only the fluorescence is detected. With the possibility to selectively attach dyes to objects of interest, this method has great success in biology, where it is routinely used. More information on this can be found in References [152] and [154]. In this thesis, confocal microscopy is not used to image tissue, but to have a good suppression of unwanted background light when addressing single photon emitters.

4.2. Single Photon Collection Efficiency

After the introduction of optical microscopy in Section 4.1, in this section different approaches to enhance the collection efficiency of single photons beyond what is possible with standard microscopy schemes are introduced. This is very important, since fundamental experiments and applications in nanophotonics deal with small amounts of light, down to the limit of single photons emitted from single emitters (see Section 2). Moreover, it is crucial not to lose the photons due to a low collection efficiency, since an ideal single photon source, which is crucial for linear optics quantum computing (see Section 2.3) [34], has to emit exactly one photon per excitation – never two and never zero. For such a photon gun [46], two requirements have to be met: (1) The quantum efficiency of the emitter has to approach unity, and (2) the photon collection efficiency of the optical system has to be near 100 %. The first requirement can be met by choosing an efficient emitter and if necessary further enhancing its emission resonantly via Purcell enhancement in resonant optical structures (see Section 2.2) [158]. The second requirement needs either the

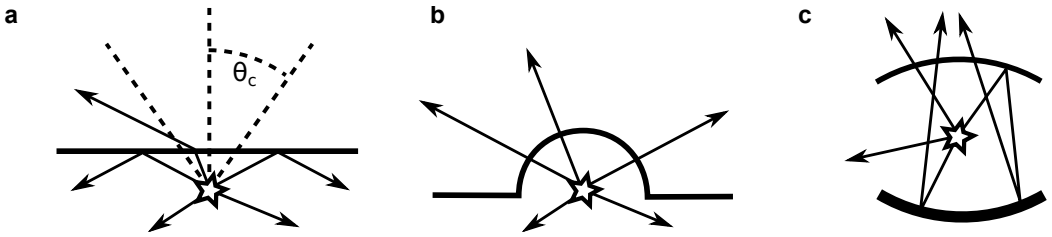

Figure 4.3.: Single photon collection schemes. (a) Due to total internal reflection, only photons propagating inside a cone with opening angle Θ_c can be collected. (b) Using a geometrical approach the number of photons being collected can be increased. (c) In the resonant approach a resonant structure enhanced the emitter and directs the light into one desired mode.

collection optics to cover a solid angle of 4π – which is impracticable for almost all applications – or the photons to be directed exclusively into a small solid angle. Directing the photons can again be achieved via the Purcell effect by resonantly enhancing emission in one desired spatial mode, or by employing geometrical optics to non-resonantly direct the photons [159].

The challenges in working with single photon sources lie not only in identifying a suitable single photon emitter, but also in collecting the emitted single photons efficiently. For solid state quantum emitters like molecules, quantum dots, and defect centres, the photons need not only to be directed to the collection apparatus, they also need to be extracted from their host material. Diamond for example has an index of refraction of 2.41 at 638 nm [160]. This leads to a critical angle Θ_c of less than 25 degrees at a diamond-air interface. So only photons inside a cone with that opening angle can pass through the interface, the rest is lost due to total internal reflection (see Figure 4.3 (a)). There are mainly two approaches to address this problem, a geometrical one as shown in Figure 4.3 (b) and a resonant one shown in Figure 4.3 (c) [159].

4.2.1. Geometrical Approach

In this approach, the geometry of the material surrounding the single photon emitter is changed in a way that more of the photons are directed towards the collection optics. A simple example of this is the hemispherical solid immersion lens (SIL) in Figure 4.3 (b) [161]. The problem with total internal reflection is avoided by placing the emitter in the centre of a hemisphere. By doing so, the light will hit the surface only under normal incidence and can therefore exit the host material without being hindered by total internal reflection. Since SILs act as an immersion medium analogous to the immersion oil in oil immersion microscopy, due to their elevated

refractive index, they increase the effective numerical aperture of a light collecting system [161, 162]. Commercial SILs made from transparent high-index materials such as zirconium dioxide [144] are commonly only available as half spheres. Using micro-structuring processes like focussed ion beam milling [163] or a combination of mechanical and laser techniques [164], SILs can be fabricated directly from the material hosting an emitter. Since in this approach the emitter is embedded in a homogeneous medium, the maximum amount of collected photons is 50 %. This limit can be overcome by introducing a dielectric interface, because light will be emitted preferably in the direction of the optically thicker material, i.e., the direction of the SIL, if the refractive index of the SIL is the higher one [165]. However, with a dielectric interface present, hemispherical SILs tend to direct most of the light from an emitter on its surface to very shallow angles, which makes collection via subsequent optics very difficult [144]. One way to improve on this disadvantage is to use the so called Weierstrass or super-hemisphere geometry (a sphere cut at a height of $h = 1 + \frac{1}{n}$ with n being the SIL's index of refraction). In this geometry, photons are diffracted into a smaller solid angle [162]. In Section 4.3 another – more efficient – variant of a SIL geometry is investigated.

When not relying on SILs, there are other possibilities to enhance the collection efficiency geometrically: With a carefully designed dielectric slab consisting of a sapphire cover glass and polyvinyl alcohol (PVA), it was shown that nearly every photon can be directed to the collection optics [166]. To achieve this, molecules of known orientation were placed in the middle the PVA layer and imaged through the sapphire substrate with a high numerical aperture objective. However, this large value comes at a cost. Very high numerical aperture collection optics are needed in order to collect all the photons. By employing an additional mirror layer, these large angels can be reduced [167], but still, the resulting mode-profile has little overlap with a Gaussian beam, making fibre coupling extremely challenging. Both aspects are disadvantageous, for example when it is difficult to use large numerical aperture optics, a situation often present when extracting light from emitters in cryostats. Furthermore, the emitter has to be fully embedded in a medium, restricting this approach to to very simple single photon emitters. Application to more complex nano-engineered structures is not possible [91, 108, 144, 168–172].

Another possibility of exploiting the effects arising from the sample geometry is coupling of the emitters directly to a waveguiding structure. This can be done by coupling directly to the evanescent field from tapered fibres [113, 173, 174], coupling to the mode directly by putting the emitter on the waveguides facet [175] (see also Section 6.2), or embedding the emitter into the waveguide's material [176, 177] (see also Section 7.4).

In Section 7.5.2, an approach to enhance the collection efficiency using a reflecting parabolic antenna is introduced and experimentally verified.

4.2.2. Resonant Approach

In this approach, the local density of optical states (LDOS) is engineered [159]. Via Fermis's golden rule [178]:

$$W_{i\to f} = \frac{2\pi}{\hbar} |V_{fi}|^2 \rho(E_f), \tag{4.6}$$

a direct dependence of the transition probability on the LDOS is found. Here, $W_{i\to f}$ denotes the transition probability from an initial state i to a final state f, V_{fi} is the transition matrix element, and $\rho(E_f)$ is the density of states at the final state's energy E_f (see also Chapter 9, where the LDOS is measured). This provides the possibility to enhance certain transitions by increasing the LDOS and also to suppress others by reducing the LDOS [158, 179]. In this way, the spatial emission pattern as well as the spectral properties of the emitted light can be influenced, so that the collection efficiency can be improved. On resonance with optical cavities, where the LDOS is high, the enhancement is called Purcell effect (see Section 2.2 for details) [30]. The Purcell enhancement factor P reads:

$$P = \frac{3}{4\pi^2} \left(\frac{\lambda}{n}\right)^3 \frac{Q}{V}, \tag{4.7}$$

where λ is the vacuum wavelength, n the refractive index, Q the cavity's quality factor and V the mode volume [158]. An emitter's emission falling into the spectral line of the mode will be enhanced by this factor. From Equation 4.7 it is clear, that for a high enhancement a high quality factor and, at the same time, a small mode volume is needed. An example of enhancing the emission of the zero phonon line of a nitrogen vacancy centre can be found in Section 6.1.

4.3. Elliptical Solid Immersion Lenses

Now, solid immersion lenses, as introduced in Section 4.2.1 to enhance photon collection efficiency, are investigated. Extensive finite difference time domain (FDTD; see Appendix C) simulations are used in order to show the advantageous light collection and mode profile characteristics of a non-spherical SIL design. Theoretical design guidelines for the non-spherical solid immersion lenses, here referred to as elliptical SILs (eSILs) [180], are presented. With modern fabrication techniques, such as two-photon direct laser-writing (DLW, see Section 7.2) [181, 182], it is possible to fabricate such structures easily. In particular for small NAs, the FDTD calculations show a highly increased light collection efficiency compared to ordinary SILs.

While the eSILs cannot increase the overall amount of photons emitted in one

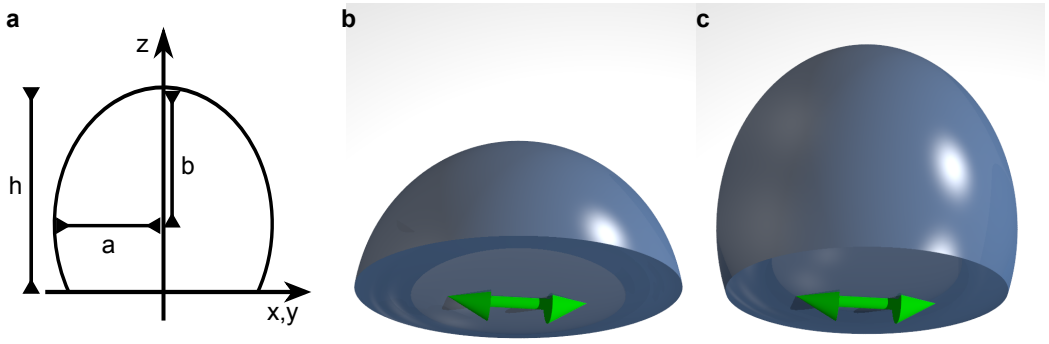

Figure 4.4.: Elliptical solid immersion lens geometry. (a) shows the geometrical parameters of the eSILs. The spheroid's two semi-axes are denoted as a and b and it's truncated height is denoted as h. (b) is an illustration of a standard SIL with parameter $r = \frac{a}{b} = 1$ and $s = \frac{h}{2 \cdot b} = 0.5$ while (c) shows a eSIL with parameters $r = 0.8$ and $s = 0.75$. The green arrow indicates the emitting dipole. (Figure adapted from [149])

half space compared to a standard SIL, which is given by the refractive indices of SIL and surrounding medium, they can drastically increase directionality of photon emission and hence significantly enhance collection efficiency.

4.3.1. Geometry and Simulation Details

Elliptical SILs are truncated three-dimensional spheroids, i.e., ellipsoids with two equal semi-diameters which are cut at one end. Details about geometry can be extracted from Figure 4.4 on the basis of the following notation:

$$\frac{x^2 + y^2}{a^2} + \frac{z^2}{b^2} = 1, \quad r = \frac{a}{b}, \quad s = \frac{h}{2 \cdot b}, \tag{4.8}$$

where a and b are the semi-axes of the spheroid, the dimensionless parameter r denotes the fraction the spheroid's axes, and the truncation parameter s is defined as the fraction of the height h along the optical axis of the truncated spheroid to the height of the entire spheroid. Two-dimensional ovals with a specific parameter r were recently investigated for the focusing of light [183].

In the simulations of the eSILs, b is set to be 5 µm and a is varied from 0.5 µm to 5 µm. This sizes are chosen in order to avoid resonant effects from very small structures while keeping the simulation region small enough for fast computation. As a second parameter, the truncation s is changed in steps of 0.416 µm, which correspond to $\frac{b}{12}$.

The numerical analysis of the optical properties of the eSILs is conducted using a

commercial FDTD simulation software (Lumerical Solutions Inc. FDTD). In order to receive comparable results, the simulation region has the same size for each configuration, with the largest mesh cell of the size of under 30 nm, i.e., the minimum number of mesh points per wavelength is around 24. Convergence was checked by varying the mesh size.

The light source used is a single emitter approximated by a radiating dipole emitting at a central wavelength of 717 nm, indicated by a green arrow in Figure 4.4 (b,c). Due to the rotational symmetry of the eSIL geometry, only two perpendicular orientations need to be evaluated in order to calculate the optical properties of any other dipole orientation. The refractive index of the eSIL is set to $n_{eSIL} = 1.5$ to match the refractive index of glass and commonly used photoresists used in two-photon direct laser-writing.

For some of the simulated geometries, resonance effects analogous to whispering gallery modes occurred in the simulations [184]. In these cases, the light extraction is not purely due to geometrical optics anymore and is heavily dependent on the actual size of the SIL. In order to eliminate these data and focus on the geometrical aspect of light extraction, these results are discarded. The criterion to discard the simulations is that the total energy in the simulation volume after a time of 600 fs did not decline to 10^{-4} of the energy injected.

4.3.2. Collection Efficiency of eSILs

In order to quantify the light collection efficiency, a study of the angular emission distribution of the combined emitter–eSIL system is performed. Using the far-field transformation implemented in the commercial software package, the far-field radiation pattern of a dipole centred on a eSIL is calculated. In Figure 4.5 far-field distributions for a standard and elliptical SILs are shown. Obviously, the angular distribution of the light is compressed by the eSILs for both dipole orientations. Since a dipole source at an interface radiates preferentially in the material with higher refractive index [185], special attention to the definition of collection efficiency has to be paid. Changing the eSIL's geometric parameters results in different sized air–medium interfaces at the eSIL's bottom for the various simulated geometry configurations. Hence, the total power emitted by the dipole as well as its angular radiation pattern changes [185]. Thus, by normalising with respect to the power radiated in the upper hemisphere, the different far-field results can be compared in a plausible way. Another way to achieve reliable results is to compare the fraction of power collected and the total power radiated. In the following, both methods of normalisation will be used.

An important figure of merit of eSILs is the fraction of light from an emitting dipole that can be directed into a specific solid angle. Therefore, the light collection in dependence of the numerical aperture of the collection optics is calculated.

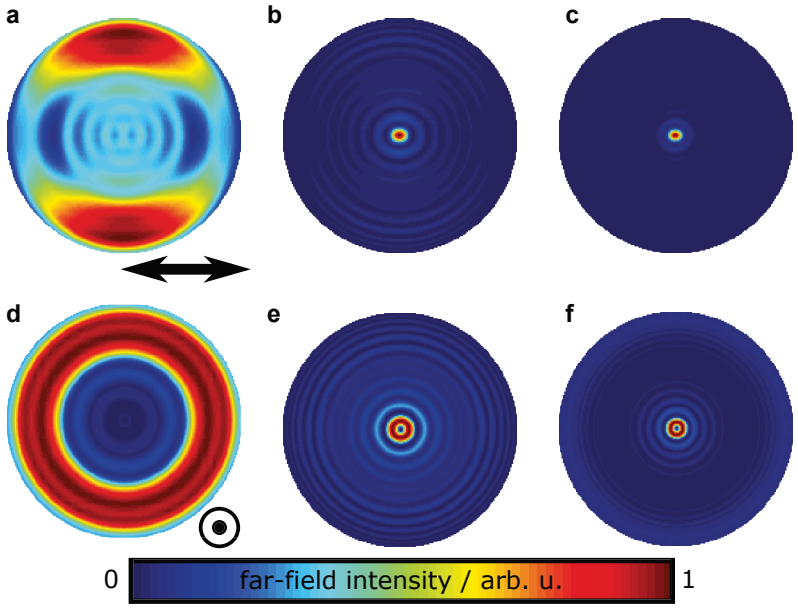

Figure 4.5.: Angular far-field intensity distributions of eSILs. (a,b,c) are far-field intensity distributions for a dipole parallel to the planar SIL surface while the dipole in (d,e,f) is perpendicular. (a,d) are the distributions for a standard SIL, while (b,e) and (c,f) are for eSILs with parameters $r = 0.8$, $s = 0.875$, and $r = 0.6$, $s = 0.708$, respectively. The colour scale shows the light intensity normalised to the total intensity radiated in the upper hemisphere. (Figure adapted from [149])

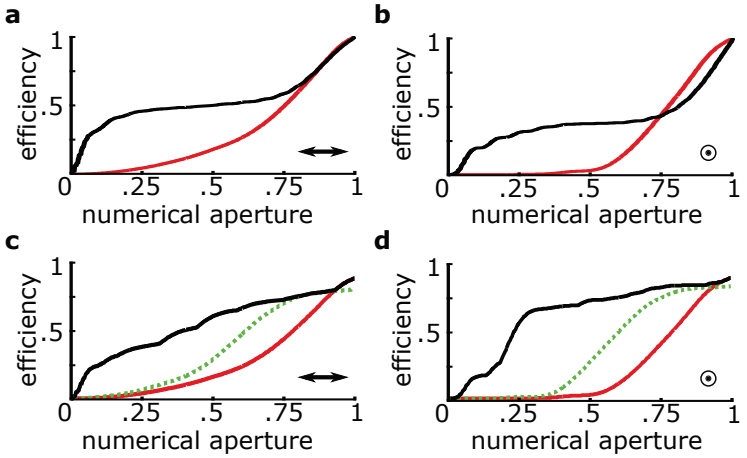

Figure 4.6.: Collection efficiency of eSILs. (a) and (b) are for a eSIL with parameters $r = 0.8$ and $s = 0.75$ (black line) in comparison with a standard SIL (red/grey line) for dipoles parallel and perpendicular to the planar SIL surface, respectively. Especially for small numerical apertures of the collection optics, the collection efficiency is enhanced. Efficiencies in (a) and (b) are normalised to the intensity emitted into the upper hemisphere, i.e., the efficiency equals 1 for NA=1. (c) and (d) are curves like in (a) and (b), but piecewise for the best suited eSIL for a numerical aperture and with normalisation to the total power. (Figure adapted from [186])

Figure 4.6 (a,b) shows as an example the result for two dipole orientations for a SIL and eSIL with parameters $r = 0.8$ and $s = 0.75$. In particular, for small numerical apertures of the collecting optics, the directionality can be increased drastically using the eSIL design. For instance, with a numerical aperture of 0.2 the simulation indicates that the collected intensity is about 276 times higher compared to a standard hemispherical SIL. The total amount of light collected with this exemplary eSIL for a NA as low as 0.2 is 27.2 %. In a typical experimental configuration, the numerical aperture of the collecting optics is given. Therefore, one has to look for the optimum SIL geometry for each value of numerical aperture of the collecting optics ranging from 0 to 1. The attainable collection efficiency for the best optimised (varying) eSIL is plotted in Figure 4.6 (c,d) as black line and compared to a Weierstrass (green/dotted) and a hemispherical geometry (red/grey). It can be seen that especially at lower numerical apertures the eSIL outperform the light collection efficiencies of standard and Weierstrass SIL configurations by far. On top of that, for a NA as low as 0.3 more than 65 % of the total light emitted by a dipole can be collected. A more detailed view on the influence of the design parameters r and s is given in Figure 4.7, where the total collection efficiency for two different

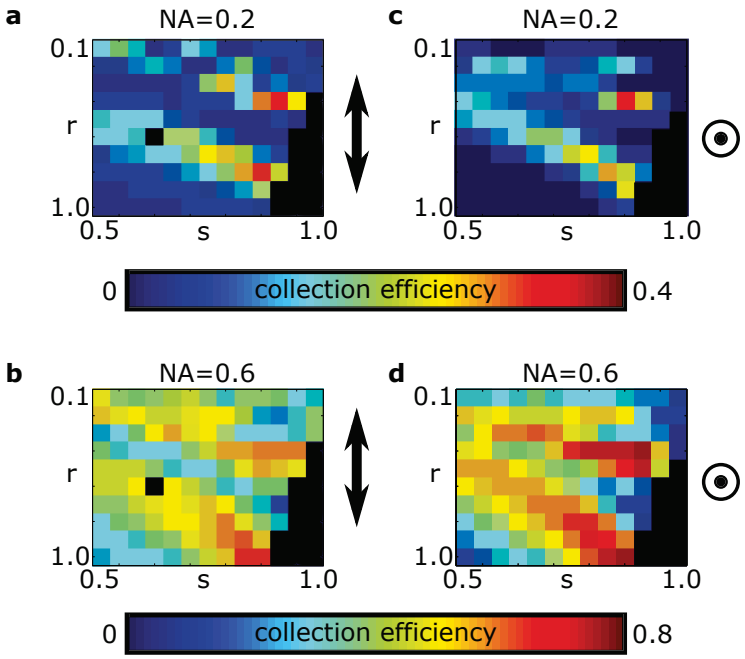

Figure 4.7.: Collection efficiency as a function of the variations of design parameters r and s at fixed NAs. (a,b) show the influence of changes in the parameters for a fixed NA of 0.2 for the two different dipoles while (c,d) show this for an NA of 0.6. Black data points correspond to cases where the data is discarded due to unwanted resonances. (Figure adapted from [186])

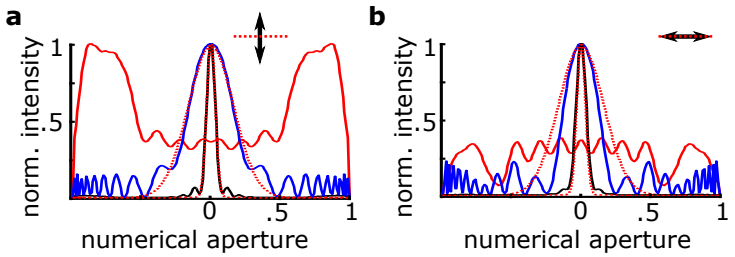

Figure 4.8.: Comparison of the intensity distributions. (a) and (b) show the far-field intensity distributions perpendicular and parallel to the in plane emitting dipole. The results for the standard SIL are shown in red while in back and blue results for eSILs with parameters $r = 0.8,\ 0.2$ and $s = 0.88,\ 0.83$ are shown. The dotted red lines are Gaussian fits to the data. (Figure adapted from [186])

NAs is shown.

Another important property of the eSILs is that using them a Gaussian intensity distribution can be achieved in the far-field, as can be seen in Figure 4.8, where a comparison of the far-fields of a standard SIL and two eSILs is shown.

For the fabrication of eSILs, a very flexible way in terms of the material properties is provided by using polymers. A prominent technique to manufacture nearly arbitrary shaped three-dimensional microstructures is two-photon direct laser-writing [181, 182]. With this technique, it is possible to build SILs with a non-spherical shape in high quality. In Section 7.2, a description of DLW is given and it is shown that DLW is also an ideal method to fabricate three-dimensional quantum optical elements by functionalisation of DLW-photoresists with optically stable quantum emitters [177] – a technique that also can be easily applied to the eSILs. Examples of eSILs fabricated with DLW are shown in Figure 4.9. The eSILs shown are fabricated in a single step of DLW. In order to maintain a refractive index contrast at their lower side, the eSIls are fabricated sitting on small pedestals. Integration of emitters using the techniques introduced in Section 7.2 is in principle possible, but has not been done yet. This would open a way to versatile, robust, and inexpensive optical elements for efficient integrated single photon sources and optical interconnects between individual quantum systems. The lenses are applicable for any kind of emitter, such as molecules, quantum dots, or defect centres in diamond. Most importantly, even for a realistic low numerical aperture of the collection optics, the presented design leads to a drastic increase in collection efficiency.

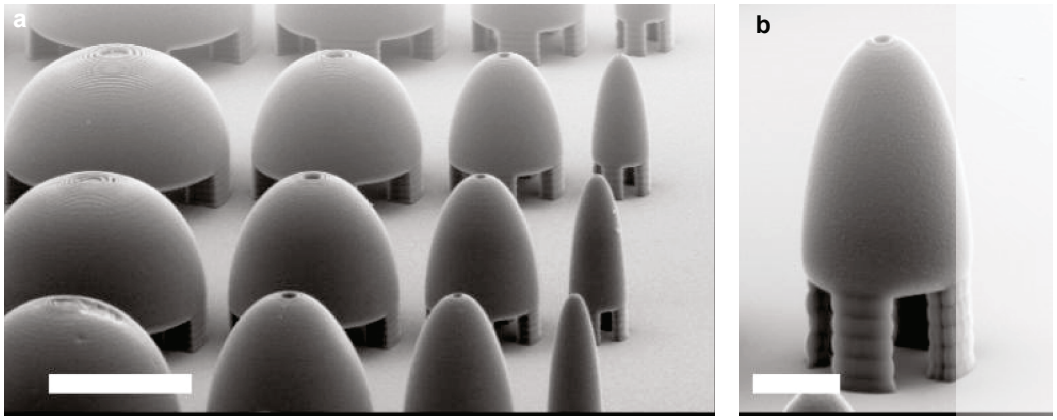

Figure 4.9.: Laser-written elliptical SILs. In (a), a scanning electron micrograph of eSILs with varied parameters is shown while (b) is a zoom to one particular eSIL. The eSILs are mounted on small pedestals in order to maintain a contrast in refractive index at their lower surface. Scalebars are 10 µm and 2 µm in (a) and (b), respectively. (Figure adapted from [187])

Chapter Summary: Collecting Photons

In this chapter, at first the basics of optical microscopy, and especially confocal microscopy, were briefly reviewed from an experimentalist's point of view. For the collection of single photons from nano-sized emitters like NV centres, microscopy using high numerical aperture objectives is the standard way. In the second part of this chapter, two ways to increase the efficiency of photon collection, a resonant and a geometrical approach, were introduced. For efficient collection of photons using the geometrical approach, numerical calculations of elliptical solid immersion lenses were carried out. These lenses enable for highly efficient photon collection even with small numerical aperture optics. Later in this thesis, in Section 7.5, another geometry for collecting photons, parabolic nanoantennas, will be fabricated and characterised.

Having now ways to collect single photons from quantum emitters, the next step towards fabrication of hybrid quantum devices is controlled integration of quantum emitters. For this, in the next chapter the techniques of atomic force microscopy and nanomanipulation are introduced.

5. Atomic Force Microscopy and Nanomanipulation

After the introduction of optical microscopy in the previous chapter, here, the basics of atomic force microscopy are introduced in Section 5.1. Atomic force microscopy not only enables for imaging of nano-sized objects, but also enables for changing the objects' positions. In Section 5.2, techniques for manipulation the position of particles on the nanoscale are introduced. One special technique of nanomanipulation, the pick-and-place procedure, which allows for placing of pre-characterised nanoparticles in a very controlled way, is explained in Section 5.3. This technique is published in *Review of Scientific Instruments* with the title *A scanning probe-based pick-and-place procedure for assembly of integrated quantum optical hybrid devices* [91].

5.1. Atomic Force Microscopy

Atomic force microscopy is probably the most versatile technique in the field of scanning probe microscopy. Since its invention by Binning, Quate, and Gerber [188] it has found applications ranging from material science and nanotechnology [189, 190] over chemistry [191, 192] to biology and medicine [193, 194]. It also serves as the basis for many other scanning probe techniques, because its feedback signal allows for easy and reliable height control. This is not necessarily the case for several other types of probes, including many of the today used schemes for scanning near-field optical microscopes [195, 196]. One special kind of such a microscope, the quantum emitter fluorescence lifetime imaging microscope, will be introduced in Section 9.3. In the following, an introduction to the basic working principles of an atomic force microscope (AFM) is given. This introduction is focussed on what is needed and used in later chapters and omits many exciting techniques and application. A broader overview is given for example by Eaton and West [197].

5.1.1. Operation Principle

In atomic force microscopy, the probe, usually a tip with a small radius of curvature, is brought into contact with the sample. Contact here means so close that short length-scale forces, like repulsive Coulomb or Pauli exclusion forces and attractive

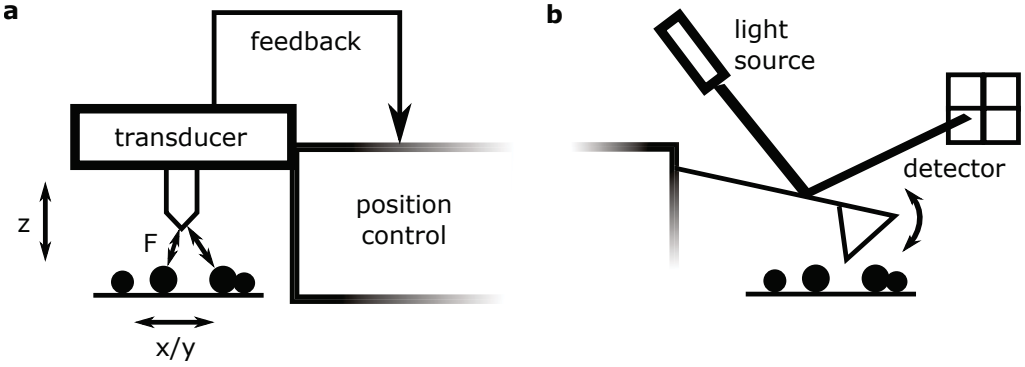

Figure 5.1.: AFM operation principle. (a) shows the scheme of operation. The force F between tip and sample is converted into an electrical signal by a transducer and is fed to a feedback loop. This loop controls the distance z between tip and sample. By scanning in x and y direction, topographic information can be acquired. (b) shows an optical lever. Bending of an cantilever leads to deflection of a light beam at a position sensitive detector.

Van-der-Waals forces [198, 199], are dominating. These forces between tip and sample are converted into an electrical signal and then used in a feedback loop to control the tip's height. This working principle is shown in Figure 5.1 (a).

The transducer can be anything capable of transforming the force on the tip to an electrical signal with high precision. Today however, the so called optical lever [200] is used nearly exclusively. It consists of a collimated light source (usually a laser), whose beam is reflected by a cantilever onto a position sensitive detector (usually a quadrant photodiode). The AFM tip is mounted at the free end of the cantilever, so that any force applied to it leads to a bending of the cantilever. This bending now is detected on the position sensitive detector as a deflection of the reflected beam. A sketch of an optical lever is shown in Figure 5.1 (b).

In order to image a sample with an AFM, the tip or the sample have to be raster scanned in x/y-direction, also the tip-sample distance has to be controlled. Today, these movements are mostly done using piezoelectric scanners, which can offer a sub-Angstrom resolution while having scan ranges of many micrometres.

The feedback usually is realised using a PID (proportional-integral-derivative) controller [201]. Often the derivative part is omitted, but the device still called PID controller [197].

5.1.2. Operation Modes

An atomic force microscope can be operated in many different ways, depending on what kind of forces are dominating the interaction and how transducer and feedback

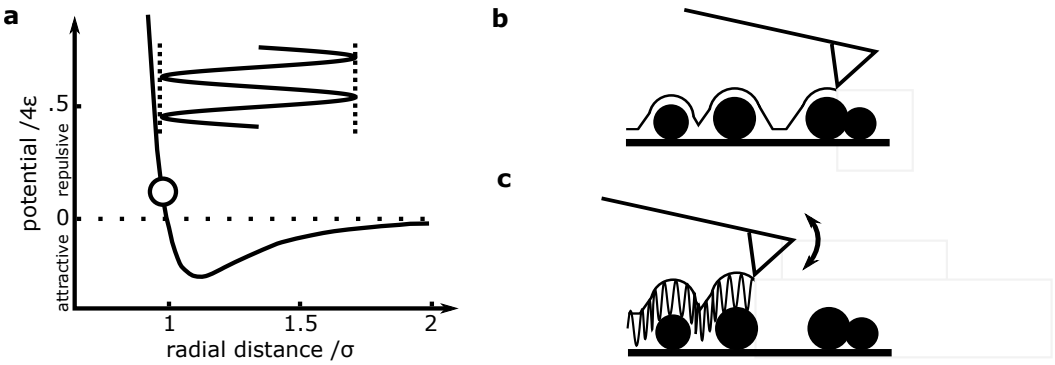

Figure 5.2.: Modes of AFM operation. (a) shows the Lennard-Jones-potential in units of 4ϵ and σ (see Equation 5.1). The circle indicates the set point in contact mode, which is a constant force mode. The sine indicates the range of distances used in tapping mode, where the amplitude of an oscillation is used for feedback. (b) is an illustration of contact mode operation. The tip moves along a line of constant force. (c) shows tapping mode operation. The tip oscillates over the surface with a controlled amplitude.

are realised. In this work, only two of the modes are used, namely contact mode and tapping mode (also called intermittent contact mode). To illustrate these modes, Figure 5.2 (a) shows an often used approximation for the tip-sample potential, i.e., a Lennard-Jones-potential. It describes the interactions between uncharged and non-chemically bound particles and is of the form [202]:

$$\Phi(r) = 4\epsilon \left[\left(\frac{\sigma}{r} \right)^{12} - \left(\frac{\sigma}{r} \right)^{6} \right], \tag{5.1}$$

with two parameters ϵ and σ. The power of 12 in the repulsive term of this potential is chosen for convenience, the only constraint on it is to be higher than the power of 6 at the attractive dipole term. The use of a Lennard-Jones-potential here is a rather coarse approximation which omits many effects, for example chemical bonds or capillary forces, that can be very strong under ambient conditions. Measuring and modelling this potential is the subject of force spectroscopy, an non-imaging AFM technique where the forces are measured when the probe is approached to and retracted from an object of interest [199].

When the AFM is operated in contact mode, or more specific constant force contact mode, the feedback is set to achieve a constant force (in vertical direction) between sample and probe. In optical lever AFMs, this corresponds to a constant deflection in the vertical direction on the quadrant photodiode. Contact mode AFM is a so called static mode, where probe does not oscillate, opposed dynamic modes

like tapping mode. Contact mode atomic force microscopy makes the probe stay on an iso-force surface, as shown in Figure 5.2 (b). The forces that have to be applied in contact mode to get a reasonable feedback signal are typically higher than the forces in tapping mode. This will be important in Section 5.2, since control over the force is one crucial point in doing nanomanipulation.

Tapping mode is a dynamic mode, where a mechanical oscillation of the cantilever is driven at a high oscillation amplitude, as shown in Figure 5.2 (a) [197]. During the cantilever's oscillation period, it is both, distant to the sample in the attractive region of the potential and in contact. The large oscillation amplitude makes tapping mode very robust against disturbances and allows for relatively easy detection. With a lock-in amplifier, amplitude and phase are deduced. Usually, in tapping mode only the amplitude is used for feedback. Nonetheless the phase signal can carry a lot of information, for example on the dissipated energy and hence on the mechanical properties of a surface [203].

5.2. Nanomanipulation

In addition to its imaging modes, there exist a lot of more ways in which an AFM can be operated. With precise control over the applied forces, it is a useful tool for manipulating objects on the nanoscale [190, 204]. This is important in order to build nanodevises, where several different objects are coupled in order to control light matter interaction [205, 206]. Another often used tool for nanomanipulation, which will not be introduced here in detail, is a scanning electron microscope with additional manipulators, for example piezo-driven tungsten tips [207], inside the vacuum chamber [208].

In AFM nanomanipulation, the two modes introduced in Section 5.1.2 can be used. Since the same tip is used for imaging and for manipulation, it is not possible to acquire live-images while manipulating a sample as it is possible in the case for SEM manipulation. To have some kind of independent imaging system, AFMs are often mounted on optical microscopes. However, since optical microscopes are bound to the diffraction limit [209] (unless complicated and/or time consuming superresolution techniques are used [210]), this is not a real substitute for scanning with the AFM when doing nanomanipulation.

Usually tapping mode is used for mapping and contact mode is used for manipulation, hence the process of moving nanoparticles works as follows:

- the area of interest is identified
- a scan in tapping mode reveals the positions of the particles without changing them, since only a small force is applied
- the tip is moved in contact mode along defined manipulation paths

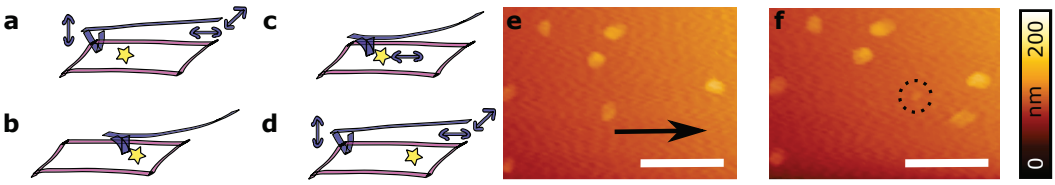

Figure 5.3.: AFM nanomanipulation. (a-d) show the process of positioning a nanoparticle. In (a), the particle's position is measured by scanning in tapping mode. (b) and (c) show how the position is then changed by moving the tip along a manipulation path in contact mode. In (d), the position is measured again in tapping mode. (e) and (f) show diamond nanoparticles before and after manipulation, respectively. Two things that can happen during manipulation are visible: a slight change in the tip shape noticeable by looking at the shape of the particles and a new particle appearing along the manipulation path (indicated by the dotted circle). Scalebar is 500 nm.

- a scan in tapping mode is performed to check the positions of the particles
- if the particles are not at the desired positions, the two previous steps are performed until success

Figure 5.3 shows a sketch of the process and an example of manipulated particles. Furthermore, with nanomanipulation it is not only possible to change the position of particles, but also their shape can be modified. In Figure 5.4 it is shown how this can be applied to chemically grown gold nanowires (see also Sections 8.2 and 9.3). Recently, this controlled shape and position manipulation of silver nanowires has been used by Kumar *et al.* to efficiently couple a nanodiamond containing a single NV centre efficiently to a plasmonic gap waveguide, where the gap waveguide was build in-situ from two silver nanowires [211].

The described process of nanomanipulation can in broad sense be seen as a kind of scanning probe nanolithography [212]. Another scanning probe nanolithography technique is dip-pen nanolithography, where molecules are transported from the tip of an AFM to a sample [213, 214]. This technique can also be applied to nanoparticles, for example nanodiamonds [206]. A controlled variant only involving exactly one pre-selected particle is introduced in Section 5.3.

Nanomanipulation itself is not limited to scanning probe techniques. There also exist other approaches, notably direct manipulation of particles by the electron beam of a scanning or transmission electron microscope [215] or trapping with near-field optical tweezers [216]. Near-fields have to be used here, since conventional far-field optical tweezers [217] work only on scales of microns, mainly due to the diffraction limit.

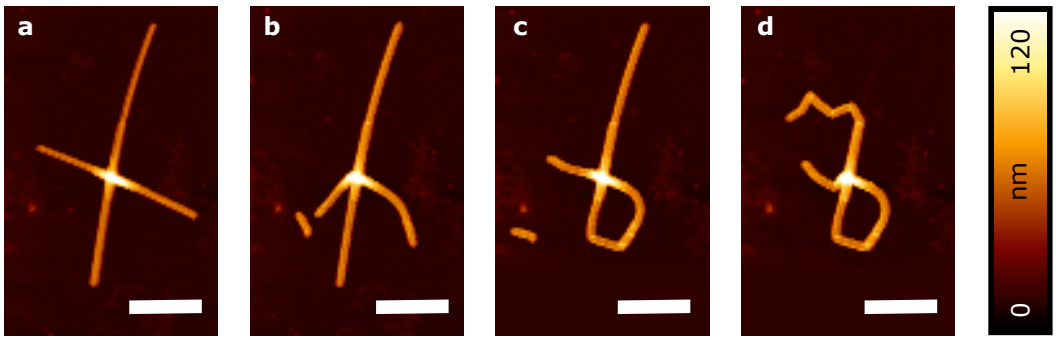

Figure 5.4.: Manipulation of gold nanowires. (a-d) show different stages of the manipulation of two crossed gold nanowires. In between these images many manipulation steps were performed in order to change the shape in a controlled way. In (b) it is visible that the wire has been cut. The piece cut of is removed from the structure in (d). Scalebars are 2 µm.

5.3. A Pick-and-Place Procedure for Nanoparticles

In the following, a newly developed technique for the deposition of single preselected particles on structures of nearly arbitrary shape is introduced. Parts of this section have also been published as *A scanning probe-based pick-and-place procedure for assembly of integrated quantum optical hybrid devices* in the journal *Review of Scientific Instruments* [91].

One possibility for the integration of single quantum emitters into nanophotonic structures such as microcavities [158], optical antennas [218] or waveguides [219] is to use the so called hybrid approach [108]. In this approach, a combination of different constituents, such as different materials, is used in order to make use of their advantages while avoiding their disadvantages. The nitrogen vacancy centre (NV centre, see Chapter 3) is especially suited for this since it is a stable and bright single photon emitter even under ambient conditions [74, 220]. In contrast to top-down approaches, where lithography is used to define structures [221, 222] and NV centres are created by ion implantation in diamond crystals [223, 224], the hybrid approach relies on fabricating a structure from the best suited material and adding a nanoparticle for functionality later on. For this purpose, diamond nanocrystals containing single defect centres are used. The nanodiamonds can be positioned using nanomanipulation either in a scanning electron microscope (SEM) with a manipulator [171, 207] or with an AFM [170, 172, 206]. While the controlled picking and placing of nanoparticles is possible [171], a technique to pick up pre-selected nanoparticles with an AFM is desired, since it works under ambient conditions and an AFM can be easily integrated into the optical microscope needed for pre-

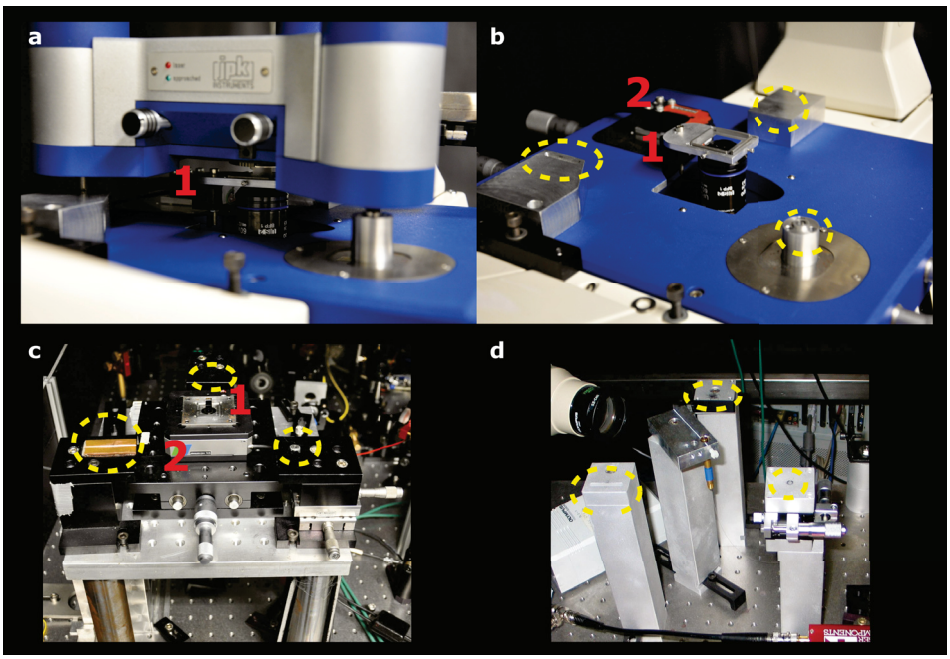

Figure 5.5.: Experimental setups for pick-and-place. Photographs of the body of a Zeiss Axiovert 200 microscope converted to a confocal microscope with the AFM atop and removed are shown in (a) and (b), respectively. (c) shows a top-view photograph of the homebuilt confocal microscope [227]. (d) is a detailed view of a special holder consisting of three posts for mounting the AFM to approach complex shaped items, e.g., an optical fibre. The dashed circles label the AFM mounts, 1 labels the sample holder, and 2 labels the piezo sample scanner. (Figure adapted from in [91])

characterisation. Picking up nanoparticles with an AFM has been achieved for metallic particles using electrostatic forces [225] or chemical treatment of the AFM tip [226], while the technique introduced here in principle works for any particle and needs no chemical treatment or other special additional forces.

5.3.1. Experimental Setup

The experimental setup for the pick-and-place process consists of an inverse confocal microscope with an AFM atop. Two different microscopes are used. One is a Zeiss Axiovert 200 (see Figure 5.5 (a) and (b)), the other one is a homebuilt system [227] (see Figure 5.5 (c)). Additionally, a special holder is constructed to allow for AFM manipulation on more complex or fragile photonic structures, such as optical fibres (Figure 5.5 (d)). While the AFM used is a tip scanner with three

axes, the confocal microscope has a 2D piezo sample stage and a piezo actuated z-axis objective positioning system. In this way, the nanoparticle sample as well as the AFM tip can be positioned independently relative to the laser focus.

A sample is produced by spin-coating of an ensemble of nanodiamonds from a solution on a glass cover slip. The solution is a suspension of centrifuge cleaned nanodiamonds in water with 0.02 % polyvinyl alcohol added. On such a sample, individual nanodiamonds are pre-characterised prior to the pick up procedure. Light from a pulsed laser with a wavelength of 532 nm and a repetition rate of 10 MHz is focussed on a nanodiamond via a high numerical aperture objective. Its fluorescence is dispersed by a grating spectrometer to identify a characteristic NV spectrum. Autocorrelation measurements of the fluorescence were performed with the help of a Hanbury Brown and Twiss setup consisting of a 50/50 beam splitter and two avalanche photo diodes (see Section 2.4.2). By evaluating the autocorrelation function $g^{(2)}(\tau)$ at $\tau = 0$, the number of emitting NV centres in the nanodiamond is determined. Only nanodiamonds containing a single NV centre, i.e., those with a vanishing peak at $g^{(2)}(0) = 0$ were used for the subsequent pick-and-place procedure.

A homebuilt nanosecond pulse counter is used for monitoring the optical signal and for converting the digital signal of the APDs to an analog voltage which is fed to one of the analog to digital converter of the AFM. This provides the opportunity to directly overlay topography and optical signal. The AFM is controlled with its standard software while home made software and a multi-function data acquisition card are used to control the confocal microscope.

5.3.2. The Pick-and-Place Procedure

In the actual pick-and-place procedure, the pre-characterised nanodiamond is placed into the optical focus of the confocal microscope and is identified with the AFM by scanning the tip over the focus in intermittent contact mode. In addition to the standard AFM images like topography and phase, also the optical signal from the optical microscope versus tip position is recorded. To suppress the excitation light, a longpass filter at $\lambda = 590$ nm is used. With the AFM approached, an additional shortpass filter at $\lambda = 740$ nm is employed in order to suppress the infra-red AFM laser.

The optical signal consists of two contributions. Firstly, there is a constant fluorescence signal from the NV centre in the laser focus. A second contribution stems from fluorescence of the AFM tip, which depends on the position of tip relative to the focus. Thus, scanning the tip over the laser focus results in an AFM topography image together with an optical image of the focus area. Figure 5.6 (a,b) show the AFM topography and the optical image, respectively, with a single nanodiamond in the laser focus. In some cases (Figure 5.6 (b)) the fluorescence drops at

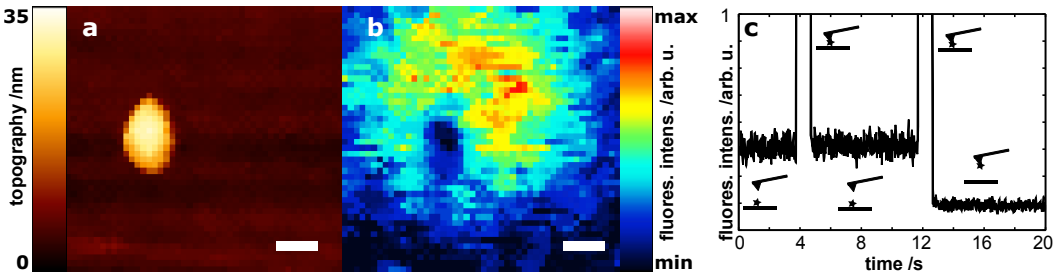

Figure 5.6.: Pick-and-place process. (a) shows a topography image of a nanodiamond in the spot of a confocal microscope's laser. (b) is an optical image, i.e., it shows the detected fluorescence signal versus tip position. In this measurement, the collected fluorescence is reduced when the tip scans across the diamond nanoparticle (see text). Scalebars in (a,b) are 100 nm. (c) shows the detected fluorescence signal when picking up the diamond. In this measurement, the fluorescence increases when the tip is at the sample surface. After a first unsuccessful attempt where the fluorescence had fully recovered the pick up procedure was repeated, and finally the nanodiamond is picked up indicated by a drop of the fluorescence signal to the background level. (Figure adapted from [91])

the nanodiamond's location. This is either due to a modified scattering of the tip's fluorescence towards the collection optics of the confocal microscope when the tip is scanned across the nanodiamond or quenching of the nanodiamonds fluorescence due to the tip (see Chapter 9). If the density of nanodiamonds on the substrate is sufficiently low, a single diamond nanoparticle can be identified in the laser focus unambiguously.

The pick up procedure is started by positioning the AFM tip above the nanodiamond. Then, the tip is pressed on the centre of the particle in contact mode. A force of up to 1 µN is applied, which is sufficient to attach the particle to the tip due to surface adhesion. Simultaneously, the fluorescence is observed. If the nanodiamond is picked up successfully, the fluorescence signal drops to background level after the tip is retracted (see Figure 5.6 (c)). In order to ensure that the nanodiamond is picked up by the tip and not only pushed out of the laser focus, the sample stage is used to scan the vicinity of the original nanodiamond position. If the pick up was not successful the tip is pressed on the nanodiamond again until it is finally picked up. From time to time, an additional topography image with the AFM in intermittent contact mode is taken in order to determine the diamond's position. This is necessary, because the diamond sometimes moves a distance on the order of the tip radius when touched by the AFM tip. In the experiments performed here, a pick up was always possible, even if it could take a large number of approaches (sometimes over 50).

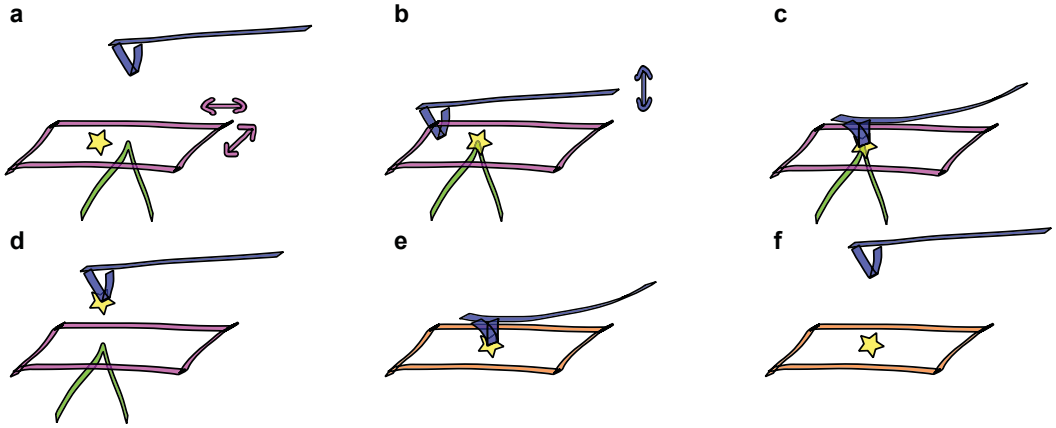

Figure 5.7.: Scheme of the nanodiamond pick-and-place procedure. In (a), the sample is scanned in the confocal microscope in order to find and optically characterise a nanodiamond. In (b), the AFM tip is scanned across the focal region of the microscope to identify the chosen nanodiamond. In (c), the tip is pressed on the nanodiamond. In (d), the nanodiamond sticks to the tip. In (e), the tip is pressed on a new structure to deposit the nanodiamond. Finally, in (f), the diamond is positioned at the desired position. (Figure adapted from [91])

After being picked up, the nanodiamond can be transferred to any structure accessible with the AFM. It is even possible to transport the whole AFM to another setup without losing the nanodiamond. If the new structure is not suitable for confocal microscopy with simultaneous AFM access, care has to be taken that the diamond can be clearly identified after it has been deposited. Therefore, a small area (e.g., 0.1 μm^2) on the targeted structure is scanned by the AFM in intermittent contact mode. In this scanning process it is unlikely to lose the diamond as long as there are no sharp edges on the target surface. The diamond is then deposited by pressing the tip on the surface with a force of up to 1 μN and the area is scanned again. This is repeated until the nanodiamond appears on the topography image.

In contrast to the pick up process, this is not always successful. Only approximately one third of the diamonds picked up could be placed again. This is attributed to nanodiamonds sticking at the side of the tip instead of the tip apex. When pressed to the surface, these nanodiamonds are pushed further along the side of the tip until they can not reach the surface anymore. Obviously, there is always a competition among adhesion between the nanoparticle and the tip and the nanoparticle and the target surface, respectively. When a diamond is lost, a new cantilever is used to make sure that the diamond deposited is really the one pre-characterised before. A sketch of the whole procedure is given in Figure 5.7.

The technique is presented here for nanodiamonds, but in principle, it is possible

to extend it to any other nanoparticle since it only relies on surface adhesion and does not require a chemical functionalisation of the surfaces.

The pick-and-place procedure has to be refined if the targeted structures have sharp edges near the desired nanoparticle position. Examples are photonic crystal cavities (see Section 6.1) [228] or photonic crystal fibres (see Section 6.2) [229]. In this case, a two-step process is needed. The nanodiamond is first placed on a smoother area of the target structure. Then, an AFM topography image of the targeted region can be taken with the bare tip. In this way, the risk of losing the nanodiamond when scanning tip and nanodiamond across sharp edges is avoided. With the targeted region well identified via the AFM topography image, the diamond is finally transferred to its target position by a second pick-and-place process. One disadvantage of this two-step process is the lack of optical control during the second pick up, what makes the whole process more time consuming, since after each try an AFM scan has to be performed in order to determine if the nanodiamond has been picked up.

In principle, the pick-and-place procedure can be performed with any AFM cantilever, but for optimum performance, there are some requirements. First, it is advantageous for the cantilever tip to have a radius of curvature which is large, since the probability for the nanodiamond to attach to the tip's side rather than to its apex decreases with increasing radius. On the other hand, the radius of curvature has to be sufficiently small to identify single nanoparticles in an AFM topography image. Second, ductile tips are preferred because they do not break when being pressed multiple times on the sample. Third, the tip material is important, because the adhesion forces strongly depend on the involved materials [230]. Experiments performed showed that these requirements are best met by metal coated silicon tips, which are commercially available, for example Au and Pt/Ti coated cantilevers from MicroMasch. These tips seldomly break compared to uncoated ones, have a higher radius of curvature (approx. 40 nm), and it is possible to deform them by pressing them on the substrate or on a nanodiamond. Examples of used Pt/Ti coated tip can be seen in Figure 5.8.

An intuitive example which underlines the versatility of the pick-and-place process is its application to diamond crystals grown by chemical vapour deposition on iridium [231]. These diamonds use nanodiamonds as seeds and are grown to a size of several hundreds of nanometres. The diamonds were provided by Christoph Becher's group in Saarbrücken. They are known to host single silicon-vacancy centres (see Section 2.5.4) [76, 231], what makes control over their position especially interesting.

The diamonds are grown on an iridium surface on a silicon substrate, which is non-transparent and therefore makes optical feedback by looking from beneath impossible. For this reason, just the feasibility of picking the diamonds up and placing them again is shown here. This technique then can be applied to pre-

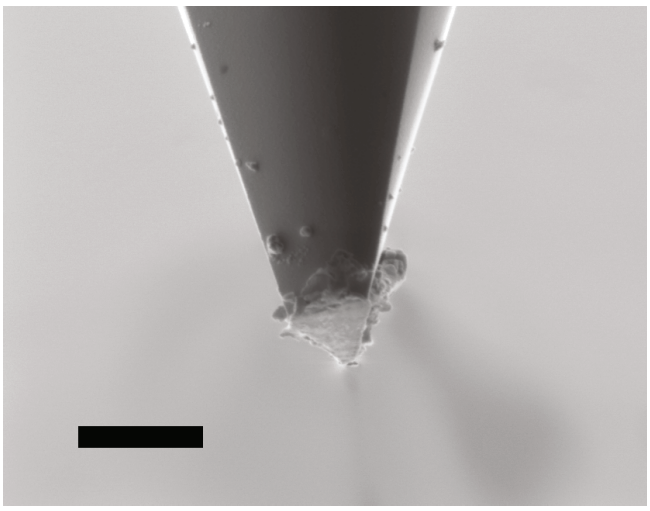

Figure 5.8.: SEM image of Pt/Ti coated cantilever used for the pick-and-place procedure. The tip is flattened by being pressed on the surface in order to pick up a nanodiamond. Scalebar is 1 µm. (Figure also published in [91])

characterised and structured samples in order to pick up that diamond that matches the requirements for a specific task. In Figure 5.9 AFM images of CVD diamonds and the application of the pick-and-place process is shown.

Chapter Summary: Atomic Force Microscopy and Nanomanipulation

In the first section of this chapter, the technique of atomic force microscopy was introduced. Using atomic force microscopy, nanoscale objects can be imaged with high resolution. Also, different modes and contrast mechanisms can be used, making an AFM a very versatile instrument. In the second section, it was shown how the positions of nanoparticles can be manipulated with an AFM. This enables for precise positioning and complex arrangements of nanoparticles. In the last section, a technique to pick up a pre-selected nanoparticle and place it at another position in a very controlled way was shown. Together with the concepts and methods introduced so far in the previous chapters (the introduction of single photons and the NV centre in nanodiamond in Chapters 2 and 3, respectively, as well as techniques to collect single photons efficiently in Chapter 4), the pick-and-place technique allows for the assembly of hybrid quantum devices, as shown in the next chapter.

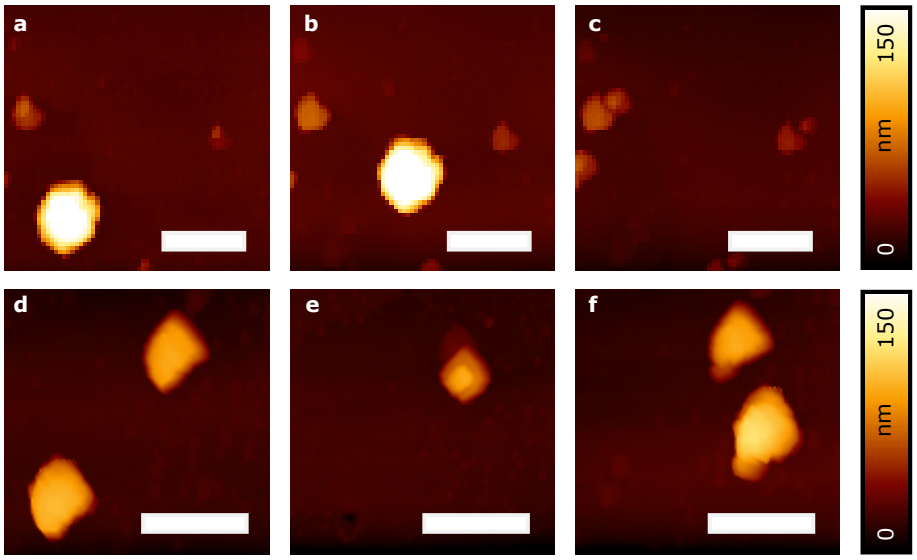

Figure 5.9.: Pick-and-place of CVD diamonds. In (a-c), a diamond is moved and subsequently picked up with the AFM. Note the clear modification of the topography image in (c), which results from the change of the tip's effective shape when the diamond is attached. In (d-f), the diamond in the lower left is picked up and placed again. Scalebars are 400 nm.

6. Nanoassembled Hybrid Photonic Structures

In this chapter, hybrid photonic structures are shown. The structures are build using nanomanipulation processes as reported on in Chapter 5. Especially the pick-and-place process will be used. The hybrid structures introduced are based on single NV centres in nanodiamond as single photon emitters.

In the first part, resonant enhancement of the zero phonon line of a NV centre via the Purcell effect by integration of a NV centre in a photonic crystal cavity is shown. In the second part, a directly fibre integrated single photon source is introduced which consists of a nanodiamond placed onto the cleaved facet of an optical fibre. The experimental results in this chapter have been reported in *Applied Physics Letters* wit the title *Enhancement of the zero phonon line emission from a single nitrogen vacancy center in a nanodiamond via coupling to a photonic crystal cavity* [228], in *physica status solidi (b)* with the title *Coupling of single nitrogen-vacancy defect centers in diamond nanocrystals to optical antennas and photonic crystal cavities* [232], and in *Nano Letters* with the title *Fiber-Integrated Diamond-Based Single Photon Source* [229].

6.1. NV Centre in Photonic Crystal Cavity

The NV centre in diamond (see Chapter 3) is a very promising resource for quantum information processing [233], since it emits single photons [74], can serve as qbit [121], and even entanglement between remote NV centres has been demonstrated [35]. But besides many advantages, there are some drawbacks of the NV centre, namely its small Debye-Waller factor [234] and its coupling strength to electromagnetic fields, which is small when compared to other solid-state systems such as quantum dots [235]. While the small electromagnetic coupling leads to a comparably small photon emission rate, the small Debye-Waller factor reduces the number of photons emitted in the zero phonon line (ZPL) to about 3 % even at liquid helium temperatures [234].

One way to mitigate these drawbacks is to enhance the zero phonon line of the NV centre via the Purcell effect [30] by putting it inside an optical microcavity. As a reminder to Section 2.2, the governing formula is introduced here again. Due to the Purcell effect, the spontaneous emission gets enhanced by a factor, the so called

Purcell factor F_P [28]:

$$F_P = \frac{3}{4\pi^2}\frac{\lambda_c^3}{n^3}\frac{Q}{V_{eff}}, \tag{6.1}$$

with the wavelength of the cavity resonance λ_c, the quality factor (Q factor) of the cavity Q, the refractive index of the cavity n, and the effective mode volume V_{eff}. Clearly, the figure of merit to maximise here is the ratio Q/V_{eff}.

6.1.1. Gallium Phosphide Photonic Crystal Cavities

One system, which yields high values of Q/V_{eff}, are cavities in two-dimensional photonic crystal slabs [28, 158]. They have the ability to confine light to a volume of the order of the cubic wavelength, while still having a high quality factor. For example in Reference [236] a volume $V_{eff} = 1.7\frac{\lambda^3}{n^3}$ and a quality factor of $Q = 9 \cdot 10^5$ is reached for a cavity in silicon. Since here the coupling of of a NV centre to the cavity is desired, another material, which is transparent in the corresponding spectral range, is needed. For this purpose, gallium phosphide is chosen. It has a high refractive index of 3.3 [237], is transparent at a wavelength of 638 nm, and there exist fabrication processes that allow for creation and structuring of free standing membranes and hence the production of photonic crystal cavities (PCCs) [238]. The PCCs used here are made from a 70 nm thick heteroepitaxial gallium phosphide layer grown on a Si(100) substrate, which is under etched after the PCCs are structures via electron-beam lithography and subsequent dry etching [232].

The photonic crystal cavities produced are so called L3 cavities [239] with a designed resonance frequency of 638 nm. They consist of three missing holes in a photonic crystal slab with some of the surrounding holes shifted for optimisation [240]. An scanning electron microscopy image of such a structure is shown in Figure 6.3 (c). Their Q factors are around 10^3.

6.1.2. Process of Coupling PCC and Nanodiamond

To bring a NV centre inside the cavity, the pick-and-place approach is used, i.e., a nanodiamond containing a single NV centre is transferred to the cavity by means of nanomanipulation (see Section 5.2). This is in contrast to the bulk diamond approach, where the whole cavity is built from diamond and either naturally occurring or implanted centres are used [241–243].

The detailed process of bringing a single NV centre into the PCC works as follows:

1. A nanodiamond on a cover slip is pre-characterised in terms of the spectral position of its zero phonon line and $g^{(2)}(0)$ value.

2. PCCs are characterised and one with a matching or slightly higher resonance wavelength of the fundamental mode is chosen.

3. If necessary, the tuning technique described below is used to match the resonance frequencies of ZPL and PCC.

4. The diamond is picked up and placed on the PCC sample near the photonic crystal membrane. (for details of the two-step pick-and-place procedure see Section 5.3)

5. To enable for direct placing of the nanodiamond inside the cavity, the cavity is scanned with the AFM, so that it can be directly addressed with the AFM later.

6. The diamond is picked up again and placed directly inside the cavity.

7. AFM nanomanipulation techniques are used to fine-position the diamond.

In step 2, a way of characterising the PCCs is needed. This can be done in different ways like using crossed polarisation imaging [237, 244], coating the cavities with dye molecules [245], or using the autofluorescence of the material itself [246]. Here, the latter technique is used. A 532 nm laser is focussed on the PCC and excites autofluorescence. At the spectral position of the cavity resonances this gets enhanced via the Purcell effect (see Equation 6.1), the same effect which will be used to enhance the NV centre.

In step 3, the cavity is tuned. This is done by shining in a focussed 407 nm laser beam, which gets absorbed by the membrane, because its photon energy is higher than the gallium phosphide band gap [247]. Shining in the laser causes the PCC resonance to shift to longer wavelengths due to heating of the membrane, but after the laser is turned off the resonance is permanently shifted to shorter wavelengths. It is assumed that this permanent effect is caused by an oxidation process, which alters the effective cavity geometry [248]. The size of the shift is found to depend mainly on the power of the incoming laser, not on the time it is shone in (see Figure 6.1 (a)). Also, the quality factors are unaffected by this process, as long as the tuning distances do not get to large (see Figure 6.1 (b)).

6.1.3. Experiment of Coupling PCC and Nanodiamond

Following the coupling process described in Section 6.1.2, at first the steps 1-3 are carried out. The diamond is pre-characterised, a cavity is chosen and tuned to the wavelength of the NV centre's ZPL. The results of this pre-characterisation are shown in Figure 6.2. A clear antibunching dip in the measured autocorrelation function is visible at zero time delay indicating single photon emission from the NV centre. Also, the spectral position of the ZPL is matched to the cavity resonance. Now, the pick-and-place nanomanipulation can be applied in order to couple ZPL and cavity.

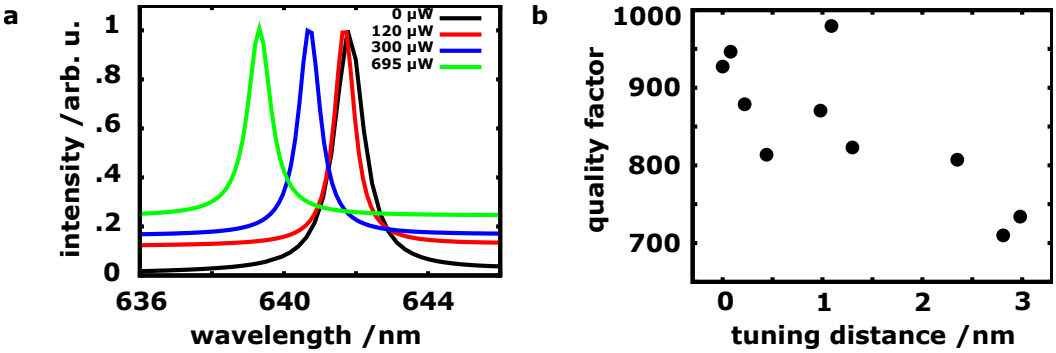

Figure 6.1.: Photonic crystal cavity tuning. (a) shows the effect of tuning for different laser powers. With increasing power, the measured resonance of a GaP PCC (as shown in Figure 6.3 (c)) shifts permanently to lower wavelengths. In (b) the dependence of the cavity's quality factor on the tuning distance is shown. It can be seen, that for moderate tuning distances the quality factor is nearly constant. Only for large distances over 1 nm it clearly decreases. (Figure adapted from [232])

After successful nanomanipulation, the diamond is located in the centre of the photonic crystal cavity, as can be seen in the atomic force and scanning electron micrographs shown in Figure 6.3 (a,c). In Figure 6.3 (b) a FDTD calculation (see Appendix C) of the PCC based on the geometry measured with the AFM is shown. Clearly, the maximum enhancement of the electric field lies in the middle of the cavity where the nanocrystal is placed. Due to this high overlap of field and emitter, a huge emission enhancement is expected and in fact, as can be seen in Figure 6.3 (d), an enhancement factor of 12.1 is observed. This factor is lower than the theoretical value of $F_P = 61$ obtained by Equation 6.1 when putting in the values for the quality factor $Q = 603$ and the mode volume $V_{eff} = 0.75(\lambda/n)^3$ inferred from FDTD calculations. The main reasons for the difference are that the field maximum of the cavity lies inside the GaP slab, inaccessible for the diamond and that the NV centre's dipoles' orientation is not controlled and hence possibly not matched to the fields in the cavity.

The coupling process and the large enhancement obtained here are an important step towards more complex integrated hybrid devices, since the enhanced emission of the zero phonon line can serve as a source of narrow band photons. Further improvements possible are to use PCCs with higher Q values and cooling the system down to liquid helium temperatures, where the phonon sidebands of the NV centres are less pronounced and more photons are emitted on the ZPL from the start (see Chapter 3). It is also noteworthy, that the coupling procedure employed works not only for NV centres, but can be also applied to other centres in nanodiamonds or to completely different emitters, as long as they exist in the form of nanoparticles.

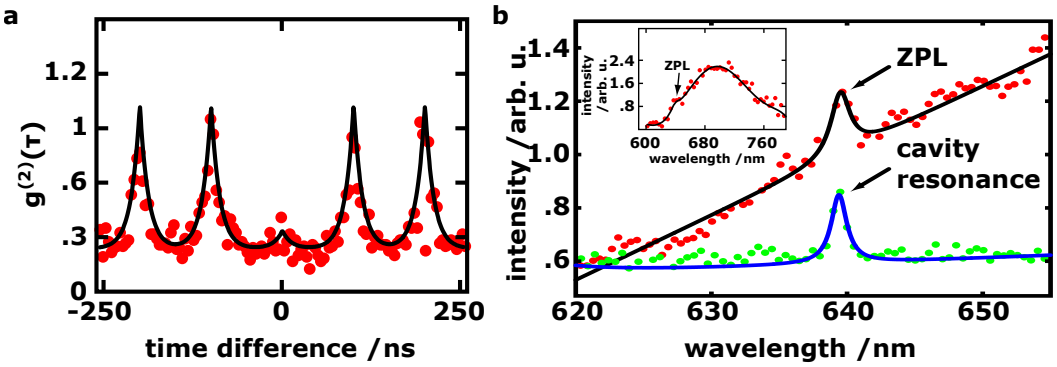

Figure 6.2.: Pre-characterisation of NV centre and PCC. (a) shows the autocorrelation measurement done to pre-characterise the NV centre, which is subsequently put into a PCC. The measurement is performed under pulsed excitation with a repetition rate of 10 MHz. (b) shows the spectra of NV centre and PCC in red and green, respectively. The PCC is already tuned to match the ZPL. The inset shows the whole spectrum acquired from the NV centre. (Figure adapted from [228])

Other groups have coupled nanodiamonds to PCCs as well, for example Englund *et al.* [249], who moved a PCC over a substrate containing nanodiamonds – a non-scalable way of coupling – or Van der Sar *et al.* [169], who used a manipulator in an electron microscope. Both groups did not enhance the ZPL, but the phonon sideband. Recently, in an approach using structured diamond membranes, Purcell enhancement by a factor of 70 was demonstrated using a single NV centre at liquid helium temperatures [242].

All these results obtained by different approaches show the feasibility of coupling NV centres to PCCs. In future experiments it will turn out which approach is best suited for which application, since all have their individual strengths and drawbacks.

6.2. Fibre Integrated Single Photon Source

Hybrid assembly using the pick-and-place technique can not only be used to enhance transitions of single photon emitters, but also to build a robust single photon source with efficient photon collection. The most direct approach in coupling the single photons from an emitter to the guided modes of an optical waveguide is to directly couple the emitter to the modes, without any additional optics. In the following, this approach is pursed with a diamond nanocrystal lying directly on the facet of an optical fibre. These results have been published in *Nano Letters* with the title *Fiber-Integrated Diamond-Based Single Photon Source* [175].

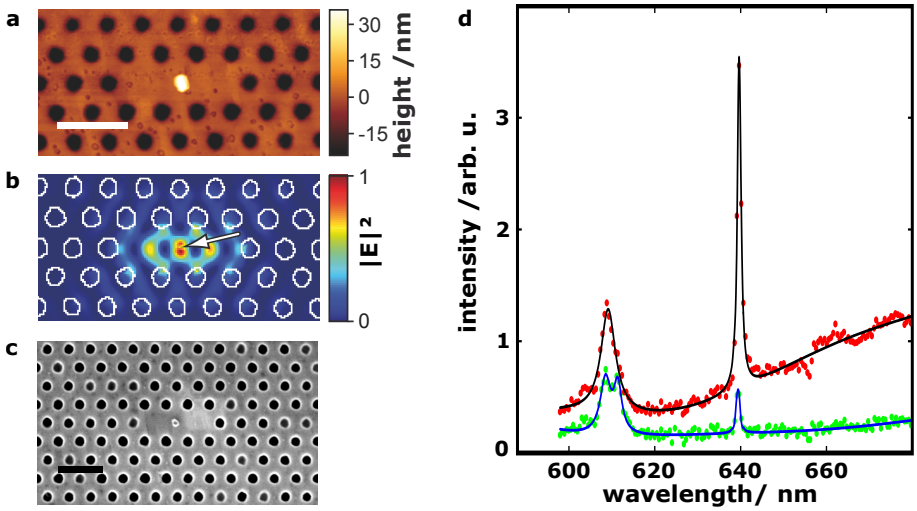

Figure 6.3.: NV centre coupled to a PCC. (a) shows an AFM image of the PCC with a diamond nanocrystal. The image is taken after the diamond's position was fine-adjusted by moving it to the position, where the field maximum is expected. Scalebar is 400 nm. (b) is a FDTD simulation showing the cavity's mode while in (c) a scanning electron image of the assembled system is shown. Scalebar is 400 nm. In (d) fluorescence spectra of the PCC before (green dots/blue line) and after (red dots/ black line) assembly are shown. By comparison with the uncoupled spectrum of the NV centre an enhancement factor of 12.1 is found. (Figure adapted from [228, 232])

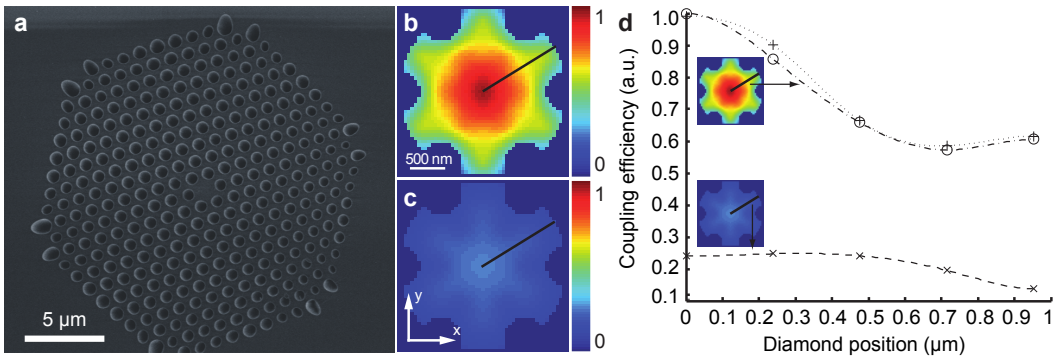

Figure 6.4.: FDTD calculations of the dipole-fibre coupling efficiency. (a) shows a scanning electron micrograph of the fibre facet. (b) and (c) show calculated coupling efficiencies for different positions of the dipole on the fibre for a dipole perpendicular and parallel to the fibre interface, respectively. (d) shows the characteristics of the normalised coupling efficiency along the black lines in (b) and (c). (Figure adapted from [229])

6.2.1. Preliminary Considerations

For fabrication of a NV centre based fibre integrated single photon source, a fibre, a NV centre, and a method of coupling both are needed. As in Section 6.1, the nanomanipulation techniques introduced in Section 5.2 are used. The NV centre's are provided in a standard way by spin-coating a nanodiamond solution on a glass cover slip, however, the choice of an optimal fibre is more difficult. Since it proves to be very hard to hinder all the excitation light from entering the fibre, the fibre has to be made from a material with very low fluorescence. Furthermore, this would allow for exciting the NV centre in a remote way with the excitation light coupled through the fibre. Fibres with a pure silica core are hence superior to, for example, germanium doped ones. It has to be noted that depending on the type of fibre and manufacturer, even pure silica fibres may fluoresce strongly due to impurities. Also, the numerical aperture of the fibre should be large in order to collect as many photons as possible. Due to the dielectric air-fibre interface at the fibre facet, in a solid-immersion-like manner, a majority of the photons will be emitted into the fibre (see Chapter 4). This leads to an enhancement of the effective numerical aperture of the fibre. For the type of fibre used in the experiment (NL-1.5-590, NKT Photonics, NA=0.45), FDTD calculations (see Section C) show that this effect leads to a effective numerical aperture of up to 0.77 for a dipole perpendicular to the optical axis of the fibre. In Figure 6.4 (b-d), results of these calculations are shown.

The geometry of the fibre used for the single photon source can be seen in Fig-

ure 6.4 (a). The hexagonal lattice has a pitch of 1.07 µm and the holes have a diameter of 0.7 µm. The core is realised as a single missing hole. The length of the fibre is chosen to be on the order of 10 cm. This length still suitable for first applications, but the background fluorescence, which scales with length, is as low as possible.

6.2.2. Coupling of Nanodiamonds and Optical Fibres

The two-step coupling process used here is very similar to the process used in Section 6.1. It consists of the following steps:

1. By pre-characterisation a suitable nanodiamond is chosen.
2. The diamond is picked up and placed on the fibre facet near the core.
3. To enable for direct placing of the nanodiamond on the core, the core is scanned with the AFM, so that it can be directly addressed with the AFM later.
4. The diamond is picked up again and placed directly on the core.
5. AFM nanomanipulation techniques are used to fine position the diamond.

With this process, nanodiamonds containing single NV centres are placed on a variety of different fibres as can be seen in Figure 6.5. In Figure 6.5 (a) a silicon AFM cantilever approaching an optical fibre is shown. This can be used for characterisation and manipulation purposes, whereas the pick-and-placing is carried out with platinum coated tips.

6.2.3. Fibre Integrated Diamond Based Single Photon Source

After successful assembly of the fibre integrated single photon source from a fibre and a nanodiamond (see Figure 6.6 (b) for an AFM image), optical characterisation of the system is carried out. For this, three different experimental configurations are implemented, as sketched in Figure 6.6 (a). In all configurations, the excitation light is a green laser and the detected fluorescence light is filtered by a 650 nm long pass filter. Configuration I is a confocal configuration where excitation and detection are done free-space using an objective lens with a numerical aperture of 0.9. In configuration II, the excitation is still performed via free-space, but the fluorescence light is collected through the fibre and in configuration III, excitation as well as detection are done through the fibre. Images acquired by scanning the excitation laser over the fibre facet in configurations I and II can be found in Figure 6.6 (e,f). Increased fluorescence at the nanodiamond's position is found in both configurations, indicating that the NV centre's emission is visible from both

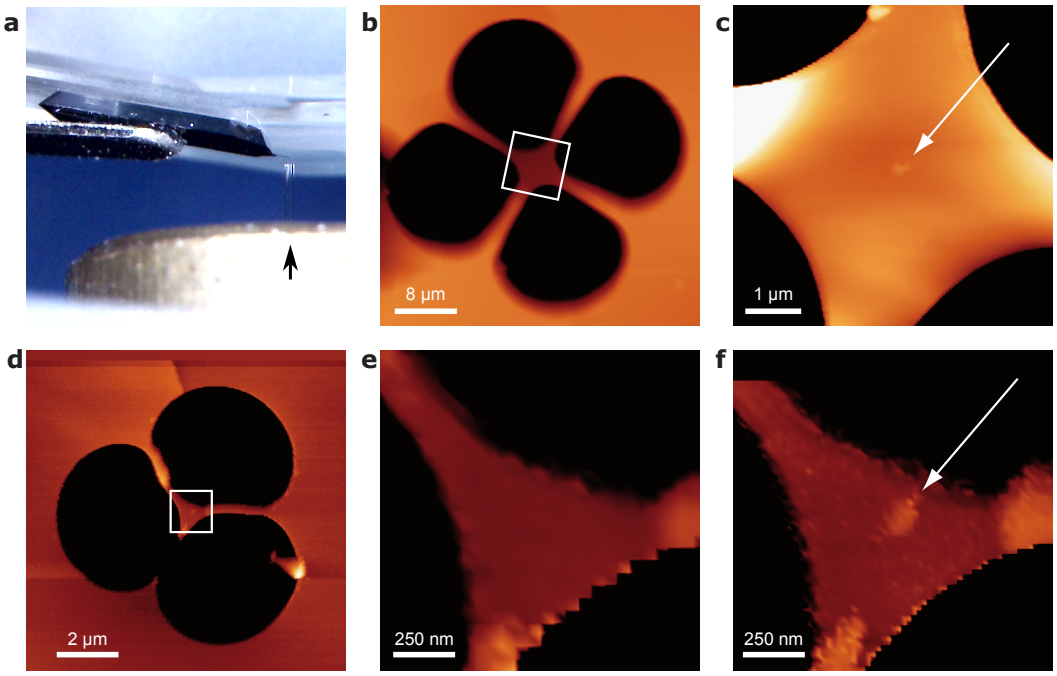

Figure 6.5.: Nanodiamonds on fibre cores. (a) shows an AFM cantilever chip (black object in the middle) clamped to a glass block approaching an optical fibre which sits in a brass mount. The black arrow indicated where the fibre emerges from the its mount. (b-f) show AFM images of fibre facets of cloverleaf (b,c) and wagon-wheel (d,e,f) microstructured fibres. (b,d) give an overview of the core regions while (c,e,f) are zooms to the white squares in (b,d). While in (c,f) the nanodiamond (indicated by an arrow) is already put on the core, in (e) the fibre's core prior to coupling the nanodiamond is shown. For an AFM image of the fibre used in the fibre integrated diamond based single photon source see Figure 6.6. ((b-f) adapted from [229])

sides. When looking at the emission spectrum through the fibre (Figure 6.6 (c)), large lines from Raman scattering and other background light from the fibre is visible (black line), but after filtering with the 650 nm filter, nearly all of this light is filtered out.

For a functional single photon source, the photon statistics (see Section 2.1.3) is of great importance. The $g^{(2)}(0)$ (cf. Equation 2.16) has to be sufficiently low. Only if its value is below 0.5, the main contribution to the photons stems from a single emitter. Ideally, a single photon source has a $g^{(2)}(0) = 0$ which is a value that can not be reached in presence of any background. Using continuous wave excitation light, measurements of the $g^{(2)}$-function are shown in Figure 6.7 (d,e) for the confocal configuration (I) and detected through the fibre (configuration II), respectively. The $g^{(2)}(0)$-values (deduced from a fit to a model found for example in Jelezko *et al.* [89]) are $g^{(2)}(0) = 0.45$ at an excitation power of 40 µW in configuration I and $g^{(2)}(0) = 0.36$ at an excitation power of 49 µW in configuration II. It has to be noted that no background correction has been applied to any of these data, since for a single photon source all the photons emitted play a role.

After it is shown that the source emits single photons, the next important quantity is the rate of emitted photons when the emitter is fully saturated. The corresponding measurements are shown in Figure 6.7 (a,b) for configurations I and II, respectively. A fit (red lines) yields maximum count rates of $R_{inf} = 52.6$ kcts/s in configuration I and $R_{inf} = 43.2$ kcts/s in configuration II. Here, background correction for a linear background is applied to the data, so in contrast to the $g^{(2)}$-functions in Figure 6.7 (d,e), only photons stemming from the NV centre contribute to these values.

By comparison of the photon count rate collected through the NA=0.9 microscope objective and the count rate collected through the fibre, it is possible to estimate the effective numerical aperture NA_{eff} of the fibre, which should be higher than the nominal NA of the fibre due to near-field interaction at the dielectric-air interface at the fibre facet. Assuming a uniform emission of the NV centre, this estimate is $\mathrm{NA}_{eff} = 0.82$. This value is similar to values of usual high-NA optics, but with an integrated and alignment-free way of coupling.

For most applications, synchronisation of different parts is required. Hence, pulsed single photon sources are needed. It is straightforward to implement a pulsed laser as excitation source in the integrated single photon source. By exploiting the pulsed nature of the laser, another type of filtering can be implemented: time gating. Here, only photons from defined time intervals are evaluated and others are excluded in the TCSPC (for TCSPS see Section 2.4.1). In Figure 6.7 (c), an antibunching measurement using time gating is shown. Photons arriving in a time span of 3.5 ns after a laser pulse are discarded in the evaluation. In this way, all the Raman scattering and fast decaying fluorescent background light does not contribute while, due to its long lifetime, photons from the NV centre are still detected.

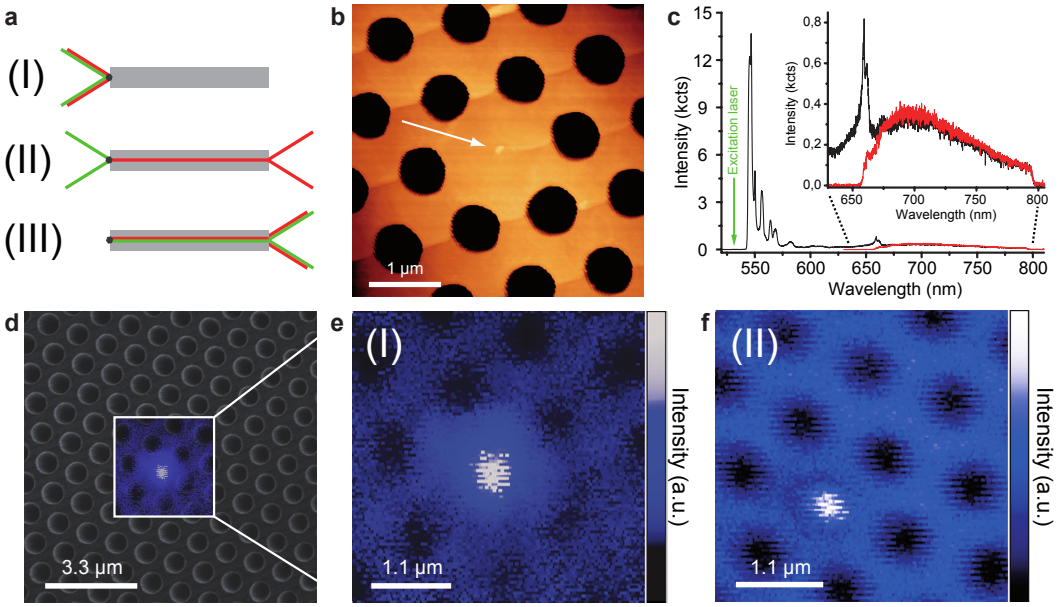

Figure 6.6.: Characterisation of the fibre-coupled single photon source. (a) is a sketch of the three different excitation and detection schemes used. Either excitation and detection happens in confocal manner (I), the diamond is excited from top and the photons are collected through the fibre (II), or both, excitation and detection happen through the fibre (III). (b) is an AFM micrograph of the assembled system with the white arrow indicating the diamond nanocrystal hosting a single NV centre. An optical spectrum of the emission collected through the fibre is shown in (c) as black line. The red line shows the spectrum after adding a 650 nm long pass filter. The inset is a zoom to a part of the recorded spectrum. (d) is an overlay from scanning electron beam and confocal image while (e) is the confocal measurement only (configuration (I)). (f) is a micrograph measured in configuration (II). Clearly, the fluorescence is highest at the position of the NV centre. (Figure adapted from [229])

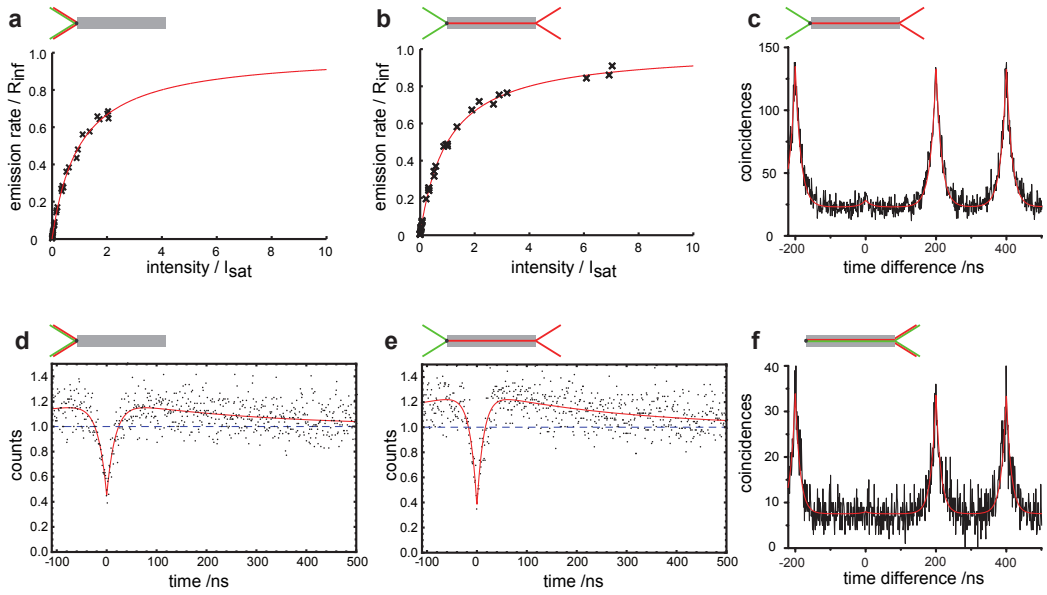

Figure 6.7.: Optical characterisation of the fibre-coupled single photon source. (a) and (b) show measurements of the saturation behaviour for the configurations I and II, respectively. The red line is a fit to a three level model system. Saturation count rates are $R_{inf} = 52.6$ kcts/s in configuration I and $R_{inf} = 43.2$ kcts/s in configuration II. (c-e) show autocorrelation measurements in different configurations under continuous wave excitation (d,e) and under pulsed excitation with time gating applied (c,f). Red lines are fits to a theoretical model yielding $g^{(2)}(0) = 0.21$ in (c), $g^{(2)}(0) = 0.45$ in (d), $g^{(2)}(0) = 0.36$ in (e), and $g^{(2)}(0) = 0.23$ in (f). (Figure adapted from [229])

The measured $g^{(2)}(0)$-value in configuration II is with $g^{(2)}(0) = 0.21$ significantly smaller than without the time gating.

With time gating, it is also possible to measure in configuration III, where excitation as well as detection is performed through the fibre. Exciting through the fibre means that all the green excitation light has to go through the fibre. Furthermore, it means that the light is less focused at the nanodiamond's location, because the mode field diameter of the fibre is larger than the laser focus used in configurations I and II, what makes higher excitation powers necessary. This leads to increased background, which then is suppressed by time gating. An autocorrelation function measured in configuration III is shown in Figure 6.7 (f). It yields $g^{(2)}(0) = 0.23$. An interesting aspect of this configuration is that no direct optical access to the fibre facet is needed – the source is completely fibre coupled. Also, this configuration can be used as a sensor when the environment of the NV centre is changed.

Chapter Summary: Nanoassembled Hybrid Photonic Structures

In this chapter, two implementations of nanoassembeld hybrid photonic structures were reported. The first structure was built in order to enhance the zero phonon line of a NV centre resonantly by coupling it to a photonic crystal cavity. An enhancement factor of 12.1 was observed. The second structure was a directly integrated and efficient single photon source, consisting of a nanodiamond with NV centre and a photonic crystal fibre. There are many interesting devices, which can be nanoassembled with the pick-and-place technique and more structures can be found in References [114, 250]. An alternative way to build quantum hybrid devices without nanoassembling techniques will be shown in the next chapter.

7. Hybrid Structures Using Nanodiamonds and Photoresist

In this chapter, development and application of hybrid structures using a combination of photoresist and nanodiamonds with single NV centres is described. Usage of a hybrid material is an alternative and a complement for hybrid integration using the nanoassembly techniques described in Chapter 5. Parts of the following has been published in *Scientific Reports* under the title *Three-dimensional quantum photonic elements based on single nitrogen vacancy-centres in laser-written microstructures* [177] and other parts are submitted with the title *Laser-written parabolic micro-antennas for efficient photon collection from single NV centers.*

7.1. Hybrid Materials

On-chip photonic circuits working at the single quantum level play an important role for future quantum information processing technology [219]. Such a fully integrated quantum optical technology requires active quantum systems incorporated into resonant optical microstructures interconnected in three dimensions via photonic wires. NV centres (see Chapter 3) are ideal candidates as emitters in such architectures [72, 89]. Extensive research efforts to couple NV centres to photonic structures such as optical microresonators [251, 252], microcavities [169, 228, 241], and waveguides [113, 222, 229] have been pursued either by top-down fabrication via etching of diamond membranes [241, 252] or by sophisticated bottom-up assembly of hybrid structures using diamond nanocrystals [169, 228, 251].

Besides the top-down and hybrid approach based on nanomanipulation (see Section 5.2), there exists another approach based on hybrid materials. In this approach, nanoparticles are added to the materials before building structures, instead of combining ready-made structures and particles later. Recently, the incorporation of nanodiamonds in soft glass via a melting process has been introduced, what makes it possible to build, e.g., optical fibres [176].

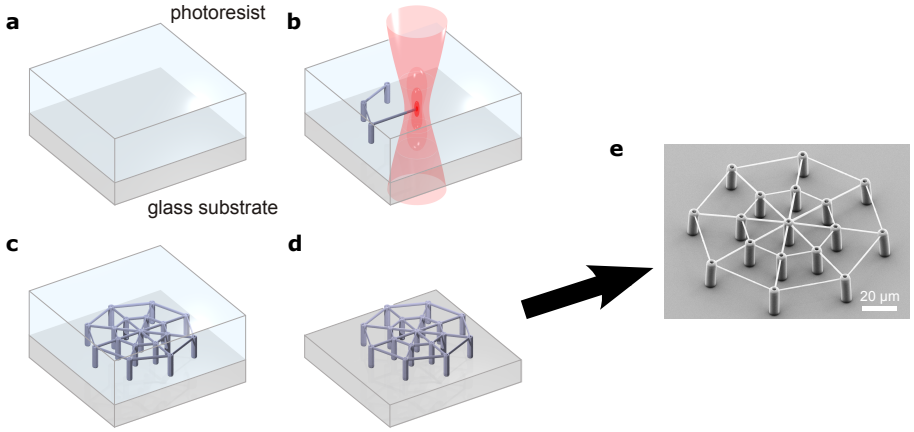

Figure 7.1.: Process of two-photon direct laser-writing. The process starts with a photoresist, usually on a glass substrate, as shown in (a). Then, in (b), a tightly focusses pulsed laser polymerises the resist via a two-photon process. Due to the non-linear nature of this process, only a spot in the focal volume is polymerised. After the polymerisation (see (c)) the sample is developed in solvents which dissolve only the unexposed resist, leaving behind the polymerised structure (see (d)). In (e), a scanning electron micrograph of a fabricated structure is shown (in this case a structure for experiments with biological cells). (Figure adapted from [253])

7.2. Two-Photon Direct Laser-Writing

An easy and low-cost way of fabricating photonic structures is optical lithography via direct laser-writing (DLW) [181, 182], where a tightly focussed femtosecond laser beam is used to expose a photoresist (see Figure 7.1 (a,b)). Due to the non-linear nature of the multi-photon absorption process, the photoresist only polymerises in the laser focus, where the intensity is high. In this way multi-photon absorption enables a sequential three-dimensional (3D) exposure by scanning the sample or the focus of the laser. For common negative-tone photoresists, unexposed parts are removed during a development step and the 3D polymer structures remain (see Figure 7.1 (c,d)). DLW is well known for the fabrication of photonic crystals [182] or other photonic elements like resonators [254, 255] and waveguides [256].

7.3. Diamond Doped Photoresist

In order to functionalise the structures with optically active material, fluorescent dyes [257], quantum dots [258] and metal nanoparticles [259] have been incorporated in structures produced by DLW. Here, small amounts of nanodiamonds from

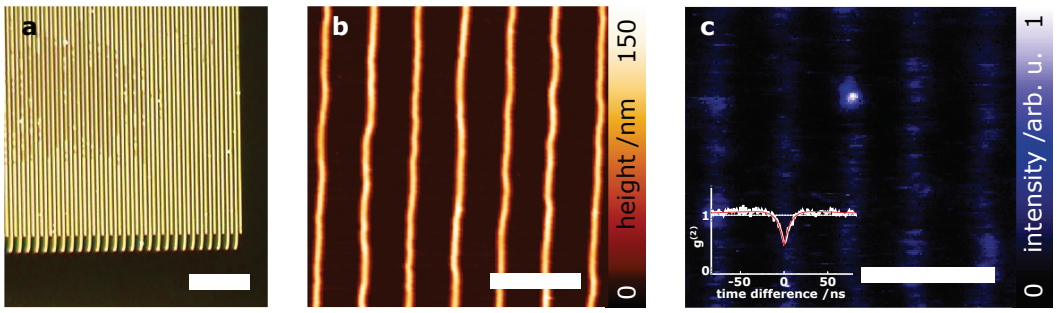

Figure 7.2.: Characterisation of a test grating. (a) shows a dark-field microscopy image of a test grating produced using the diamond doped photoresist. In (b), an atomic force microscope image is shown. The material is only where intended and there are no diamonds elsewhere. A confocal microscope scan is shown in (c). A NV centre is clearly visible as bright spot in the middle of the upper half. The inset shows the $g^{(2)}(\tau)$ measured at that spot. No background correction is applied to the data. Scalebars are 20 µm in (a) and 3 µm in (b,c), respectively. (panel (a) courtesy of J. Fischer)

solution are directly mixed into a photoresist.

The photoresist used is based on the monomer pentaerythritol tetraacrylate (PETTA) which contains 350 ppm monomethyl ether hydroquinone as inhibitor [260]. Next, 0.25 % wt of the photoinitiator 7-diethylamino-3-thenoylcoumarin are added. Last, 2 % wt of an ethanol-based nanodiamond suspension are added and stirred overnight. Nanodiamonds are of type 1b and had a median diameter of 25 nm (Microdiamant AG).

This special photoresist allows for the fabrication of transparent optical elements made from an acrylate polymer containing nanodiamonds. The nanodiamonds contain NV centres which are photostable even after exposure by the DLW laser. After the DLW process they serve as integrated single photon sources. It is especially noteworthy that this technique is not limited to NV centres in diamond nanocrystals. It can be applied to any photostable single photon emitter in nanocrystalline material, e.g., other diamond defect centres, such as silicon vacancy centres [231], or other deep defect centres in large band gap material [261].

As a first test of the single emitter containing photoresist, test gratings are written. The characterisation of these gratings is shown in Figure 7.2. Figure 7.2 (a) shows a dark-field microscope image of a grating. Distinct lines are visible along with some imperfections. With an atomic force microscope, it is verified that the spaces between the lines are free from nanodiamonds (see Figure 7.2 (b)). Finally, the grating is scanned with a confocal microscope in order to find nanodiamonds containing single NV centres. In the scan in Figure 7.2 (c), a single NV centre is

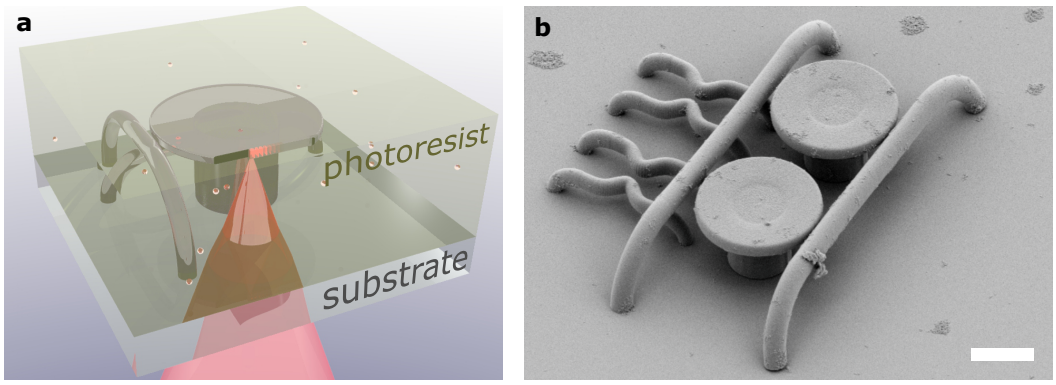

Figure 7.3.: Direct laser-writing in nanodiamond photoresist. (a) is a sketch of the direct laser writing process. A femtosecond laser beam is focussed into the photoresist in order to polymerise well defined 3D structures. (b) shows a scanning electron micrograph of such a structure after development. It contains several key photonic elements, such as waveguides, couplers and microdisc resonators. Scale bar is 5 µm (Figure adapted from [177]).

seen as a bright spot. Also visible are the lines of the grating, which are fluorescing as well. In contrast to the NV centre, it is possible to bleach most of the photoresists fluorescence, as it was done prior to taking this image. To prove that the object found is an NV centre and not some other unwanted fluorescing particle, the second order autocorrelation function $g^{(2)}(\tau)$ is measured (inset in Figure 7.2 (c)). Due to some residual fluorescence of the polymerised photoresist, a value of $g^{(2)}(0) > 0$ is found.

After this first proof that the hybrid material is working in principle, meaning that it still can be used for DLW and that (single) NV centres can be found, the next step is to manufacture more complex structures. Figure 7.3 illustrates the production of such structures, in particular of the waveguides and resonators used in Section 7.4.

7.4. Diamond Doped Laser-Written Microstructures

In this section, functionality and interaction of key building blocks for quantum photonic circuitry fabricated by DLW is demonstrated. Key building blocks are interconnects (i.e., waveguides) and functional elements like resonators and emitters. Combining these interconnects is one of the main requirements for on-chip integrated photonics.

7.4.1. Whispering Gallery Mode Resonators

As a first component for integrated photonic circuits, disc resonators with a disc diameter of 20 µm and a disc thickness of approximately 1.2 µm on a stem with diameter 10 µm are fabricated using the photoresist functionalised with nanocrystals (see Section 7.3).

The mode structure of the whispering gallery modes (WGMs) in the disc resonators is analysed by means of coupling in a tunable external-cavity diode laser at around 770 nm via the evanescent fields of a tapered optical fibre. A sketch of the measurement technique is shown in Figure 7.4 (a). By tuning the frequency of the laser over the distinct whispering gallery modes, light is coupled into the resonator (see Figure 7.4 (c)) and different modes can be observed as Lorentzian shaped dips in the transmitted power. The polarisation of the incoming light is chosen to maximise coupling depth. For normalisation of the data sets, at first a reference scan with the fibre taper not being coupled is performed. These data are then compared with the results when the same tapered fibre is coupled to the resonator. Corresponding quality factors (Q factors) are calculated from the dips by a Lorentzian fit function with an additional linear term to better match the local environment of the resonances. All measurements are performed with the tapered fibre in full contact. The observed free spectral range of 6.5 nm of the resonator shown in Figure 7.4 (d) fits well to the expected value of 6.4 nm for a disc with diameter 20 µm derived from geometrical considerations assuming an index of refraction of 1.5. The highest Q factors are as large as 10^4 at a wavelength of around 770 nm (see Figure 7.4 (e)).

Next, a homebuilt confocal microscope is used to raster scan the fabricated resonator discs (see Figure 7.5 (a)) and to identify single NV centres by measuring the second-order autocorrelation function $g^{(2)}(\tau)$ in a Hanbury Brown and Twiss interferometer (see Section 2.4.2). In parallel, a grating spectrometer is used to resolve the emission spectra of the individual emitters. Figure 7.5 (b) shows a confocal scan of a resonator where fluorescent defects can be identified as bright spots on the resonator. Encircled is a spot on the resonator's outer rim where coupling to the disc's whispering gallery modes is expected. Figure 7.5 (d) displays an autocorrelation measurement of fluorescence collected from that spot. A clear antibunching dip is observed reaching a value of $g^{(2)}(0) = 0.31 \pm 0.04$ as deduced from the fit shown as red curve. No background correction is applied to these data. This measurement shows that the bright spot indeed corresponds to a single NV centre in the disc resonator.

The fluorescence spectrum of a NV centre at room temperature is typically broadened over 200 nm from approx. 600 nm to 800 nm by phonon sidebands (see Chapter 3). This corresponds well to the measured emission spectrum shown in Figure 7.5 (c). The peak at approximately 630 nm stems from fluorescence of the

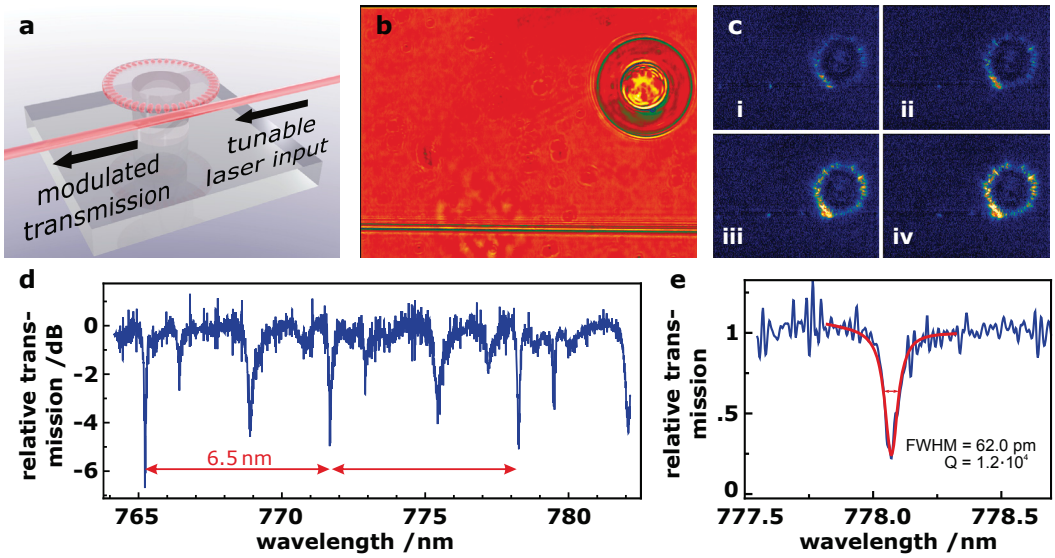

Figure 7.4.: Mode measurements of whispering gallery resonators produced using the DLW in the hybrid photoresist. In (a) a tunable laser is coupled to a disc resonator via a tapered fibre. Upon sweeping the laser frequency, the transmitted light is modulated by the modes of the resonator. (b) shows the 20 µm resonator being approached by a 1.5 µm thick tapered fibre, while in (c) the scattered light when a tapered fibre is coupled to a resonator is shown. In panels i-iv the frequency of the light coupled to the resonator is changed from the off-resonant case to resonance. (d) shows a scan of the laser wavelength over many modes with a free spectral range of 6.5 nm indicated by the red arrows. (e) is a scan of a single resonator mode with a quality factor Q of 1.2×10^4. ((a,d,e) adapted from [177])

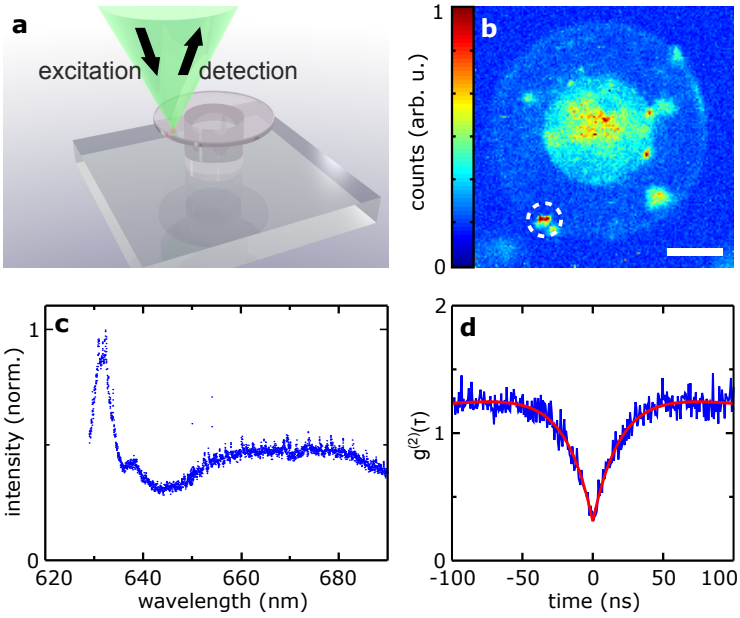

Figure 7.5.: DLW resonator containing single NV centres. A diamond nanocrystal containing a single NV centre is coupled to whispering gallery modes of a DLW disc resonator. (a) shows the measurement scheme. Detection and excitation take place at the same point in a confocal configuration. (b) is a scanning confocal microscope image of the resonator disc. The circle indicates a bright spot identified as single NV centre. Its fluorescence is analysed in (c) and (d). Scalebar is 5 µm. (c) shows the spectrum of the collected fluorescence. The resonator modes are seen as modulation on the broad NV centre phonon sidebands. The peak at 630 nm stems from the photoresist and can be bleached over time. The autocorrelation function of the fluorescence from the NV centre is shown in (d). A clear antibunching behaviour can be seen. The red curve is a fit to the data with $g^{(2)}(0) = 0.31 \pm 0.04$. (Figure source: [177])

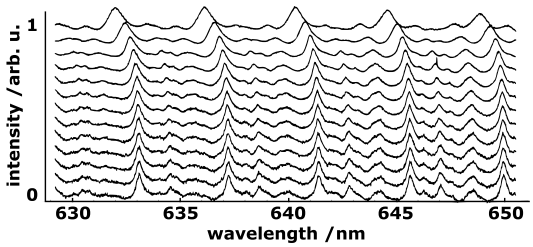

Figure 7.6.: Tuning of DLW written resonator by a 405 nm laser. Each spectrum is integrated for 30 second while the laser is focussed on the resonator's rim inside a vacuum atmosphere. Vertical offsets are added for clarity and increase with increasing time. (Figure adapted from: [177])

photoresist and bleaches after long excitation. For confocal scans and correlation measurements this background light is suppressed by spectral filtering. In addition, there is a fine modulation of the spectrum due to the cavity resonances. It is attributed to photons that are initially emitted into the resonator modes and afterwards scattered out by the diamond nanocrystal. Hence, these photons are detected in addition to the flat unmodulated spectrum emitted directly out of the disc.

Having now single NV centres coupled to the modes of a whispering gallery resonator, for efficient coupling two more requirements have to be met: Firstly, the system has to be compatible with the environment in a cryostat, because in order to get a sharper zero phonon line, the NV centres need to be cooled to liquid helium temperatures. Secondly, there need to be ways of tuning the resonance of the resonator, in order to match them to the zero phonon line. Both requirements are met by the resonator-emitter system. Cooling it down in a liquid helium flow cryostat does not destroy the structures. Also, its modes can be tuned by shining in a focussed 405 nm laser. This laser causes a permanent change in the resonator's material and in this way changes the mode structure. Similar techniques are used in References [228, 248] and in Section 6.1, but with the difference, that in the cryostat there is vacuum. So, oxidation as process can be ruled out and the change is probably due to a heat-induced modification of the material composition. In Figure 7.6, subsequently acquired spectra are shown while of the resonator's modes are tuned.

7.4.2. Waveguides

As a second photonic element, arc waveguides from the hybrid material are built. They have a width of 1.8 µm and a length of 40 µm. The waveguides are fabricated close to the disc resonator in order to enable evanescent coupling to the resonator's

modes (see Figure 7.7 (a)). Their ability to guide light within a broad spectral range is demonstrated by illuminating one end of the waveguide with light from a halogen lamp as seen in Figures 7.7 (b) and (c). The blue and red circular spots correspond to the input and output of the arc waveguide, respectively.

Coupling via the waveguides to the resonator modes is confirmed by shining an excitation laser (wavelength of 532 nm) into one port of the waveguide and, after blocking excitation light by a dichroic mirror, analysing the light coming out of the other port. Obviously, the 532 nm laser excites background fluorescence in the resonator, which is then coupled back into the waveguide. The measured fluorescence spectrum in Figure 7.7 (e) thus shows the characteristic modulation by resonator modes and proves a good coupling between guided modes in the arc waveguide and confined modes in the resonator.

By moving the excitation spot of a second objective over a waveguide (see Figure 7.7 (e)), individual nanodiamonds inside can be addressed and identified as spots with higher fluorescence. The intensity cross-correlation between the waveguide's two outputs shows a clear antibunching behaviour. In this way, the two output ports can be regarded as two arms of a HBT correlator. This result highlights a way of coupling single emitters to thin waveguides, which can possess very high collection efficiencies, as demonstrated recently using tapered optical fibres [113, 114, 173]. Here, direct on-chip integration of such devices is shown with both waveguide ends accessible. Detection at the waveguide's ends can yield high count rates of after spatial and spectral filtering. The autocorrelation function at zero time delay of the fluorescence collected in this way is $g^{(2)}(0) = 0.37 \pm 0.13$ showing the single photon character of the light (see Figure 7.7 (g)). At high excitation powers the number of background corrected counts from the defect centre is measured to be 65000 cts/s after an additional beamsplitter, equivalent to 130000 cts/s without the beamsplitter.

7.4.3. An Integrated 3D Photonic Circuit

Finally, the active quantum functionality of a coupled 3D system consisting of emitter, resonator, and waveguide is verified, i.e., single photon emission to resonator modes as well as subsequent collection and routing via a coupled waveguide is demonstrated. In order to do so, raster scans of the excitation spot over the resonator disc are performed while the photons from one of the waveguide's ends are collected (see Figure 7.8 (a)). When the excitation laser hits the outer rim of the resonator, the created fluorescence light is coupled to the resonator modes and subsequently out to the waveguide, as can bee seen in Figure 7.8 (b). Therefore, the outer rim of the resonator appears bright in the raster scanned image. Bright spots indicate possible positions of NV centres. To identify NV centres via their non-classical light emission, a HBT setup with the laser-written arc waveguide serving

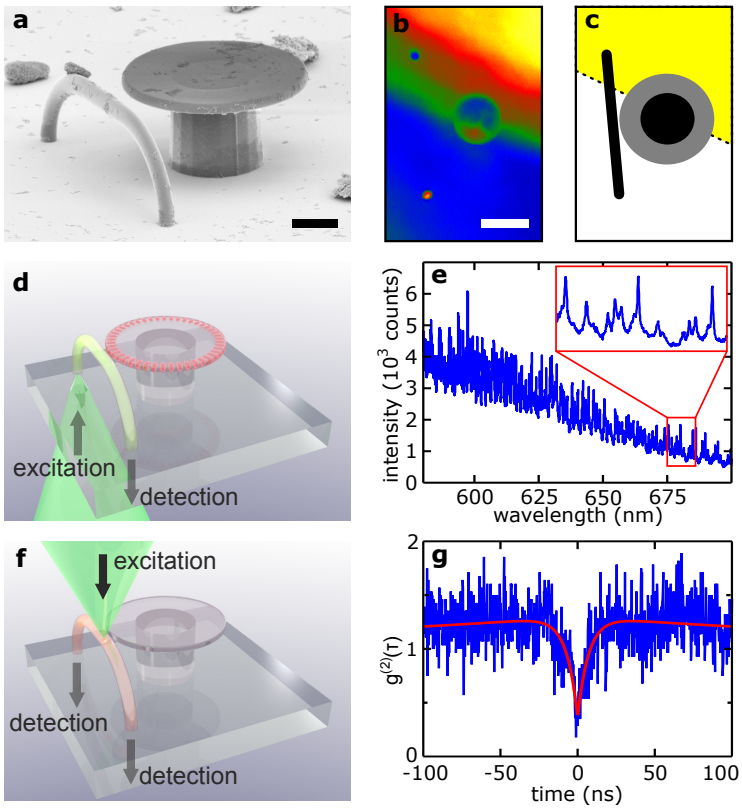

Figure 7.7.: Arc waveguide coupled to resonator. (a) shows a scanning electron micrograph of a 3D arc waveguide-resonator assembly. Length of the scalebar is 5 µm. In (b), the waveguide resonator assembly is seen through the cover slip. The upper half of the image is illuminated from below by white light. Efficient light guiding through the arc waveguide can be seen. Scalebar is 10 µm. (c) is a sketch of the region shown in (b) with the illuminated area marked yellow. (d) is an illustration how the spectrum in (e) was acquired. (e) shows the spectrum of the fluorescence detected at one of the waveguide's ports while exciting through the other. Resonator modes can be clearly identified. (f) is an illustration of the experimental configuration for the autocorrelation measurement in (g). A second microscope objective is used for excitation. (g) shows the measured autocorrelation function of a NV centre inside a waveguide. It is acquired at both output ports of the waveguide in a cross-correlation configuration. (Figure adapted from [177])

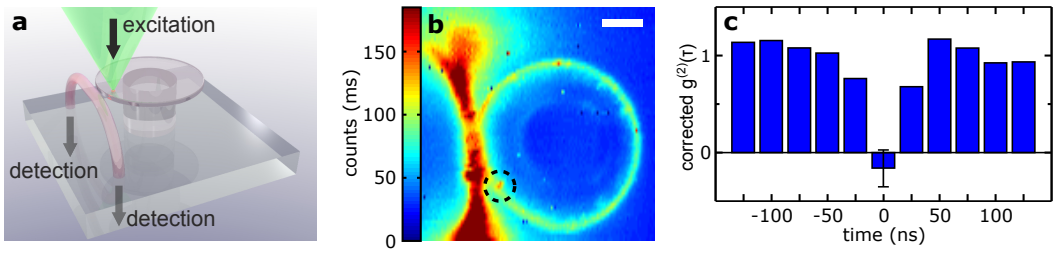

Figure 7.8.: Waveguide coupling of a single NV centre inside a resonator. (a) is a sketch of the experimental configuration. The excitation spot is scanned over the resonator disc. Photons are detected at both waveguide outputs simultaneously. In (b) the photon counts collected at one end of the waveguide while scanning the excitation spot with a second objective are shown. The circle highlights the position of a single NV centre. Shape distortions are due to non closed-loop piezo-scanning. Scalebar is 5 µm. (c) is the cross correlation (background corrected) between the waveguide output ports when the NV centre marked by a circle in (b) is excited. The bin size corresponds to the repetition rate of 40 MHz. (Figure source: [177])

as beamsplitter, is used.

Figure 7.8 (b) shows this correlation measurement for the NV centre encircled in Figure 7.8 (a). The data shown are acquired with a pulsed laser at 40 MHz repetition rate. Background correction is applied to the data (a detailed discussion of the background correction applied is found in Appendix D). The value of $g^{(2)}(0) = -0.18 \pm 0.21$ is far below the threshold $g^{(2)}(0) = 0.5$ for having equal contributions of two centres and proves that the main contribution to the signal stems from a single NV centre. This clearly indicates that the NV centre emits single photons into resonator modes, which are then coupled out and redirected by the arc waveguide. With a single source in a resonator coupled to a waveguide, this device represents a key integrated 3D quantum photonic circuit.

The device was produced in a one-step fabrication scheme that is easy to implement and requires no elaborate clean-room environment. The method furthermore is not limited to NV centres in nanodiamond, but can be extended to any other stable quantum emitter embedded in nanocrystals. The flexibility of DLW enables immediate scaling up to more complex structures (see Figure 7.3 (b)) where single photons are collected, sent through beamsplitters, interferometers, or other optical elements inter-connected by waveguides in a 3D architecture. Tuning of individual components, e.g., the resonator, and operation at cryogenic temperatures is possible as well. With (partial) metallisation of the structures embedding single photon emitters in 3D, plasmonic structures or in metamaterials [262] can be envisioned. The next logical step, as shown in the next section, is to perform DLW of perfectly aligned 3D structures around emitters of known position. Such a process enables

for on-demand fabrication of arbitrary 3D quantum photonic architectures.

7.5. Fabrication of Site-Controlled Parabolic Antennas

After the diamond doped photoresist is established, the ultimate goal would be site-controlled fabrication of structures around diamonds floating in the resist. This requires some improvements on the photoresist, as it should be highly viscous and low-fluorescent, so that the nanodiamonds can be identified without floating away. A first step towards this goal is multi-step site-controlled fabrication, as shown in the following at the example of parabolic antennas for light extraction. Parts of the following have been submitted with the title *Laser-written parabolic micro-antennas for efficient photon collection from single NV centers.*

7.5.1. Site-Controlled Fabrication of Light Collecting Structures

As discussed in Chapter 4, controlled and efficient photon extraction from single emitters is a key requirement for practical single photon sources needed in quantum information technology [1]. Usually, extraction is done via microscope objectives. However, even high numerical aperture microscope objectives only cover a solid angle less than 2π, leading to a limited collection efficiency. The effective numerical aperture can be increased using rather complicated 4Pi microscopy, which requires access with two microscope objectives from two sides and two perfectly aligned focal volumes [263]. Also, many single photon emitters, like the NV centre, require cryogenic temperatures to work properly. This usually results in heavy restrictions on the geometry of collection optics and use of oil immersion is not possible due to restrictions imposed by the cryogenic setups. The challenge in that case is to not only direct as many photons as possible to one side, but also to have them in a very small solid angle (see Chapter 4). Then, they can be easily collected even with low NA optics and, ideally, by optical fibres. To send the photons to a small solid angle, plasmonic nanocavities for resonant enhancement together with gratings for directed emission have been employed on nitrogen vacancy centres in diamond recently [264]. The properties of plasmonic structures are discussed in Chapter 8. When trying to address a single pre-characterised emitter, site-controlled fabrication, where structures are build exactly at the position of the emitter, is needed. Site-controlled fabrication of solid immersion lenses using a focused ion beam was recently introduced to extract photons from nitrogen vacancy centres in bulk diamond [265]. Another example of site-controlled fabrication is shown in Badolato *et al.*, where a single quantum dot out of a random two-dimensional distribution is localised and subsequently a photonic crystal structure is fabricated around it [266].

Here, the approach of on-site fabrication of a three-dimensional optical element around a single quantum emitter on a surface is introduced. More precisely, the site-

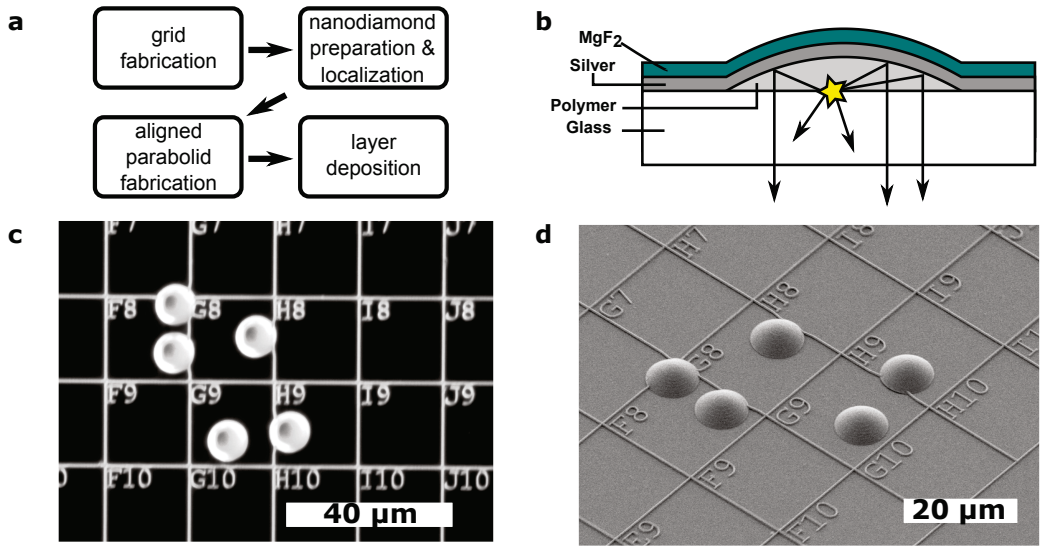

Figure 7.9.: On-site fabricated parabolic microantennas. (a) shows a schematics of the fabrication process. In a first step, a grid is fabricated on a cover-slip using DLW, subsequently, in a second step, nanodiamonds are spin-coated, pre-characterised, and localised. In a third step, the diamonds are covered in photoresist and DLW is used for site-controlled fabrication. After the non-polymerised resist is removed, a metal layer followed by a cover layer for protection is added. In this way, a parabolic mirror aligned to a nanodiamond is fabricated. (b) shows a schematic of the antenna structure. Photons emitted into the upper hemisphere are redirected towards the collection optics in a very small solid angle. (c) is an optical dark-field image of the laser-written paraboloids and the marker grid before evaporation of the reflective silver film. (d) is a scanning electron micrograph of the structures after the fabrication process is completed.

controlled fabrication of parabolic microantennas at the positions of pre-selected nitrogen vacancy centres in nanodiamonds is shown.

7.5.2. Site-controlled Fabrication of Parabolic Microantennas

Due to their high numerical aperture, parabolic mirrors have been used to collect light from single molecules [137, 267] or serve as imaging devices in confocal microscopy [268–270]. When having constraints imposed by the geometry of an experimental setup, parabolic mirrors are particularly interesting, e.g., in cathodoluminescence setups [271], scanning near-field microscopes [272], and ion traps [273]. By using a micro-scale implementation of the concept for light extraction from NV centres, ultra-high saturation count rates from continuous emitting NV centres are

obtained.

A scheme of the fabrication process can be found in Figure 7.9. Nanodiamonds are spin-coated on a cover slip, on which beforehand a marker grid is laser-written using a photoresist described elsewhere (photoresist D in Fischer *et al.* [274]). With the marker grid it is possible to measure the relative position of nanodiamonds containing NV centres in order to be able to re-locate them later. To prove the single emitter nature of the NV centres, autocorrelation measurements are performed. With the nanodiamonds' positions known, a second photoresist (photoresist C in Fischer *et al.* [274]) is drop-casted on the substrate and parabolic mirrors (diameter $d = 10\ \mu\text{m}$) with their focal point at the nanodiamond's location are fabricated in the following way: By exposure of the photoresist a solid three-dimensional paraboloid is created and remaining unexposed material is removed by development in 2-propanol and rinsing with acetone and water. Afterwards, the sample is covered with 100 nm of silver as a reflective layer and 30 nm of magnesium fluoride as protection layer by means of electron beam evaporation. Figure 7.9 (b) shows a sketch of the parabolic mirror made from these layers. Figure 7.9 (c) shows the laser-written paraboloids in a dark-field microscope before evaporation of the silver layer while Figure 7.9 (d) shows the antennas after fabrication is completed. Also, in both images, the marker grid used to pre-localise the nanodiamonds is visible. It is noteworthy that the yield of the fabrication process is very high. From a total of six fabricated mirrors all six are well aligned to the pre-localised NV centres.

7.5.3. Optical Characterisation

When optically characterising the antennas, there are two important quantities to be measured: the total count rate of the saturated emitter and the angular distribution of the emission. While it is desired to have the saturated count rate as high as possible, the emission at the same time has to be as directional as possible.

The total count rate is measured by exciting the NV centre with a focused continuous wave laser beam at a wavelength of 532 nm. Light emitted is collected through the same objective (NA=1.35), split at a beamsplitter, and focused on the active areas of two avalanche photo diodes. In this focusing, care is taken that the size of the image of the parabolic mirror is smaller than the active area. With this setup, the dependence of the count rate on excitation power is measured and fitted to the saturation dependence of a three level system which can be used to describe NV centres [89]. Due to the high count rates achieved, the non-linearity of the APDs and electronics is not negligible and has to be corrected for. This correction is done with a calibration curve acquired by shining an attenuated laser beam on the APDs and comparison of the count rates with the known laser power. No other corrections such as correcting for losses in the optics and the quantum efficiency are performed. Figure 7.10 shows an example of such saturation curves for a single

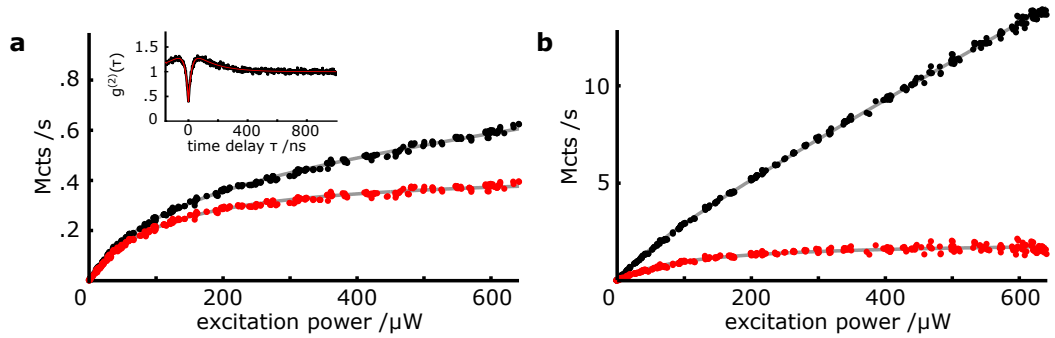

Figure 7.10.: Saturation curves of a single NV centre under a parabolic antenna. (a) shows the saturation curve in confocal configuration. In this configuration, most of the signal reflected from the mirror is blocked by an aperture. The measured signal is shown as black points while for the red points a linear background is subtracted. Grey lines are a fit to a three level model [89]. The saturation intensity I_{sat} is 109 µW (measured before entering the microscope objective). The inset shows the autocorrelation function of the photons collected from a NV centre under a parabolic antenna in confocal configuration. The red line is a fit to the data. In (b), the signal without spatial filtering is shown. Here, the photons reflected by the mirror are not blocked and can reach the detector. An overall NV centre saturation rate of 2.02 Mcts/s is reached.

NV centre lying under a parabolic mirror. In Figure 7.10 (a), a confocal pinhole is used to suppress the light reflected from the parabolic mirror, resulting in a signal consisting almost exclusively of light that is emitted towards the objective lens in the first place. Since in this measurement also any background fluorescence is suppressed by its confocal nature, it is used to determine the saturation intensity I_{sat}. In Figure 7.10 (b), however, the pinhole is removed and photons from the whole area of the mirror are directed to the APDs. Here, the level of background fluorescence is much higher than in Figure 7.10 (a) due to the lack of confocality. This background makes it difficult to deduce the correct saturation excitation intensity and therefore the correct saturation count rate directly from the data in Figure 7.10 (b). Hence, the value for the saturation excitation intensity for the confocal case is used, which, stemming from the same emitter, is equal to the non-confocal case. The highest saturation count rate found in this experiment stemming from a single NV centre is 2.04 Mcts/s and the mean rate for the six produced mirrors is 1.7 Mcts/s. Here, it has to be pointed out that the huge amount of background light accompanying these photons from the NV centre hinders direct use of the parabolic antenna structures as single photon sources. Nevertheless, with improved low-fluorescent photoresists or narrow-band single photon emitters, like the SiV centre in diamond [231], this can be improved.

Figure 7.11 (a,c) show confocal fluorescence images of the parabolic antennas. The images are acquired by sample scanning under excitation with a focused green laser (wavelength 532 nm) and subsequent spectral and spatial filtering. In Figure 7.11 (a), the pre-characterised NV centre, indicated by a dotted white circle, is in the middle of the mirror, which boundaries can be seen as a fluorescent circle. Obviously, the on-site fabrication is working and emitter and micro-mirror are very well aligned. It is noteworthy, that on this sample, out of six site-controlled fabrication attempts, six resulted in aligned structures. The horizontal line in the image is a part of the marker grid which was written using the first photoresist (photoresist D in Fischer *et al.* [274]), which possesses a higher fluorescence than the resist used to fabricate the paraboloids. In this way, the marker grid will also stay visible when fabricated structures overlap with the grid. Since in both resists the polymer is the same, no disturbing refractive index mismatch occurs. In Figure 7.11 (c), as compared to Figure 7.11 (a), the nanodiamonds are randomly distributed. The positions of three single NV centres are marked by white dotted circles.

Besides getting high overall count rates, the other goal of coupling to the microantennas is to direct the photons to very small solid angles – a goal that the parabolic antennas achieve as is shown in the following. Measuring the angular distribution is achieved by back focal plane imaging [275]: The fields in the back focal plane of an objective lens correspond to a 2D Fourier transform of the fields in the focal plane [276] and, consequently, lateral positions in the back focal plane correspond to lateral k-vector components of the emission pattern. Hence, the mi-

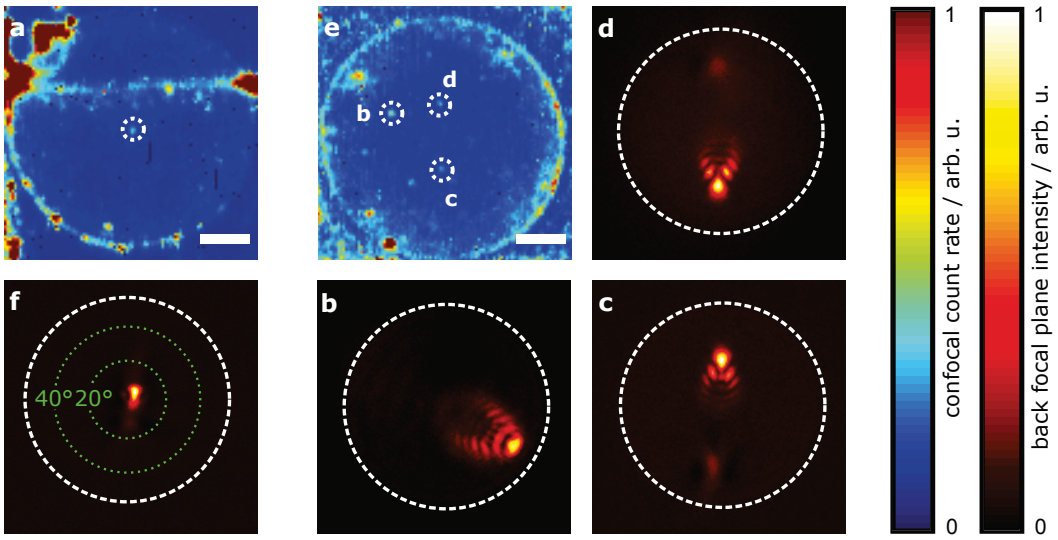

Figure 7.11.: Confocal and back focal plane images of parabolic mirrors. In (a), a confocal scan of a parabolic mirror centred over a nanodiamond containing a single NV centre is shown. (d) is the corresponding back focal plane image. In the back focal plane it is visible that the photons reflected from the mirror are directed into a very small solid angle. (b) shows a confocal scan of a parabolic mirror with multiple single NV centres at off-centre locations. When these NV centres are excited, the photons reflected are not directed exactly on the optical axis of the collection optics, but under an angle. In this way, beam-steering is achieved. (c,e,f) show the back focal plane images corresponding to the diamonds marked with c,e,f in panel (b), respectively. Scalebars in (a,b) are 2 μm. The dashed circles in (c-f) corresponds to the numerical aperture of the collection optics used (NA=1.35) and the green circles indicate in (c) the angle under which the photons are emitted.

croscope objective's back focal plane is imaged on an EMCCD camera in order to obtain the angular distribution of the emission. Examples of such a measurement are found in Figure 7.11 (c-f). In all back focal plane images background correction was performed by subtracting the average intensity acquired at of four positions adjacent to the diamonds position. It is found that the emission reflected by the parabolic mirror is send to a solid angle equivalent to a NA smaller than 0.2 (derived from the extent of the peak in the back focal plane images). It is noteworthy, that in this small angle alone more photons are contained than would be collected using a conventional microscope objective alone: the photons emitted to the entire upper hemisphere are collected by the mirror (NA=1.52) and sent into this narrow beam – a value higher than conventional objectives can reach. In this setup, the beam is furthermore accompanied by the photons collected using our conventional microscope objective (NA=1.35) resulting in the high count rates observed. By evaluating all the light in the back focal plane and assuming isotropic emitters, a directivity of 16 dB is found.

By looking at NV centres not located in the centre of the parabolic mirrors, beam steering as well as the influence of spherical aberrations can be shown (see Figure 7.11 (c,e,f)). Since the mirrors are fabricated using direct laser-writing, which allows for nearly arbitrary shapes, in future experiments also mirrors could be used which cancel these aberrations while maintaining the beam-steering capabilities. In this way, efficient three-dimensional photon routing, e.g., for single photon optical interconnects, can be fabricated.

Using the parabolic antennas, there is a drastic increase in photon collection efficiency and emission directivity of single photon emitters. The site-controlled fabrication process introduced here enables for achieving ultra-high count rates of up to 2 Mcts/s from a single centre – without correcting for losses in the optics and detector efficiencies. The high emission directivity enables for efficient photon collection even when there are heavy constrictions on the collection optics geometry, e.g., in a cryogenic setup.

Chapter Summary: Hybrid Structures Using Nanodiamonds and Photoresist

In this chapter, a hybrid material has been introduced. The hybrid material consists of a photoresist which is mixed with nanodiamonds. In this way, a material was created, from which by selectively polymerisation via two-photon direct laser-writing nearly arbitrarily shaped structures can be fabricated. This was used to fabricate on-chip quantum photonic circuits consisting of single emitters coupled to resonators and waveguides. Also, in a site-controlled fabrication process where the position of the nanodiamonds was known, parabolic microantennas for the efficient

collection of photons from single photon emitters were built. A future improvement of building devices from the hybrid material developed will be the identification and characterisation of emitters inside the material while fabrication the structures. This will enable for deterministic fabrication and coupling of different hybrid structures.

So far, the hybrid quantum devices built were combination of dielectric materials and single photon emitters. In the next chapter, a third ingredient will be added: plasmonic materials like metals.

8. Surface Plasmon Polaritons in Nanostructures

Surface plasmon polaritons (SPPs) are combined excitations of electron density oscillations in a metal and a propagating electromagnetic field. In this chapter, studies of SPPs in nanostructures are presented, which yield some interesting and useful effects, as will be shown in the following. At first, in Section 8.1, surface plasmon polaritons are introduced and their properties and applications are explained. Then, in Section 8.2, it is reported on an experiment where single SPPs are launched on a silver nanowire. Finally, in Section 8.3, a coupling structure coupling photons from a dielectric waveguide to SPPs on a plasmonic waveguide is shown. Parts of this chapter are published in *Optics Express* with the title *Single defect centers in diamond nanocrystals as quantum probes for plasmonic nanostructures* [168], have been reported on in *physica status solidi (b)* with the title *Coupling of single nitrogen-vacancy defect centers in diamond nanocrystals to optical antennas and photonic crystal cavities* [232], and the calculations on the photon-to-plasmon coupler are also shown in *Applied Physics Letters* with the title *Design and numerical optimisation of an easy-to-fabricate photon-to-plasmon coupler for quantum plasmonics* [277].

8.1. Surface Plasmon Polaritons

In this section, surface plasmon polaritons are introduced. This will start with a short reminder on macroscopic electrodynamics and the optical properties of metals (Sections 8.1.1–8.1.3), which is followed by derivation of SPPs at planar interface and in the presence of losses (Sections 8.1.4 and 8.1.5). It is concluded by highlighting their most important properties in Sections 8.1.6–8.1.9.

8.1.1. Macroscopic Electrodynamics

Electrodynamics in a macroscopic medium can be described by the four Maxwell equations, three constitutive relations, and the Lorentz law. The word macroscopic here means that in this equations one does not care about the individual charges, like single electrons in a medium, but performs an average to make the otherwise

unmanageable problem computable [23]. A derivation of the macroscopic Maxwell equations form the microscopic ones can be found in Appendix B.

In the SI unit system, the four macroscopic Maxwell equations are given by:

$$\nabla \cdot \mathbf{D} = \rho, \tag{8.1}$$

$$\nabla \cdot \mathbf{B} = 0, \tag{8.2}$$

$$\nabla \times \mathbf{E} = -\frac{\partial \mathbf{B}}{\partial t}, \tag{8.3}$$

$$\nabla \times \mathbf{H} = \mathbf{J} + \frac{\partial \mathbf{D}}{\partial t}, \tag{8.4}$$

with $\mathbf{E}$ and $\mathbf{B}$ being the averages over the microscopic electric field and magnetic induction, respectively, $\mathbf{D}$ and $\mathbf{H}$ the electric displacement and magnetic field and $\mathbf{J}$ and ρ are the averages of the microscopic currents and charges expressed as densities.

The constitutive relations connecting the fields $\mathbf{E}$, $\mathbf{D}$, $\mathbf{H}$ and $\mathbf{B}$ are:

$$\mathbf{D} = \epsilon_0 \mathbf{E} + \mathbf{P}, \tag{8.5}$$

$$\mathbf{H} = \tfrac{1}{\mu_0}\mathbf{B} - \mathbf{M}, \tag{8.6}$$

where $\mathbf{P}$ and $\mathbf{M}$ describe the macroscopic quantities polarization and magnetisation, which depend on the material involved. The permittivity of vacuum ϵ_0 and the permeability of vacuum μ_0 are also introduced. Further,

$$\mathbf{D} = \mathbf{D}(\mathbf{E}, \mathbf{B}) = \epsilon\epsilon_0 \mathbf{E}, \tag{8.7}$$

$$\mathbf{H} = \mathbf{H}(\mathbf{E}, \mathbf{B}) = \mu\mu_0 \mathbf{B}, \tag{8.8}$$

$$\mathbf{J} = \mathbf{J}(\mathbf{E}, \mathbf{B}) = \sigma \mathbf{E}, \tag{8.9}$$

with ϵ, μ and σ being the dielectric constant, magnetic permeability and the specific conductivity, respectively. Here the brackets are signalling any arbitrarily complex dependence on $\mathbf{E}$ and $\mathbf{B}$ and the second equal sign only holds for the case of a linear dependence [23].

Finally, the Lorentz equation describing the force $\mathbf{F}$ affecting a particle with

charge q moving with velocity $\mathbf{v}$ is [209]

$$\mathbf{F} = q\left(\mathbf{E} + \mathbf{v} \times \mathbf{B}\right). \tag{8.10}$$

With these equations at hand, all the phenomena of classical electrodynamics can be described, including relativistic effects. Only effects arising from the quantum nature of the fields need an alternative theory, giving rise to quantum electrodynamics. However, further specifications, i.e., the explicit form of Equations 8.7, 8.8, and 8.9, are needed when applying the theory to a realistic situation. In these equations, even in the linear case, the proportionality factors are different for different materials and can depend on many variables, e.g., frequency or temperature.

8.1.2. Optical Material Properties

In macroscopic electrodynamics, the material properties are completely defined via equations 8.7, 8.8 and 8.9, but the actual form of these equations has to be determined independently, either with a microscopic theory or via experiments. To simplify things, in the following only the linear version is used. For an overview over the consequences of the nonlinear parts it is referred to the book of Boyd [278]. In this section, also only isotropic media are considered.

In optics, often the refractive index $\tilde{n} = n + i\kappa$ is used instead of ϵ, μ and σ. Here, the tilde is used to distinguish it from its real part n. Note that here other complex quantities are split according to the form $\xi = \xi' + \xi''$. For most materials $\mu \approx 1$, so in the following $\mu = 1$ is set, but it has to be kept in mind that this is not necessarily the case for every optical material, what can lead to interesting physical effects not covered here. The imaginary part of the complex dielectric function ϵ can approximately be connected to the conductivity via [209]:

$$\epsilon'' = \frac{\sigma}{\epsilon_0 \omega}, \tag{8.11}$$

where ω is the frequency of a time harmonic field.

The connection of $\mathbf{n}$ and ϵ is given by [279]:

$$\epsilon' = n^2 - \kappa^2, \tag{8.12}$$

$$\epsilon'' = 2n\kappa, \tag{8.13}$$

$$n = \sqrt{\frac{\sqrt{\epsilon'^2 + \epsilon''^2} + \epsilon'}{2}}, \tag{8.14}$$

$$\kappa = \sqrt{\frac{\sqrt{\epsilon'^2 + \epsilon''^2} - \epsilon'}{2}} = \frac{\epsilon''}{2n}. \tag{8.15}$$

While the imaginary part of the dielectric function ϵ vanishes in this approximation for non-conductors, it plays a major role in the behaviour of metals. In the following, the Drude-model is introduced, which describes this behaviour for most metals used in plasmonics sufficiently good.

8.1.3. Drude-Model

One classical microscopic model to describe the dielectric function of metals is the Drude-model [279], where the conduction band electrons are described as a free electron gas. The electrons' equation of motion then is:

$$m\ddot{\mathbf{x}} + b\dot{\mathbf{x}} = e\mathbf{E}, \tag{8.16}$$

with the electric field $\mathbf{E}$ acting locally on one of the electrons, the damping b, and the mass m, which does not need to be identical with the electron mass m_e. By combining Equations 8.5 and the linear version of Equation 8.7, the dielectric constant ϵ can be expressed in terms of the electric field and polarisation:

$$\epsilon = \frac{\epsilon_0\mathbf{E} + \mathbf{P}}{\epsilon_0\mathbf{E}}. \tag{8.17}$$

The polarisation $\mathbf{P}$ can be connected to positions $\mathbf{x}$ of the electrons by noting that each one of the electrons induces a dipole moment $\mathbf{p} = e\mathbf{x}$ and that polarisation is just dipole moment per unit volume [279]. Solving the electrons' equation of motion, Equation 8.16, and putting everything together yields the dielectric function ϵ of a free electron gas:

$$\epsilon = 1 - \frac{\omega_p^2}{\omega^2 + i\gamma\omega}, \tag{8.18}$$

where the damping is now expressed by $\gamma = b/m$ and the plasmon frequency ω_p is introduced. ω_p is given by:

$$\omega_p = \sqrt{\frac{\rho e^2}{\epsilon_0 m}}, \tag{8.19}$$

with the number of electrons per unit volume ρ.

Drude-Lorentz-Model

The optical properties of some metals, like aluminium, are in good agreement with the Drude-model (Equation 8.18), while for other metal interband transitions limit

the validity of the model. To account for these transitions, it is possible to add oscillator terms like they are used in the Lorentz-model [279] to describe the optical behaviour of the bound electrons in dielectrics. In this so called Drude-Lorentz-model, the dielectric function ϵ is given by [279]:

$$\epsilon = 1 - \frac{\omega_{pe}^2}{\omega^2 + i\gamma_e\omega} + \sum_j \frac{\omega_{pj}^2}{\omega_j^2 - \omega^2 - i\gamma_j\omega}, \tag{8.20}$$

where the index e denotes contributions from the free electrons and the sum runs over all oscillator terms j with their undamped frequency ω_j.

Values for the parameters in Equation 8.20 for the most common materials in plasmonics, gold, and in the visible to near-infrared wavelength range can be found in [280].

Limits of the Model

The Drude-model is based on the assumption of free electrons. Obviously, when the electrons hit the surface of the metal, this is no longer true. A significant contribution of this effect is expected, when the dimensions of the metal get comparable to the mean free path of the electrons. From the shape and size of an object, an effective mean free path L can be calculated (for example $L = \frac{4}{3}R$ for a sphere of radius R) [281]. This leads to a modified damping γ [281]:

$$\gamma_{mod} = \gamma_{bulk} + \frac{v_F}{L}, \tag{8.21}$$

with the Fermi velocity v_F.

While the effect of the reduced mean free path can be described within the framework of the Drude-model by the small adjustment given in Equation 8.21, the description of quantum effects requires more complex theories. In recent experiments, the onset of the regime of quantum theory was shown by observing tunnelling effects when plasmonic structures are brought close together [282, 283].

8.1.4. SPPs at a Planar Interface

In this section, a short derivation of surface plasmon polaritons at a planar interface as solutions of the macroscopic Maxwell's equations (Equations 8.1-8.4) is given. The following is based on the book of Maier [284] (another derivation can be found in this review article: [285]).

By combining the two curl equations, Equations 8.3 and 8.3, with the assumption of time harmonic fields and negligible variations in $\epsilon\mathbf{r} = \epsilon$, the Helmholtz equation

can be derived:

$$\nabla^2\mathbf{E} + k_0^2\epsilon\mathbf{E} = 0, \tag{8.22}$$

with the wave vector of a propagating wave in vacuum $k_0 = \frac{\omega}{c}$.

For a one-dimensional problem – here with an ϵ only depending on z – one can look for propagating modes. The symmetry of the problem leads to $\mathbf{E}(x, y, z) = \mathbf{E}(z)$ and without loss of generality the propagation direction can be chosen to be x. This leads to an ansatz for the electric field:

$$\mathbf{E} = \mathbf{E}(z)e^{i\beta x}, \tag{8.23}$$

with the x-component of the wave vector $\beta = k_x$, also called propagation constant. Putting this ansatz into Equation 8.22 yields:

$$\frac{\partial^2\mathbf{E}(z)}{\partial z^2} + (k_0^2\epsilon - \beta^2)\mathbf{E} = 0. \tag{8.24}$$

For the magnetic field **H**, a similar equation can be derived the same way.

By evaluating the curl Maxwell's equations, Equations 8.3 and 8.3, componentwise, it can be shown that for the conditions chosen above, there exist two sets of solutions, i.e., transverse magnetic (TM) modes and transverse electric (TE) modes [284]. For the TM set of modes, only E_x, E_z, and the transverse magnetic component H_y are non zero while for TE modes the non zero components are H_x, Hz, and the transverse electric component E_y. This reduces the curl equations and the Helmholtz equation 8.24 for TM modes to:

$$E_x = -i\frac{1}{\omega\epsilon_0\epsilon}\frac{\partial H_y}{\partial z}, \tag{8.25}$$

$$E_z = -\frac{\beta}{\omega\epsilon_0\epsilon}H_y, \tag{8.26}$$

$$\frac{\partial^2 H_y}{\partial z^2} + (k_0^2\epsilon - \beta^2)H_y, \tag{8.27}$$

and for TE modes to:

$$H_x = i\frac{1}{\omega\mu_0}\frac{\partial E_y}{\partial z}, \tag{8.28}$$

$$H_z = \frac{\beta}{\omega\mu_0}E_y, \tag{8.29}$$

$$\frac{\partial^2 E_y}{\partial z^2} + (k_0^2\epsilon - \beta^2)E_y. \tag{8.30}$$

Knowing the equations for TE and TM modes, the easiest structure where SPPs can exist, an infinite planar metal dielectric interface, can be examined.

The geometry is defined as the half space with $z < 0$ being metal having a dielectric function ϵ_m with $\epsilon'_m = \mathrm{Re}(\epsilon_m) < 0$ and the half space with $z > 0$ being a dielectric with ϵ_d and $\epsilon'_d = \mathrm{Re}(\epsilon_d) > 0$. Solving the TM equations (Equations 8.25–8.27) yields for $z > 0$:

$$H_y(z) = A_2 e^{i\beta x} e^{-k_{z,2} z}, \tag{8.31}$$

$$E_x(z) = i A_2 \frac{k_{z,2}}{\omega \epsilon_0 \epsilon_d} e^{i\beta x} e^{-k_{z,2} z}, \tag{8.32}$$

$$E_z(z) = -A_2 \frac{\beta}{\omega \epsilon_0 \epsilon_d} e^{i\beta x} e^{-k_{z,2} z}, \tag{8.33}$$

and for $z < 0$:

$$H_y(z) = A_1 e^{i\beta x} e^{k_{z,1} z}, \tag{8.34}$$

$$E_x(z) = i A_1 \frac{k_{z,1}}{\omega \epsilon_0 \epsilon_m} e^{i\beta x} e^{k_{z,1} z}, \tag{8.35}$$

$$E_z(z) = -A_1 \frac{\beta}{\omega \epsilon_0 \epsilon_d} e^{i\beta x} e^{k_{z,1} z}, \tag{8.36}$$

with the $k_{z,1}$ and $k_{z,2}$ denoting the z component of the wave vector in metal and dielectric, respectively. From continuity conditions at the interface [23] it follows directly that

$$A_1 = A_2 \tag{8.37}$$

and

$$\frac{k_2}{k_1} = -\frac{\epsilon_d}{\epsilon_m}. \tag{8.38}$$

Evaluation of Equation 8.27 in both half spaces yields:

$$k_1^2 = \beta^2 - k_0^2 \epsilon_m, \tag{8.39}$$

$$k_2^2 = \beta^2 - k_0^2 \epsilon_d. \tag{8.40}$$

Combining equations 8.38, 8.39, and 8.40 leads to the dispersion relation of a surface plasmon polariton at a planar interface between dielectric and metal:

$$\beta = k_0 \sqrt{\frac{\epsilon_m \epsilon_d}{\epsilon_m + \epsilon_d}}. \tag{8.41}$$

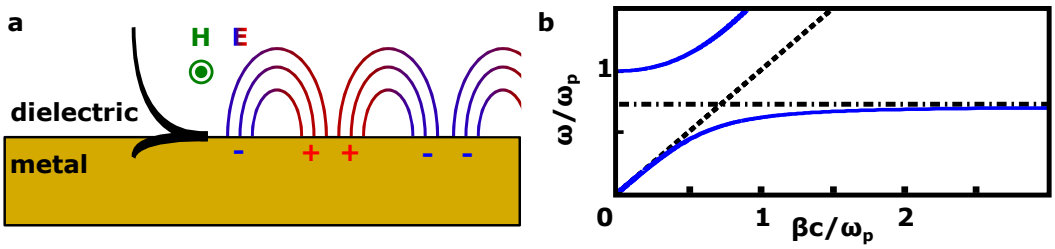

Figure 8.1.: Surface plasmon polaritons at a planar interface. In (a), the electromagnetic fields and charge oscillations of a SPP at a metal dielectric interface are sketched. Black is the amplitude of the evanescent field in z-direction. Its decay is much steeper at the metal side due to a shorter penetration depth. In (b), the lower branch is the dispersion relation of a SPP on an infinitesimal damped Drude metal is shown. For low β it lies close to the light line (dashed) and is photon like while for large β it converges to the surface plasmon frequency $\frac{\omega_p}{\sqrt{2}}$ (dash dotted). The upper branch corresponds to non-bound modes. ((a) inspired by [286])

A sketch of such an SPP is shown in Figure 8.1 (a). For air and a Drude metal with infinitesimal damping $\gamma = \eta$, the dispersion relation can be evaluated further. Putting dielectric function of a Drude metal

$$\epsilon_m = 1 - \frac{\omega_p^2}{\omega(\omega + i\eta)} \tag{8.42}$$

into Equation 8.41 and setting $\epsilon_d = 1$ for a metal in vacuum yields [285]:

$$\beta = k_0 \sqrt{\frac{\omega^2 - \omega_p^2}{2\omega^2 - \omega_p^2}}. \tag{8.43}$$

This relation is plotted in Figure 8.1 (b). It features two branches, whereas the lower energy branch corresponds to a SPP. For small values of β, it lies close to the light line and hence shows photon like behaviour. For large values of β, it converges to the surface plasmon frequency $\frac{\omega_p}{\sqrt{2}}$. The higher energy branch does not describe a mode bound to the metal dielectric interface, as it lies above the light line. Hence, in the following, it will not be considered anymore.

When neglecting the imaginary parts ϵ'', it follows directly from Equations 8.38 and 8.41, that bound modes only exist when

$$\epsilon'_m \cdot \epsilon'_d < 0 \tag{8.44}$$

and

$$\epsilon'_m + \epsilon'_d < 0. \tag{8.45}$$

So far only the TM modes were considered. When trying to solve the TE equations Equations 8.25–8.27, it turns out that there is no non-trivial solution. The above problem is only solvable for TM modes. These TM solutions are the so called surface plasmon polariatons – the main subject of this chapter. Colloquially, they are also referred to as plasmons or surface plasmons.

8.1.5. SPPs in the Presence of Loss

For the SPP dispersion relation in Figure 8.1 (b), damping has been neglected – an assumption that is not justified for most situations with real metals at optical frequencies. Figure 8.2 shows the SPP dispersion relation at a metal-dielectric interface 8.41 for gold and silver as metals and different constant refractive indices for the dielectrics. The experimental data for the dielectric function of gold and silver is taken from Johnson and Christy [287] and the purely real refractive index of the dielectric is chosen to be $\tilde{n} = n = 1,\ 1.5, \text{and } 2.4$. These refractive indices resemble the materials air or vacuum, glasses or polymers, and diamond, respectively. The shape of the dispersion relation differs significantly from the dispersion relation of an infinitesimal damped Drude metal given in Equation 8.43 and Figure 8.1. For silver, which can be well described by the Drude model, this is mainly explained by the introduction of loss, while for gold additional deviations are introduced by interband transitions.

The most important difference is, that in the presence of loss it is not possible to reach the regime of very large wave vectors [288], where the wavelength is very short – a possibility Figure 8.1 implies. As a consequence, it is not possible to concentrate SPPs on a planar interface far beyond the diffraction limit of the corresponding light (see the light line in Figure 8.2). For example, for gold-air and gold-glass interfaces like they are often used in plasmonics, the difference in wavelength is in the best case a factor of 1.1 and 1.3, respectively. For a low loss metal like silver and a high refractive index material like diamond this factor is 4.4 maximally. The higher the dielectric material's refractive index, the more the lossless dispersion is approached.

Because real metals are not perfectly conducting, SPPs get damped by Ohmic losses as they propagate. Especially in the optical frequency range this damping can be huge. The 1/e decay length L for the intensity is given by [185]:

$$L = \frac{1}{2\,\mathrm{Im}[\beta]}, \tag{8.46}$$

where $\mathrm{Im}[x]$ denotes the imaginary part of x. At a wavelength of 700 nm and an index of refraction $n = 1$ for the dielectric this corresponds to 140 µm on silver and

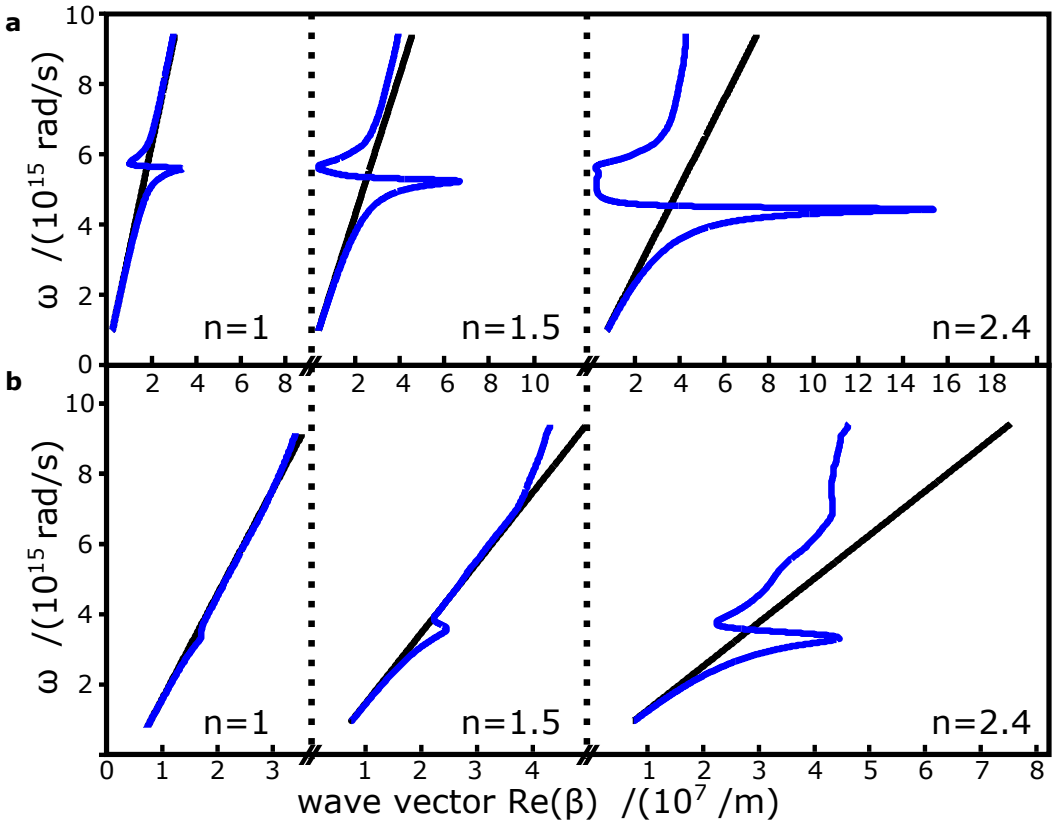

Figure 8.2.: SPP dispersion relation in presence of loss. (a) and (b) show the dispersion relation SPPs at a metal-dielectric interface for silver and for gold, respectively. Different purely real indices of refraction n were used for the dielectrics: $n = 1$ for vacuum, $n = 1.5$ for glass or similar materials, and $n = 2.4$ for diamond. The blue curves are the dispersion relations while the corresponding light lines are given in black. Data for the dielectric functions is taken from Johnson and Christy [287].

26 µm on gold. For a refractive index of $n = 2.4$ the values for silver and gold are 7 µm and 1.1 µm, respectively. When working at telecommunication wavelengths, i.e., around 1500 nm, the propagation lengths are considerably longer. For $n = 1$ they are 1100 µm on silver and 270 µm on gold (the dielectric functions for these calculations were again taken from Johnson and Christy [287]).

Regardless of the short distances an SSP can travel at optical wavelengths, there has been put a lot of effort into controlling and waveguiding SPPs because of their unique ability of concentrating energy and efficiently couple to emitters (see Section 8.1.7) [286, 289, 290].

8.1.6. Excitation of SPPs

To excite SPPs, an obvious approach is to excite them with photons. However, as SPPs are bound modes (see their construction in Section 8.1.4), they do not couple directly to photons. The dispersion relation in Figure 8.1 shows that the SPP branch lies always below the light line. Therefore, it is impossible to satisfy the need for energy and momentum conservation at the same time – at least for the geometry of a single, planar, and infinite interface considered so far.

By altering the geometry, it can be achieved to couple photons to SPPs. One approach, so called prism coupling, incorporates a second dielectric layer with an index of refraction n_2 higher than the index of the first material. Photons undergoing total internal reflection at the second layer's interface will have an in-plane momentum of $k_x = \frac{\omega}{c} n_2 \sin(\theta)$ [284], which can be higher than the wave vector β of the plasmon at the metal-first dielectric interface. In the so called Kretschmann configuration, the metal layer lies between the dielectrics [291], while in the Otto configuration [292] the lower refractive index dielectric is in the middle. In these configurations, the SPPs are excited by photons leaking evanescently through one of the layers, either through the metal layer in Kretschmann configuration or through the lower refractive index dielectric layer in Otto configuration. Since this process is reciprocal, both configuration give rise to additional damping of the SPPs through leakage radiation. Both coupling geometries are depicted in Figure 8.3 (a) and (b), respectively.

Another way for the excitation of SPPs through photons is not to add an additional layer to the geometry, but to structure the layers. In fact, the first report of the observation SPPs dates back to the year 1902, when R. W. Wood wondered about the uneven light distribution in the spectrum of a metal grating [293]. At that time no satisfying interpretation of Wood's results was found and the features observed were called Wood's anomalies [294]. What happens when SPPs get excited through a grating is that the missing momentum is provided by the grating

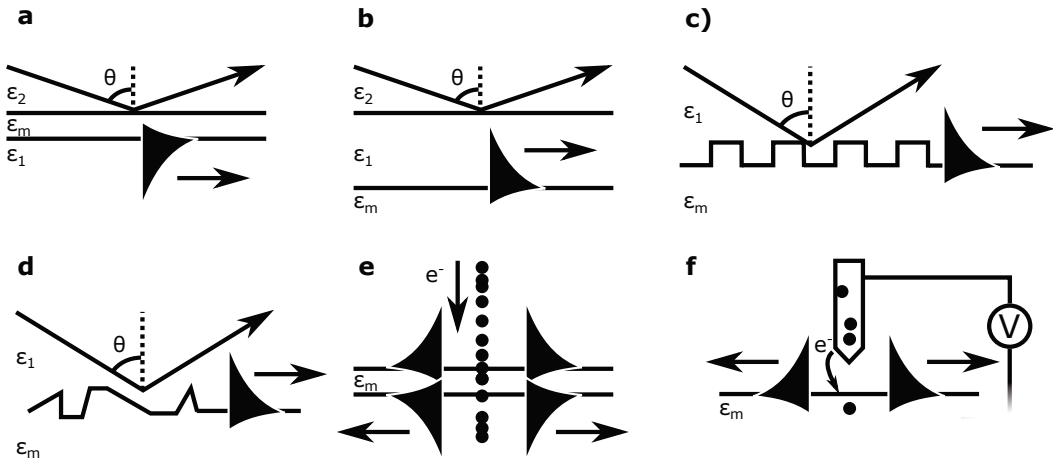

Figure 8.3.: Different schemes for the excitation of SPPs. (a) and (b) show the Kretschmann and Otto configurations, respectively. By introducing a third layer with a higher refractive, index phase matching is achieved for SPPs at the lower index material to metal boundary. In (c) and (d), the symmetry in propagation direction is broken in order to achieve phase matching. A grating is introduced in (c) while in (d) surface roughness is present. In (e) and (f), SPPs are excited by electrons. An electron beam is passing a metal layer in (e) and a scanning tunnelling microscope is used in (f). Not shown is the direct excitation with an emitter like it is used in Section 8.2.

according to the formula [284]:

$$\beta = \frac{\omega}{c} n \sin(\theta) \pm \nu g, \tag{8.47}$$

with the reciprocal grating vector $g = \frac{2\pi}{a}$ of a grating with period a and $\nu \in [1, 2, 3, ...]$. Grating coupling of SPPs is shown in Figure 8.3 (c). Noticing that this coupling only relies on the broken symmetry of the problem to match the momenta, it becomes clear that SPPs can also excited at rough surfaces or the end of one layer as depicted in Figure 8.3 (d).

The effect of discontinuities is also used by apertureless scanning near-field optical microscopes [295] to excite or scatter out SPPs. In contrast, in aperture scanning near-field optical microscopy [296], an effect similar to prism coupling is used. By funnelling light through a subwavelength hole, its momentum distribution is broadened so that phase matching becomes possible.

SPPs can not only be excited by photons, it is also possible to excite them directly with an electromagnetic emitter, like the ones introduced in Section 2.5. For this process to happen, the emitter has to be in the near-field of the SPP (see Section 8.2). Then, in addition to its optical decay channels, plasmonic ones open up, which can become dominating, depending on the actual geometry. This process can be imaged using quantum emitter fluorescence lifetime imaging microscopy, as it is introduced in Section 9.

A completely different way of exciting SPPs is by using electrons [284]. In electron energy loss spectroscopy (EELS) in this way the SPPs energies can be measured [297]. A monochromatic electron beam is transmitted trough the plasmonic structure and its energy loss is measured by an electron spectrometer. By scanning the electron beam over the sample, it is possible to access even spatially varying SPPs states. It is furthermore possible to inject electrons into the material by means of an electron tunnelling microscope and excite SPPs this way [298]. Figure 8.3 (e,f) show two possibilities of exciting SPPs with electrons.

8.1.7. SPP Waveguiding

So far, only SPPs propagating along plane metal interfaces were considered. To be able to work with SPPs in a controlled way on the nanoscale, to integrate plasmonic elements into nano optical devices, and especially for efficient coupling to emitters, it is crucial to be able to route the SPPs via waveguides and to concentrate their energy in a small volume. Waveguiding of SPPs is, similar to conventional fibres or integrated optics, usually achieved by structuring the waveguide along the propagation direction. A variety of different SPP waveguides has been developed, featuring different properties suitable for different situations. An extensive review of this topic can be found in Reference [289]. Here, on this basis, the topic is

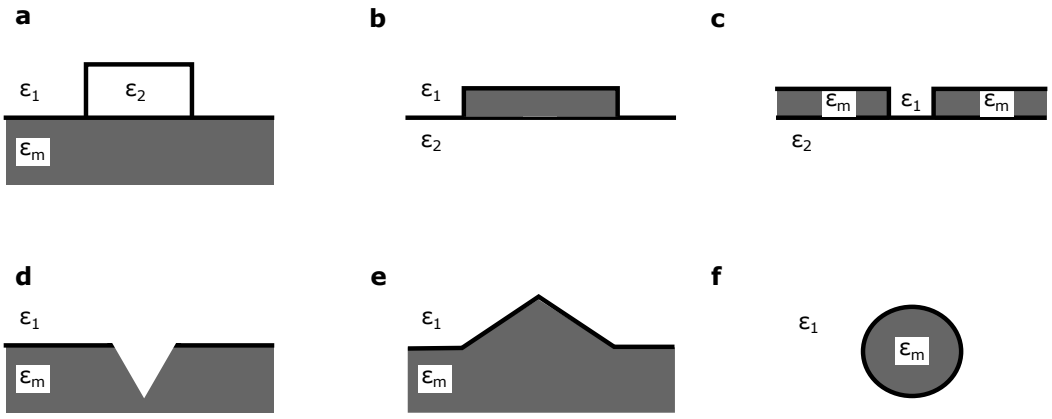

Figure 8.4.: Selection of SPP waveguide geometries. (a) shows a dielectric loaded waveguide, where the dielectric above a metal surface is structured. (b) is a stripe waveguide, where a thin metal stripe is used to guide the SPPs. In (c) a gap waveguide is shown, where the SPPs are confined to the gap between to metal surfaces. (d) and (e) show a groove and a ridge waveguide, respectively. (f) is a nanowire waveguide. In contrast to the other waveguides shown here, it can be grown chemically.

presented in compressed form.

The straightforward way of building an SPP waveguide is to structure the dielectric environment in close resemblance of conventional integrated optics. The so called dielectric loaded SPP waveguides are made by stripes of a dielectric with an index of refraction different from its surrounding [299, 300]. This leads to a confinement since the wave vector β (see Equation 8.41) is different for the different regions. Not structuring of the dielectric environment, but the metal is used in so called stripe SPP waveguides. These waveguides are a metal stripe on a dielectric substrate. Since there is only metal where the stripes are, the SPPs can only propagate along the stripe. Usually these stripes support modes at the boundary to the substrate and at the boundary to the superstrate. When the thickness of the metal layer is small enough, these modes couple and can form supermodes. Usually, one of the supermodes is advantageous for propagation and posses a smaller damping than the others (so called long range SPPs [301]). Another approach for SPP waveguides are gap SPP waveguides [302]. Here, variants of a metal-insulator-metal geometry are used to guide the modes. These waveguides offer the opportunity to concentrate the field in the insulator part [303]. Two more types of waveguides are the wedge waveguide [304], which guides the mode along a metal ridge, and the groove waveguide [305], where the SPPs are guided along grooves in the metal.

Besides structures which are created in a top-down fabrication process in a clean-

room environment, there exist other structures, which are chemically synthesised. These structures have the advantage of their mono-crystallinity and therefore a greatly reduced damping [306]. One type of such structures, which plays an important role in Section 8.2 and Chapter 9, are metal nanowires. Their metallic part has a circular symmetry and if the surrounding dielectrics have the same symmetry, analytical solutions for their modes exist [307]. With nanowires, a high confinement of the modes can be reached, as the fundamental mode has no cutoff and decays exponentially away from the wire [289]. An overview of the different waveguide types introduced here can be found in Figure 8.4.

To couple light into SPP waveguides, mostly the techniques shown in Figure 8.3 (a-d) are used. One popular technique is end fire coupling, which works the same way as it is known from optical waveguides: at the end of the plasmonic waveguide a mode matched light source (mostly a fibre or another waveguide) is positioned to excite the guided modes. This can be seen as a subgroup of the coupling at discontinuities and is, depending on the mode's overlap, very efficient (e.g., in Reference [308] a coupling efficiency of 36 % is reached). Also it is possible to first couple in light to an integrated optical waveguide and subsequently convert it to SPPs. In Section 8.3, a way of such integrated in plane excitation of strip waveguide modes is introduced.

8.1.8. SPP Nanofocussing

One of the remarkable properties of SPP waveguides, which lead to a fast development of the field in recent years, is their ability to not only guide SPPs in a very confined way, but also to focus energy at nanoscale volumes [309]. This ability is due to the fact that on shrinking the lateral dimensions of the waveguides, for some SSP modes, the confinement gets tighter. This is in sharp contrast to what happens with dielectric waveguides, where the confinement gets only tighter until it reaches the order of the light's wavelength, where the mode starts to expand in the surrounding medium – an effect often used when coupling tapered fibres to microresonators (see Section 7.4.1) [158], but not suitable for nanofocussing. In Figure 8.5, this fundamental difference between a dielectric and a plamonic waveguide is sketched. Note that not all SPP waveguides introduced in Section 8.1.7 are capable of confining the SPPs to nanoscale volumes. In similarity to the dielectric waveguides, also dielectric loaded SPP waveguides and also the long range SPPs on strip waveguides lose their confinement when their dimensions get to small [289, 309].

Knowing that for a smaller waveguide the SPPs get more confined, nanofocussing of propagating SPPs can now be achieved by tapering down the lateral dimensions of an SSP waveguide [310–312]. As an additional effect, upon tapering down the waveguide, group and phase velocity of the SPPs can get reduced, what can lead to giant field strengths due to an adiabatic transformation of the SPPs to localised

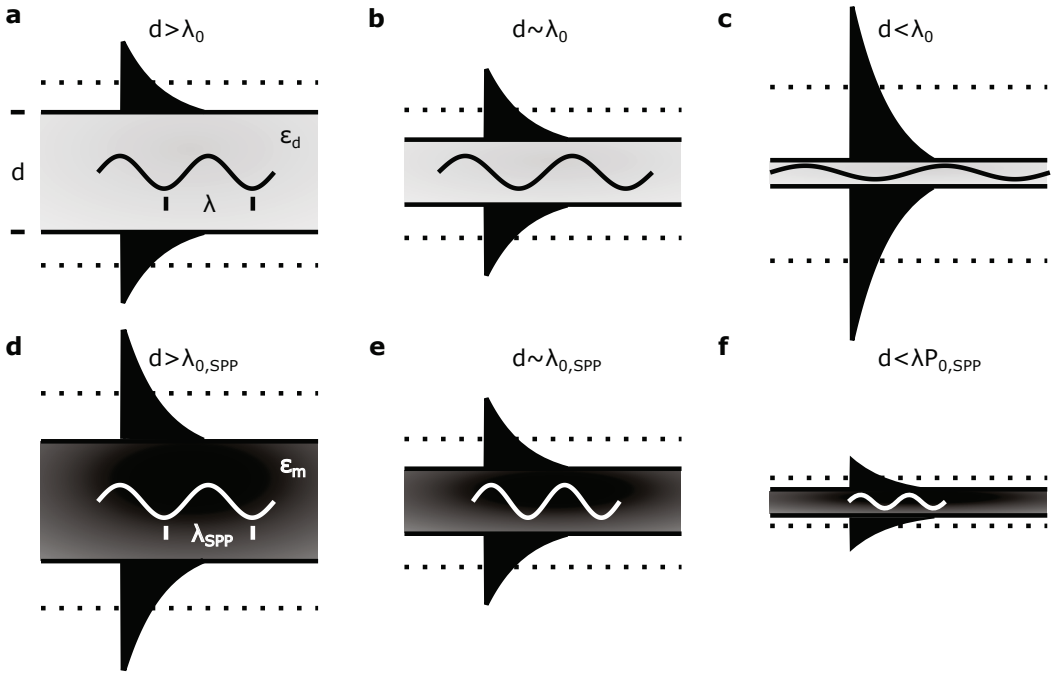

Figure 8.5.: Evolution of field distributions for decreasing waveguide diameters. In (a-c), the reduction of the diameter d of a dielectric waveguide is shown. As the diameter reduces below the order of the vacuum wavelength λ_0, the lateral size of the mode (indicated by the dotted lines) increases. Also the wavelength of the guided wave approaches the vacuum wavelength λ_0. In contrast, for an SPP waveguide, as shown in (d-f), the wavelength decreases and the mode gets more confined. (Image inspired by [309])

surface plasmons [313].

8.1.9. Applications of SPPs

In recent years, there has been a great interest in SPPs in many different fields of physics and technology. Their ability to be guided on volumes far below the optical diffraction limit makes them possible candidates for highly integrated optical information processing and communication [309, 314]. This is especially true in the near-infrared, where their losses (see Section 8.1.5) become more tolerable than at visible frequencies, but are still a major hurdle. To date, practical devices are still missing.

The ability of SPPs to focus and confine energy at the nanoscale, in contrast, has found a lot more of applications. Highly concentrated SPPs at the end of metal tips can be used in near field microscopy to have very localised excitation [315]. Emitters can be interfaced very efficiently via SPPs, what, possibly in combination with a photonic to SPP converter (see Section 8.3) can be used in devices like a proposed single photon transistor [290]. Another, and maybe the most important, application of SPPs lies in sensing. Information on an analyte is obtained by measuring the coupling condition of a light beam to SPPs (see Section 8.1.6). A change in refractive index of the analyte will shift this condition and from the corresponding shift information on the sample is obtained [316, 317].

Here, only some applications of propagating SPPs, which are the ones most important in this thesis, are reviewed, but it has to be noted that there are many other applications of plasmonics. Reviews on plasmonics can be found, for example, in References [284, 318, 319].

8.2. Generation of Single SPPs on a Nanowire

In this section, as a very fundamental experiment for quantum plasmonics, controlled generation, waveguiding, and splitting of single SPPs is shown. Even though SPPs involve collective oscillations of many electrons, it is possible to have single SPPs with properties similar to the properties described for photons in Chapter 2. A basic demonstration of this is shown in the following, where single SPPs are excited on a silver nanowire. Parts of this have also been published in *Optics Express* with the title *Single defect centers in diamond nanocrystals as quantum probes for plasmonic nanostructures* [168].

The nitrogen vacancy centre in diamond (NV centre, see Chapter 3) can create a well defined optical excitation which can then be launched into a nearby system under investigation [320]. The generation of a single photon from a NV centre can thus be regarded as an ultimate quantum limit of a pump pulse in a pump-probe experiment.

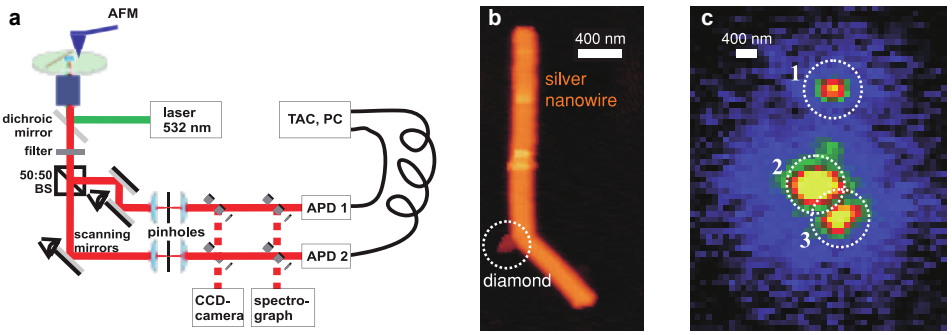

Figure 8.6.: Coupling of a diamond nanocrystal with a single NV centre to a silver nanowire and excitation of single surface plasmon polaritons. (a) is a scheme of the experimental setup used. (b) shows an AFM image of the diamond nanocrystal (indicated by the dashed circle) positioned at the side of a bent silver nanowire. (c) shows a microscope photoluminescence image of the same configuration. Positions 1 and 3 indicate the ends of the nanowire, while position 2 marks the location of the diamond nanocrystal. (Figure adapted from [168])

Excitation of SPPs by a single NV centre and guiding along a metal nanowire was demonstrated using structures which were randomly assembled by deposition of metal nanowires and quantum emitters on a sample surface [321–324]. In these experiments, on-demand positioning and change of a once assembled configuration was not possible.

Here, a setup consisting of a confocal microscope combined with an atomic force microscope (AFM, see Figure 8.6 (a) and also Section 5.2) is used for a more controlled experiment. This combination allows both, optical detection of photons and nanomanipulation of the nanodiamond [170, 206]. Photon correlation measurements are performed with a Hanbury Brown and Twiss configuration of two avalanche photo diodes with a quantum efficiency at 700 nm of approximately 30 %. A diamond nanocrystal containing a single NV defect centre is first optically characterised on a cover slip and then individually picked up by the AFM tip (see Section 5.3 for details of this process). Then, the nanocrystal is transferred to a cover slip with chemically synthesised silver nanowires and placed on-demand near a previously selected wire which serves as SPP waveguide. With this technique, one can be sure that there is exactly one diamond containing exactly one single NV defect centre on the whole sample. Hence, there is no possibility of accidentally measuring photons coming from multiple diamond crystals or a diamond containing more than one defect centre. Subsequent nanomanipulation with the AFM tip allows for fine-positioning of the nanocrystal and launching of a single excitation at arbitrary positions along the wire.

Figure 8.6 (b) shows an AFM image of the nanowire used in this experiment. Its diameter is approximately 80 nm. A sharp bend separates the nanowire into two arms of 1.9 µm and 0.7 µm length. Under continuous wave laser excitation of the NV centre (at a wavelength of 532 nm), photoluminescence directly from the NV centre (position 2 in Figure 8.6 (c)) as well as light emerging from the bend and from the ends of the nanowire (positions 1 and 3 in Figure 8.6 (c)) is visible. Since there is a strong fluorescence background emerging from the bend of the nanowire while exciting the diamond, for further measurements the diamond was placed at another position, so that the nanowire bend is no longer in the excitation spot (position 2 in Figure 8.7 (c)). Already this repositioning of the nanocrystal shows the advantage of nanomanipulation. Accidental inconvenient configurations can be corrected and experiments can be repeated under otherwise unchanged conditions. At the same time, the ability to reposition is crucial in more complex structures, since slight changes of the position of an emitter with respect to a plasmonic structure may already modify its emission as well as the structure's plasmonic properties significantly. Despite the possibility to perform near-field simulations, under experimental conditions an a-priori prediction of an optimum position for an emitter or nanoprobe is often impossible [325].

With the new position of the diamond nanocrystal, there is now an additional fluorescent spot observable on the nanowire. One (position 2 in Figure 8.7 (b)) corresponds to the emission of fluorescence directly from the nanodiamond. An autocorrelation measurement on this spot shows a pronounced antibunching behaviour (Figure 8.7 (c)) confirming the single photon character of emission from a single NV centre in the nanodiamond. The other spots correspond to three output ports for single excitations launched into the wire via the nanodiamond.

In order to prove the quantum nature of the excitations, cross-correlation measurements between the light directly emitted from the nanodiamond (position 2 in Fig. 8.7 (b)) and the light emitted from both ends of the nanowire (positions 1 and 3 in Figure 8.7 (b)) are performed. Again, a clear antibunching is observed, proving that indeed light from the single NV centre is converted into single SPPs which propagate to the output ports. The nanowire thus represents a plasmonic beamsplitter with three output ports, a key building block for quantum plasmonic elements.

Recently, this technique of launching single SPPs with a NV centre has been used in a number of further experiments, including pulsed excitation [172] and extensive nanomanipulation of the waveguiding silver wire [211]. In this thesis, in Section 9.3.2, the plasmonic properties of silver nanowires are further investigated.

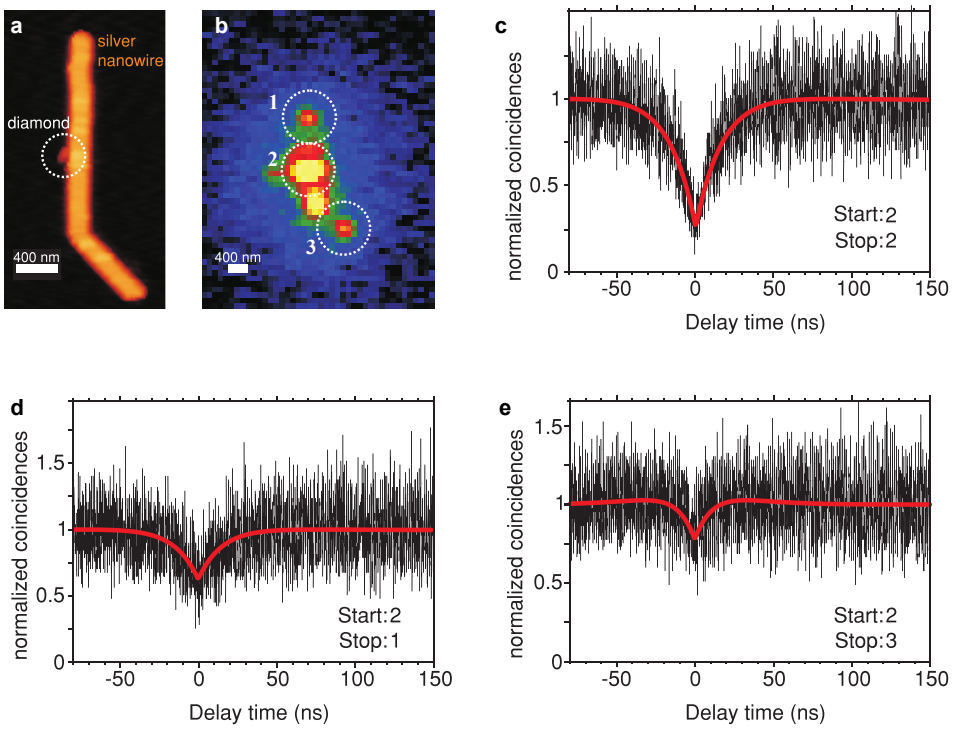

Figure 8.7.: Nanodiamond with single NV centre launching single plasmonic excitations. (a,b) are AFM and fluorescence image showing a silver nanowire and a nanodiamond with a single NV centre. The bright spot between position 2 and 3 in (b) emerges from the bend of the nanowire. (c) shows the autocorrelation of the photons from the diamond measured at point 2. (d,e) are cross-correlations between the photons emitted from position 2 and from positions 1 and 3, respectively. The antibunching dip in the curves clearly reveals the non-classical properties. (Figure adapted from [168])

8.3. A Dielectric Waveguide to SSP Coupler

In this section, the design of a coupling structure for converting single photons in a dielectric waveguide to guided single SPPs and vice versa is shown. In order for this structure to be maximally efficient, numerical calculations are carried out.

8.3.1. Design Parameters and Operation Principle

When trying to build advanced quantum optical elements using SPPs [325], SPPs need to be interfaced with lossless channels, since a main obstacle for routing of SPPs is their loss (see Section 8.1.5). The obvious choice for this channels are photonic waveguides, so SPPs have to be converted to photons and vice versa. This conversion has to be highly efficient when working at the level of single quanta. At this level, no classical amplification is possible, so loss will dramatically reduce the fidelity of any experiment. Also, scalability of the experiment (and future applications) favors an integrated approach which can be produced using standard clean-room processes. As introduced in Section 8.1.6, excitation of SPPs with photons requires phase matching of photons and SPPs. To achieve this efficiently, a special coupler has to be designed.

In the following, a dielectric waveguide to SPP coupler, which satisfies the resulting experimental requirements, is introduced. The coupler should:

- interface a mono-mode dielectric waveguide with a single plasmonic mode,
- work in a wavelength range, where single photon emitters like molecules, defect centres, or quantum dots emit, since interfacing emitters is crucial in quantum plasmonics [325],
- be accessible with single emitters,
- be easy and reliable to fabricate in standard processes.

With these demands in mind, the material system and geometrical boundaries of the coupler are chosen.

For the incoming dielectric waveguide, a rectangular silicon nitride waveguide lying on silica is used, as both materials are transparent in the red spectral range, where the planned wavelength of operation ($\lambda = 780$ nm) is situated. As material for the plasmonic part, gold is chosen, which is done not for efficiency (silver would have had a lower loss; see Section 8.1.5), but for stability, since silver nanostructures may degrade under ambient environment [326]. The SPP waveguide part of the coupler is a strip waveguide. Such a waveguide allows for easy coupling of emitters to the SPP modes and also for nanofocussing by tapering down the waveguide (see Section 8.1.8). To facilitate nanopositioning of emitters near the structures, the

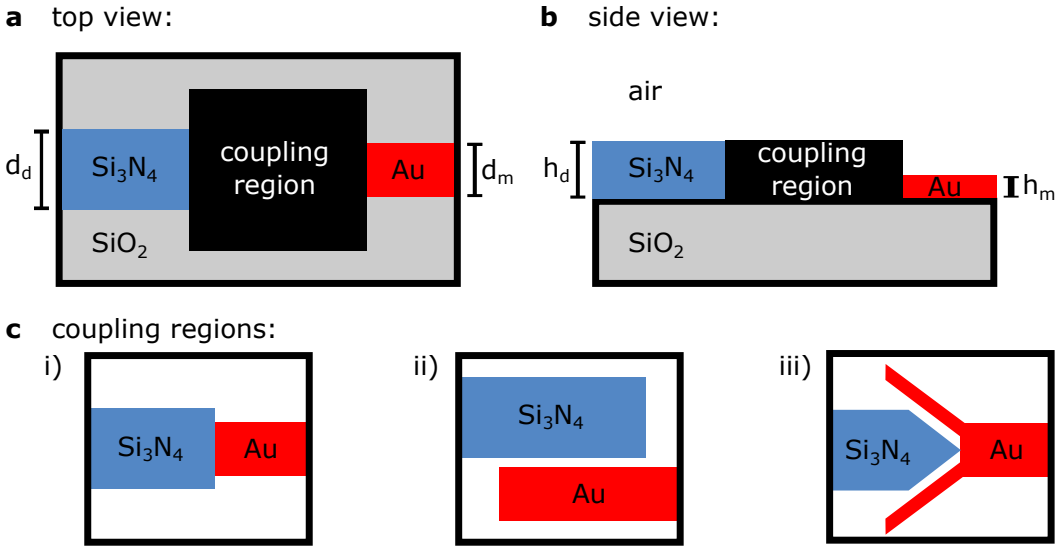

Figure 8.8.: Constraints and possibilities for SPP coupler design. (a) and (b) show top and side view of the geometry considered, respectively. The waveguides are defined by their widths $d_{d/m}$ and their heights $h_{d/m}$. The coupler itself is shown as black box, which is a placeholder for different possible designs. In (c) i-iii), some of the possible designs are shown. Butt coupling in i), directional coupling in ii), and a design similar to the one used in the remainder of this section in iii).

structures must not be capped, so the upper layer of material is air. To avoid additional fabrication steps, the metal layer is designed to directly lie on the silica. This leads to a vertical offset of the centres of the modes in dielectric and SPP waveguide. The basic design parameters are visualised in Figure 8.8.

For a fast and efficient design process, it is important to have some tools to understand what happens for different geometries. It can not be overestimated how just "getting a feeling" can speed up development. For this reason, many coupling structures (some are shown in Figure 8.8) are simulated with a finite difference time domain code (FDTD Solutions, Lumerical; for FDTD see Appendix C) and the spatial and temporal distributions of them are monitored. The insights obtained were then used to develop new ideas and designs. Note that to save time, these simulation were carried out an a relative coarse three-dimensional mesh ($\approx \frac{\lambda}{18}$) and convergence of the simulations is not checked. After a design which works reasonably well is found, it is parameterised and an optimisation is carried out using a finite element method (FEM) [327] code for further simulations (JCMSuite, JCMWave). The parameterised design found in this way is shown in Figure 8.8 (c iii).

When the dielectric and SPP waveguide's geometries are given as boundary con-

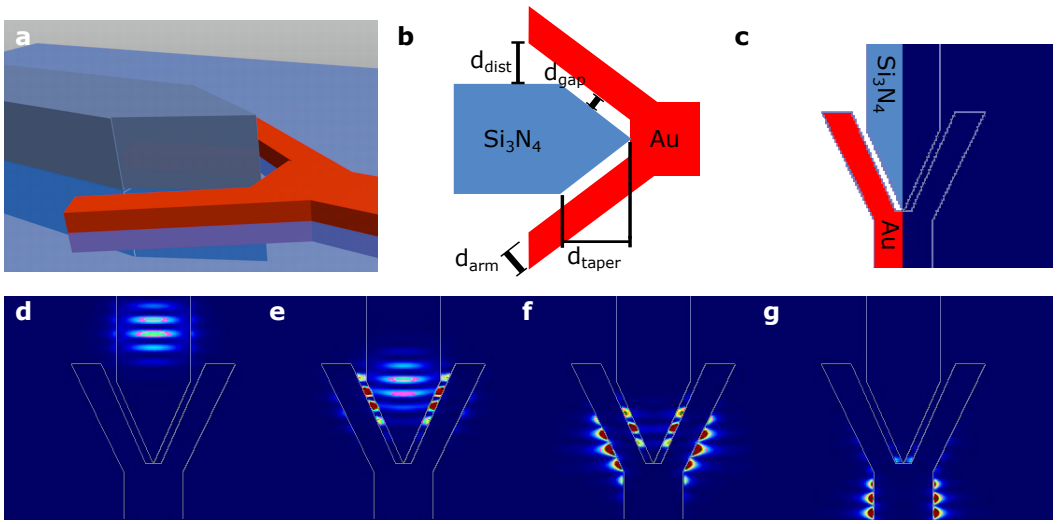

Figure 8.9.: Design and operation principle of the SPP coupler. (a) and (b) show the layout of the coupler, which is fully described by the properties of incoming and outgoing waveguide and the four parameters (d_{dist}, d_{gap}, d_{arm}, d_{taper}). (c) clarifies the geometry used in (d-g), where the operation principle of the coupler is shown via electric field distributions in a FDTD simulation. In (d), a pulse propagates downwards along the dielectric waveguide. In (e), high field strengths start to build up in the gap, which subsequently couple to the outside of the metal arm as shown in (f). In (g), the excited SPP mode is shown. ((a) courtesy of G. Kewes)

ditions, the coupler design finally used for optimisation has four free design parameters, as shown in Figure 8.9 (b). Before showing the FEM simulations performed in order to get quantitative results for the coupling efficiency, the working principle of the coupler is introduced. Figure 8.9 (d-g) show the operation mechanism of the coupler. The images are taken from the FDTD simulations used to find a good coupler design. As source, a pulse is sent in the dielectric waveguide's mode and the electric field strengths are shown for different time steps. At first, the pulse is guided towards the coupling region by the dielectric waveguide (Figure 8.9 (d)). Inside the coupling region, the field is concentrated in the gap between the dielectric taper region and the coupler's metal arm (Figure 8.9 (e)), which acts as an SPP waveguide. On the outside of the coupler's metal arm, also an SPP mode exists. Mode beating between the mode on the inside and the one on the outside of the arm leads to an energy transfer from mode to mode. When the tapered region has the right length, it can be achieved that almost all of the energy is on the outside of the arm at the end of the taper (Figure 8.9 (f)). In this case, the SPP starts propagating on the outside of the SPP waveguide, as shown in Figure 8.9 (f). From

this working principle, it can also be concluded that it is possible to excite SPPs in a gap waveguide with this coupling scheme just by elongating the taper until the mode beating has its maximum on the inside of the coupler's arms.

8.3.2. Simulation and Optimisation of the Coupling Efficiency

For coupling of devices, the figure of merit is the maximum coupling efficiency η that can be reached. Here, optimisation of the coupling efficiency for the coupler designed in Section 8.3.1, which especially suites the needs of experiments with single SPPs and single emitters, is desired. The operation wavelength is $\lambda = 780$ nm, a wavelength where single photon emitters exist, but which also is sufficiently long to reduce losses in the metal (see Section 8.1.5).

In the following, FEM simulations using the commercial JCMSuite (JCMwave) code are carried out. The geometry simulated is the coupler shown in Figure 8.9 (b) with the parameters:

- distance of dielectric waveguide to the metal arms d_{dist},
- gap between taper and arms d_{gap},
- width of the metal arms d_{arm},
- length of the tapered region d_{taper},
- height of the dielectric material h_{diel},
- height of the metal h_{metal},
- width of the dielectric waveguide w_{diel},
- width of the metal waveguide w_{metal}.

Of these parameters, the geometry of the incoming dielectric waveguide, i.e., its height h_{diel} and its width w_{diel}, are chosen to be $h_{diel} = 200$ nm and $w_{diel} = 510$ nm. Furthermore, the geometry of the metal waveguide is set to have a height $h_{metal} = 50$ nm and a width of $w_{metal} = 510$ nm. Note that these choices are arbitrary, only constrained by fabrication capabilities and the requirement for single mode operation. No mode matching between incoming dielectric and outgoing metal waveguide has to be taken into account, since the working principle of the coupler does not rely on that. In fact, simulations with a propagation mode solver lead to the effective refractive indices $n_{eff,TE} = 1.597$ for the transverse electric mode of the dielectric waveguide and $n_{eff,TM} = 1.537$ for the transverse magnetic mode of the dielectric waveguide, compared to $n_{eff,m1} = 1.604 + i0.0186$ and $n_{eff,m2} = 1.681 + i0.0156$ for the two modes of the SPP waveguide [277]. For this simulations

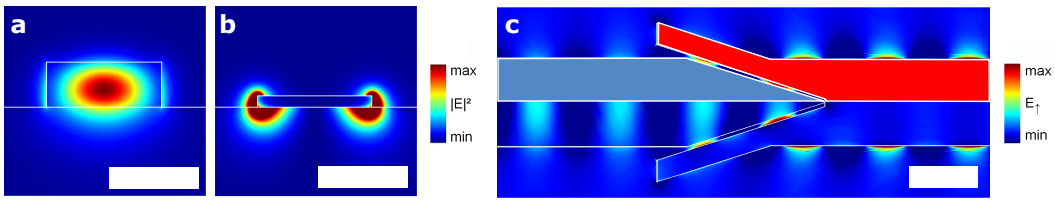

Figure 8.10.: Field distributions of waveguides and coupler. (a) shows the electric field's intensity of the transversal electric mode in the dielectric waveguide while in (b) the mode of the SPP waveguide is shown. Note the high field concentration at the edges of the SPP waveguide (the colour scale is normalised to the dielectric mode). In (c), the in-plane electric field component perpendicular to the propagation direction at the substrate-air interface is shown for the optimised coupler. In the upper half in the overlay shows the dielectric (blue) and plasmonic (red) part. Scalebars are 400 nm. (adapted from [277])

and for the following, the values of the dielectric function for the materials involved are $\epsilon_{Silica} = 2.37$ [328], $\epsilon_{SiNi} = 3.99$ [329], and $\epsilon_{Au} = -22.46 + i1.39$ [287]. Since the coupler is designed for single mode operation, a single input mode has to be selected. Here, as input mode the TE mode is chosen. Its transverse electric field are able to excite the SPPs in the metal arms more efficiently than the electric field of the TM mode. On the SPP output side of the coupler, single mode operation then is ensured due to symmetry – the second SPP mode exhibits a breathing mode character, which does not fit to the incoming TM mode [277]. Simulated field distributions of the two modes used are shown in Figure 8.10 (a,b).

Now, fully three-dimensional simulations with the obtained TE mode as input field distribution are performed. One example of the electric field from such simulations can be found in Figure 8.10 (c). However, before looking into the details, the method of obtaining the coupling efficiency η is introduced. Directly after the coupler, there are two different kinds of contributions to the electromagnetic fields, namely the bound SPP mode one wants to excite efficiently and scattered fields. For the calculation of η, only the SPP mode has to be taken into account, so it is important to distinguish the different contributions. This is done by adding 5 µm of straight SPP waveguide to the simulated coupler and evaluating the energy flux Φ through surfaces perpendicular to the waveguide at different distances z. For the guided SPPs, this energy flux is decaying mono-exponentially:

$$A = A_0 e^{-\alpha z}, \tag{8.48}$$

while the scattered fields decay faster. Furthermore, the decay constant $\alpha = 4\pi \frac{\mathrm{Im}[n_{eff,m1}]}{\lambda}$ of the guided SPP mode can be calculated with the propagation mode

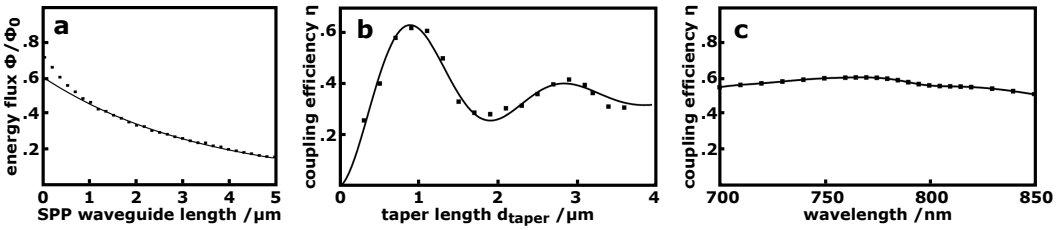

Figure 8.11.: Calculation of the coupling efficiency. In (a), the power flux through a surface perpendicular to the SPP waveguide is shown. The line shown is an exponential fit of the decay at long distances according to Equation 8.48. In (b), the length of the taper is varied. The coupling efficiency shows the oscillatory behaviour expected from the working principle of the coupler. . (c) shows the coupling efficiency of the coupler when the wavelength is varied. The lines in (b,c) are guides to the eye. (adapted from [277])

solver, so that the amplitude of the exponential A_0 directly leads to the coupling efficiency. Figure 8.11 (a) shows this behaviour with normalisation to the source energy Φ_0, i.e., $A = \frac{\Phi(z)}{\Phi_0}$.

Optimising the four free parameters of the coupler d_{dist}, d_{gap}, d_{arm}, and d_{taper} using the Taguchi method [277, 330] yields an optimal coupler with a coupling efficiency $\eta = 60\,\%$ for the parameters $d_{dist} = 80$ nm, $d_{gap} = 20$ nm, $d_{arm} = 120$ nm, and $d_{taper} = 800$ nm. Figure 8.10 (c) shows the field distribution obtained for this optimal coupler.

A value of $\eta = 60\,\%$ is comparable to other couplers found in literature, where theoretical values of up to 90 % are reached [331] for a dielectric loaded coupler in at a wavelength of 1550 nm (see Reference [289] for a review). In contrast to the other schemes, the coupler introduced here satisfies the needs specified in Section 8.3.1. In addition many values found in literature might be overestimated, due to only performing two dimensional simulations (e.g., in References [332–334]). The coupling efficiency of the coupler can be also easily enhanced by changing the design restrictions and changing the materials involved. With silver as SPP waveguide material for example, a coupling efficiency of $\eta_{silver} = 68\,\%$ is found. In addition, by changing the refractive indices of the involved media, e.g., by using magnesium fluoride ($n = 1.38$ [335]) instead of glass as substrate, the efficiency possibly can be enhanced further due to lower absorption of the SPP mode (see Section 8.1.5).

To further evaluate the properties of the coupler and to gain more insight into its working principle, parameter scans are performed starting from the optimal coupler found with the Taguchi method. Figure 8.11 (b) shows a variation of the taper length d_{taper} as well as a variation of the operating wavelength with unchanged

geometry is shown. The coupling efficiency η shows a damped oscillatory behaviour for a variation of d_{taper} as it is expected from the considerations in Section 8.3.1. The wavelength dependency shown in Figure 8.11 (c) also gives an important result: the coupler can be operated over a broad wavelength range of at least 150 nm without suffering from significant additional losses. Hence, this type of coupler can be used to interface different emitters without the need to perform an extra optimisation run each time.

In summary, the coupler simulated and optimised in this section satisfies the requirements for doing quantum plasmonic experiments while having a reasonable high coupling efficiency and is easy to fabricate. The possibility to couple single emitters to it using the nanomanipulation techniques described in Section 5.2 makes it a good interface between integrated waveguide and quantum photonic or plasmonic structures.

Chapter Summary: Plasmonics

In this chapter, surface plasmon polaritons were introduced. At first, a review on macroscopic electrodynamics and the optics of metals was given. Then, the properties of propagating SPPs were examined and their applications discussed. It was reported on an experiment on the generation of single SPPs using a hybrid quantum system. The pick-and-place technique was used to place a nanodiamond with single NV centre near a silver nanowire, which served as waveguide. Last, to address the problem of damping for propagating SPPs, a coupler from SPPs to photons was designed and investigated via numerical calculations. Such a coupler enables for efficient conversion and therefore makes it possible to use the unique properties of SPPs, e.g., the possibility for nanofocussing, just where they are needed, while the photons are used to guide excitations over long distances.

Having shown that concepts for hybrid integration also work with plasmonic structures, what is needed next is a technique to quantitatively measure their properties on the nanoscale. Such a technique will be introduced in the next chapter.

9. Quantum Emitter Fluorescence Lifetime Microscopy

This chapter deals with mapping the local density of optical states (LDOS) at the nanoscale. In the first section, an introduction to the concept of the LDOS is given while in the following sections methods of measuring the LDOS using NV centres are introduced. Parts of this have been published in *Optics Express* with the title *Single defect centers in diamond nanocrystals as quantum probes for plasmonic nanostructures* [168] and *Nano Letters* under the title *Scanning Single Quantum Emitter Fluorescence Lifetime Imaging: Quantitative Analysis of the Local Density of Photonic States* [186].

9.1. Theoretical Pre-Considerations

Spontaneous decay is a purely quantum mechanical phenomenon, it can not be explained classically. Nevertheless, when the emitter is mostly in its ground state, i.e., in the so called perturbation limit, a quantum mechanical two-level system can be described classically [336]. In order to make this chapter more accessible for the reader, the fundamentals of light matter interaction (compare Chapter 2) are introduced starting from the fundamental level. The following discussion will be oriented on Novotny and Hecht [185] and Barnes [337].

9.1.1. Spontaneous Decay and Local Density of Optical States

The spontaneous emission is not an intrinsic property of an emitter. Instead, it is determined also by the emitter's environment. A good starting point for calculation the decay rate of an emitter is Fermi's golden rule:

$$\gamma_{i\to f} = \frac{2\pi}{\hbar} \sum_f \left| \langle i | \, \hat{H}_{int} \, | f \rangle \right|^2 \delta(E_i - E_f), \tag{9.1}$$

where $\gamma_{i\to f}$ is the transition probability from an initial state $|i\rangle$ to a final state $|f\rangle$, $\hbar$ is the reduced Planck constant, the sum runs over all final states, and $\hat{H}_{int}$ is the interaction Hamiltonian which in dipole approximation reads $\hat{H}_{int} = -\hat{\boldsymbol{\mu}} \cdot \hat{\boldsymbol{E}}$, with the dipole operator $\hat{\boldsymbol{\mu}}$ and the electric field operator $\hat{\boldsymbol{E}}$. Using annihilation

and creation operators $\hat{a}_{\boldsymbol{k}}^{\dagger}$ and $\hat{a}_{\boldsymbol{k}}$ for the modes $\boldsymbol{k}$ defined by:

$$\hat{a}_{\boldsymbol{k}}^{\dagger}(t) = \hat{a}_{\boldsymbol{k}}^{\dagger}(0)e^{(i\omega_{\boldsymbol{k}}t)}, \tag{9.2}$$

$$\hat{a}_{\boldsymbol{k}}(t) = \hat{a}_{\boldsymbol{k}}(0)e^{(i\omega_{\boldsymbol{k}}t)}, \tag{9.3}$$

the electric field operator $\boldsymbol{E}$ at the position $\boldsymbol{r} = \boldsymbol{r_0}$ can be written as:

$$\hat{\boldsymbol{E}} = \sum_{\boldsymbol{k}} \left[\boldsymbol{E}_{\boldsymbol{k}}^{+} \hat{a}_{\boldsymbol{k}}(t) + \boldsymbol{E}_{\boldsymbol{k}}^{-} \hat{a}_{\boldsymbol{k}}^{\dagger}(t) \right], \tag{9.4}$$

with the frequency of a mode $\omega_{\boldsymbol{k}}$ and the positive and negative frequency parts of the complex field $\boldsymbol{E}_{\boldsymbol{k}}^{+} = (\boldsymbol{E}_{\boldsymbol{k}}^{-})^{*}$.

Evaluation for a two level system (not shown here, see Novotny and Hecht [185]) leads to the following result:

$$\gamma_{i\to f} = \frac{2\omega}{3\hbar\epsilon_0} \left|\boldsymbol{\mu}\right|^2 \rho_{\mu}(\boldsymbol{r}_0, \omega_0), \tag{9.5}$$

$$\rho_{\mu}(\boldsymbol{r}_0, \omega_0) = 3 \sum_{k} \left[\boldsymbol{n}_{\mu} \cdot (\boldsymbol{u}_k \boldsymbol{u}_k^{*}) \cdot \boldsymbol{n}_{\mu} \right] \delta(\omega_k - \omega_0), \tag{9.6}$$

where the partial local density of states $\rho_{\mu}(\boldsymbol{r}_0, \omega_0)$, the frequency ω_0 corresponding to the energy E_i, unit vectors $\boldsymbol{n}_{\mu}$ in the direction of $\boldsymbol{\mu}$, and the dipole matrix element $\boldsymbol{\mu} = \langle i | \, \hat{\boldsymbol{\mu}} \, | f \rangle$ are introduced. The word partial in partial local density of states here means that this quantity depends on the dipole's orientation. For convenience, new normal modes following:

$$\boldsymbol{E}_{\boldsymbol{k}}^{(+/-)} = \sqrt{\frac{\hbar\omega_k}{2\epsilon_0}} \boldsymbol{u}_{\boldsymbol{k}}^{(1/*)}, \tag{9.7}$$

are chosen. The notation $(\boldsymbol{u}_k \boldsymbol{u}_k^{*})$ means the outer product of the normal modes. Furthermore, the normal modes introduced can be expressed using the dyadic Green's function $\boldsymbol{G}(\boldsymbol{r}, \boldsymbol{r}'; \omega_0)$ (a derivation can be found in Novotny and Hecht [185]):

$$\rho_{\mu}(\boldsymbol{r}_0, \omega_0) = \frac{6\omega_0}{\pi c^2} \left[\boldsymbol{n}_{\mu} \cdot \mathrm{Im} \left(\boldsymbol{G}(\boldsymbol{r}_0, \boldsymbol{r}_0; \omega_0) \right) \cdot \boldsymbol{n}_{\mu} \right]. \tag{9.8}$$

With this formula, the problem to calculate the spontaneous emission and the partial local density of states is reduced to calculation of the Green's dyadic at the position of the two-level system.

To derive the total local density of states $\rho(\boldsymbol{r}_0, \omega_0)$ from this result, often referred to simply as LDOS, the dipole orientations are averaged out leading to a result for

the LDOS:

$$\rho_\mu(\boldsymbol{r}_0, \omega_0) = \frac{2\omega_0}{\pi c^2} \mathrm{Im}\left(Tr[\boldsymbol{G}(\boldsymbol{r}_0, \boldsymbol{r}_0; \omega_0)]\right). \tag{9.9}$$

Quantum mechanically, the LDOS can be interpreted as vacuum fluctuations and classically, as the ability of the environment to support photons [337].

At this point, is should be noted that in Equation 9.5 two terms enter, the discussed partial LDOS, which is only dependent on the emitters environment, and the transition matrix element $\boldsymbol{\mu} = \langle i | \hat{\boldsymbol{\mu}} | f \rangle$, which is an intrinsic property of the emitter. Changes in the matrix element are only expected when the wavefunction of the emitter changes. This only happens when the environment of the emitter perturbs its wavefuction, an effect happening only when the distance to the perturbing object is on the order of the extend of the wavefunction, i.e., approximately 1 Å [337]. In the following, the matrix element is assumed to be constant.

9.1.2. The Radiating Dipole

In the classical description, a radiating dipole in an inhomogeneous environment is described as a damped harmonic oscillator. It experiences a driving field that stems from the light it emitted that is coming back due to scattering from the inhomogeneous environment. This situation is described by [185]:

$$\frac{\mathrm{d}^2}{\mathrm{d}t^2}\boldsymbol{\mu}(t) + \gamma_0 \frac{\mathrm{d}}{\mathrm{d}t}\boldsymbol{\mu}(t) + \omega_0^2 \boldsymbol{\mu}(t) = \frac{q^2}{m}\mathbf{E}_s(t), \tag{9.10}$$

where $\boldsymbol{\mu}(t)$ is the oscillating dipole moment, γ_0 is its damping, ω_0 the undriven dipole's oscillation frequency, q the charge, m the mass, and $\mathbf{E}_s(t)$ the secondary local field due to the scattering. The homogeneous solution of this differential equation yields:

$$\boldsymbol{\mu}(t) = \mathrm{Re}\left[\boldsymbol{\mu}_0 e^{-i\omega_0\sqrt{1-(\gamma_0^2/4\omega_0^2)}t} e^{-\gamma_0 t/2}\right]. \tag{9.11}$$

In order to stay in the classical regime where the average energy stored in the dipole is defined, $\gamma_0 \ll \omega_0$ is required so that the average absolute dipole moment only changes slightly during one oscillation. With the requirement of energy conversation, meaning that the energy radiated by the oscillating dipole equals the damping, an expression for γ_0 can be found [185]:

$$\gamma_0 = \frac{1}{4\pi\epsilon_0}\frac{2q^2\omega_0^2}{3mc^3}, \tag{9.12}$$

where ϵ_0 is the vacuum permittivity and c the speed of light.

Going back to the full differential equation, Equation 9.10, the effect of $\boldsymbol{E}_s(t)$

will be a modification of the damping as well as of the oscillation frequency. With a new damping γ and a new frequency ω, two trial solutions are inserted for $\boldsymbol{\mu}(t)$ and $\mathbf{E}_s(t)$:

$$\boldsymbol{\mu}(t) = \mathrm{Re}\left[\boldsymbol{\mu}_0 e^{i\omega t} e^{-\gamma t/2}\right], \tag{9.13}$$

$$\boldsymbol{E}_s(t) = \mathrm{Re}\left[\boldsymbol{E}_0 e^{i\omega t} e^{-\gamma t/2}\right]. \tag{9.14}$$

With the additional assumption of a weak interaction, this leads to an expression for the decay rate γ [185]:

$$\frac{\gamma}{\gamma_0} = 1 + \frac{6\pi\epsilon_0}{|\boldsymbol{\mu}_0|^2}\frac{1}{k^3}\mathrm{Im}[\boldsymbol{\mu}_0^* \cdot \boldsymbol{E}_s(\boldsymbol{r}_0)], \tag{9.15}$$

where $\boldsymbol{r}_0$ is the dipoles origin and $k = \omega/c$ the wavenumber. In this equation, the magnitude of the dipole moment cancels out, since the scattered field $\boldsymbol{E}_s(\boldsymbol{r}_0)$ is proportional to it. So an important result is found: The projection of $\boldsymbol{E}_s(\boldsymbol{r}_0)$ in the direction of the dipole does alter the decay rate. Calculations of this effect for a simple geometry like an dielectric interface can be found for example in two papers by Lukosz and Kunz [338, 339].

9.2. Mapping the LDOS With a Single Quantum Emitter

Using the considerations of the previous section, now a single emitter is used as a probe for the LDOS. In addition to its intrinsically enhanced spatial resolution, the ultimate control of a nanoemitter probe allows for absolute measurements of the electromagnetic environment of arbitrary nanophotonic structures.

9.2.1. Motivation for Single Emitter Experiments

Quantum physics enables measurements with a precision overcoming the classical limit [8]. Therefore, quantum-enhanced sensing has become one of the major fields in quantum technology [219]. Single quantum systems represent ideal sensing probes [340], not only because of their intrinsic quantum properties, but also due to the fact that they are typically very small. They can explore local fields of single atoms or a local environment consisting of only a few molecules. Optical quantum probes, such as single quantum emitters, provide the additional advantage of reliable initialisation as well as efficient and easy read-out. High sensitivity sensing of electric [127] or magnetic fields [126, 341] has been demonstrated.

First scanning quantum probes that utilise optical emitters have appeared more than 10 years ago [342] in fluorescence microscopy. They detect vacuum fields via modifications of the emitter's spontaneous lifetime which is not an intrinsic property

of an emitter, but is rather determined by the local density of states as discussed above.

More generally speaking, any light-matter coupling, as described on the fundamental level by a single dipole coupled to modes of the electromagnetic field, can be engineered by changing the LDOS. By carefully designing the LDOS, it is possible to significantly enhance the functionality of devices in photonics and plasmonics. Examples are spontaneous emission engineering for fast optical modulators [343], for energy-efficient lasing [179], or for improving light trapping in solar cells [344]. The design of the LDOS is particularly important for engineering fundamental quantum optical few-photon devices, e.g., for efficient and fast single photon sources needed in optical quantum information processing systems [219]. Photonic structures such as microcavities [158], photonic crystals [345], optical antennas [346], and photonic metamaterials [347] allow for designing the LDOS in all three spatial dimensions. Therefore, techniques to obtain precise information about the LDOS on the nanoscale are needed. There exist several approaches to obtain this information, for instance coating of the structures of interest with fluorescent dyes [348], mapping with scanning near-field microscopes [349–351], nanopositioning of defect centres [168] or colloidal quantum dots [352], using optically trapped nanocrystals [353], or employing a scanning electron microscope [354]. Most of the previous fluorescent probes utilise large ensembles of emitters like molecules in nanobeads [355] to determine the LDOS via the observed lifetime changes.

However, due to averaging over an ensemble with different spatial positions and electromagnetic environments, the excitation decay curve often is multi-exponential. This makes it difficult to quantify modifications of the decay dynamics when scanning the probe. Additionally, the ultimate spatial resolution is still given by the diameter of the doped beads and there is no information on the vectorial character of the coupling of the emitters to the nanostructure under investigation.

A fundamental fluorescence lifetime imaging microscopy (FLIM) probe would consist of a single atom. However, single ions in an ultra-high vacuum environment do not meet the requirement for a robust scanning probe where a point-like fluorescent dipole is located at a scanning tip, which can be actively stabilised and scanned across an arbitrary substrate. Defect centres in nanodiamonds (see Chapter 3) exhibit ideal properties for this purpose [168, 356, 357], since they are optically stable even at room temperature. The single emitter nature of a NV centre leads to an increase in obtainable resolution only limited by the size of a single NV centre.

9.2.2. Mapping the LDOS of Plasmonic Antennas

Large changes in the LDOS are especially expected for plasmonic structures (see Chapter 8). Therefore, in a first experiment, a NV centre in nanodiamond is used as a probe for measuring the LDOS at different positions in a plasmonic antenna.

Plasmonic antennas are highly desired in experiments on the level of single quantum emitters for the following reasons: Using them the quantum emitter is exited more efficiently, more photons are extracted from the quantum emitter, and the emitted photons can be spatially directed towards a specific direction [218, 358, 359].

Gold bowtie antennas fabricated with electron-beam lithography are investigated on a glass substrate with a nanodiamond probe. In contrast to a configuration where the antenna is decorated with several emitters in a purely random manner [360], here, AFM nanomanipulation (see Section 5.2) is utilised. In this way, control of the position of the nanodiamond with nanometre precision is achieved. By nanomanipulation, it is possible to investigate different configurations of exactly the same constituents. For example, it is possible to alter the antenna [361] or to change an emitter's position. Mapping of the electromagnetic environment via observing the optical properties of a nanoprobe is thus possible.

For the measurements, a confocal microscope is used (see Figure 8.6 (a) for details). The excitation laser is operating in pulsed mode at 10 MHz repetition rate and has a wavelength of 532 nm. All measurements are performed at a power of 40 μW at the back of the slightly overfilled NA=1.35 oil immersion objective.

There are different processes when coupling an emitter to a plasmonic antenna. The excitation as well as the radiative rate are enhanced, but additional non-radiative decay channels may open up [362]. Also, the modified spatial emission pattern may change the number of the detected photons on a detector of finite solid angle [275]. By repeatedly measuring the lifetime and changing the nanodiamond's position with the AFM (see Figure 9.1 (a-f)), the lifetime maps depicted in Figure 9.2 (a,b) are obtained. The lifetimes are measured via time correlated single photon counting (see Section 2.4.1). In order to suppress short-lived emission from the gold, count events within the first few nanoseconds are not taken into account for the fitting to the decay curves (see Fig. 9.1 (g,h)).

The antennas used are fabricated to have a gap of 10 nm and consist of two isosceles triangles whose height equals their short side. Their short sides are designed to be 140 nm (Figure 9.2 (a)) and 150 nm (Figure 9.2 (b)), respectively. This geometries result in fundamental modes in the infra-red. In Figure 9.2 (a) a diamond with a height of approximately 60 nm and an oval shape is used for the mapping. This nanodiamond is too large to fit in the antenna gap. The exact position of the NV centre in this nanodiamond has also an a-priori uncertainty of the same size, i.e., approximately 60 nm. For this reason, in another measurement depicted in Figure 9.2 (b), a nanodiamond of 15 nm height is used in order to reduce this uncertainty. The two-dimensional maps in Figure 9.2 resemble an ultimate limit of fluorescence lifetime nanoscopy in a sense, that only one quantum emitter present. However, this still can be improved, as shown in Section 9.3.

Beyond the mapping of the electromagnetic environment of the antenna the data provides information about the actual enhancement of the fluorescence rate of the

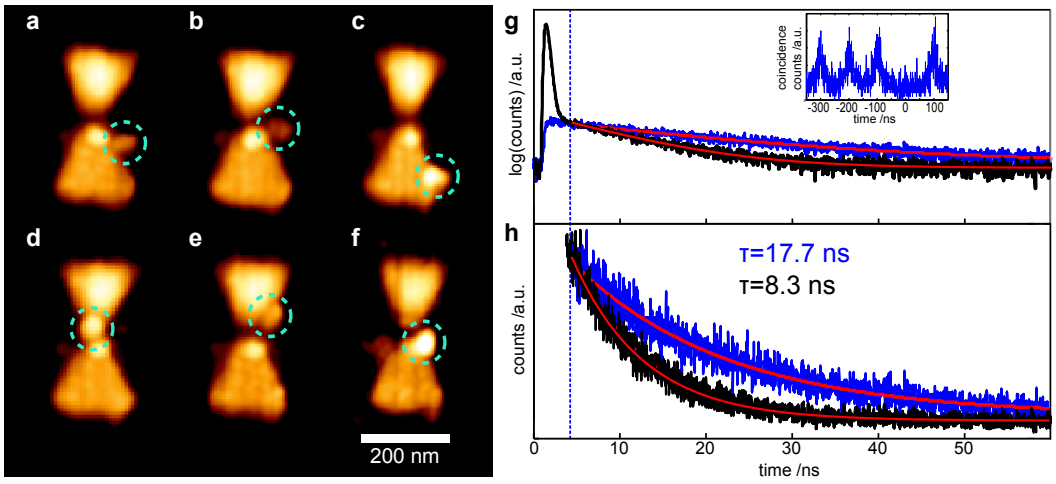

Figure 9.1.: Coupling of nanodiamond and gold bowtie antenna. (a-f) show the alignment of the probe. A single nanodiamond containing a single NV centre is moved with the AFM to different positions with respect to a bowtie antenna. Small changes in the measured topography are due to changes of the AFM tip's shape during the manipulation process. Circles highlight the positions of the nanodiamond. (g,h) are fluorescence lifetime histograms of a uncoupled nanodiamond (blue) and the nanodiamond coupled to a bowtie antenna (black). The initial peak stems from short-lived fluorescence from the gold of the bowtie antenna, which is not resolved by the detectors used. Only counts occurring 3 ns after the emission peak (indicated by the blue vertical line) are used to fit (red curves) the fluorescence decay from the NV centre in the nanodiamond. The inset in (g) shows the coincidences for the uncoupled diamond measured with the HBT setup. The absence of a peak at coincidence time zero indicates single photon emission. (Figure adapted from [168])

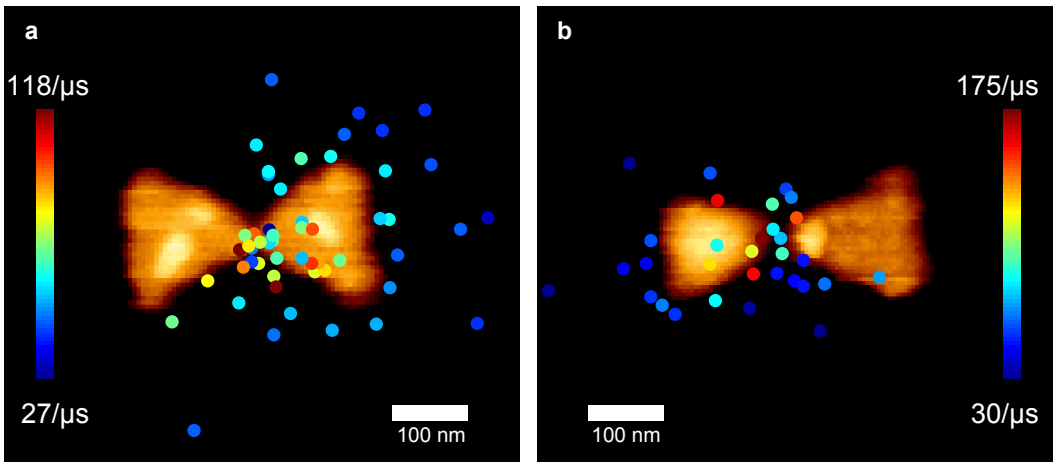

Figure 9.2.: NV centre decay rates at nanoantennas. (a,b) are maps showing the decay rate of the excited state of the NV centre in the nanodiamond probe for different positions with an underlay of the corresponding AFM image of the antennas. In (a), a diamond of approx. 60 nm height and an oval shape is used. In (b), the diamond's height is about 15 nm. (Figure adapted from [168])

NV centre in the nanodiamond. For a quantitative analysis, the uncoupled diamond has to be compared to the situation where the nanodiamond is coupled to the antenna in an optimum position. The nanodiamond is placed in the antenna gap, where an excellent alignment of the diamond with respect to the excitation laser spot is possible. The uncoupled diamond has a lifetime of $\tau_u = 17.7$ ns, which is reduced to $\tau_c = 8.3$ ns when the diamond is in the antenna gap. Also the photon emission rate from the diamond is changed from $R_u = 2.5$ kHz to $R_c = 2.2$ kHz. This reduction is due to additional loss channels which open up close to the metal surface. However, care has to be taken in the analysis since pulsed excitation is performed at a fixed excitation rate and a single NV centre only can get excited once per cycle, if the duration of the excitation pulse is small compared to the NV centre's lifetime. Due to coupling to the antenna, both radiative and non-radiative decay is enhanced, i.e., the lifetime of the excited state is significantly shortened. This means that although the probability of generating a photon after excitation is reduced, photons can be provided in principle at a much higher rate.

The key number is the rate of photon emission under continuous saturated excitation, which could in principle be calculated from the emission's power dependence under pulsed excitation. Since melting of the gold nanoantennas is observed at an excitation power of ca. 50 µW [232], which is clearly below the saturation intensity, it is not possible to determine the enhancement factor with adequate accuracy.

The technique for acquiring information on the LDOS at the nanoscale presented

here enables for a better understanding of nanophotonic and plasmonic structures. The two-dimensional maps of plasmonic antenna structures derived provide insight into the near-field properties of antenna structures allowing optimisation of the designs [363]. The method of repeatedly repositioning the quantum emitter and mapping the lifetime can in principle be extended to almost any system of interest, if they are accessible with an AFM [228, 229]. The technique introduced here enables for measurements of the LDOS at the nanoscale, but there are still some drawbacks: pushing the diamond to different positions is time consuming, due to uncontrolled orientation of the emitter and therefore the emission dipoles the coupling changes, and the technique is confined to only two dimensions. For getting more detailed insight, this clearly has to be improved. Hence, in the next section, a way raster scanning a sample is introduced.

9.3. Quantum Emitter Fluorescence Lifetime Imaging Microscopy

In this section, the technique of quantum emitter fluorescence lifetime imaging microscopy (QEFLIM) is presented. This technique allows raster scanning in all three spatial dimensions with high resolution. It is the direct, but heavily improved, successor of the experiment shown in Section 9.2. As a proof-of-principle experiment, QEFLIM is performed on a single silver nanowire.

9.3.1. Experimental Setup and Probe Characterisation

The experimental setup for QEFLIM is again a confocal microscope combined with an atomic force microscope for simultaneous measurements. In contrast to the experiment in Section 9.2, here, a more complex electronic setup and measurement scheme is used. A sketch of the optical setup and measurement process is shown in Figure 9.3. Photon detection event are recorded using time tagging data acquisition electronics (see Section 2.4.1). Markers for spatial coordinates are also fed to the electronics and are collected within the time tag stream. To extract three-dimensional lifetime information, in addition to the current scanning position, the cantilever's oscillation is also fed to the correlation electronics. With that information, the photon detection events at each pixel of the scanned sample area can be attributed to different height bins. Since for each position of a scanned area the detected photons are sorted with respect to the actual height of the oscillating cantilever, continuous feedback while mapping all dimensions of the sample in a single scan is possible. Data in each pixel is histogrammed with respect to the cantilever height and fitted with a mono-exponential decay to calculate the lifetime (see Figure 9.3 (c)). As in Sections 6.2 and 9.2, time gating is applied by not using

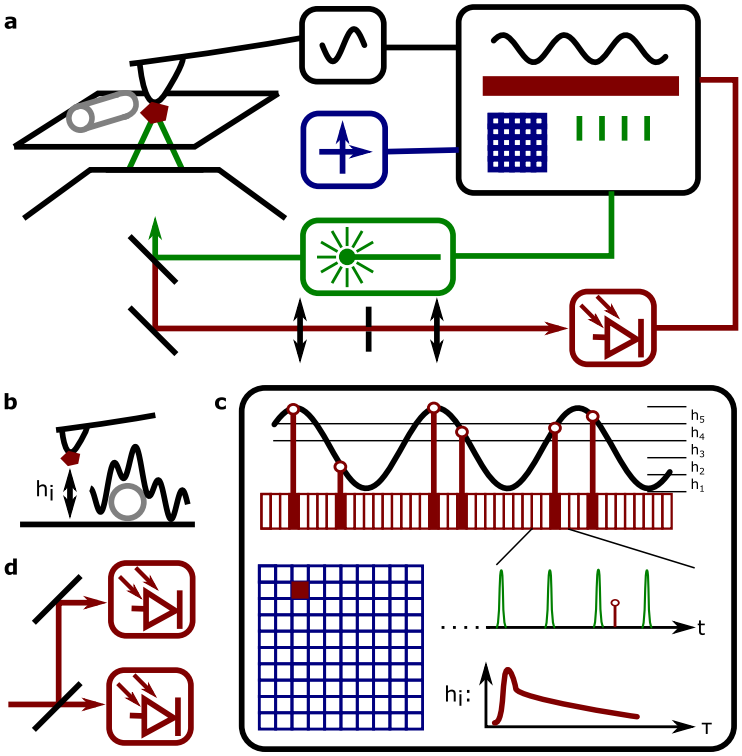

Figure 9.3.: Measurement apparatus and scheme of QEFLIM. In (a), a nanodiamond containing a single NV centre is glued to the tip of an AFM cantilever. The AFM is operated in tapping mode and the cantilever is positioned in the focal volume of a scanning confocal microscope equipped with a pulsed laser and an avalanche photodiode. Cantilever oscillation, coordinates, laser timing, and photon time tags are recorded simultaneously. Being operated in tapping mode, at different times the AFM tip is at different heights h_i as shown in (c). In (c), the electronic setup is shown. For each pixel of the scanned sample area, the photon detection events are sorted according to the current height h_i of the AFM tip. In this way, the probe in a single scan reaches different heights, with the maximum height being the oscillation's amplitude. The lifetime is determined for different height bins h_i by histogramming the arrival times with respect to the laser pulse and by making a fit to the tail of the exponential decay. This makes it possible to gather real 3D lifetime data while always maintaining feedback from the tapping mode AFM. (d) is a scheme of a Hanbury Brown and Twiss interferometer as it is used to prove the single emitter character of the probe. (Figure from [186])

events directly after the laser pulse in order to avoid artefacts from fast decaying background contributions. Here, the first 5 ns are omitted.

In order to glue [364] a nanodiamond containing a single NV centre to the AFM's tip, a process similar to the process used in the pick-and-place nanomanipulation approach is used (see Section 5.3). The tip is coated with poly-L-lysine prior to picking up the nanodiamond, what makes the nanodiamond stick at it's apex [365].

A very important task in quantitative QEFLIM is the characterisation of the probe. It has to be a single emitter with known properties such as orientation, lifetime, and quantum efficiency. All these parameters can be deduced from controlled measurements and comparison to theory. The excited state lifetime of the probe can be extracted from the measurements depicted in Figure 9.4 (a). Mono-exponential decay curve of the NV centre's excited state for different situations are shown: black for the nanodiamond on a cover slip (43.5 ns $\pm$ 1.4 ns), blue for the nanodiamond glued to the tip far from the surface (19.8 ns $\pm$ 0.2 ns), and red with the tip close to a silver nanowire (9.2 ns $\pm$ 0.1 ns). After the nanodiamond is glued to the tip, the lifetime only varies when the environment, and therefore the LDOS, changes, e.g., when approaching a silver nanowire (red curve in Figure 9.4 (a). To prove the single emitter character of the probe, measurements of the autocorrelation function $g^{(2)}(\tau)$ are performed using a Hanbury Brown and Twiss setup before and after the nanodiamonds are attached to the tip (see Figure 9.4 (b)). A value of $g^{(2)}(0) < 0.5$ indicates that the main photon contribution stems from a single emitter. Figure 9.4 (c) shows detailed data of nanodiamond probes approaching a glass surface. When the emitter approaches the surface, an oscillatory behaviour is visible. A careful numerical and analytical analysis examining explicitly the influence of the silicon AFM tip reveals that the approach curves can also be derived in good approximation by an analytical theory (see Appendix E). Using these theoretical curves, the QEFLIM probe can be fully characterised, i.e., the NV centre's orientation, its position within the nanodiamond, as well as the quantum efficiency of its optical transition can be derived as shown in Reference [186].

9.3.2. QEFLIM Measurements at Silver Nanowires

With a fully pre-characterised and scanable single quantum emitter, the LDOS can now be mapped on the nanoscale in all three spatial dimensions with high resolution. A first example is shown in Figure 9.5, where silver nanowires, the drosophila of plasmonics, are raster-scanned by QEFLIM (For a non-scanning experiment of coupling a NV centre to a silver nanowire see Section 8.2). Figure 9.5 (a,d) are AFM topography scans showing a wire and a wire network, respectively. In Figure 9.5 (b,e) and (c,f), lifetimes images are shown for the emitter being in in the highest quarter of it's tapping mode height oscillation and in the lowest, respectively. The emitter's lifetime decreases close to the surface due to the higher index

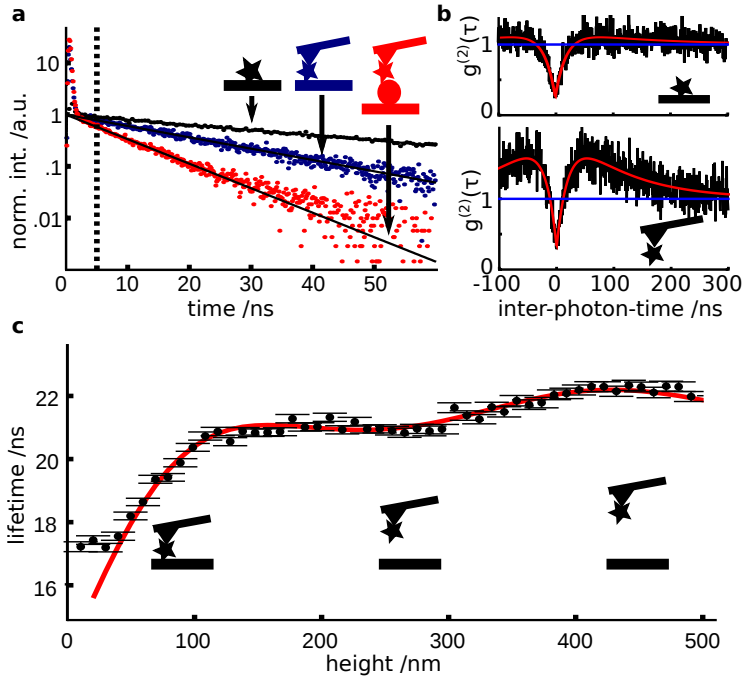

Figure 9.4.: Probe characterisation. In (a), the lifetime of the NV centre used in the scans shown in Figures 9.5–9.7 is measured. The black curve is for the nanodiamond prior to glueing it to the cantilever. A fit yields a lifetime of 43.5 ns ± 1.4 ns. The blue and red curve are for the diamond on the tip at the glass interface and at a silver nanowire, respectively. Corresponding lifetimes are 19.8 ns ± 0.2 ns and 9.2 ns ± 0.1 ns. Only photons after the dotted line are used for lifetime fits. In (b), autocorrelation curves $g^{(2)}(\tau)$ of the NV centre in a nanodiamond used in the scans lying on a glass cover slip (upper panel) and glued to the AFM tip (lower panel) are shown. The red line is a fit to the data according to Jelezko *et al.* [89]. It yields $g^{(2)}(0) = 0.25$ and $g^{(2)}(0) = 0.31$, respectively. A change in the bunching behaviour indicates a change in the NV centre's environment. Count rates are 120000 cts/s and 110000 cts/s, respectively. In (c), the lifetime of a NV centre versus height over a glass surface is plotted. The red curves is following an analytical theory for a dipole over a dielectric interface. In Appendix E, it is shown that this approximation is justified. No background correction was applied to any of the data. (Figure from [186])

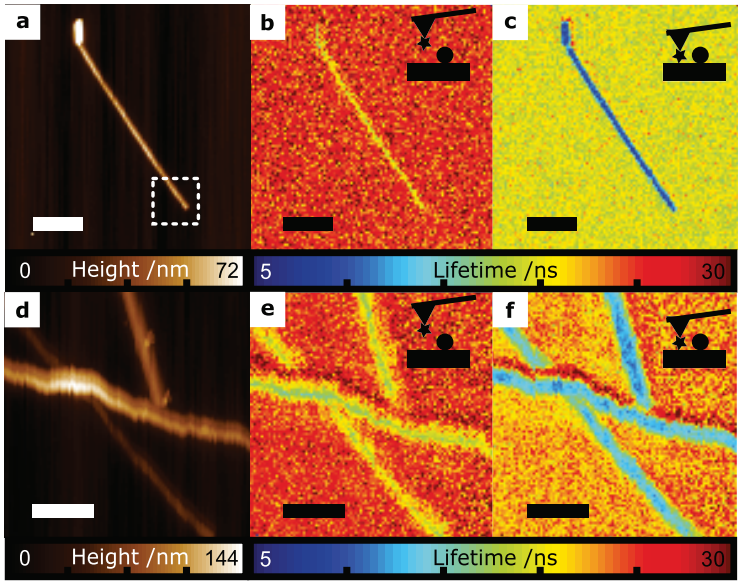

Figure 9.5.: Silver nanowires imaged by QE-FLIM. (a) shows an atomic force microscope image of a silver nanowire of diameter 50 nm acquired in tapping mode. The dashed rectangle indicates the region, which is investigated in more detail in Figure 9.6. (b,c) are simultaneously recorded lifetime images for the AFM tip being in the highest quarter of its tapping mode height oscillation and in the lowest, respectively. Scalebars in (a-c) are 1 µm. (d-f) show data for a network of single nanowires. At the nearly horizontal wire, in addition to the expected decrease of the lifetime, an increase is found. This is is a feature stemming from topography and the nanodiamond's position on the tip, which gives information on the NV centres position at the tip. Scalebars are 500 nm. Cantilever oscillation amplitudes are 37 nm for (b,c) and 74 nm in (e,f) and data acquisition times per pixel are 25 ms for (b,c) and 50 ms in (e,f). (Figure adapted from [186])

of refraction and therefore higher LDOS. Close to the nanowire, the additional plasmonic modes account for an even more reduced lifetime. In Figure 9.5 (d-f), a network of crossed wires is scanned with QEFLIM. When scanning along the nearly horizontal wire, the expected decrease of the emitter's lifetime is observed, however, also an increase in lifetime is found in a scan parallel to it. This feature is often regarded as a topography artefact in scanning near-field microscopy. Here, it can not only be corrected using the recorded full three-dimensional information, but there also can be extracted valuable information on the NV centre's position at the AFM tip.

Another striking feature that shows up when looking at silver nanowires, are oscillations of the plasmonic channels of the LDOS along the direction of the wire. They arise due to interference of surface plasmon polaritons (see Chapter 8) reflected at the wire's ends and the ones directly launched into the wire. When the SPPs are excited by a single emitter, as it is done here (see figure 9.4 (b)), the phenomenon can also be discussed in terms of wave-particle duality [321]. Figure 9.6 shows a detailed scan of a nanowire's end. Interestingly, the decay of these oscillations away from the wire's ends is much faster than it would be expected by effects of Ohmic plasmon damping and dephasing from the NV centre's broad spectrum alone [306]. In order to explain the fast decay, it is necessary to take into account higher-order plasmonic modes on the silver wire. As confirmed via ab-initio three-dimensional discontinuous Galerkin time-domain (DGTD) [366, 367] numerical simulations (see Figure 9.6 (h)), this multi-mode nature gives rise to additional dephasing. The observation of this previously disregarded effect demonstrates the power of QEFLIM – it offers the possibility to study the behaviour of the LDOS at the nanoscale in such a controlled way, that not only qualitative, but also quantitative comparisons with theory are possible. The modulation observed is in phase with the modulation of the lifetime, meaning that more photons are collected when the lifetimes are longer. This behaviour is due to the fact that the additional decay channels, which shorten the lifetime, are of plasmonic nature and bound to the wire. The majority of the SPPs gets either absorbed or leaves the confocal volume of the microscope before getting scattered out – an effect often misunderstood as fluorescence quenching.

An additional unique feature of 3D QEFLIM is the possibility to derive topography-corrected lifetime images. Whereas Figure 9.5 displayed lateral scans for two different relative positions of the scanning cantilever, Figure 9.7 shows a scan crossing a silver nanowire in a plane perpendicular to the sample surface. The amplitude of the cantilever's oscillation of 128 nm is divided in 25 height bins. At the same time, for each pixel the absolute height of the sample is acquired with the AFM. Therefore, Figure 9.7 (a) represents a lifetime image with completely known spatial coordinates avoiding artefacts which often appear in scanning probe images. The observed rate enhancement by a factor of 2.6 is of the order that is expected from previous experiments dealing with the coupling of nanodiamonds to silver

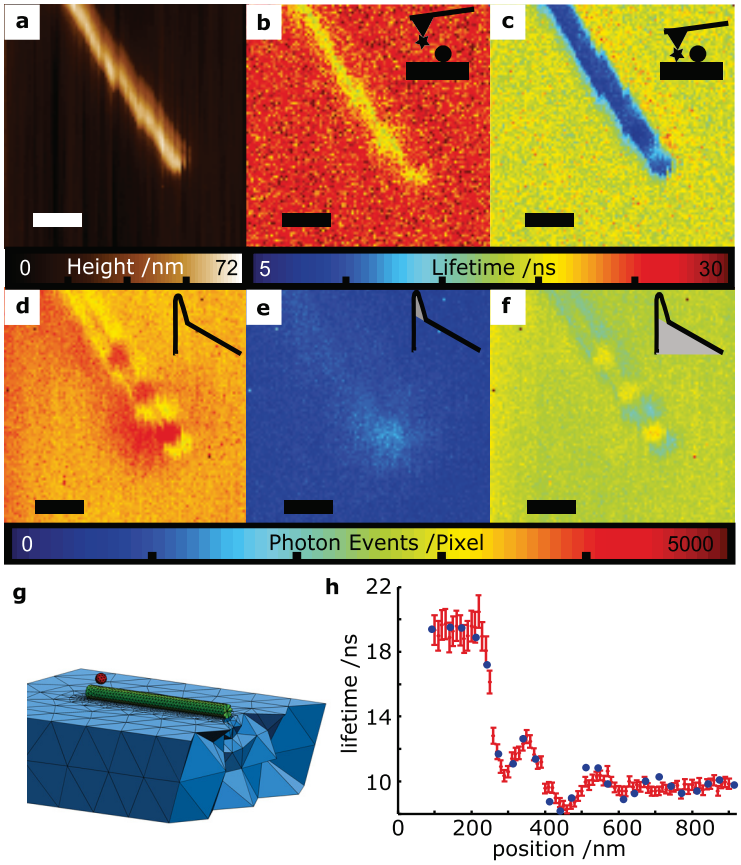

Figure 9.6.: Oscillations of the LDOS at an wire's end. (a) shows a zoom to the end of a silver wire, as indicated in Figure 9.5 (a). (b,c) show the lifetime in the upper and lower quarter of the cantilevers oscillation, respectively. (d) is the intensity measured while scanning. (e,f) are the intensities in the lower quarter of the background photons and the photons stemming from the diamond, respectively. An oscillation of the photonic intensity due to plasmonic modes back-reflected at the wire's end is visible. Scalebars are 200 nm and data acquisition time per pixel is 25 ms. (g) shows the mesh used in the three-dimensional DGTD simulations. The emitter (red) interacts with a silver nanowire (green) lying on a glass substrate (blue). (h) is the lifetime dependence of the NV centre when scanned along the wire. Big blue dots are results from simulations. An excellent quantitative agreement from ab-initio simulations and experimental data is found. (Figure from [186])

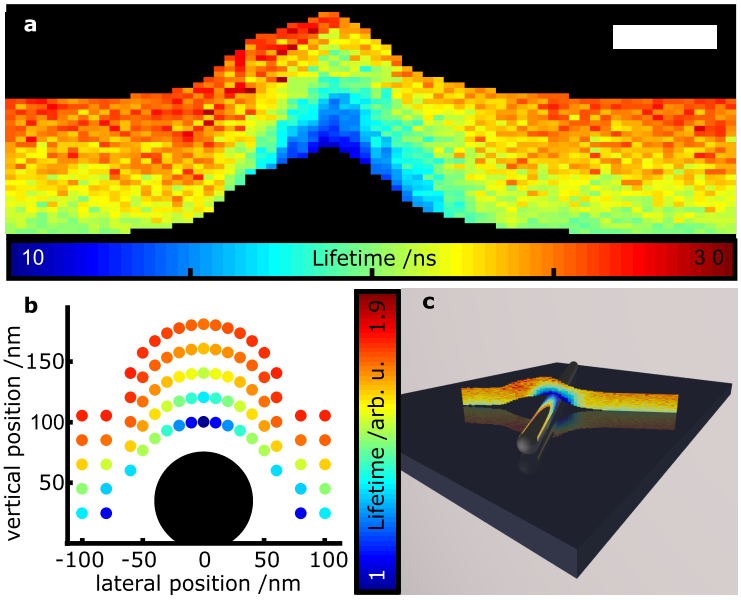

Figure 9.7.: Two-dimensional stripe scan across a silver nanowire. (a) shows the colour coded lifetime data as a function of height and position perpendicular to a silver nanowire. The absolute height is corrected according to the topography data acquired simultaneously with the AFM. In this way, topography artefacts are corrected as well. Height and position axis are scaled equally and the scalebar is 100 nm. Data acquisition time is 200 ms per pixel. (b) shows numerical simulation corresponding to the data in (a). As in (a), the same probe as in Figure 9.6 is used, the probe parameters used for the simulations correspond. (c) is an artists view clarifying the geometry of silver wire and data in (a,b). (Figure from [186])

nanowires [172, 321].

9.3.3. Resolution of QEFLIM

The resolution of standard optical far-field microscopy is limited by the far-field diffraction limit (see Section 4.1). Using the Sparrow criterion (Equation 4.5), the maximum obtainable resolution under incoherent illumination can be calculated to be [209]:

$$d = 0.51\frac{\lambda_0}{\mathrm{NA}} \approx 264\ \mathrm{nm}, \tag{9.16}$$

with the free space wavelength λ_0 and the numerical aperture of the microscope objective NA. The value given is calculated for an NA = 1.35 oil-immersion objective and a value for $\lambda_0 = 700$ nm for the free space wavelength. This limit is slightly smaller for confocal microscopy and can be further lowered in some cases by so called superresolution microscopy [210] or by detecting the near-field in scanning near-field optical microscopy.

In near-field approaches, the resolution is limited by the size of the probe. This is because the detected signal is a convolution of the measured quantity's actual spatial extend and the size of the probe. Note that this limit is fundamentally different from the diffraction limit in far-field microscopy, where non-propagating components of the signal just do not reach the distant detector and thus the resolution is limited by the propagating components only. Additionally, in near-field microscopy, it is possible that the probe alters the sample locally and hence introduces artefacts, which are hard to quantify, since they depend on the particular sample measured. Further information on the problem of defining a resolution in near-field microscopy can be found in Reference [368].

When trying to quantify the resolving power of QEFLIM using single defect centres in nanodiamond, this means in the first place that the obtainable resolution is limited by the size of a single defect centre, i.e., on the order of the lattice constant (0.36 nm for diamond [369]). The host crystal of the defect centre (and the AFM tip) will alter the fields which the defect probes. Hence, measuring the resolving power of a probe in QEFLIM requires a test structure where the LDOS varies on a length scale shorter than the expected resolution. No such sample is measured here, however, a first upper bound can be estimated by looking at the cross-section of a silver nanowire and comparing its actual size with its size in QEFLIM. In order to make this number comparable with other near-field methods, the lower quarter of the oscillation where the probe is closest to the sample surface is used and no three-dimensional correction for topography is applied. Figure 9.8 shows the feature size (full width half maximum, FWHM) of a wire scanned with QEFLIM. It is approximately 110 nm. The lateral extension of the silver wire can be estimated assuming that the silver wires have equal height and width to be 50 nm. This

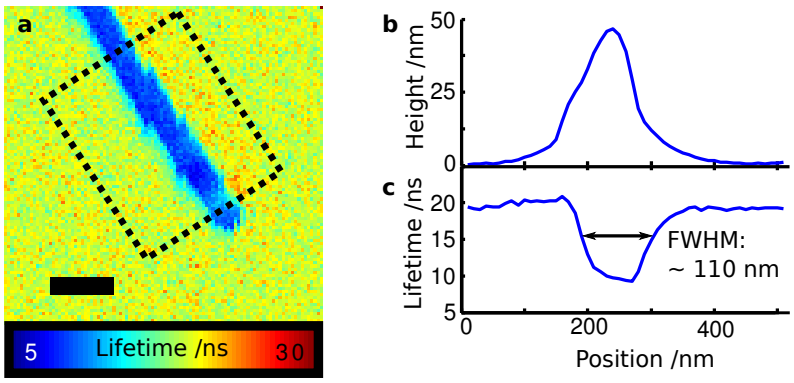

Figure 9.8.: Determining an upper bound for the spatial resolution. (a) shows a lifetime image of a silver nanowire with a diameter of 50 nm. The area indicated by the dotted rectangle is averaged to derive the plots (b) and (c). The scale bar is 200 nm. (b) shows the averaged AFM height signal perpendicular to the silver nanowire. It is inferred that the nanowire has indeed a diameter of approximately 50 nm. (c) is the corresponding lifetime signal. The 50 nm silver nanowire provides a lifetime signal with a full width half maximum (FWHM) of 110 nm. (Figure from [186])

means that an object of 50 nm is imaged as being 110 nm wide, corresponding to an additional 30 nm on each side.

It has to be pointed out, that 30 nm is only an upper bound for the spatial resolution of the microscope, since the LDOS at a wire decays on the same length scale.

9.3.4. Prospects of QEFLIM

The experimental and theoretical analysis of the LDOS above has introduced QEFLIM as an ultimate limit of optical scanning probe microscopy. It showed that a stable and fully characterisable point-like probe is mandatory to go hand-in-hand with full ab-initio three-dimensional numerical simulation. By collecting the photons from a single emitter glued to an AFM tip and time tagging synchronised with the cantilever position, lifetime data in all three dimensions can be acquired in a single scan without topography artefacts. The obtained three-dimensional data sets give detailed insight to the electromagnetic environment at the nanoscale with sub-diffraction-limit resolution. Beyond mapping of the local density of optical states, the vectorial role of emitter-field coupling is revealed as a crucial information to characterise arbitrary nanophotonic and nanoplasmonic structures. Future experiments may include, for example, measuring the modes of coupled nanoplas-

monic structures, mapping photonic structures like photonic crystal cavities, and identifying buried structures only via their effect on the LDOS. Combinations with magnetic [126], electric [127], or temperature sensing [129] are possible enhancements of the microscope. By adding a microwave setup, it is possible to access the rich physics the spin of the NV centre provides (see Section 3.3) [89].

Also, in future experiments, the type of emitter can be changed to another defect centre in nanodiamond, e.g., the SiV centre [231]. The, compared to NV centres, narrow-band emission from SiV centres would make it possible to map narrow band modes with a higher resolution. It is also possible to change the emitting system completely. So far, with the NV centre, only an emitter emitting with an electric dipole transition is used. Using emitters which decay predominantly via magnetic dipole transitions like trivalent erbium, europium, or terbium, it is possible to access the magnetic local density of states [370]. Probing the electric and magnetic LDOS independently using different emitter would bring additional insight for designing electromagnetic structures at the nanoscale.

Chapter Summary: Quantum Emitter Fluorescence Lifetime Microscopy

In this chapter, the feasibility of a single solid-state emitter for measuring the local density of optical states at the nanoscale was investigated. After theoretical preconsiderations, in a first experiment, a single NV centre was repeatedly repositioned at a bowtie nanoantenna and its excited state decay rate measured. This gives information on the LDOS, but the technique is time consuming and the uncontrolled orientation of the NV centre introduces errors. Hence, in a second experiment, a scanning probe method for this measurement was developed. By mapping the LDOS with a singe NV centre in nanodiamond glued to an AFM in tip in all three spatial dimension, QEFLIM was established. This imaging method can be applied to a variety of structures and valuable information, e.g., for optimisation hybrid quantum systems, can be extracted.

10. Summary and Outlook

Here, the contents and results of this thesis are reviewed chapter by chapter. After this, an outlook on the continuation of the experiments and future prospects is given.

10.1. Summary

Chapter 2 introduced basic aspects of single photon generation and detection.

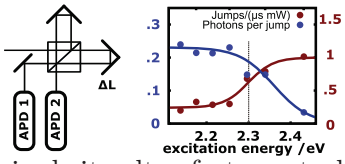

In **Chapter 3**, one particular single photon emitter – the NV centre in diamond – has been introduced. This emitter is used throughout the experiments shown in this thesis. In Chapter 3, one important property of NV centres in nanodiamond is characterised: its ultra-fast spectral diffusion. Typical rates of spectral jumps are found to lie in the microsecond range. A linear dependence of the jump rate on the excitation power is found, what is a strong indication that the excitation light is the main source of spectral diffusion. By variation of the excitation light's wavelength, a threshold at circa 2.3 eV is found. Currently, the source of this threshold is unknown. The experiment on measuring the ultra-fast spectral diffusion is reported in [82].

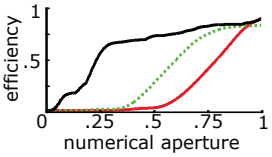

In **Chapter 4**, after a review on microscopy, techniques for collecting single photons from solid-state single photon emitters were shown. Finite difference time domain simulations were employed to study a design for elliptical solid immersion lenses. These eSILs were found to be able not only to collect much of the emitted light, as standard SILs do, but also to direct the light into very small numerical apertures. For example, with a low numerical aperture of only 0.3, 65 % of the light emitted by a dipole can be collected. Furthermore, with the technique of two-photon direct laser-writing, fabrication of such SILs is feasible. Simulations and design of the eSILs is reported in [149].

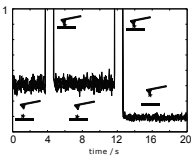

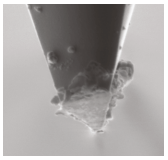

In **Chapter 5**, the technique of atomic force microscopy was introduced. Its general working principle and methods of nanomanipulation were shown.

In detail, a newly developed pick-and-place method
was explained and demonstrated using nanodiamonds. The pick-and-place technique enables for controlled placing of nanoparticles at any position, as long as an AFM can reach it. This technique, described in detail in Reference [91], forms the basis of these publications: [114, 168, 228, 229, 232, 250].

In **Chapter 6**, the pick-and-place technique described in Chapter 5 was used in order to build quantum hybrid systems with NV centres in nanodiamond as optical emitters. By placing a nanodiamond containing a single NV centre inside a photonic crystal cavity, a resonant enhancement of the NV centre's zero phonon line by a factor of over 12 was achieved. This is a ground-breaking result for using of NV centres in integrated quantum networks. Later, other groups employing different approaches have achieved even higher values for the enhancement of a NV centre's zero phonon line [242]. In the second part of Chapter 6, a nanodiamond containing a single NV centre was coupled to the core of a photonic crystal fibre using the pick-and-place technique. The resulting directly fibre coupled single photon source possesses a very high collection efficiency (effective numerical aperture of 0.82) and is intrinsically stable without any need for alignment. Stable and efficient single photon sources are another important ingredient for integrated quantum networks. The experiments on the hybrid devises assembled here are reported in [228, 229, 232].

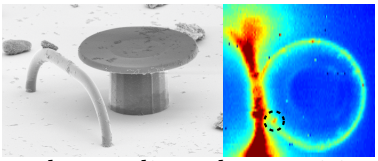

In **Chapter 7**, another approach for the integration of nanodiamonds in hybrid systems was shown. In contrast to the pick-and-place technique used in Chapter 6, here a hybrid material was used. The new hybrid material consists of a photoresist for two-photon direct laser-writing combined with nanodiamonds. Using two-photon direct laser-writing, on-chip integrated quantum photonic circuits are build, which consist of three basic components: quantum emitters, resonators, and waveguides. The functionality of the concept has been proven by showing single photon emission from a NV centre inside a whispering gallery mode resonator by measuring the statistics of the photons at the output ports of a waveguide. Using a similar technique, but with pre-localised nanodiamonds, parabolic antennas for enhanced single photon collection were fabricated. These antennas redirect photons emitted from single NV centres to a very small solid angle. Ultra-high photon rates of approximately two million counts per seconds are achieved in this way. Structures created using the approach with a hybrid material are shown in [177].

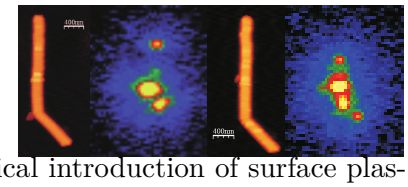

Chapter 8 dealt with using surface plasmon polaritons for the enhancement of light matter interaction and routing of surface plasmon polaritons on the single particle level. After the theoretical introduction of surface plasmon polaritons, generation of single SPPs with a NV centre was shown. The NV centre was coupled to a silver nanowire which served as SPP waveguide and emission of antibunched light at the ends of the wire was detected. This shows the feasibility of creating single SPPs and working with them in controlled way. Using nanomanipulation techniques, it is furthermore possible to adjust the waveguide emitter coupling in a very controlled way. In the last part of Chapter 8, a dielectric to plasmon coupler is designed and numerically investigated. Since guiding excitations along tightly confined plasmonic waveguides is lossy, it is favourable to use dielectric waveguides and coupled to plasmonic waveguides just when it is needed, e.g., to couple to quantum emitters. Experiments and simulations shown here are reported in [168, 232, 277].

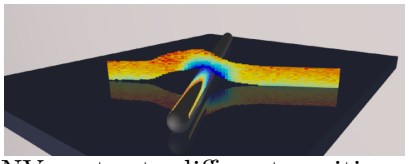

In **Chapter 9**, single NV centres in nanodiamonds were used as probes for the local density of optical states at the nanoscale. In a first experiment, plasmonic bowtie nanoantennas were investigated by nanomanipulating the same single NV centre to different positions and measuring its decay rate. Limitations to this experiment were that the technique is time consuming and that the orientation of the NV centre is uncontrolled, since the nanodiamond can accidentally rotate on being manipulated. To overcome these limitations, the technique of three-dimensional quantum emitter fluorescence lifetime imaging microscopy (QEFLIM) has been developed. Here, a nanodiamond containing a single NV centre was glued to the tip of an AFM cantilever and used as a scanning probe. As a proof-of-principle experiment, the LDOS in the vicinity of a silver nanowire was mapped and the results were compared to numerical calculations. The high degree of agreement between experiment and theory proves that QEFLIM is a valuable new tool for quantitative measurements on the nanoscale. Experiments on measuring the LDOS at the nanoscale using single emitters are reported in [168, 186].

10.2. Outlook

On the basis of the results found and methods developed in this thesis, many future experiments in various directions are possible. Here, three directions for

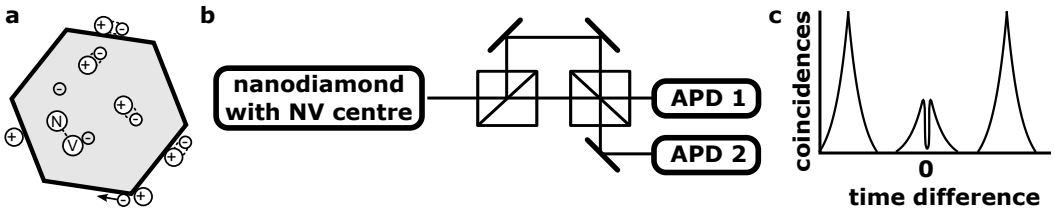

Figure 10.8.: Two-photon quantum interference from a NV centre. (a) shows a toy model for the source of spectral diffusion. Charges at the surface or inside the crystal, e.g., at impurities, are fluctuating. (b) shows a setup to measure two photon quantum interference from a single emitter (see Section 2.3). The stream of photons is split into two paths of which one has a delay longer than the emitter's lifetime. (c) expected result under pulsed excitation. The dip at time difference zero is due to quantum interference. It's shape reveals the dynamics of spectral diffusion. ((a) adapted from [82])

future experiments are highlighted. These directions are focussed on how to proceed research with nanoscale **Quantum Emitters**, the prospects of **Quantum Hybrid Devices**, and the further development of **Sensing and QEFLIM**.

10.2.1. Quantum Emitters

In nearly all experiments presented in this thesis, the NV centre in nanodiamond is used as an emitter. There are two main reasons for this: Firstly, as shown in Chapter 3, NV centres are a highly valuable resource for quantum optics and secondly, being abundant in most kinds of diamond, they are easily available. However, especially in nanodiamonds, their properties are degraded. One example for this is the ultra-fast spectral diffusion measured in Section 3.6. At the measured rates with more than one jump per detected photon, it is basically impossible to interface two different NV centres. Currently, the exact mechanism of the ultra-fast spectral diffusion is unknown, but for working with NV centres in nanodiamonds, understanding it is mandatory. For this, measurements on different types of nanodiamonds with different sizes, impurity concentrations, and surface terminations will be needed. A future experiment that could yield more information on spectral diffusion is a measurement of two-photon quantum interference [32] from a single NV centre (see Figure 10.8 and Section 2.3). Delayed photons from the centre are sent to a beamsplitter together with non-delayed ones. The shape of the dip in the correlation measurement will then contain the information. With improvements on the NV centres in nanodiamonds, controlled quantum interference from different centres will be possible. This, as already shown in bulk diamond, will enable for many quantum optical experiments like entanglement [35] and teleportation [123],

but with nanodiamonds, which are better suited for hybrid integration than bulk diamond.

Besides improving NV centres in nanodiamond, other quantum emitters (see Section 2.5) can be investigated as well, some of which are also available as nanoparticles. All the techniques shown in this thesis have the potential to be applied to any of them. This underlines the strength of the hybrid approach: parts can be easily changed in order to always work with the best suited components. More work has to be done in order to characterise these alternative emitters and to identify new candidates for quantum technology.

10.2.2. Hybrid Quantum Devices

Hybrid devices can be built using the technology developed in this thesis. The techniques developed are not limited to the devices shown in Chapters 6 and 7. In fact, there are many more devices one can envision. Some of these hybrid structures have already been built, such as a NV centre coupled efficiently to a tapered fibre [114] or a NV centre in an all-fibre cavity leading to an enhancement in photon emission by two orders of magnitude (see Figure 10.9 (a-c)) [250].

So far, the devices assembled only have one active emitter. For real applications and even more interesting physics, this number has to be increased. Setting aside the fact that current emitters have to be improved as discussed above, this will enable for fabrication of scalable integrated quantum circuits. Generally, increasing the number of emitters is not possible with random techniques like spin-coating or drop-casting, since here the probability to have all emitters at the right place scales in a very disadvantageous way. The pick-and-place approach as well as hybrid-material approach can easily be adapted to multi-emitter devices. In the pick-and-place technique, the process of placing a pre-characterised emitter just has to be repeated multiple times. In the hybrid material approach, either the pre-localisation technique as shown with the microantennas in Section 7.5.2 can be employed, or an approach for the in-situ localisation of the emitters can be used. With the same microscope as the laser-writing is performed, suitable emitters are searched in the material and when enough emitters and their positions are known, the multi-emitter structure is fabricated. In liquid photoresist, it may also be possible to trap the emitters in optical tweezers [353] and arrange them before polymerisation. Two possible structures which can be build are shown in Figure 10.9 (d) and (e).

Another ingredient in hybrid systems is plasmonics. In Section 8.2, interfacing a NV centre in nanodiamond with a plasmonic silver nanowire has been shown, however, this is only the first step. Using plasmonic nanofocussing (see Section 8.1.8), the coupling of emitters to guided modes can be greatly enhanced. Using the dielectric to plasmonic couplers designed in Section 8.3, the SPPs can subsequently be converted to photons and the other way round, the emitter can be excited very

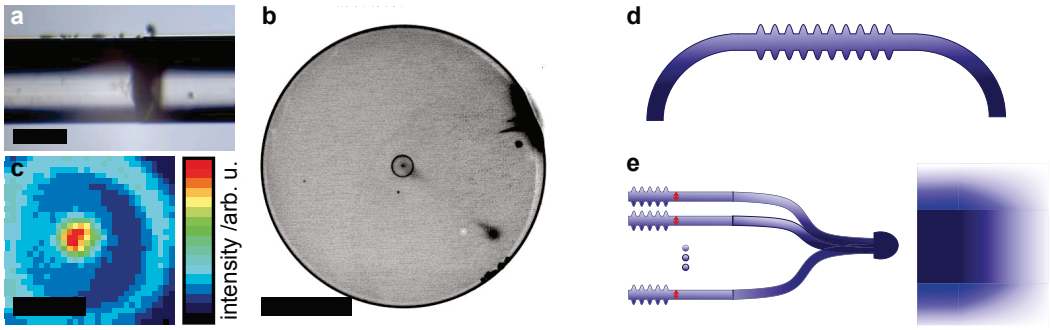

Figure 10.9.: Possible hybrid structures. (a) shows a micrograph of two fibres with concave mirrors fabricated on their facets. The fibres are aligned in a way to form a cavity. (b) shows one of the fibres facet, where a nanodiamond with a single NV centre is placed. The corresponding confocal microscope image can be seen in (c). This system allows for an enhancement of the NV centres transition in a controlled way by two orders of magnitude [250]. Scalebars in (a-c) are 80 µm, 40 µm, and 4 µm, respectively. (d,e) show two envisioned devices which can be produced using the hybrid material approach. (d) is a waveguide containing a Bragg grating and (e) shows a device that combines the emission of several single emitters (red) into efficiently into a multimode fibre (right). Such a device can be useful as an intensity standard in metrology. ((a,b,c) adapted from [250])

efficiently. First experiments to achieve this are carried out using the plasmon to dielectric coupler and dibenzoterrylene molecules.

10.2.3. Sensing and QEFLIM

With the technique of quantum emitter fluorescence lifetime imaging microscopy shown in Chapter 9, a new method for imaging at the nanoscale was introduced and its working principle confirmed. It is now straightforward to use this technique to image other plasmonic and non-plasmonic structures in order to optimise their design and fabrication processes. The technique can furthermore be used to search for buried structures via their effect on the LDOS, what can lead to applications for example in material science and biology. By performing QEFLIM measurements, it will be possible to sense marker particles buried under or even inside cell membranes.

Besides applying the technique directly, it is on one hand possible to extend the sensitivity and distinguish the magnetic part of the LDOS from the electrical one. This can be done easily by changing the emitter used for sensing from a NV centres to quantum dots [371] or rare earth doped crystals [372].

QEFLIM is based on measuring the lifetime of an emitter, which is a quantity

not used in other scanning probe methods. Therefore, QEFLIM can be combined with those other methods in a straightforward way. The NV centre, which is used in the presented implementation of QEFLIM, is known to be also a very good sensor for many quantities such as magnetic [126] and electric [127] fields as well as for temperature [129, 130]. The corresponding measurements are based on the NV centre's spin system (see Section 3.3) and can be read out simultaneously with QEFLIM. In this way, a new valuable functionality can be added to existing scanning probe microscopes.

In QEFLIM and other scanning probe techniques using quantum emitters, one problem is how to collect the photons. If the sample of interest is opaque, collection with an oil-immersion objective as in Chapter 9 is not possible. Usually, in this case photons are collected from the side. Due to these geometrical restrictions, only small numerical aperture optics can be used which drastically reduces the amount of photons collected. One way to circumvent this problem is provided by the directly fibre coupled single photon source introduced in Section 6.2. The emitter sitting at the very end of the fibre can be used as sensor and the photons carrying the information are directly collected. Recently, for magnetic sensing, a first implementation of this technique was reported using a large core multi-mode fibre and a bulk diamond crystal containing many NV centres [373]. Getting this to the single emitter level will enable for more controlled experiments, ultimately leading to a single photon fibre endoscope for precise measurements and imaging on the nanoscale.

A. List of Equipment Used in the Experiments

Here, a list of the important equipment and materials used in the different experiments is given. Many of the experiments were carried out on similar experimental setups or different versions of the same setup, so there is a large overlap. Note that in order to keep its size reasonable, this list does not contain standard items, e.g. cameras for imaging or the brand of standard AFM cantilevers used. If not stated otherwise, in all experiments where the following items are used, they are:

sample scanner:	PXY 80 D12, piezosystem jena
z-axis piezo-actuator:	MIPOS 100, piezosystem jena
grating spectrometer:	SpectraPro-500i, Acton
or very similar:	SpectraPro-2500i, Acton
spectrometer camera:	iDus, Andor
or very similar:	LN/CCD 1340/100 F, Roper Scientific
avalanche photodiodes:	SPCM-AQR-14, Perkin Elmer
or very similar:	SPCM-AQRH-14, Perkin Elmer
correlation electronics:	TimeHarp 200, PicoQuant
	Picoharp 300, PicoQuant
multi-function data acquisition:	PCI-6014, National Instruments
atomic force microscope:	NanoWizard, JPK Instruments
nanodiamonds:	MSY 0.05 GAF, Microdiamant AG

A.1. Equipment in Section 3.6.2

For the measurement of the ultra-fast spectral diffusion in nanodiamonds the following is used:

beam scanner:	Scanning Lenses
excitation laser:	LDH-P-FA-530, PicoQuant
	SuperK, Koheras
microscope objective:	100X Plan Apo HR, Mitutoyo
cryostat:	Konti Micro , Cryovac
avalanche photodiodes:	Count, Laser Components
nanodiamonds:	type Ib, provided by J. Wrachtrupp and F. Jelezko
solid immersion lenses	ZnO half sphere, Mikrop

A.2. Equipment in Section 5.3

The pick-and-place process for nanodiamonds is demonstrated using the following:

sample scanners:	PXY 80 D12, piezosystem jena
	PXY100 ID, piezosystem jena
microscope objectives:	UPlanSApo 60XO, Olympus
	PlanApo 60XO, Olympus
excitation laser:	LDH-P-FA-530, PicoQuant
avalanche photodiodes:	PDM Series, Micro Photon Devices
	SPCM-AQR-14, Perkin Elmer
AFM cantilevers:	Au or Pt/Ti coated, MicroMash

A.3. Equipment in Section 6.1

The zero phonon line enhancement of a nanodiamond in a photonic crystal cavity is done using:

microscope objective:	NA=0.9 M=100x, NIKON

A.4. Equipment in Section 6.2

The fibre integrated diamond based single photon source is built and characterized using:

microscope objectives:	NA=0.9 M=100x, NIKON
excitation laser:	Verdi V10 Coherent
	LDH-P-FA-530, PicoQuant
photonic crystal fibre:	NL-1.5-590, NKT Photonics

A.5. Equipment in Section 7.4

The experiment on laser written microstructures from a hybrid material uses:

sample scanner:	PXY 80 D12, piezosystem jena
laser scanner:	PXY100 ID, piezosystem jena
microscope objective:	UPlanSApo 60XO, Olympus
	NA=0.95 M=150x, Olympus
	NA=0.8 M=100x NIR, Olympus
excitation laser:	LDH-P-FA-530, PicoQuant
	GL532, SLOC Lasers
tunable laser:	Tunalbe Diode Laser 6312, Velocity

A.6. Equipment in Section 7.5

The items used for the experiment on the parabolic micro mirrors are:

microscope objectives:	UPlanSApo 60XO, Olympus
excitation laser:	GL532, SLOC Lasers
camera (back focal plane):	iXon, Andor

A.7. Equipment in Section 8.2

Single propagation surface plasmon polaritons on silver wires are measured and generated using:

microscope objective:	UPlanSApo 60XO, Olympus
excitation laser:	Verdi V10 Coherent
avalanche photodiodes:	PDM Series, Micro Photon Devices
silver wires:	provided by Plasma Chem

A.8. Equipment in Section 9.2

The following is used for probing the LDOS with a nanodiamond:

microscope objective:	UPlanSApo 60XO, Olympus
excitation laser:	LDH-P-FA-530, PicoQuant
avalanche photodiodes:	PDM Series, Micro Photon Devices

A.9. Equipment in Section 9.3

The experiment on quantum emitter fluorescence lifetime imaging uses the following:

microscope objective:	UPlanSApo 60XO, Olympus
glue:	poly-L-lysine
silver wires:	50 nm nominal diameter, Plasma Chem

B. Derivation of the Macroscopic Maxwell's Equations

A consistent derivation of the macroscopic Maxwell equations starting from the microscopic ones is given here. The microscopic Maxwell equations are given by [23]:

$$\nabla \cdot \mathbf{E} = \rho_m/\epsilon_0, \tag{B.1}$$

$$\nabla \cdot \mathbf{B} = 0, \tag{B.2}$$

$$\nabla \times \mathbf{E} = -\frac{\partial \mathbf{B}}{\partial t}, \tag{B.3}$$

$$\nabla \times \mathbf{B} = \mu_0 \mathbf{J_m} + \frac{\partial \mathbf{E}}{c^2 \partial t}, \tag{B.4}$$

with the electric field $\mathbf{E}$, magnetic field $\mathbf{B}$, microscopic charge density ρ_m, microscopic electric current $\mathbf{J_m}$, permittivity of vacuum ϵ_0, permeability of vacuum μ_0, and the speed of light $c = \sqrt{\frac{1}{\epsilon_0 \mu_0}}$.

To get the macroscopic Maxwell equations, a relationship between the microscopic quantities ρ_m and $\mathbf{J_m}$ and their macroscopic counterparts, ρ and $\mathbf{J}$, has to be established. Also two new fields, the electric displacement field $\mathbf{D}$ and the H-field $\mathbf{H}$ are defined, which account for polarisation $\mathbf{P}$ and magnetisation $\mathbf{M}$ in the following way:

$$\mathbf{D} = \epsilon_0 \mathbf{E} + \mathbf{P}, \tag{B.5}$$

$$\mathbf{B} = \mu_0 \mathbf{H} + \mu_0 \mathbf{M}. \tag{B.6}$$

Combining B.5 with B.1 and B.6 with B.4 yields:

$$\nabla \cdot \mathbf{D} = \sum \rho_m - \epsilon_0 \nabla \cdot \mathbf{P}, \tag{B.7}$$

$$\nabla \times \mathbf{H} = \mu_0 \sum \mathbf{J_m} + \frac{\epsilon_0 \partial \mathbf{E}}{\partial t} - \nabla \times \mathbf{M}. \tag{B.8}$$

It now would be convenient if parts of the sums over the microscopic quantities

cancel against the divergence term in B.7 and the rotation term in B.8. The relation linking σ and $\mathbf{J}$ is the continuity equation [209]:

$$\frac{\partial \rho}{\partial t} + \nabla \cdot \mathbf{J} = 0. \tag{B.9}$$

The sum over the microscopic currents is now split in three parts:

$$\sum \mathbf{J_m} = \mathbf{J_1} + \mathbf{J_2} + \mathbf{J_3}, \tag{B.10}$$

of which the third one $\mathbf{J_3}$ is required to cancel out the rotation of the magnetization:

$$\mathbf{J_3} = \nabla \times \mathbf{M}. \tag{B.11}$$

By looking at the continuity equation B.9 one can find that this term is not connected to a change of the charge ρ, since the divergence of a rotation is zero. The divergence term in Equation B.7 can be eliminated in similar manner. The sum over the microscopic charges is split in two parts:

$$\sum \rho_m = \rho_1 + \rho_2, \tag{B.12}$$

of which the second part can be chosen to cancel out the divergence of the polarization:

$$\rho_2 = \epsilon_0 \nabla \cdot \mathbf{P}. \tag{B.13}$$

Via the continuity Equation B.9, this choice leads to a current:

$$\frac{\partial \rho_2}{\partial t} = \epsilon_0 \nabla \cdot \frac{\partial \mathbf{P}}{\partial t} = \nabla \cdot \mathbf{J}' = \nabla \cdot \mathbf{J_2}. \tag{B.14}$$

In the last step, the current is identified with $\mathbf{J_2}$ of equation B.10, what leads to:

$$\mathbf{J_2} = \frac{\partial \mathbf{P}}{\partial t}. \tag{B.15}$$

After this, the macroscopic Maxwell equations take the following, well known, form:

$$\nabla \cdot \mathbf{D} = \rho, \tag{B.16}$$

$$\nabla \cdot \mathbf{B} = 0, \tag{B.17}$$

$$\nabla \times \mathbf{E} = -\frac{\partial \mathbf{B}}{\partial t}, \tag{B.18}$$

$$\nabla \times \mathbf{H} = \mathbf{J} + \frac{\partial \mathbf{D}}{\partial t}. \tag{B.19}$$

Note that this form was reached starting from the microscopic equations just by performing two at first arbitrary divisions of microscopic currents (equation B.10) and charges (Equation B.12), which later were used to cancel out specific terms mathematically in a convenient way. Nevertheless, the different terms of this division can be interpreted physically meaningful. ρ_1 and $\mathbf{J_1}$ correspond to charges and currents not absorbed in the transition from the microscopic to macroscopic equations, i.e., free charges and currents, not bound to any material property. The charges ρ_2 are the sources of polarization while the currents $\mathbf{J_2}$ are currents associated with polarization changes. Finally, the currents $\mathbf{J_3}$ represent eddy currents, they do not give rise to a charge transfer but are responsible for magnetization.

C. Finite Difference Time Domain Calculations

Maxwell's equations (Equations 8.1-8.4) are only analytically solvable in special cases. Therefore, different numerical techniques have been established. Here, the finite difference time domain (FDTD) [374] method, which is used in Sections 6.1, 6.2 and 8.3, is introduced.

In the FDTD method, in the macroscopic curl Maxwell's equations:

$$\nabla \times \mathbf{E} = -\frac{\partial \mathbf{B}}{\partial t}, \tag{C.1}$$

$$\nabla \times \mathbf{H} = \mathbf{J} + \frac{\partial \mathbf{D}}{\partial t}, \tag{C.2}$$

the time derivatives are substituted by finite differences according to:

$$\frac{\partial F(\xi)}{\partial \xi} \longrightarrow F_x = \frac{F(\xi + \frac{\Delta\xi}{2}) - F(\xi - \frac{\Delta\xi}{2})}{\Delta\xi}, \tag{C.3}$$

where F is a function (a field component of E- or H-field) and ξ is a variable (either t for time derivatives or x, y, z in for derivatives in Cartesian space). The resulting set of equations is evaluated for finite time steps $\Delta t = \frac{t}{n}$, where t is time and n is the step number.

To evaluate the resulting equations, grids in space and time need to be defined. Usually, electric and magnetic field are stored at different locations and times. Ideally, the chosen geometry should take into account the form of the curl Maxwell's equations. The most common implementation is the so called Yee cell [375] for the spatial coordinates and a leap frog scheme for the time domain (see Figure C.1).

One advantages of FDTD algorithms is that they are conceptually simple, since they directly discretise Maxwell's equations. They directly calculate the time evolution of a given problem and are therefore very useful when interested in the time evolution of fields. Their mesh can be applied to any geometry, but with the risk of staircasing effects due to the cubic mesh cells used in FDTD (see Figure C.1 (a)). One disadvantage here is that the mesh can not be adapted to the geometry, so much computation power is used to calculate the fields in regions, where not much is happening.

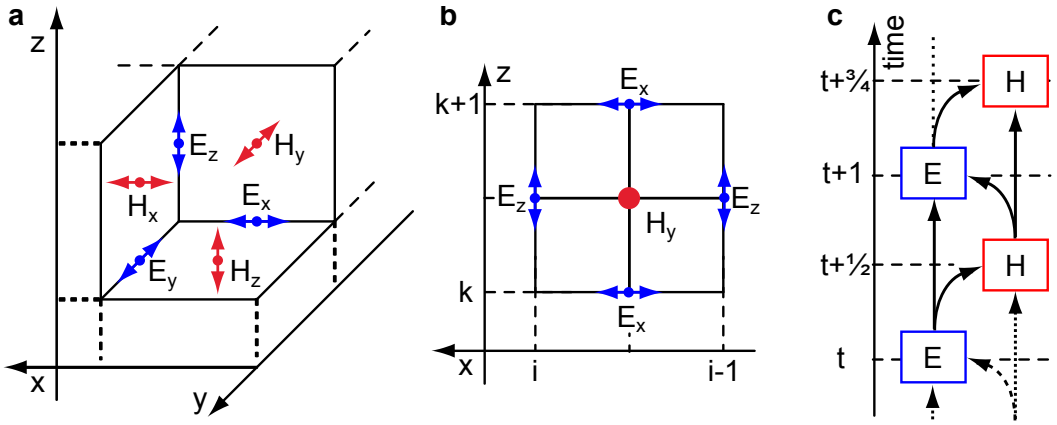

Figure C.1.: Yee cell and leap frog algorithm. (a) shows the Yee cell. Different components of electric and magnetic field are calculated at different positions in order to map the mathematical structure of Maxwell's equations. This is shown in (b), where it can be seen that the magnetic field H_y is generated by the adjacent electric field components E_x and E_z. (c) shows the leap frog style propagation of the fields in time. The E-(H)-fields at $t+1$ are calculated using the E-(H)-fields at time t and the H-(E)-fields at time $t+\frac{1}{2}$. (Panel (a) adapted from [376])

Alternatives to FDTD where the mesh can be chosen according to the actual geometry are algorithms using the finite element method (FEM) [327], or discontinuous Galerkin time-domain (DGTD) [366, 367] methods.

D. Background Correction Applied in Section 7.4.3

When performing a background correction on antibunching curves, it is very important to be careful to not adulterate the data. Here, e a short derivation of the background correction used for the antibunching in Figure 7.8 is given.

In the case of continuous excitation of an emitter with intensity $< n_a >= a$, second order correlation functions $g_a^{(2)}$, and the quantum mechanically uncorrelated background of the intensity $< n_b >= b$ with $g_b^{(2)} = 1$, the joint second order correlation function is given by:

$$g_{ab}^{(2)} = \frac{a^2 g_a^{(2)} + b^2 + 2ab}{(a+b)^2}. \tag{D.1}$$

By knowing the intensities a and b one can calculate the $g_a^{(2)}$ function of the bare emitter a from a measurement of the joint correlation function $g_{ab}^{(2)}$.

In case of pulsed excitation, this background correction is more complicated, since the emission of emitter and background are correlated by the excitation laser. This problem can be avoided by only looking at time intervals corresponding to one laser period. In the analysis of an experiment's $g^{(2)}$-data acquired with a Hanbury Brown and Twiss setup, this can be achieved by binning together all events in the time windows $T_{\frac{max}{min}} = n\Delta T \pm \frac{\Delta T}{2}$, with the laser repetition time ΔT (= 25 ns in this experiment) and n being an integer.

Figure D.1 (a) and (b) show the normalised coincidence counts measured with pulsed excitation at the location of a NV centre at the resonator's rim (in (a)) and at a location without a NV centre next to it also on the rim (in (b)), respectively. Thus the data in Figure D.1 (a) corresponds to coincidences from signal and background whereas Figure D.1 (b) represents the background coincidences only. Binning to intervals of 1.28 ns is performed for better visibility. Normalisation is done by averaging for long times (>1.3 µs over 256 periods), where contributions from the NV centre's bunching behaviour are negligible. Also, the photons missed in an HBT like start-stop configuration are taken into account. A comparison of the background photons rate with the intensity of the combined signal gave $a = \frac{1}{3}$ and $b = \frac{2}{3}$, equivalent to a background to signal ratio of 2. Figure D.1 (c) shows the resulting corrected $g^{(2)}(\tau)$ function, with bins sizes corresponding to the laser

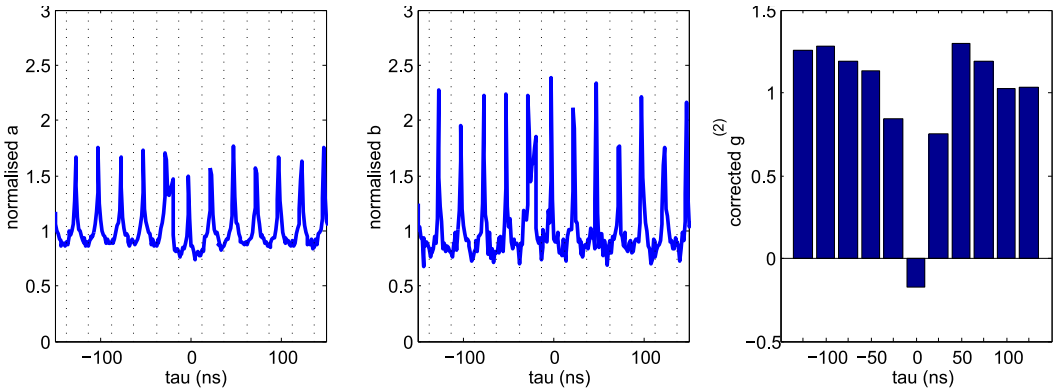

Figure D.1.: Data used for the background correction. (a) and (b) are normalised coincidence counts measured with pulsed excitation at the location of a NV centre at the resonator's rim (in (a)) and at a location without a NV centre next to it also on the rim (in (b)), respectively. Both are normalised to an average of one at long times >1.3 µs over 256 periods). A binsize of 1.28 ns is used. The dotted lines show the bins, which are used to obtain (c). (c) shows the resulting antibunching with a $g^{(2)}(0) = -0.18 \pm 0.21$. (Figure source: [177])

repetition time.

For zero time delay $g^{(2)}(0) = -0.18$. The error bar for this value stems from three contributions, with the main contribution originating from the uncertainties in the ratio $\frac{b}{a}$, which we assumed to be 10 % ($\frac{b}{a} = 2.0 \pm 0.2$). This error is due to the fact that background and signal were measured at neighbouring positions on the resonator's rim, but not at the same one. The other two contributions are the statistical variations in the photon number for the zero time delay bin, which were both assumed to be Possonian ($\Delta(a) = 0.01$ and $\Delta(b) = 0.07$). This results in an error of $\Delta(g^{(2)}(0)) = 0.21$ after adding the contributions via Gaussian error propagation.

E. Dipole Approximation of a QEFLIM Probe

In QEFLIM (see Section 9.3), information on the LDOS is obtained by measuring the lifetime of an emitter at different positions in a scanning fashion. To enable for this scanning, the emitter is glued to the blunted tip of an atomic force microscope (see Section 5). For a quantitative and reliable measurement, it is important to know the influence the tip has on the emitter. In the following, it is shown for the case of a single NV centre as probe, that a probe consisting of emitter and tip can be viewed as an effective emitter. For this, the analytical theory for an emitter over a dielectric interface [185, 338] is compared with discontinuous Galerkin time-domain calculations [366, 367]. More details on the simulations can be found in the supplementary information of [186].

When working with NV centres in nanodiamonds (see Section 3.4), the quantum yield of the emitter is not unity and can vary widely [109]. For this reason, Equation 9.15 has to be modified taking into account the quantum yield [185]:

$$\frac{\gamma_i}{\gamma_0} = 1 + QY \cdot \mathcal{F} \frac{1}{\omega^3} \mathrm{Im}[\mathbf{d}_i^* \cdot \mathbf{E}_s(\mathbf{r}_0)], \tag{E.1}$$

with the emitter's quantum yield $QY = \frac{\gamma_{\mathrm{r},0}}{\gamma_{\mathrm{r},0}+\gamma_{\mathrm{nr},0}}$, the emitter's dipole $\mathbf{d}_i$, its frequency ω, its decay rate γ_i, and its free space decay rate γ_0. The factor $\mathcal{F}$ is used to subsume all other constants. It can be derived from numerical calculations using the relation [377]:

$$\frac{\gamma_i}{\gamma_0} = \frac{P}{P_0}, \tag{E.2}$$

which links the decay rates of the emitter with the dissipated energy P and the free space dissipated energy P_0. Since a NV centre has two transition dipoles (see Section 3), both transition rates have to be added. This is done assuming incoherent coupling:

$$\gamma = \gamma_1 + \gamma_2. \tag{E.3}$$

To model the spectral properties of the NV centre, its room temperature spectrum (see Figure 3.2 (c)) is approximated by a Gaussian with a central wavelength of $\lambda_0 = 700$ nm and a width of $\sigma = 50$ nm.

In the numerical calculations, the tip is modelled as a truncated cone with an

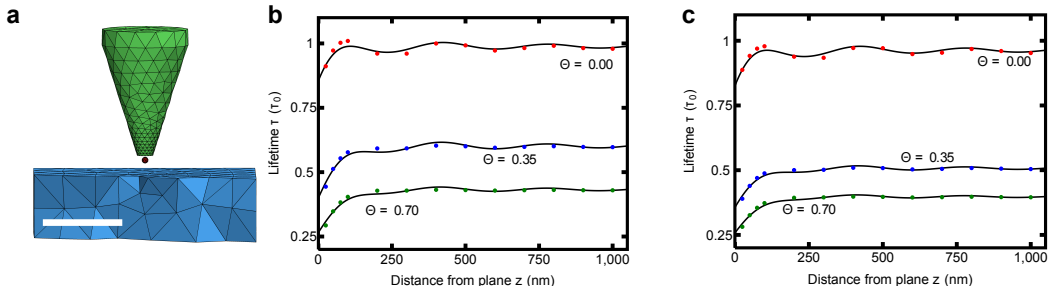

Figure E.1.: Comparison of analytical and numerical calculation. (a) shows the geometry used in the DGTD calculations performed in order to show that the probe can be approximated by an effective emitter for the symmetric case. The distance of the probe to the substrate (refractive index $n \approx 1.5$) is varied. In the asymmetric case, the emitter at the tip is offset to one side by a distance of 30 nm. The results are show in (b) and (c) as dots for the symmetric and asymmetric case, respectively. The black lines are fits to the analytical theory without the tip present. The good agreement indicates that the probe can be approximated by an effective emitter. Scalebar in (a) is 500 nm. (Figure adapted from: [186])

aperture angle of 17.65°. It has a radius of 50 nm at the height where it is truncated and its length in the calculations is 800 nm. A sketches of tip and dipole used in the numerical calculations carried out to show that the probe can be approximated by an effective emitter is shown in Figure E.1 (a).

In order to describe the tip and NV centre as an effective emitter, an effective quantum yield QY_{eff} and an effective orientation are introduced. For this, the total decay rate is written as:

$$\gamma_i = \gamma_{\text{nr}} + \gamma_{\text{r},0} + \gamma_{\text{Tip-Sample}}, \tag{E.4}$$

with the non-radiative decay rate γ_{nr}, the uncoupled radiative decay rate $\gamma_{\text{r},0}$, and the additional decay due to tip-sample interaction $\gamma_{\text{Tip-Sample}}$. It is further assumes that the non-radiative decay rate γ_{nr} is independent on the interaction with the environment $\gamma_{\text{nr}} = \gamma_{\text{nr},0}$ and that $\gamma_{\text{Tip-Sample}}$ can be written as $\gamma_{\text{Tip-Sample}} = \gamma_{\text{Tip}} + \gamma_{\text{Sample}}$, neglecting coupling of the contributions due to coupling of tip and sample.

Inserting this into Equation E.1 and adding contributions of two dipoles leads to (for details see supplementary information of [186]):

$$\frac{\gamma}{\gamma_{0,\text{eff}}} = \frac{1}{\mathcal{T}_{\mathbf{d}_1,\mathbf{d}_2}} \left\{ \frac{1}{QY_{\text{eff}}} + \mathcal{F}\frac{1}{\omega^3}\text{Im}[\mathbf{d}_1^* \cdot \mathbf{E}_s(\mathbf{r}_0)] + \mathcal{F}\frac{1}{\omega^3}\text{Im}[\mathbf{d}_2^* \cdot \mathbf{E}_s(\mathbf{r}_0)] \right\}. \tag{E.5}$$

This equation relates the decay rate γ to the effective decay rate of the probe $\gamma_{0,\text{eff}}$. This means, that with the effective quantum yield for two dipoles QY_{eff} with $\frac{1}{QY_{\text{eff}}} = \frac{1}{QY_{\text{eff},1}} + \frac{1}{QY_{\text{eff},2}}$ and the factor $\mathcal{T}_{\mathbf{d}_1,\mathbf{d}_2}$, which compensates for different coupling strengths of the two dipoles to the tip, the probe can be described as an effective probe. The factor $\mathcal{T}_{\mathbf{d}_1,\mathbf{d}_2}$ is defined via [186]:

$$\gamma_{0,\text{eff}} = 2 \cdot (\gamma_{\text{r},0} + \gamma_{\text{nr},0}) + \gamma_{\text{Tip},\mathbf{d}_1} + \gamma_{\text{Tip},\mathbf{d}_2} \equiv \mathcal{T}_{\mathbf{d}_1,\mathbf{d}_2}\gamma_{r,0}. \tag{E.6}$$

The possibility to describe the probe in QEFLIM as an effective probe greatly simplifies the computations needed to describe the experiments. For the numerical calculations in Figures 9.6 and 9.7, the probe consisting of AFM tip and NV centre in nanodiamond is approximated as two incoherently coupled dipoles giving a high degree of agreement.

Abbreviations

2D	two-dimensional
3D	three-dimensional
AFM	atomic force microscope
APD	avalanche photodiode
BASD	bead assisted sonic disintegration
cf.	confer
cts	counts
CCD	charge coupled device
DGTD	discontinuous Galerkin time-domain
DLW	direct laser-writing
EELS	electron energy loss spectroscopy
e.g.	exempli gratia (for example)
EMCCD	electron multiplying CCD
et al.	et alii (and others)
etc.	et cetera (and so forth)
eSIL	elliptical SIL
i.e.	id est (that is)
fcc	face centred cubic
FDTD	finite difference time domain
FEM	finite elements method
FLIM	fluorescence lifetime imaging microscopy
FWHM	full width half maximum
HBT	Hanbury Brown and Twiss
HOM	Hong-Ou-Mandel
HPHT	high-pressure high-temperature
ISC	inter-system-crossing
LDOS	local density of optical states
LOQC	linear optics quantum computing
NA	numerical aperture
NV centre	nitrogen vacancy centre
ODMR	optically detected magnetic resonance
PETTA	pentaerythritol tetraacrylate
PCC	photonic crystal cavity
PID	proportional-integral-derivative

PMT	photomultiplier tube
PSF	point spread function
PVA	polyvinyl alcohol
Q factor	quality factor
qbit	quantum bit
QEFLIM	quantum emitter fluorescence lifetime imaging microscopy
RWA	rotating wave approximation
SEM	scanning electron microscope
SIL	solid immersion lens
SiV centre	silicon vacancy centre
SPP	surface plasmon polariton
TCSPC	time correlated single photon counting
TE	transverse electric
TM	transverse magnetic
TTTCSPC	time tagged TCSPC
TTTR	time tagged time resolved
WGM	whispering gallery mode
ZPL	zero phonon line

Bibliography

[1] M. A. Nielsen and I. L. Chuang. *Quantum computation and quantum information*. Cambridge university press, 2010.

[2] H.-K. Lo, M. Curty, and K. Tamaki. Secure quantum key distribution. *Nature Photonics*, 8(8):595–604, 2014.

[3] W. K. Wootters and W. H. Zurek. A single quantum cannot be cloned. *Nature*, 299(5886):802–803, 1982.

[4] D.G.B.J. Dieks. Communication by EPR devices. *Physics Letters A*, 92(6): 271–272, 1982.

[5] A. Steane. Quantum computing. *Reports on Progress in Physics*, 61(2):117, 1998.

[6] T. D. Ladd, F. Jelezko, R. Laflamme, Y. Nakamura, C. Monroe, and J. L. O'Brien. Quantum computers. *Nature*, 464(7285):45–53, 2010.

[7] J. L. O'Brien. Optical quantum computing. *Science*, 318(5856):1567–1570, 2007.

[8] M. T. Jaekel and S. Reynaud. Quantum limits in interferometric measurements. *EPL (Europhysics Letters)*, 13(4):301, 1990.

[9] V. Giovannetti, S. Lloyd, and L. Maccone. Quantum-enhanced measurements: Beating the standard quantum limit. *Science*, 306(5700):1330–1336, 2004.

[10] V. Giovannetti, S. Lloyd, and L. Maccone. Advances in quantum metrology. *Nature Photonics*, 5(4):222–229, 2011.

[11] D. F. Walls. Squeezed states of light. *Nature*, 306(5939):141–146, 1983.

[12] R. E. Slusher, L. W. Hollberg, B. Yurke, J. C. Mertz, and J. F. Valley. Observation of squeezed states generated by four-wave mixing in an optical cavity. *Physical Review Letters*, 55:2409–2412, 1985.

[13] C. Gerry and P. Knight. *Introductory quantum optics*. Cambridge university press, 2005.

[14] T. Ono, R. Okamoto, and S. Takeuchi. An entanglement-enhanced microscope. *Nature Communications*, 4:2426, 2013.

[15] J. Aasi, J. Abadie, B. P. Abbott, R. Abbott, T. D. Abbott, M. R. Abernathy, C. Adams, T. Adams, P. Addesso, R. X. Adhikari, C. Affeldt, O. D. Aguiar, P. Ajith, B. Allen, E. Amador Ceron, D. Amariutei, S. B. Anderson, W. G. Anderson, K. Arai, M. C. Araya, C. Arceneaux, S. Ast, S. M. Aston, D. Atkinson, P. Aufmuth, C. Aulbert, L. Austin, B. E. Aylott, S. Babak, P. T. Baker, S. Ballmer, Y. Bao, J. C. Barayoga, D. Barker, B. Barr, L. Barsotti, M. A. Barton, I. Bartos, R. Bassiri, J. Batch, J. Bauchrowitz, B. Behnke, A. S. Bell, C. Bell, G. Bergmann, J. M. Berliner, A. Bertolini, J. Betzwieser, N. Beveridge, P. T. Beyersdorf, T. Bhadbhade, I. A. Bilenko, G. Billingsley, J. Birch, S. Biscans, E. Black, J. K. Blackburn, L. Blackburn, D. Blair, B. Bland, O. Bock, T. P. Bodiya, C. Bogan, C. Bond, R. Bork, M. Born, S. Bose, J. Bowers, P. R. Brady, V. B. Braginsky, J. E. Brau, J. Breyer, D. O. Bridges, M. Brinkmann, M. Britzger, A. F. Brooks, D. A. Brown, D. D. Brown, K. Buckland, F. Brückner, B. C. Buchler, A. Buonanno, J. Burguet-Castell, R. L. Byer, L. Cadonati, J. B. Camp, P. Campsie, K. Cannon, J. Cao, C. D. Capano, L. Carbone, S. Caride, A. D. Castiglia, S. Caudill, M. Cavaglià, C. Cepeda, T. Chalermsongsak, S. Chao, P. Charlton, X. Chen, Y. Chen, H-S. Cho, J. H. Chow, N. Christensen, Q. Chu, S. S. Y Chua, C. T. Y. Chung, G. Ciani, F. Clara, D. E. Clark, J. A. Clark, M. Constancio Junior, D. Cook, T. R. Corbitt, M. Cordier, N. Cornish, A. Corsi, C. A. Costa, M. W. Coughlin, S. Countryman, P. Couvares, D. M. Coward, M. Cowart, D. C. Coyne, K. Craig, J. D. E. Creighton, T. D. Creighton, A. Cumming, L. Cunningham, K. Dahl, M. Damjanic, S. L. Danilishin, K. Danzmann, B. Daudert, H. Daveloza, G. S. Davies, E. J. Daw, T. Dayanga, E. Deleeuw, T. Denker, T. Dent, V. Dergachev, R. DeRosa, R. DeSalvo, S. Dhurandhar, I. Di Palma, M. Díaz, A. Dietz, F. Donovan, K. L. Dooley, S. Doravari, S. Drasco, R. W. P. Drever, J. C. Driggers, Z. Du, J-C. Dumas, S. Dwyer, T. Eberle, M. Edwards, A. Effler, P. Ehrens, S. S. Eikenberry, R. Engel, R. Essick, T. Etzel, K. Evans, M. Evans, T. Evans, M. Factourovich, S. Fairhurst, Q. Fang, B. F. Farr, W. Farr, M. Favata, D. Fazi, H. Fehrmann, D. Feldbaum, L. S. Finn, R. P. Fisher, S. Foley, E. Forsi, N. Fotopoulos, M. Frede, M. A. Frei, Z. Frei, A. Freise, R. Frey, T. T. Fricke, D. Friedrich, P. Fritschel, V. V. Frolov, M-K. Fujimoto, P. J. Fulda, M. Fyffe, J. Gair, J. Garcia, N. Gehrels, G. Gelencser, L. Á. Gergely, S. Ghosh, J. A. Giaime, S. Giampanis, K. D. Giardina, S. Gil-Casanova, C. Gill, J. Gleason, E. Goetz, G. González, N. Gordon, M. L. Gorodetsky, S. Gossan, S. Goßler, C. Graef, P. B. Graff, A. Grant, S. Gras, C. Gray, R. J. S. Greenhalgh, A. M. Gretarsson, C. Griffo, H. Grote, K. Grover, S. Grunewald, C. Guido, E. K. Gustafson, R. Gustafson, D. Ham-

mer, G. Hammond, J. Hanks, C. Hanna, J. Hanson, K. Haris, J. Harms, G. M. Harry, I. W. Harry, E. D. Harstad, M. T. Hartman, K. Haughian, K. Hayama, J. Heefner, M. C. Heintze, M. A. Hendry, I. S. Heng, A. W. Heptonstall, M. Heurs, M. Hewitson, S. Hild, D. Hoak, K. A. Hodge, K. Holt, M. Holtrop, T. Hong, S. Hooper, J. Hough, E. J. Howell, V. Huang, E. A. Huerta, B. Hughey, S. H. Huttner, M. Huynh, T. Huynh-Dinh, D. R. Ingram, R. Inta, T. Isogai, A. Ivanov, B. R. Iyer, K. Izumi, M. Jacobson, E. James, H. Jang, Y. J. Jang, E. Jesse, W. W. Johnson, D. Jones, D. I. Jones, R. Jones, L. Ju, P. Kalmus, V. Kalogera, S. Kandhasamy, G. Kang, J. B. Kanner, R. Kasturi, E. Katsavounidis, W. Katzman, H. Kaufer, K. Kawabe, S. Kawamura, F. Kawazoe, D. Keitel, D. B. Kelley, W. Kells, D. G. Keppel, A. Khalaidovski, F. Y. Khalili, E. A. Khazanov, B. K. Kim, C. Kim, K. Kim, N. Kim, Y-M. Kim, P. J. King, D. L. Kinzel, J. S. Kissel, S. Klimenko, J. Kline, K. Kokeyama, V. Kondrashov, S. Koranda, W. Z. Korth, D. Kozak, C. Kozameh, A. Kremin, V. Kringel, B. Krishnan, C. Kucharczyk, G. Kuehn, P. Kumar, R. Kumar, B. J. Kuper, R. Kurdyumov, P. Kwee, P. K. Lam, M. Landry, B. Lantz, P. D. Lasky, C. Lawrie, A. Lazzarini, A. Le Roux, P. Leaci, C-H. Lee, H. K. Lee, H. M. Lee, J. Lee, J. R. Leong, B. Levine, V. Lhuillier, A. C. Lin, V. Litvine, Y. Liu, Z. Liu, N. A. Lockerbie, D. Lodhia, K. Loew, J. Logue, A. L. Lombardi, M. Lormand, J. Lough, M. Lubinski, H. Lück, A. P. Lundgren, J. Macarthur, E. Macdonald, B. Machenschalk, M. MacInnis, D. M. Macleod, F. Magaña-Sandoval, M. Mageswaran, K. Mailand, G. Manca, I. Mandel, V. Mandic, S. Márka, Z. Márka, A. S. Markosyan, E. Maros, I. W. Martin, R. M. Martin, D. Martinov, J. N. Marx, K. Mason, F. Matichard, L. Matone, R. A. Matzner, N. Mavalvala, G. May, G. Mazzolo, K. McAuley, R. McCarthy, D. E. McClelland, S. C. McGuire, G. McIntyre, J. McIver, G. D. Meadors, M. Mehmet, T. Meier, A. Melatos, G. Mendell, R. A. Mercer, S. Meshkov, C. Messenger, M. S. Meyer, H. Miao, J. Miller, C. M. F. Mingarelli, S. Mitra, V. P. Mitrofanov, G. Mitselmakher, R. Mittleman, B. Moe, F. Mokler, S. R. P. Mohapatra, D. Moraru, G. Moreno, T. Mori, S. R. Enhanced sensitivity of the ligo gravitational wave detector by using squeezed states of light. *Nature Photonics*, 7(8):613–619, 2013.

[16] A. M. Zagoskin. Quantum engineering. *Quantum Engineering, by AM Zagoskin, Cambridge, UK: Cambridge University Press, 2011*, 1, 2011.

[17] M. O. Scully. Quantum photocell: Using quantum coherence to reduce radiative recombination and increase efficiency. *Physical Review Letters*, 104: 207701, 2010.

[18] M. Planck. Zur Theorie des Gesetzes der Energieverteilung im Normalspec-

trum. *Deutsche Physikalische Gesellschaft. Verhandlungen*, 2(17):237245, 1900.

[19] A. Einstein. Uber einen die Erzeugung und Verwandlung des Lichtes betreffenden heuristischen Gesichtspunkt. *Annalen der Physik*, 322(6):132–148, 1905.

[20] G. N. Lewis. The Conservation of Photons. *Nature*, 118:874–875, 1926.

[21] R. Loudon. *The quantum theory of light. 3rd edition*. Oxford University Press, 2000.

[22] P. Meystre and M. Sargent. *Elements of quantum optics*, volume 4. Springer, 2010.

[23] J. D. Jackson. *Classical Electrodynamics, 3rd Edition*. 1998.

[24] L. D. Landau and E. M. Lifschitz. *Lehrbuch der theoretischen Physik: Mechanik*. Akademie Verlag Berlin, 1990.

[25] J. J. Sakurai and S. F. Tuan. *Modern quantum mechanics*, volume 1. Addison-Wesley Reading, Massachusetts, 1985.

[26] D. F Walls and G. J Milburn. *Quantum optics*. Springer, 1995.

[27] M. O. Scully and M. S. Zubairy. *Quantum Optics*. Cambridge University Press, 1997.

[28] A. Kavokin, J. J. Baumberg, G. Malpuech, and F. P. Laussy. *Microcavities*. Series on Semiconductor Science and Technology. OUP Oxford, 2011.

[29] J. Wolters. *Integrated Quantum Hybrid Systems*. Pan Stanford Publishing, 2015.

[30] E. M. Purcell. Spontaneous emission probabilities at radio frequencies. volume 69, pages 681+, 1946.

[31] Z.-Y. J. Ou. *Multi-photon quantum interference*. Springer, 2007.

[32] C. K. Hong, Z. Y. Ou, and L. Mandel. Measurement of subpicosecond time intervals between two photons by interference. *Physical Review Letters*, 59: 2044–2046, 1987.

[33] P. Kok, W. J. Munro, K. Nemoto, T. C. Ralph, J. P. Dowling, and G. J. Milburn. Linear optical quantum computing with photonic qubits. *Review of Modern Physics*, 79:135–174, 2007.

[34] E. Knill, R. Laflamme, and G. J. Milburn. A scheme for efficient quantum computation with linear optics. *Nature*, 409(6816):46–52, 2001.

[35] H. Bernien, B. Hensen, W. Pfaff, G. Koolstra, M. S. Blok, L. Robledo, T. H. Taminiau, M. Markham, D. J. Twitchen, L. Childress, and R. Hanson. Heralded entanglement between solid-state qubits separated by three metres. *Nature*, 497(7447):86–90, 2013.

[36] D. C. Burnham and D. L. Weinberg. Observation of simultaneity in parametric production of optical photon pairs. *Physical Review Letters*, 25:84–87, 1970.

[37] M. Wahl, T. Röhlicke, H.-J. Rahn, R. Erdmann, G. Kell, A. Ahlrichs, M. Kernbach, A. W. Schell, and O. Benson. Integrated multichannel photon timing instrument with very short dead time and high throughput. *Review of Scientific Instruments*, 84(4):043102, 2013.

[38] H. J. Kimble. The quantum internet. *Nature*, 453(7198):1023–1030, 2008.

[39] A. J. Bennett, R. B. Patel, C. A. Nicoll, D. A. Ritchie, and A. J. Shields. Interference of dissimilar photon sources. *Nature Physics*, 5(10):715–717, 2009.

[40] S. V. Polyakov, A. Muller, E. B. Flagg, A Ling, N Borjemscaia, E Van Keuren, A Migdall, and G S. Solomon. Coalescence of single photons emitted by disparate single-photon sources: The example of inas quantum dots and parametric down-conversion sources. *Physical Review Letters*, 107:157402, 2011.

[41] R. H. Hadfield. Single-photon detectors for optical quantum information applications. *Nature Photonics*, 3(12):696–705, 2009.

[42] W. Becker. *Advanced time-correlated single photon counting techniques*. Springer, 2005.

[43] R. Q. Twiss R. Hanbury Brown. A Test of a New Type of Stellar Interferometer on Sirius. *Nature*, 178:1046–1048, 1956.

[44] C. K. Hong and L. Mandel. Experimental realization of a localized one-photon state. *Physical Review Letters*, 56:58–60, 1986.

[45] J. Kim, O. Benson, H. Kan, and Y. Yamamoto. A single-photon turnstile device. *Nature*, 397(6719):500–503, 1999.

[46] B. Lounis and M. Orrit. Single-photon sources. *Reports on Progress in Physics*, 68(5):1129, 2005.

[47] M. D. Eisaman, J. Fan, A. Migdall, and S. V. Polyakov. Invited review article: Single-photon sources and detectors. *Review of Scientific Instruments*, 82(7): 071101, 2011.

[48] H. J. Kimble, M. Dagenais, and L. Mandel. Photon antibunching in resonance fluorescence. *Physical Review Letters*, 39:691–695, 1977.

[49] A. Kuhn, M. Hennrich, and G. Rempe. Deterministic single-photon source for distributed quantum networking. *Physical Review Letters*, 89:067901, 2002.

[50] D. J. Wineland, R. E. Drullinger, and F. L. Walls. Radiation-Pressure Cooling of Bound Resonant Absorbers. *Physical Review Letters*, 40:1639–1642, 1978.

[51] W. Neuhauser, M. Hohenstatt, P. Toschek, and H. Dehmelt. Optical-Sideband Cooling of Visible Atom Cloud Confined in Parabolic Well. *Physical Review Letters*, 41:233–236, 1978.

[52] E. L. Raab, M. Prentiss, A. Cable, S. Chu, and D. E. Pritchard. Trapping of neutral sodium atoms with radiation pressure. *Physical Review Letters*, 59: 2631–2634, 1987.

[53] S. Chu, J. E. Bjorkholm, A. Ashkin, and A. Cable. Experimental observation of optically trapped atoms. *Physical Review Letters*, 57:314–317, 1986.

[54] N. Schlosser, G. Reymond, I. Protsenko, and P. Grangier. Sub-poissonian loading of single atoms in a microscopic dipole trap. *Nature*, 411(6841):1024–1027, 2001.

[55] M. Weber, J. Volz, K. Saucke, C. Kurtsiefer, and H. Weinfurter. Analysis of a single-atom dipole trap. *Physical Review A*, 73:043406, 2006.

[56] T. Legero, T. Wilk, M. Hennrich, G. Rempe, and A. Kuhn. Quantum beat of two single photons. *Physical Review Letters*, 93:070503, 2004.

[57] F. Diedrich and H. Walther. Nonclassical radiation of a single stored ion. *Physical Review Letters*, 58:203–206, 1987.

[58] D. Stick, W. K. Hensinger, S. Olmschenk, M. J. Madsen, K. Schwab, and C. Monroe. Ion trap in a semiconductor chip. *Nature Physics*, 2(1):36–39, 2006.

[59] B. Lounis and W. E. Moerner. Single photons on demand from a single molecule at room temperature. *Nature*, 407(6803):491–493, 2000.

[60] Th. Basché, W. E. Moerner, M. Orrit, and H. Talon. Photon antibunching in the fluorescence of a single dye molecule trapped in a solid. *Physical Review Letters*, 69:1516–1519, 1992.

[61] L. Fleury, J.-M. Segura, G. Zumofen, B. Hecht, and U. P. Wild. Nonclassical photon statistics in single-molecule fluorescence at room temperature. *Physical Review Letters*, 84:1148–1151, 2000.

[62] P. Kask, P. Piksarv, and Ü. Mets. Fluorescence correlation spectroscopy in the nanosecond time range: Photon antibunching in dye fluorescence. *European Biophysics Journal*, 12(3):163–166, 1985.

[63] G. Wrigge, I. Gerhardt, J. Hwang, G. Zumofen, and V. Sandoghdar. Efficient coupling of photons to a single molecule and the observation of its resonance fluorescence. *Nature Physics*, 4(1):60–66, 2008.

[64] W. E. Moerner and M. Orrit. Illuminating single molecules in condensed matter. *Science*, 283(5408):1670–1676, 1999.

[65] F. W. Wise. Lead salt quantum dots: the limit of strong quantum confinement. *Acc. Chem. Res.*, 33(11):773–780, 2000.

[66] S. V. Gaponenko. *Optical Properties of Semiconductor Nanocrystals*. 1998.

[67] T. Takagahara. Biexciton states in semiconductor quantum dots and their nonlinear optical properties. *Physical Review B*, 39:10206–10231, 1989.

[68] B. Stébé, G. Munschy, L. Stauffer, F. Dujardin, and J. Murat. Excitonic trion X^- in semiconductor quantum wells. *Physical Review B*, 56:12454–12461, 1997.

[69] P. Michler, A. Imamoglu, M. D. Mason, P. J. Carson, G. F. Strouse, and S. K. Buratto. Quantum correlation among photons from a single quantum dot at room temperature. *Nature*, 406(6799):968–970, 2000.

[70] A. J. Morfa, B. C. Gibson, M. Karg, T. J. Karle, A. D. Greentree, P. Mulvaney, and S. Tomljenovic-Hanic. Single-photon emission and quantum characterization of zinc oxide defects. *Nano Letters*, 12(2):949–954, 2012.

[71] S. Castelletto, B. C. Johnson, V. Ivady, N. Stavrias, T. Umeda, A. Gali, and T. Ohshima. A silicon carbide room-temperature single-photon source. *Nature Materials*, 13(2):151–156, 2014.

[72] I. Aharonovich, S. Castelletto, D. A. Simpson, C.-H. Su, A. D. Greentree, and S. Prawer. Diamond-based single-photon emitters. *Reports on Progress in Physics*, 74(7):076501, 2011.

[73] A. M. Zaitsev. Vibronic spectra of impurity-related optical centers in diamond. *Physical Review B*, 61:12909–12922, 2000.

[74] C. Kurtsiefer, S. Mayer, P. Zarda, and H. Weinfurter. Stable Solid-State Source of Single Photons. *Physical Review Letters*, 85:290–293, 2000.

[75] T. Gaebel, I. Popa, A. Gruber, M. Domhan, F. Jelezko, and J. Wrachtrup. Stable single-photon source in the near infrared. *New Journal of Physics*, 6 (1):98, 2004.

[76] C. Wang, C. Kurtsiefer, H. Weinfurter, and B. Burchard. Single photon emission from siv centres in diamond produced by ion implantation. *Journal of Physics B: Atomic, Molecular and Optical Physics*, 39(1):37, 2006.

[77] I. Aharonovich, S. Castelletto, D. A. Simpson, A. Stacey, J. McCallum, A. D. Greentree, and S. Prawer. Two-level ultrabright single photon emission from diamond nanocrystals. *Nano Letters*, 9(9):3191–3195, 2009.

[78] S. Pezzagna, D. Rogalla, D. Wildanger, J. Meijer, and A. Zaitsev. Creation and nature of optical centres in diamond for single-photon emission overview and critical remarks. *New Journal of Physics*, 13(3):035024, 2011.

[79] D. M. Toyli, C. D. Weis, G. D. Fuchs, T. Schenkel, and D. D. Awschalom. Chip-scale nanofabrication of single spins and spin arrays in diamond. *Nano Letters*, 10(8):3168–3172, 2010.

[80] I. Aharonovich, A. D. Greentree, and S. Prawer. Diamond photonics. *Nature Photonics*, 5(7):397–405, 2011.

[81] I. I. Vlasov, A. A. Shiryaev, T. Rendler, S. Steinert, S.-Y. Lee, D. Antonov, M. Voros, F. Jelezko, A. V. Fisenko, L. F. Semjonova, J. Biskupek, U. Kaiser, O. I. Lebedev, I. Sildos, P. R. Hemmer, V. I. Konov, A. Gali, and J. Wrachtrup. Molecular-sized fluorescent nanodiamonds. *Nature Nanotechnology*, 9(1):54–58, 2014.

[82] J. Wolters, N. Sadzak, A. W. Schell, T. Schröder, and O. Benson. Measurement of the ultrafast spectral diffusion of the optical transition of nitrogen vacancy centers in nano-size diamond using correlation interferometry. *Physical Review Letters*, 110:027401, 2013.

[83] Encyclopædia Britannica Online. diamond. Web accesed 21. June, 2014.

[84] Ch. Kittel. *Einführung in die Festkorperphysik, 14. Auflage.* Oldenbourg Wissenschaftsverlag GmbH, 2006.

[85] M. Kamo, Y. Sato, S. Matsumoto, and N. Setaka. Diamond synthesis from gas phase in microwave plasma. *Journal of Crystal Growth*, 62(3):642–644, 1983.

[86] L. Wei, P. K. Kuo, R. L. Thomas, T. R. Anthony, and W. F. Banholzer. Thermal conductivity of isotopically modified single crystal diamond. *Physical Review Letters*, 70:3764–3767, 1993.

[87] F.C. Waldermann, P. Olivero, J. Nunn, K. Surmacz, Z.Y. Wang, D. Jaksch, R.A. Taylor, I.A. Walmsley, M. Draganski, P. Reichart, A.D. Greentree, D.N. Jamieson, and S. Prawer. Creating diamond color centers for quantum optical applications. *Diamond and Related Materials*, 16(11):1887 – 1895, 2007.

[88] C. Santori, D. Fattal, and Y. Yamamoto. *Single-photon devices and applications*. John Wiley & Sons, 2010.

[89] F. Jelezko and J. Wrachtrup. Single defect centres in diamond: A review. *physica status solidi (a)*, 203(13):3207–3225, 2006.

[90] M. V. Hauf, B. Grotz, B. Naydenov, M. Dankerl, S. Pezzagna, J. Meijer, F. Jelezko, J. Wrachtrup, M. Stutzmann, F. Reinhard, and J. A. Garrido. Chemical control of the charge state of nitrogen-vacancy centers in diamond. *Physical Review B*, 83:081304, 2011.

[91] A. W. Schell, G. Kewes, T. Schröder, J. Wolters, T. Aichele, and O. Benson. A scanning probe-based pick-and-place procedure for assembly of integrated quantum optical hybrid devices. *Review of Scientific Instruments*, 82(7): 073709, 2011.

[92] A. Batalov, V. Jacques, F. Kaiser, P. Siyushev, P. Neumann, L. J. Rogers, R. L. McMurtrie, N. B. Manson, F. Jelezko, and J. Wrachtrup. Low temperature studies of the excited-state structure of negatively charged nitrogen-vacancy color centers in diamond. *Physical Review Letters*, 102:195506, 2009.

[93] Lucio Robledo, Hannes Bernien, Toeno van der Sar, and Ronald Hanson. Spin dynamics in the optical cycle of single nitrogen-vacancy centres in diamond. *New Journal of Physics*, 13(2):025013, 2011. URL `http://stacks.iop.org/1367-2630/13/i=2/a=025013`.

[94] Ph. Tamarat, T. Gaebel, J. R. Rabeau, M. Khan, A. D. Greentree, H. Wilson, L. C. L. Hollenberg, S. Prawer, P. Hemmer, F. Jelezko, and J. Wrachtrup. Stark shift control of single optical centers in diamond. *Physical Review Letters*, 97:083002, 2006.

[95] F. Jelezko, I. Popa, A. Gruber, C. Tietz, J. Wrachtrup, A. Nizovtsev, and S. Kilin. Single spin states in a defect center resolved by optical spectroscopy. *Applied Physics Letters*, 81(12):2160–2162, 2002.

[96] E. van Oort, N. B. Manson, and M. Glasbeek. Optically detected spin coherence of the diamond n-v centre in its triplet ground state. *Journal of Physics C: Solid State Physics*, 21(23):4385, 1988.

[97] F. Jelezko and J. Wrachtrup. Read-out of single spins by optical spectroscopy. *Journal of Physics: Condensed Matter*, 16(30):R1089, 2004.

[98] Data aquired by N. Nikolay and B. Sontheimer.

[99] V. M. Acosta, A. Jarmola, E. Bauch, and D. Budker. Optical properties of the nitrogen-vacancy singlet levels in diamond. *Physical Review B*, 82:201202, 2010.

[100] M. W. Doherty, N. B. Manson, P. Delaney, F.Jelezko, J. Wrachtrup, and L. C.L. Hollenberg. The nitrogen-vacancy colour centre in diamond. *Physics Reports*, 528(1):1 – 45, 2013.

[101] F. Jelezko, T. Gaebel, I. Popa, A. Gruber, and J. Wrachtrup. Observation of coherent oscillations in a single electron spin. *Physical Review Letters*, 92: 076401, 2004.

[102] N. Bar-Gill, L. M. Pham, A. Jarmola, D. Budker, and R. L. Walsworth. Solid-state electronic spin coherence time approaching one second. *Nature Communications*, 4:1743, 2013.

[103] M. V. G. Dutt, L. Childress, L. Jiang, E. Togan, J. Maze, F. Jelezko, A. S. Zibrov, P. R. Hemmer, and M. D. Lukin. Quantum register based on individual electronic and nuclear spin qubits in diamond. *Science*, 316(5829):1312–1316, 2007.

[104] P. C. Maurer, G. Kucsko, C. Latta, L. Jiang, N. Y. Yao, S. D. Bennett, F. Pastawski, D. Hunger, N. Chisholm, M. Markham, D. J. Twitchen, J. I. Cirac, and M. D. Lukin. Room-temperature quantum bit memory exceeding one second. *Science*, 336(6086):1283–1286, 2012.

[105] A. Krueger. Beyond the shine: recent progress in applications of nanodiamond. *Journal of Materials Chemistry*, 21:12571–12578, 2011.

[106] E. Neu, C. Arend, E. Gross, F. Guldner, C. Hepp, D. Steinmetz, E. Zscherpel, S. Ghodbane, H. Sternschulte, D. Steinmüller-Nethl, Y. Liang, A. Krueger, and C. Becher. Narrowband fluorescent nanodiamonds produced from chemical vapor deposition films. *Applied Physics Letters*, 98(24):243107, 2011.

[107] R. S. Lewis, T. Ming, J. F. Wacker, E. Anders, and E. Steel. Interstellar diamonds in meteorites. *Nature*, 326(6109):160–162, 1987.

[108] O. Benson. Assembly of hybrid photonic architectures from nanophotonic constituents. *Nature*, 480(7376):193–199, 2011.

[109] A. Mohtashami and A. F. Koenderink. Suitability of nanodiamond nitrogen vacancy centers for spontaneous emission control experiments. *New Journal of Physics*, 15(4):043017, 2013.

[110] C. Bradac, T. Gaebel, N. Naidoo, M. J. Sellars, J. Twamley, L. J. Brown, A. S. Barnard, T. Plakhotnik, A. V. Zvyagin, and J. R. Rabeau. Observation and control of blinking nitrogen-vacancy centres in discrete nanodiamonds. *Nature Nanotechnology*, 5(5):345–349, 2010.

[111] J. Tisler, G. Balasubramanian, B. Naydenov, R. Kolesov, B. Grotz, R. Reuter, J.-P. Boudou, P. A. Curmi, M. Sennour, A. Thorel, M. Börsch, K. Aulenbacher, R. Erdmann, P. R. Hemmer, F. Jelezko, and J. Wrachtrup. Fluorescence and spin properties of defects in single digit nanodiamonds. *ACS Nano*, 3(7):1959–1965, 2009.

[112] M. Leifgen, T. Schröder, F. Gädeke, R. Riemann, V. Metillon, E. Neu, C. Hepp, C. Arend, C. Becher, K. Lauritsen, and O. Benson. Evaluation of nitrogen- and silicon-vacancy defect centres as single photon sources in quantum key distribution. *New Journal of Physics*, 16(2):023021, 2014.

[113] T. Schröder, M. Fujiwara, T. Noda, H.-Q. Zhao, O. Benson, and S. Takeuchi. A nanodiamond-tapered fiber system with high single-mode coupling efficiency. *Optics Express*, 20(10):10490–10497, 2012.

[114] L. Liebermeister, F. Petersen, A. v. Münchow, D. Burchardt, J. Hermelbracht, T. Tashima, A. W. Schell, O. Benson, T. Meinhardt, A. Krueger, A. Stiebeiner, A. Rauschenbeutel, H. Weinfurter, and M. Weber. Tapered fiber coupling of single photons emitted by a deterministically positioned single nitrogen vacancy center. *Applied Physics Letters*, 104(3):031101, 2014.

[115] A. Lohrmann, S. Pezzagna, I. Dobrinets, P. Spinicelli, V. Jacques, J.-F. Roch, J. Meijer, and A. M. Zaitsev. Diamond based light-emitting diode for visible single-photon emission at room temperature. *Applied Physics Letters*, 99(25): 251106, 2011.

[116] N. Mizuochi, T. Makino, H. Kato, D. Takeuchi, M. Ogura, H. Okushi, M. Nothaft, P. Neumann, A. Gali, F. Jelezko, J. Wrachtrup, and S. Yamasaki. Electrically driven single-photon source at room temperature in diamond. *Nature Photonics*, 6(5):299–303, 2012.

[117] A. Beveratos, R. Brouri, T. Gacoin, A. Villing, J.-P. Poizat, and P. Grangier. Single photon quantum cryptography. *Physical Review Letters*, 89:187901, 2002.

[118] J. Wolters, M. Strauß, R. S. Schoenfeld, and O. Benson. Quantum Zeno phenomenon on a single solid-state spin. *Physical Review A*, 88:020101, 2013.

[119] G. Waldherr, P. Neumann, S. F. Huelga, F. Jelezko, and J. Wrachtrup. Violation of a temporal bell inequality for single spins in a diamond defect center. *Physical Review Letters*, 107:090401, 2011.

[120] R. E. George, L. M. Robledo, O. J. E. Maroney, M. S. Blok, H. Bernien, M. L. Markham, D. J. Twitchen, J. J. L. Morton, G. A. D. Briggs, and R. Hanson. Opening up three quantum boxes causes classically undetectable wavefunction collapse. *Proceedings of the National Academy of Sciences*, 110 (10):3777–3781, 2013.

[121] P. Kok and B. W. Lovett. Materials science: Qubits in the pink. *Nature*, 444 (7115):49–49, 2006.

[122] J. Wrachtrup and F. Jelezko. Processing quantum information in diamond. *Journal of Physics: Condensed Matter*, 18(21):S807, 2006.

[123] W. Pfaff, B. Hensen, H. Bernien, S. B. van Dam, M. S. Blok, T. H. Taminiau, M. J. Tiggelman, R. N. Schouten, M. Markham, D. J. Twitchen, and R. Hanson. Unconditional quantum teleportation between distant solid-state quantum bits. *Science*, 345(6196):532–535, 2014.

[124] R. Schirhagl, K. Chang, M. Loretz, and C. L. Degen. Nitrogen-vacancy centers in diamond: Nanoscale sensors for physics and biology. *Annual Review of Physical Chemistry*, 65(1):83–105, 2014.

[125] J. R. Maze, P. L. Stanwix, J. S. Hodges, S. Hong, J. M. Taylor, P. Cappellaro, L. Jiang, M. V. Gurudev Dutt, E. Togan, A. S. Zibrov, A. Yacoby, R. L. Walsworth, and M. D. Lukin. Nanoscale magnetic sensing with an individual electronic spin in diamond. *Nature*, 455(7213):644–647, 2008.

[126] G. Balasubramanian, I. Y. Chan, R. Kolesov, M. Al-Hmoud, J. Tisler, C. Shin, C. Kim, A. Wojcik, P. R. Hemmer, A. Krueger, T. Hanke, A. Leitenstorfer, R. Bratschitsch, F. Jelezko, and J. Wrachtrup. Nanoscale imaging magnetometry with diamond spins under ambient conditions. *Nature*, 455: 648–651, 2008.

[127] F. Dolde, H. Fedder, M. W. Doherty, T. Nobauer, F. Rempp, G. Balasubramanian, T. Wolf, F. Reinhard, L. C. L. Hollenberg, F. Jelezko, and J. Wrachtrup. Electric-field sensing using single diamond spins. *Nature Physics*, 7(6):459–463, 2011.

[128] V. M. Acosta, E. Bauch, M. P. Ledbetter, A. Waxman, L.-S. Bouchard, and D. Budker. Temperature dependence of the nitrogen-vacancy magnetic resonance in diamond. *Physical Review Letters*, 104:070801, 2010.

[129] P. Neumann, I. Jakobi, F. Dolde, C. Burk, R. Reuter, G. Waldherr, J. Honert, T. Wolf, A. Brunner, J. H. Shim, D. Suter, H. Sumiya, J. Isoya, and J. Wrachtrup. High-precision nanoscale temperature sensing using single defects in diamond. *Nano Letters*, 13(6):2738–2742, 2013.

[130] D. M. Toyli, C. F. de las Casas, D. J. Christle, V. V. Dobrovitski, and D. D. Awschalom. Fluorescence thermometry enhanced by the quantum coherence of single spins in diamond. *Proceedings of the National Academy of Sciences*, 110(21):8417–8421, 2013.

[131] M. Scala, M. S. Kim, G. W. Morley, P. F. Barker, and S. Bose. Matter-wave interferometry of a levitated thermal nano-oscillator induced and probed by a spin. *Physical Review Letters*, 111:180403, 2013.

[132] M. P. Ledbetter, K. Jensen, R. Fischer, A. Jarmola, and D. Budker. Gyroscopes based on nitrogen-vacancy centers in diamond. *Physical Review A*, 86: 052116, 2012.

[133] C.-C. Fu, H.-Y. Lee, K. Chen, T.-S. Lim, H.-Y. Wu, P.-K. Lin, P.-K. Wei, P.-H. Tsao, H.-C. Chang, and W. Fann. Characterization and application of single fluorescent nanodiamonds as cellular biomarkers. *Proceedings of the National Academy of Sciences*, 104(3):727–732, 2007.

[134] L. P. McGuinness, Y. Yan, A. Stacey, D. A. Simpson, L. T. Hall, D. Maclaurin, S. Prawer, P. Mulvaney, J. Wrachtrup, F. Caruso, R. E. Scholten, and L. C. L. Hollenberg. Quantum measurement and orientation tracking of fluorescent nanodiamonds inside living cells. *Nature Nanotechnology*, 6(6):358–363, 2011.

[135] D. Le Sage, K. Arai, D. R. Glenn, S. J. DeVience, L. M. Pham, L. Rahn-Lee, M. D. Lukin, A. Yacoby, A. Komeili, and R. L. Walsworth. Optical magnetic imaging of living cells. *Nature*, 496(7446):486–489, 2013.

[136] S. A. Empedocles, D. J. Norris, and M. G. Bawendi. Photoluminescence spectroscopy of single cdse nanocrystallite quantum dots. *Physical Review Letters*, 77:3873–3876, 1996.

[137] W. P. Ambrose and W. E. Moerner. Fluorescence spectroscopy and spectral diffusion of single impurity molecules in a crystal. *Nature*, 349(6306):225–227, 1991.

[138] N. Akopian, R. Trotta, E. Zallo, S. Kumar, P. Atkinson, A. Rastelli, O. G. Schmidt, and V. Zwiller. An artificial atom locked to natural atoms. *arXiv preprint arXiv:1302.2005*, 2013.

[139] V. M. Acosta, C. Santori, A. Faraon, Z. Huang, K.-M. C. Fu, A. Stacey, D. A. Simpson, K. Ganesan, S. Tomljenovic-Hanic, A. D. Greentree, S. Prawer, and R. G. Beausoleil. Dynamic stabilization of the optical resonances of single nitrogen-vacancy centers in diamond. *Physical Review Letters*, 108:206401, 2012.

[140] J. Seufert, R. Weigand, G. Bacher, T. Kummell, A. Forchel, K. Leonardi, and D. Hommel. Spectral diffusion of the exciton transition in a single self-organized quantum dot. *Applied Physics Letters*, 76(14):1872–1874, 2000.

[141] G. Sallen, A. Tribu, T. Aichele, R. Andre, L. Besombes, C. Bougerol, D. Richard, S. Tatarenko, K. Kheng, and J.-Ph. Poizat. Subnanosecond spectral diffusion measurement using photon correlation. *Nature Photonics*, 4(10):696–699, 2010.

[142] X. Brokmann, M. Bawendi, . Coolen, and J.-P. Hermier. Photon-correlation fourier spectroscopy. *Optics Express*, 14(13):6333–6341, 2006.

[143] L. Coolen, X. Brokmann, P. Spinicelli, and J.-P. Hermier. Emission characterization of a single cdse-zns nanocrystal with high temporal and spectral resolution by photon-correlation fourier spectroscopy. *Physical Review Letters*, 100:027403, 2008.

[144] T. Schröder, F. Gädeke, M. J. Banholzer, and O. Benson. Ultrabright and efficient single-photon generation based on nitrogen-vacancy centres in nanodiamonds on a solid immersion lens. *New Journal of Physics*, 13(5):055017, 2011.

[145] G. Waldherr, J. Beck, M. Steiner, P. Neumann, A. Gali, Th. Frauenheim, F. Jelezko, and J. Wrachtrup. Dark states of single nitrogen-vacancy centers in diamond unraveled by single shot nmr. *Physical Review Letters*, 106:157601, 2011.

[146] R.G. Farrer. On the substitutional nitrogen donor in diamond. *Solid State Communications*, 7(9):685 – 688, 1969.

[147] J. Rosa, M. Vanecek, M. Nesladek, and L.M. Stals. Photoionization cross-section of dominant defects in CVD diamond. *Diamond and Related Materials*, 8:721 –724, 1999.

[148] Y. Shen, T. M. Sweeney, and H. Wang. Zero-phonon linewidth of single nitrogen vacancy centers in diamond nanocrystals. *Physical Review B*, 77: 033201, 2008.

[149] A. W. Schell, T. Neumer, and O. Benson. Numerical analysis of efficient light extraction with an elliptical solid immersion lens. *Optics Letters*, 39 (16):4639–4642, 2014.

[150] S. Bradbury. The microscope. *Journal of the Royal Society of Arts*, pages 317–319, 1968.

[151] T. E. Furtak and M. V. Klein. Optik, 1988.

[152] M. Muller. *Introduction to confocal fluorescence microscopy*, volume 69. SPIE press, 2006.

[153] R. H. Webb. Confocal optical microscopy. *Reports on Progress in Physics*, 59(3):427, 1996.

[154] J. Pawley. *Handbook of biological confocal microscopy*. Springer, 2010.

[155] E. Hecht. Optics. *Addison Wesley*, 997:213–214, 1998.

[156] G. S. Kino and T. R. Corle. *Confocal scanning optical microscopy and related imaging systems*. Academic Press, 1996.

[157] S. W. Hell. Microscopy and its focal switch. *Nature Materials*, 6(1):24–32, 2009.

[158] K. J. Vahala. Optical microcavities. *Nature*, 424(6950):839–846, 2003.

[159] W.L. Barnes, G. Björk, J.M. Gerard, P. Jonsson, J.A.E. Wasey, P.T. Worthing, and V. Zwiller. Solid-state single photon sources: light collection strategies. *The European Physical Journal D - Atomic, Molecular, Optical and Plasma Physics*, 18:197–210, 2002.

[160] A. M. Zaitsev. *Optical properties of diamond - A data handbook*. Springer-Verlag GmbH (Berlin), 2001.

[161] S. M. Mansfield and G. S. Kino. Solid immersion microscope. *Applied Physics Letters*, 57(24):2615–2616, 1990.

[162] V. Zwiller and G. Bjork. Improved light extraction from emitters in high refractive index materials using solid immersion lenses. *Journal of Applied Physics*, 92(2):660–665, 2002.

[163] J. P. Hadden, J. P. Harrison, A. C. Stanley-Clarke, L. Marseglia, Y.-L. D. Ho, B. R. Patton, J. L. O'Brien, and J. G. Rarity. Strongly enhanced photon collection from diamond defect centers under microfabricated integrated solid immersion lenses. *Applied Physics Letters*, 97(24):241901, 2010.

[164] P. Siyushev, F. Kaiser, V. Jacques, I. Gerhardt, S. Bischof, H. Fedder, J. Dodson, M. Markham, D. Twitchen, F. Jelezko, and J. Wrachtrup. Monolithic diamond optics for single photon detection. *Applied Physics Letters*, 97(24): 241902, 2010.

[165] K. Kazuko, Y. Masahiro, B. Motoyoshi, S. Tohru, and A. Hidefumi. High collection efficiency in fluorescence microscopy with a solid immersion lens. *Applied Physics Letters*, 75(12):1667–1669, 1999.

[166] K. G. Lee, X. W. Chen, H. Eghlidi, P. Kukura, R. Lettow, A. Renn, V. Sandoghdar, and S. Götzinger. A planar dielectric antenna for directional single-photon emission and near-unity collection efficiency. *Nature Photonics*, 5: 166–169, 2011.

[167] X.-W. Chen, S. Götzinger, and V. Sandoghdar. 99% efficiency in collecting photons from a single emitter. *Optics Letters*, 36(18):3545–3547, 2011.

[168] A. W. Schell, G. Kewes, T. Hanke, A. Leitenstorfer, R. Bratschitsch, O. Benson, and T. Aichele. Single defect centers in diamond nanocrystals as quantum probes for plasmonic nanostructures. *Optics Express*, 19(8):7914–7920, 2011.

[169] T. van der Sar, J. Hagemeier, W. Pfaff, E. C. Heeres, S. M. Thon, H. Kim, P. M. Petroff, T. H. Oosterkamp, D. Bouwmeester, and R. Hanson. Deterministic nanoassembly of a coupled quantum emitter–photonic crystal cavity system. *Applied Physics Letters*, 98(19):193103, 2011.

[170] S. Schietinger, M. Barth, T. Aichele, and O. Benson. Plasmon-enhanced single photon emission from a nanoassembled metal-diamond hybrid structure at room temperature. *Nano Letters*, 9(4):1694–1698, 2009.

[171] E. Ampem-Lassen, D. A. Simpson, B. C. Gibson, S. Trpkovski, F. M. Hossain, S. T. Huntington, K. Ganesan, L. C. Hollenberg, and S. Prawer. Nano-manipulation of diamond-based single photon sources. *Optics Express*, 17: 11287–11293, 2009.

[172] A. Huck, S. Kumar, A. Shakoor, and U. L. Andersen. Controlled coupling of a single nitrogen-vacancy center to a silver nanowire. *Physical Review Letters*, 106(9):096801, 2011.

[173] M. Fujiwara, K. Toubaru, T. Noda, H.-Q. Zhao, and S. Takeuchi. Highly efficient coupling of photons from nanoemitters into single-mode optical fibers. *Nano Letters*, 11(10):4362–4365, 2011.

[174] R. Yalla, F. Le Kien, M. Morinaga, and K. Hakuta. Efficient channeling of fluorescence photons from single quantum dots into guided modes of optical nanofiber. *Physical Review Letters*, 109:063602, 2012.

[175] T. Schröder, A. W. Schell, G. Kewes, T. Aichele, and O. Benson. Fiber-integrated diamond-based single photon source. *Nano Letters*, 11(1):198–202, 2011.

[176] M. R. Henderson, B. C. Gibson, H. Ebendorff-Heidepriem, K. Kuan, S. Afshar V., J. O. Orwa, I. Aharonovich, S. Tomljenovic-Hanic, A. D. Greentree, S. Prawer, and T. M. Monro. Hybrid materials: Diamond in tellurite glass: a new medium for quantum information (adv. mater. 25/2011). *Advanced Materials*, 23(25):2772–2772, 2011.

[177] A. W. Schell, J. Kaschke, J. Fischer, R. Henze, J. Wolters, M. Wegener, and O. Benson. Three-dimensional quantum photonic elements based on single nitrogen vacancy-centres in laser-written microstructures. *Scientific Reports*, 3:1577, 2013.

[178] R. A. Arif, H. Zhao, Y.-K. Ee, and N. Tansu. Spontaneous Emission and Characteristics of Staggered InGaN Quantum-Well Light-Emitting Diodes. *IEEE Journal of Quantum Electronics*, 44:573–580, 2008.

[179] M. Fujita, S. Takahashi, Y. Tanaka, T. Asano, and S. Noda. Simultaneous inhibition and redistribution of spontaneous light emission in photonic crystals. *Science*, 308(5726):1296–1298, 2005.

[180] M. J. Mandella. Collimators and collimator arrays employing ellipsoidal solid immersion lenses, 2002.

[181] S. Kawata, H. B. Sun, T. Tanaka, and K. Takada. Finer features for functional microdevices. *Nature*, 412(6848):697–698, 2001.

[182] M. Deubel, G. von Freymann, M. Wegener, S. Pereira, K. Busch, and C. M. Soukoulis. Direct laser writing of three-dimensional photonic-crystal templates for telecommunications. *Nature Materials*, 3(7):444–447, 2004.

[183] D. McCloskey and J. F. Donegan. Planar elliptical solid immersion lens based on a cartesian oval. *Applied Physics Letters*, 103(9):091101, 2013.

[184] A. V. Boriskin, A. I. Nosich, S. V. Boriskina, T. M. Benson, P. Sewell, and A. Altintas. Lens or resonator? electromagnetic behavior of an extended hemielliptic lens for a sub-millimeter-wave receiver. *Microwave and Optical Technology Letters*, 43(6):515–518, 2004.

[185] L. Novotny and B. Hecht. *Principles of Nano-Optics*. Principles of Nano-optics. Cambridge University Press, 2006.

[186] A. W. Schell, P. Engel, J. F. M. Werra, C. Wolff, K. Busch, and O. Benson. Scanning single quantum emitter fluorescence lifetime imaging: Quantitative analysis of the local density of photonic states. *Nano Letters*, 14(5):2623–2627, 2014.

[187] A. W. Schell, . Neumer, Q. Shi, J. Kaschke, J. Fischer, M. Wegener, and O. Benson. Laser-written microstructures for enhanced single-photon collection efficiency. In *CLEO: 2014*, page JW2A.122. Optical Society of America, 2014.

[188] G. Binnig, C. F. Quate, and Ch. Gerber. Atomic force microscope. *Physical Review Letters*, 56:930–933, 1986.

[189] N. A. Burnham and R. J. Colton. Measuring the nanomechanical properties and surface forces of materials using an atomic force microscope. *Journal of Vacuum Science & Technology A: Vacuum, Surfaces, and Films*, 7(4):2906–2913, 1989.

[190] T. Junno, K. Deppert, L. Montelius, and L. Samuelson. Controlled manipulation of nanoparticles with an atomic force microscope. *Applied Physics Letters*, 66(26):3627–3629, 1995.

[191] L. Gross, F. Mohn, N. Moll, P. Liljeroth, and G. Meyer. The chemical structure of a molecule resolved by atomic force microscopy. *Science*, 325(5944): 1110–1114, 2009.

[192] F. J. Welker, J.and Giessibl. Revealing the angular symmetry of chemical bonds by atomic force microscopy. *Science*, 336(6080):444–449, 2012.

[193] P. Parot, Y. F. Dufrêne, P. Hinterdorfer, C. Le Grimellec, D. Navajas, J.-L. Pellequer, and S. Scheuring. Past, present and future of atomic force microscopy in life sciences and medicine. *Journal of Molecular Recognition*, 20(6):418–431, 2007.

[194] L. W. Francis, P. D. Lewis, C. J. Wright, and R. S. Conlan. Atomic force microscopy comes of age. *Biology of the Cell*, 102(2):133–143, 2010.

[195] H. Heinzelmann and D.W. Pohl. Scanning near-field optical microscopy. *Applied Physics A*, 59(2):89–101, 1994.

[196] M. Richter and V. Deckert. *Scanning Near-Field Optical Microscopy (SNOM)*, pages 481–497. Wiley-VCH Verlag GmbH & Co. KGaA, 2011.

[197] P. Eaton and P. West. *Atomic Force Microscopy*. Oxford University Press, 2010.

[198] R. Wiesendanger. *Scanning Probe Microscopy and Spectroscopy: Methods and Applications*. Scanning Probe Microscopy and Spectroscopy: Methods and Applications. Cambridge University Press, 1994.

[199] Y. Seo and W. Jhe. Atomic force microscopy and spectroscopy. *Reports on Progress in Physics*, 71(1):016101, 2008.

[200] G. Meyer and N. M. Amer. Novel optical approach to atomic force microscopy. *Applied Physics Letters*, 53(12):1045–1047, 1988.

[201] K. J. Aström and R. M. Murray. *Feedback systems: an introduction for scientists and engineers*. Princeton university press, 2010.

[202] N.W. Ashcroft and N.D. Mermin. *Solid state physics*. Science: Physics. Harcourt College, 1976.

[203] J. P. Cleveland, B. Anczykowski, A. E. Schmid, and V. B. Elings. Energy dissipation in tapping-mode atomic force microscopy. *Applied Physics Letters*, 72(20):2613–2615, 1998.

[204] D. M. Schaefer, R. Reifenberger, A. Patil, and R. P. Andres. Fabrication of two-dimensional arrays of nanometer-size clusters with the atomic force microscope. *Applied Physics Letters*, 66(8):1012–1014, 1995.

[205] A. Bek, R. Jansen, M. Ringler, S. Mayilo, T. A. Klar, and J. Feldmann. Fluorescence Enhancement in Hot Spots of AFM-Designed Gold Nanoparticle Sandwiches. *Nano Letters*, 8(2):485–490, 2008.

[206] M. Barth, N. Nüsse, B. Löchel, and O. Benson. Controlled coupling of a single-diamond nanocrystal to a photonic crystal cavity. *Optics Letters*, 34 (7):1108–1110, 2009.

[207] T. van der Sar, E. C. Heeres, G. M. Dmochowski, G. de Lange, L. Robledo, T. H. Oosterkamp, and R. Hanson. Nanopositioning of a diamond nanocrystal containing a single nitrogen-vacancy defect center. *Applied Physics Letters*, 94(17):173104, 2009.

[208] S. Fahlbusch, S. Mazerolle, J.-M. Breguet, A. Steinecker, J. Agnus, R. Perez, and J. Michler. Nanomanipulation in a scanning electron microscope. *Journal of Materials Processing Technology*, 167:371 – 382, 2005.

[209] M. Born, E. Wolf, and A.B. Bhatia. *Principles of Optics; Seventh (Expanded) Edition*. Cambridge University Press, 1999.

[210] B. Huang, M. Bates, and X. Zhuang. Super resolution fluorescence microscopy. *Annual review of biochemistry*, 78:993, 2009.

[211] S. Kumar, A. Huck, and U. L. Andersen. Efficient coupling of a single diamond color center to propagating plasmonic gap modes. *Nano Letters*, 13(3):1221–1225, 2013.

[212] A. A. Tseng, A. Notargiacomo, and T. P. Chen. Nanofabrication by scanning probe microscope lithography: A review. *Journal of Vacuum Science & Technology B: Microelectronics and Nanometer Structures*, 23(3):877–894, 2005.

[213] R. D. Piner, J. Zhu, F. Xu, S. Hong, and C. A. Mirkin. "dip-pen" nanolithography. *Science*, 283(5402):661–663, 1999.

[214] K. Salaita, Y. Wang, and C. A. Mirkin. Applications of dip-pen nanolithography. *Nature Nanotechnology*, 2(3):145–155, 2007.

[215] H. Zheng, U. M. Mirsaidov, L.-W. Wang, and P. Matsudaira. Electron beam manipulation of nanoparticles. *Nano Letters*, 12(11):5644–5648, 2012.

[216] D. Erickson, X. Serey, Y.-F. Chen, and S. Mandal. Nanomanipulation using near field photonics. *Lab Chip*, 11:995–1009, 2011.

[217] D. G. Grier. A revolution in optical manipulation. *Nature*, 424(6950):810–816, 2003.

[218] P. Mühlschlegel, H.-J. Eisler, O. J. F. Martin, B. Hecht, and D. W. Pohl. Resonant optical antennas. *Science*, 308(5728):1607–1609, 2005.

[219] J. L. O'Brien, A. Furusawa, and J. Vuckovic. Photonic quantum technologies. *Nature Photonics*, 3(12):687–695, 2009.

[220] R. Brouri, A. Beveratos, J.-P. Poizat, and P. Grangier. Photon antibunching in the fluorescence of individual color centers in diamond. *Optics Letters*, 25 (17):1294–1296, 2000.

[221] T. M. Babinec, J. T. Choy, K. J. M. Smith, M. Khan, and M. Loncar. Design and focused ion beam fabrication of single crystal diamond nanobeam cavities. *Journal of Vacuum Science & Technology B: Microelectronics and Nanometer Structures*, 29(1):010601, 2011.

[222] K.-M. C. Fu, C. Santori, P. E. Barclay, I. Aharonovich, S. Prawer, N. Meyer, A. M. Holm, and R. G. Beausoleil. Coupling of nitrogen-vacancy centers in diamond to a gap waveguide. *Applied Physics Letters*, 93(23):234107–3, 2008.

[223] J. Meijer, B. Burchard, M. Domhan, C. Wittmann, T. Gaebel, I. Popa, F. Jelezko, and J. Wrachtrup. Generation of single color centers by focused nitrogen implantation. *Applied Physics Letters*, 87(26):261909, 2005.

[224] J. Meijer, S. Pezzagna, T. Vogel, B. Burchard, H.H. Bukow, I.W. Rangelow, Y. Sarov, H. Wiggers, I. Plümel, F. Jelezko, J. Wrachtrup, F. Schmidt-Kaler, W. Schnitzler, and K. Singer. Towards the implanting of ions and positioning of nanoparticles with nm spatial resolution. *Applied Physics A*, 91:567–571, 2008.

[225] J. Toset, I. Casuso, J. Samitier, and G. Gomila. Deflection-voltage curve modelling in atomic force microscopy and its use in dc electrostatic manipulation of gold nanoparticles. *Nanotechnology*, 18(1):015503, 2007.

[226] Y. Tanaka and K. Sasaki. Selection and transfer of individual plasmon-resonant metal nanoparticles. *Applied Physics Letters*, 96(5):053117, 2010.

[227] S. Schietinger. *Investigation, Manipulation, and Coupling of Single Nanoscopic and Quantum Emitters*. PhD thesis, Humboldt-Universität zu Berlin, 2012.

[228] J. Wolters, A. W. Schell, G. Kewes, N. Nüsse, M. Schoengen, H. Döscher, T. Hannappel, B. Löchel, M. Barth, and O. Benson. Enhancement of the zero phonon line emission from a single nitrogen vacancy center in a nanodiamond via coupling to a photonic crystal cavity. *Applied Physics Letters*, 97(14): 141108, 2010.

[229] T. Schröder, A. W. Schell, G. Kewes, T. Aichele, and O. Benson. Fiber-integrated diamond-based single photon source. *Nano Letters*, 11(1):198–202, 2011.

[230] T. Eastman and D.-M. Zhu. Adhesion forces between surface-modified afm tips and a mica surface. *Langmuir*, 12(11):2859–2862, 1996.

[231] E. Neu, D. Steinmetz, J. Riedrich-Möller, S. Gsell, M. Fischer, M. Schreck, and C. Becher. Single photon emission from silicon-vacancy colour centres in chemical vapour deposition nano-diamonds on iridium. *New Journal of Physics*, 13(2):025012, 2011.

[232] J. Wolters, G. Kewes, A. W. Schell, N. Nüsse, M Schoengen, B Löchel, T Hanke, R. Bratschitsch, A. Leitenstorfer, T. Aichele, and O. Benson. Coupling of single nitrogen-vacancy defect centers in diamond nanocrystals to optical antennas and photonic crystal cavities. *physica status solidi (b)*, 249 (5):918–924, 2012.

[233] D. DiVincenzo. Quantum bits: Better than excellent. *Nature Materials*, 9(6): 468–469, 2010.

[234] C. Santori, P. E. Barclay, K.-M. C. Fu, R. G. Beausoleil, S. Spillane, and M. Fisch. Nanophotonics for quantum optics using nitrogen-vacancy centers in diamond. *Nanotechnology*, 21(27):274008, 2010.

[235] K. Hennessy, A. Badolato, M. Winger, D. Gerace, M. Atature, S. Gulde, S. Falt, E. L. Hu, and A. Imamoglu. Quantum nature of a strongly coupled single quantum dot-cavity system. *Nature*, 445(7130):896–899, 2007.

[236] T. Tanabe, M. Notomi, E. Kuramochi, A. Shinya, and H. Taniyama. Trapping and delaying photons for one nanosecond in an ultrasmall high-q photonic-crystal nanocavity. *Nature Photonics*, 1(1):49–52, 2007.

[237] J. Wolters, N. Nikolay, M. Schoengen, A. W. Schell, J. Probst, B. Löchel, and O. Benson. Thermo-optical response of photonic crystal cavities operating in the visible spectral range. *Nanotechnology*, 24(31):315204, 2013.

[238] K. Rivoire, A. Faraon, and J. Vuckovic. Gallium phosphide photonic crystal nanocavities in the visible. *Applied Physics Letters*, 93(6):063103, 2008.

[239] S. Noda, M. Fujita, and T. Asano. Spontaneous-emission control by photonic crystals and nanocavities. *Nature Photonics*, 1(8):449–458, 2007.

[240] Y. Akahane, T. Asano, B.-S. Song, and S. Noda. High-q photonic nanocavity in a two-dimensional photonic crystal. *Nature*, 425(6961):944–947, 2003.

[241] J. Riedrich-Moller, L. Kipfstuhl, C. Hepp, E. Neu, C. Pauly, F. Mucklich, A. Baur, M. Wandt, S. Wolff, M. Fischer, S. Gsell, M. Schreck, and C. Becher. One- and two-dimensional photonic crystal microcavities in single crystal diamond. *Nature Nanotechnology*, 7(1):69–74, 2012.

[242] A. Faraon, C. Santori, Z. Huang, V. M. Acosta, and R. G. Beausoleil. Coupling of nitrogen-vacancy centers to photonic crystal cavities in monocrystalline diamond. *Physical Review Letters*, 109:033604, 2012.

[243] J. C. Lee, A. P. Magyar, D. O. Bracher, I. Aharonovich, and E. L. Hu. Fabrication of thin diamond membranes for photonic applications. *Diamond and Related Materials*, 33(0):45 – 48, 2013.

[244] M. Galli, S. L. Portalupi, M. Belotti, L. C. Andreani, L. O'Faolain, and T. F. Krauss. Light scattering and fano resonances in high-q photonic crystal nanocavities. *Applied Physics Letters*, 94(7):071101, 2009.

[245] M. Barth, J. Kouba, J. Stingl, B. Löchel, and O. Benson. Modification of visible spontaneousemission with silicon nitride photoniccrystal nanocavities. *Optics Express*, 15(25):17231–17240, 2007.

[246] M. Barth, N. Nüsse, J. Stingl, B. Löchel, and O. Benson. Emission properties of high-q silicon nitride photonic crystal heterostructure cavities. *Applied Physics Letters*, 93(2):021112, 2008.

[247] M. R. Lorenz, G. D. Pettit, and R. C. Taylor. Band gap of gallium phosphide from 0 to 900 k and light emission from diodes at high temperatures. *Physical Review*, 171:876–881, 1968.

[248] H. S. Lee, S. Kiravittaya, S. Kumar, J. D. Plumhof, L. Balet, L. H. Li, M. Francardi, A. Gerardino, A. Fiore, A. Rastelli, and O. G. Schmidt. Local tuning of photonic crystal nanocavity modes by laser-assisted oxidation. *Applied Physics Letters*, 95(19):191109, 2009.

[249] D. Englund, B. Shields, K. Rivoire, F. Hatami, J. Vucovic, H. Park, and M. D. Lukin. Deterministic coupling of a single nitrogen vacancy center to a photonic crystal cavity. *Nano Letters*, 10(10):3922–3926, 2010.

[250] R. Albrecht, A. Bommer, C. Pauly, F. Mücklich, A. W. Schell, P. Engel, T. Schröder, O. Benson, J. Reichel, and C. Becher. Narrow-band single photon emission at room temperature based on a single nitrogen-vacancy center coupled to an all-fiber-cavity. *Applied Physics Letters*, 105(7):073113, 2014.

[251] P. E. Barclay, C. Santori, K.-M. Fu, R. G. Beausoleil, and O. Painter. Coherent interference effects in a nano-assembled diamond nv center cavity-qed system. *Optics Express*, 17(10):8081–8097, 2009.

[252] B. J. M. Hausmann, B. Shields, Q. Quan, P. Maletinsky, M. McCutcheon, J. T. Choy, T. M. Babinec, A. Kubanek, A. Yacoby, M. D. Lukin, and M. Lon-

car. Integrated diamond networks for quantum nanophotonics. *Nano Letters*, 12(3):1578–1582, 2012.

[253] J. Fischer. *Three-dimensional optical lithography beyond the diffraction limit*. PhD thesis, Karlsruher Institut für Technologie, 2012.

[254] Z. P. Liu, Y. Li, Y. F. Xiao, B. B. Li, X. F. Jiang, Y. Qin, X. B. Feng, H. Yang, and Q. Gong. Direct laser writing of whispering gallery microcavities by two-photon polymerization. *Applied Physics Letters*, 97(21):211105–211105, 2010.

[255] T. Grossmann, S. Schleede, M. Hauser, T. Beck, M. Thiel, G. von Freymann, T. Mappes, and H. Kalt. Direct laser writing for active and passive high-q polymer microdisks on silicon. *Optics Express*, 19(12):11451–11456, 2011.

[256] C.-W. Lee, S. Pagliara, U. Keyser, and J. J. Baumberg. Perpendicular coupling to in-plane photonics using arc waveguides fabricated via two-photon polymerization. *Applied Physics Letters*, 100(17):171102, 2012.

[257] H.B. Sun, T. Tanaka, K. Takada, and S. Kawata. Two-photon photopolymerization and diagnosis of three-dimensional microstructures containing fluorescent dyes. *Applied Physics Letters*, 79:1411, 2001.

[258] J. Li, B. Jia, G. Zhou, and M. Gu. Fabrication of three-dimensional woodpile photonic crystals in a PbSe quantum dot composite material. *Optics Express*, 14(22):10740–10745, 2006.

[259] S. Shukla, X. Vidal, E. P. Furlani, M. T. Swihart, K.-T. Kim, Y.-K. Yoon, A. Urbas, and P. N. Prasad. Subwavelength direct laser patterning of conductive gold nanostructures by simultaneous photopolymerization and photoreduction. *ACS Nano*, 5(3):1947–1957, 2011.

[260] J. Fischer and M. Wegener. Three-dimensional direct laser writing inspired by stimulated-emission-depletion microscopy [invited]. *Optical Materials Express*, 1(4):614–624, 2011.

[261] J. R. Weber, W. F. Koehl, J. B. Varley, A. Janotti, B. B. Buckley, C. G. Van de Walle, and D. D. Awschalom. Quantum computing with defects. *Proceedings of the National Academy of Sciences*, 107(19):8513–8518, 2010.

[262] M. S. Rill, C.e Plet, M. Thiel, I. Staude, G. von Freymann, S. Linden, and M. Wegener. Photonic metamaterials by direct laser writing and silver chemical vapour deposition. *Nature Materials*, 7(7):543–546, 2008.

[263] S. W. Hell, S. Lindek, C. Cremer, and E. H. K. Stelzer. Confocal microscopy with an increased detection aperture: type-b 4pi confocal microscopy. *Optics Letters*, 19(3):222–224, 1994.

[264] J. T. Choy, I. Bulu, B. J. M. Hausmann, E. Janitz, I. Huang, and M. Lončar. Spontaneous emission and collection efficiency enhancement of single emitters in diamond via plasmonic cavities and gratings. *Applied Physics Letters*, 103: 161101, 2013.

[265] L. Marseglia, J. P. Hadden, A. C. Stanley-Clarke, J. P. Harrison, B. Patton, Y.-L. D. Ho, B. Naydenov, F. Jelezko, J. Meijer, P. R. Dolan, J. M. Smith, J. G. Rarity, and J. L. O'Brien. Nanofabricated solid immersion lenses registered to single emitters in diamond. *Applied Physics Letters*, 98(13):133107, 2011.

[266] A. Badolato, K. Hennessy, M Atatüre, J. Dreiser, E. Hu, P. M. Petroff, and A. Imamoglu. Deterministic coupling of single quantum dots to single nanocavity modes. *Science*, 308(5725):1158–1161, 2005.

[267] L. Fleury, Ph. Tamarat, B. Lounis, J. Bernard, and M. Orrit. Fluorescence spectra of single pentacene molecules in p-terphenyl at 1.7 k. *Chemical Physics Letters*, 236(12):87 – 95, 1995.

[268] A. Drechsler, M. Lieb, C. Debus, A. Meixner, and G. Tarrach. Confocal microscopy with a high numerical aperture parabolic mirror. *Optics Express*, 9(12):637–644, 2001.

[269] N. Davidson and N. Bokor. High-numerical-aperture focusing of radially polarizeddoughnut beams with a parabolic mirror and a flat diffractivelens. *Optics Letters*, 29(12):1318–1320, 2004.

[270] J. Stadler, C. Stanciu, C. Stupperich, and A. J. Meixner. Tighter focusing with a parabolic mirror. *Optics Letters*, 33(7):681–683, 2008.

[271] E. F. Bond, D. Beresford, and G. H. Haggis. Improved cathodoluminescence microscopy. *Journal of Microscopy*, 100(3):271–282, 1974.

[272] A. Hartschuh. Tip-enhanced near-field optical microscopy. *Angewandte Chemie International Edition*, 47(43):8178–8191, 2008.

[273] R. Maiwald, D. Leibfried, J. Britton, J. C. Bergquist, G. Leuchs, and D. J. Wineland. Stylus ion trap for enhanced access and sensing. *Nature Physics*, 5(8):551–554, 2009.

[274] J. Fischer, J. B. Mueller, J. Kaschke, T. J. A. Wolf, A.-N. Unterreiner, and M. Wegener. Three-dimensional multi-photon direct laser writing with variable repetition rate. *Optics Express*, 21(22):26244–26260, 2013.

[275] A. G. Curto, G. Volpe, T. H. Taminiau, M. P. Kreuzer, R. Quidant, and N. F. van Hulst. Unidirectional emission of a quantum dot coupled to a nanoantenna. *Science*, 329(5994):930–933, 2010.

[276] J. W. Goodman. *Introduction to Fourier optics*. Roberts and Company Publishers, 2005.

[277] G. Kewes, A. W. Schell, R. Henze, R. S. Schonfeld, S. Burger, K. Busch, and O. Benson. Design and numerical optimization of an easy-to-fabricate photon-to-plasmon coupler for quantum plasmonics. *Applied Physics Letters*, 102(5):051104, 2013.

[278] R. W. Boyd. *Nonlinear optics*. Academic press, 2003.

[279] C. F. Bohren and D.R. Huffman. *Absorption and scattering of light by small particles*. Wiley science paperback series. Wiley, 1983.

[280] A. Vial, A.-S. Grimault, D. Macias, D. Barchiesi, and M. L. de la Chapelle. Improved analytical fit of gold dispersion: application to the modeling of extinction spectra with a finite-difference time-domain method. *Physical Review B*, 71:085416, 2005.

[281] U. Kreibig. Electronic properties of small silver particles: the optical constants and their temperature dependence. *Journal of Physics F: Metal Physics*, 4(7):999, 1974.

[282] K. J. Savage, M. M. Hawkeye, R. Esteban, A. G. Borisov, J. Aizpurua, and J. J. Baumberg. Revealing the quantum regime in tunnelling plasmonics. *Nature*, 491(7425):574–577, 2012.

[283] J. A. Scholl, A. Garcia-Etxarri, A. L. Koh, and J. A. Dionne. Observation of quantum tunneling between two plasmonic nanoparticles. *Nano Letters*, 13 (2):564–569, 2013.

[284] S. A. Maier. *Plasmonics: Fundamentals and Applications*. Springer Science+Business Media, LLC, 2007.

[285] J. M. Pitarke, V. M. Silkin, E. V. Chulkov, and P. M. Echenique. Theory of surface plasmons and surface-plasmon polaritons. *Reports on Progress in Physics*, 70(1):1, 2007.

[286] W. L. Barnes, A. Dereux, and T. W. Ebbesen. Surface plasmon subwavelength optics. *Nature*, 424(6950):824–830, 2003.

[287] P. B. Johnson and R. W. Christy. Optical constants of the noble metals. *Physical Review B*, 6:4370–4379, 1972.

[288] E. T. Arakawa, M. W. Williams, R. N. Hamm, and R. H. Ritchie. Effect of damping on surface plasmon dispersion. *Physical Review Letters*, 31:1127–1129, 1973.

[289] Z. Han and Sergey I. B. Radiation guiding with surface plasmon polaritons. *Reports on Progress in Physics*, 76(1):016402, 2013.

[290] D. E. Chang, A. S. Sorensen, E. A. Demler, and M. D. Lukin. A single-photon transistor using nanoscale surface plasmons. *Nature Physics*, 3(11):807–812, 2007.

[291] E. Kretschmann. Die Bestimmung optischer Konstanten von Metallen durch Anregung von Oberflächenplasmaschwingungen. *Zeitschrift für Physik*, 241 (4):313–324, 1971.

[292] A. Otto. Excitation of nonradiative surface plasma waves in silver by the method of frustrated total reflection. *Zeitschrift fur Physik*, 216(4):398–410, 1968.

[293] R. W. Wood. On a remarkable case of uneven distribution of light in a diffraction grating spectrum. *Proceedings of the Physical Society of London*, 18(1):269, 1902.

[294] D. Maystre. Theory of wood's anomalies. In Stefan Enoch and Nicolas Bonod, editors, *Plasmonics*, volume 167 of *Springer Series in Optical Sciences*, pages 39–83. Springer Berlin Heidelberg, 2012.

[295] F. Zenhausern, M. P. O'Boyle, and H. K. Wickramasinghe. Apertureless near-field optical microscope. *Applied Physics Letters*, 65(13):1623–1625, 1994.

[296] B. Hecht, B. Sick, U. P. Wild, V. Deckert, R. Zenobi, O. J. F. Martin, and D. W. Pohl. Scanning near-field optical microscopy with aperture probes: Fundamentals and applications. *The Journal of Chemical Physics*, 112(18): 7761–7774, 2000.

[297] F. J. García de Abajo. Optical excitations in electron microscopy. *Review of Modern Physics*, 82:209–275, 2010.

[298] J. K. Gimzewski, J. K. Sass, R. R. Schlitter, and J. Schott. Enhanced photon emission in scanning tunnelling microscopy. *EPL (Europhysics Letters)*, 8(5): 435, 1989.

[299] B. Steinberger, A. Hohenau, H. Ditlbacher, A. L. Stepanov, A. Drezet, F. R. Aussenegg, A. Leitner, and J. R. Krenn. Dielectric stripes on gold as surface plasmon waveguides. *Applied Physics Letters*, 88(9):094104, 2006.

[300] T. Holmgaard and S. I. Bozhevolnyi. Theoretical analysis of dielectric-loaded surface plasmon-polariton waveguides. *Physical Review B*, 75:245405, 2007.

[301] P. Berini. Long-range surface plasmon polaritons. *Advances in Optics and Photonics*, 1(3):484–588, 2009.

[302] K. Tanaka and M. Tanaka. Simulations of nanometric optical circuits based on surface plasmon polariton gap waveguide. *Applied Physics Letters*, 82(8): 1158–1160, 2003.

[303] L. Liu, Z.Han, and S. He. Novel surface plasmon waveguide for high integration. *Optics Express*, 13(17):6645–6650, 2005.

[304] D. F. P. Pile, T. Ogawa, D. K. Gramotnev, T. Okamoto, M. Haraguchi, M. Fukui, and S. Matsuo. Theoretical and experimental investigation of strongly localized plasmons on triangular metal wedges for subwavelength waveguiding. *Applied Physics Letters*, 87(6):061106, 2005.

[305] S. I. Bozhevolnyi, V. S. Volkov, E. Devaux, J.-Y. Laluet, and T. W. Ebbesen. Channel plasmon subwavelength waveguide components including interferometers and ring resonators. *Nature*, 440(7083):508–511, 2006.

[306] H. Ditlbacher, A. Hohenau, D. Wagner, U. Kreibig, M. Rogers, F. Hofer, F. R. Aussenegg, and J. R. Krenn. Silver nanowires as surface plasmon resonators. *Physical Review Letters*, 95:257403, 2005.

[307] J. Takahara, S. Yamagishi, H. Taki, A. Morimoto, and T. Kobayashi. Guiding of a one-dimensional optical beam with nanometer diameter. *Optics Letters*, 22(7):475–477, 1997.

[308] C. S. Kim, I. Vurgaftman, R. A. Flynn, M. Kim, J. R. Lindle, W. W. Bewley, K. Bussmann, J. R. Meyer, and J. P. Long. An integrated surface-plasmon source. *Optics Express*, 18(10):10609–10615, 2010.

[309] D. K. Gramotnev and S. I. Bozhevolnyi. Plasmonics beyond the diffraction limit. *Nature Photonics*, 4(2):83–91, 2010.

[310] E. Verhagen, A. Polman, and L. K. Kuipers. Nanofocusing in laterally tapered plasmonic waveguides. *Optics Express*, 16(1):45–57, 2008.

[311] V. S. Volkov, S. I. Bozhevolnyi, S. G. Rodrigo, L. Martin-Moreno, F. J. Garcia-Vidal, E. Devaux, and T. W. Ebbesen. Nanofocusing with channel plasmon polaritons. *Nano Letters*, 9(3):1278–1282, 2009.

[312] M. Schnell, P. Alonso-Gonzalez, L. Arzubiaga, F. Casanova, L. E., Hueso, A. Chuvilin, and R. Hillenbrand. Nanofocusing of mid-infrared energy with tapered transmission lines. *Nature Photonics*, 5(5):283–287, 2011.

[313] M. I. Stockman. Nanofocusing of optical energy in tapered plasmonic waveguides. *Physical Review Letters*, 93:137404, 2004.

[314] A. Polman. Plasmonics applied. *Science*, 322(5903):868–869, 2008.

[315] C. C. Neacsu, S. Berweger, R. L. Olmon, L. V. Saraf, C. Ropers, and M. B. Raschke. Near-field localization in plasmonic superfocusing: A nanoemitter on a tip. *Nano Letters*, 10(2):592–596, 2010.

[316] J. Homola, S. S. Yee, and G.Gauglitz. Surface plasmon resonance sensors: review. *Sensors and Actuators B: Chemical*, 54:3 – 15, 1999.

[317] J. Homola. Surface plasmon resonance sensors for detection of chemical and biological species. *Chemical Reviews*, 108(2):462–493, 2008.

[318] E. Ozbay. Plasmonics: Merging photonics and electronics at nanoscale dimensions. *Science*, 311(5758):189–193, 2006.

[319] J. A. Schuller, E. S. Barnard, W. Cai, Y. C. Jun, J. S. White, and M. L. Brongersma. Plasmonics for extreme light concentration and manipulation. *Nature Materials*, 9(3):193–204, 2010.

[320] A. Cuche, O. Mollet, A. Drezet, and S. Huant. "deterministic" quantum plasmonics. *Nano Letters*, 10(11):4566–4570, 2010.

[321] R. Kolesov, B. Grotz, G. Balasubramanian, R. J. Stohr, A. A. L. Nicolet, P. R. Hemmer, F. Jelezko, and J. Wrachtrup. Wave-particle duality of single surface plasmon polaritons. *Nature Physics*, 5(7):470–474, 2009.

[322] A. V. Akimov, A. Mukherjee, C. L. Yu, D. E. Chang, A. S. Zibrov, P. R. Hemmer, H. Park, and M. D. Lukin. Generation of single optical plasmons in metallic nanowires coupled to quantum dots. *Nature*, 450(7168):402–406, 2007.

[323] Y. Fedutik, V. V. Temnov, O. Schöps, U. Woggon, and M. V. Artemyev. Exciton-plasmon-photon conversion in plasmonic nanostructures. *Physical Review Letters*, 99:136802, 2007.

[324] H. Wei, D. Ratchford, X. Li, H. Xu, and C.-K. Shih. Propagating surface plasmon induced photon emission from quantum dots. *Nano Letters*, 9(12): 4168–4171, 2009.

[325] D. E. Chang, A. S. Sørensen, P. R. Hemmer, and M. D. Lukin. Quantum optics with surface plasmons. *Physical Review Letters*, 97(5):053002, 2006.

[326] J. L. Elechiguerra, L. Larios-Lopez, C. Liu, D. Garcia-Gutierrez, A. Camacho-Bragado, and M. J. Yacaman. Corrosion at the nanoscale: The case of silver nanowires and nanoparticles. *Chemistry of Materials*, 17(24):6042–6052, 2005.

[327] J. Jin. *The finite element method in electromagnetics*. John Wiley & Sons, 2014.

[328] T. Bååk. Silicon oxynitride; a material for grin optics. *Applied Optics*, 21(6): 1069–1072, 1982.

[329] G. Ghosh. Dispersion-equation coefficients for the refractive index and birefringence of calcite and quartz crystals. *Optics Communications*, 163:95 – 102, 1999.

[330] B. D. Cobb and J. M. CIarkson. A simple procedure for optimising the polymerase chain reaction (pcr) using modified taguchi methods. *Nucleic Acids Research*, 22(18):3801–3805, 1994.

[331] Q. Li, Y. Song, G. Zhou, Y. Su, and M. Qiu. Asymmetric plasmonic-dielectric coupler with short coupling length, high extinction ratio, and low insertion loss. *Optics Letters*, 35(19):3153–3155, 2010.

[332] N. Nozhat and N. Granpayeh. Analysis of the plasmonic power splitter and mux/demux suitable for photonic integrated circuits. *Optics Communications*, 284(13):3449 – 3455, 2011.

[333] B. Zhang and S. Du. Circular arc plasmonic waveguide couplers between two-dimensional dielectric slab waveguides and plasmonic waveguides. *Optics Communications*, 281(23):5756 – 5759, 2008.

[334] R. A. Wahsheh, Z. Lu, and M. A. G. Abushagur. Nanoplasmonic couplers and splitters. *Optics Express*, 17(21):19033–19040, 2009.

[335] M. J. Dodge. Refractive properties of magnesium fluoride. *Applied Optics*, 23(12):1980–1985, 1984.

[336] P. Bharadwaj, B. Deutsch, and L. Novotny. Optical antennas. *Advances in Optics and Photonics*, 1(3):438–483, 2009.

[337] W. L. Barnes. Fluorescence near interfaces: The role of photonic mode density. *Journal of Modern Optics*, 45(4):661–699, 1998.

[338] W. Lukosz and R. E. Kunz. Light emission by magnetic and electric dipoles close to a plane interface. i. total radiated power. *Journal of the Optical Society of America*, 67(12):1607–1615, 1977.

[339] W. Lukosz and R. E. Kunz. Light emission by magnetic and electric dipoles close to a plane dielectric interface. ii. radiation patterns of perpendicular oriented dipoles. *Journal of the Optical Society of America*, 67(12):1615–1619, 1977.

[340] S. K. Sekatskii and V. S. Letokhov. Single fluorescence centers on the tips of crystal needles: First observation and prospects for application in scanning one-atom fluorescence microscopy. *Applied Physics B*, 63(5):525–530, 1996.

[341] J.-P. Tetienne, L. Rondin, P. Spinicelli, M. Chipaux, T. Debuisschert, J.-F. Roch, and V. Jacques. Magnetic-field-dependent photodynamics of single nv defects in diamond: an application to qualitative all-optical magnetic imaging. *New Journal of Physics*, 14(10):103033, 2012.

[342] J. Michaelis, C. Hettich, J. Mlynek, and V. Sandoghdar. Optical microscopy using a single-molecule light source. *Nature*, 405(6784):325–328, 2000.

[343] D. Englund, A. Faraon, A. Majumdar, N. Stoltz, P. Petroff, and J. Vuckovic. An optical modulator based on a single strongly coupled quantum dot - cavity system in a p-i-n junction. *Optics Express*, 17(21):18651–18658, 2009.

[344] D. M. Callahan, J. N. Munday, and H. A. Atwater. Solar cell light trapping beyond the ray optic limit. *Nano Letters*, 12(1):214–218, 2012.

[345] U. Hoeppe, C. Wolff, J. Küchenmeister, J. Niegemann, M. Drescher, H. Benner, and K. Busch. Direct observation of non-markovian radiation dynamics in 3d bulk photonic crystals. *Physical Review Letters*, 108:043603, 2012.

[346] L. Novotny and N. van Hulst. Antennas for light. *Nature Photonics*, 5(2): 83–90, 2011.

[347] C. L. Cortes, W. Newman, S. Molesky, and Z. Jacob. Quantum nanophotonics using hyperbolic metamaterials. *Journal of Optics*, 14(6):063001, 2012.

[348] J. P. Hoogenboom, G. Sanchez-Mosteiro, G. Colas des Francs, D. Heinis, G. Legay, A. Dereux, and N. F. van Hulst. The single molecule probe: Nanoscale vectorial mapping of photonic mode density in a metal nanocavity. *Nano Letters*, 9(3):1189–1195, 2009.

[349] K. Imura, T. Nagahara, and H. Okamoto. Near-field optical imaging of plasmon modes in gold nanorods. *The Journal of Chemical Physics*, 122(15): 154701, 2005.

[350] Y. De Wilde, F. Formanek, R. Carminati, B. Gralak, P.-A. Lemoine, K. Joulain, J.-P. Mulet, and J.-J. Chen, Y.and Greffet. Thermal radiation scanning tunnelling microscopy. *Nature*, 444(7120):740–743, 2006.

[351] R. Beams, D. Smith, T. W. Johnson, S.-H. Oh, L. Novotny, and A. N. Vamivakas. Nanoscale fluorescence lifetime imaging of an optical antenna with a single diamond nv center. *Nano Letters*, 13(8):3807–3811, 2013.

[352] C. Ropp, Z. Cummins, S. Nah, J. T. Fourkas, B. Shapiro, and E. Waks. Nanoscale imaging and spontaneous emission control with a single nanopositioned quantum dot. *Nature Communications*, 4:1447, 2013.

[353] M. Geiselmann, M. L. Juan, J. Renger, J. M. Say, L. J. Brown, F. J. G. de Abajo, F. Koppens, and R. Quidant. Three-dimensional optical manipulation of a single electron spin. *Nature Nanotechnology*, 8:175–179, 2013.

[354] R. Sapienza, T. Coenen, J. Renger, M. Kuttge, N. F. van Hulst, and A. Polman. Deep-subwavelength imaging of the modal dispersion of light. *Nature Materials*, 11(9):781–787, 2012.

[355] M. Frimmer, Y. Chen, and A. F. Koenderink. Scanning emitter lifetime imaging microscopy for spontaneous emission control. *Physical Review Letters*, 107:123602, 2011.

[356] A. Cuche, A. Drezet, Y. Sonnefraud, O. Faklaris, F. Treussart, J.-F. Roch, and S. Huant. Near-field optical microscopy with a nanodiamond-based single-photon tip. *Optics Express*, 17(22):19969–19980, 2009.

[357] P. Maletinsky, S. Hong, M. S. Grinolds, B. Hausmann, M. D. Lukin, R. L. Walsworth, M. Loncar, and A. Yacoby. A robust scanning diamond sensor for nanoscale imaging with single nitrogen-vacancy centres. *Nature Nanotechnology*, 7(5):320–324, 2012.

[358] O. L. Muskens, V. Giannini, J. A. Sanchez-Gil, and J. Gomez Rivas. Strong enhancement of the radiative decay rate of emitters by single plasmonic nanoantennas. *Nano Letters*, 7(9):2871–2875, 2007.

[359] R. Esteban, T. V. Teperik, and J. J. Greffet. Optical patch antennas for single photon emission using surface plasmon resonances. *Physical Review Letters*, 104(2):026802, 2010.

[360] A. Kinkhabwala, Z. Yu, S. Fan, Y. Avlasevich, K. Mullen, and W. E. Moerner. Large single-molecule fluorescence enhancements produced by a bowtie nanoantenna. *Nature Photonics*, 3(11):654–657, 2009.

[361] J. Merlein, M. Kahl, A. Zuschlag, A. Sell, A. Halm, J. Boneberg, P. Leiderer, A. Leitenstorfer, and R. Bratschitsch. Nanomechanical control of an optical antenna. *Nature Photonics*, 2(4):230–233, 2008.

[362] J. N. Farahani, D. W. Pohl, H.-J. Eisler, and B. Hecht. Single quantum dot coupled to a scanning optical antenna: A tunable superemitter. *Physical Review Letters*, 95(1):017402, 2005.

[363] M. D. Wissert, A. W. Schell, K. S. Ilin, M. Siegel, and H.-J. Eisler. Nanoengineering and characterization of gold dipole nanoantennas with enhanced integrated scattering properties. *Nanotechnology*, 20(42):425203, 2009.

[364] G. Habenicht. *Kleben-erfolgreich und fehlerfrei: Handwerk, Praktiker, Ausbildung, Industrie*. Springer-Verlag, 2008.

[365] A. Cuche, A. Drezet, J.-F. Roch, F. Treussart, and S. Huant. Grafting fluorescent nanodiamonds onto optical tips. *Journal of Nanophotonics*, 4(1): 043506, 2010.

[366] K. Busch, M. König, and J. Niegemann. Discontinuous galerkin methods in nanophotonics. *Laser & Photonics Reviews*, 5(6):773–809, 2011. ISSN 1863-8899.

[367] S. Descombes, C. Durochat, S. Lanteri, L. Moya, C. Scheid, and J. Viquerat. Recent advances on a DGTD method for time-domain electromagnetics. *Photonics and Nanostructures - Fundamentals and Applications*, 11(4):291 – 302, 2013. ISSN 1569-4410.

[368] M. A. Paesler and P. J. Moyer. Near-field optics. In *Society of Photo-Optical Instrumentation Engineers (SPIE) Conference Series*, volume 2535, 1995.

[369] D. R. Lide, editor. *CRC Handbook of Chemistry and Physics : a ready-reference book of chemical and physical data*. CRC Press, 83 edition, 2002–2003.

[370] T. H. Taminiau, S. Karaveli, N. F. van Hulst, and R. Zia. Quantifying the magnetic nature of light emission. *Nature Communications*, 3:979, 2012.

[371] P. Tighineanu, M. L. Andersen, A. S. Sørensen, S. Stobbe, and P. Lodahl. Probing electric and magnetic vacuum fluctuations with quantum dots. *Physical Review Letters*, 113:043601, 2014.

[372] L. Aigouy, A. Cazé, P. Gredin, M. Mortier, and R. Carminati. Mapping and quantifying electric and magnetic dipole luminescence at the nanoscale. *Physical Review Letters*, 113:076101, 2014.

[373] I. V. Fedotov, L. V. Doronina-Amitonova, A. A. Voronin, A. O. Levchenko, S. A. Zibrov, D. A. Sidorov-Biryukov, A. B. Fedotov, V. L. Velichansky, and A. M. Zheltikov. Electron spin manipulation and readout through an optical fiber. *Scientific Reports*, 4:5362, 2014.

[374] D. M. Sullivan. *Electromagnetic simulation using the FDTD method*. Wiley-IEEE Press, 2013.

[375] K. Yee. Numerical solution of initial boundary value problems involving maxwell's equations in isotropic media. *Antennas and Propagation, IEEE Transactions on*, 14(3):302–307, 1966.

[376] M. Barth. *Hybrid Nanophotonic Elements and sensing Devices Based on Photonic Crystal Structures*. PhD thesis, Humboldt-Universität zu Berlin, 2010.

[377] Y. Xu, R. K. Lee, and A. Yariv. Quantum analysis and the classical analysis of spontaneous emission in a microcavity. *Physical Review A*, 61:033807, 2000.

List of Own Work

Publications Forming the Basis of this Thesis

The following publications form the basis of this thesis. Other peer-reviewed publications by the author are given in the next Section.

1. **Schell, A.W.**, Neumer, T., Shi, Q., Kaschke, J., Fischer, J., Wegener, M., Benson, O. Laser-written parabolic micro-antennas for efficient photon collection from single NV centers
   submitted (2014)
   This publication is used especially in Section 7.5.2.

2. **Schell, A. W.**, Neumer, T., Benson, O.
   Numerical analysis of efficient light extraction with an elliptical solid immersion lens
   Optics Letters 39, 4639–4642 (2014)
   This publication is used especially in Section 4.3.

3. **Schell, A. W.**, Engel P., Werra, J. F. M., Wolff, C., Busch, K., Benson, O.
   Scanning single quantum emitter fluorescence lifetime imaging: quantitative analysis of the local density of photonic states
   Nano Letters 14, 2623–2627 (2014)
   This publication is used especially in Section 9.3.

4. **Schell, A.W.**, Kaschke, J., Fischer, J., Henze, R., Wolters, J., Wegener, M., Benson, O. Three-dimensional quantum photonic elements based on single nitrogen vacancy-centres in laser-written microstructures
   Scientific Reports 3, 1577 (2013)
   This publication is used especially in Section 7.4.

5. Kewes, G., **Schell, A. W.**, Henze, R., Schönfeld, R. S., Burger, S., Busch, K., Benson, O.
   Design and numerical optimization of an easy-to-fabricate photon-to-plasmon coupler for quantum plasmonics
   Applied Physics Letters 102, 051104 (2013)
   This publication is used especially in Section 8.3.

6. Wolters, J., Sadzak, N., **Schell A. W.**, Schröder, T., Benson, O.
Measurement of the Ultrafast Spectral Diffusion of the Optical Transition of Nitrogen Vacancy Centers in Nano-Size Diamond Using Correlation Interferometry
Physical Review Letters 110, 027401 (2013)
This publication is used especially in Section 3.6.

7. Wolters, J., Kewes, G., **Schell A. W.**, Nüsse, N., Schoengen, M., Löchel, B., Hanke, T., Bratschitsch, R., Leitenstorfer, A., Aichele, T., and Benson, O.
Coupling of single nitrogen-vacancy defect centers in diamond nanocrystals to optical antennas and photonic crystal cavities
physica status solidi (b) 249, 918–924 (2012)
This publication is used especially in Sections 6.1 and 8.2.

8. **Schell A. W.**, Kewes, G., Schröder, T., Wolters, J., Aichele, T., and Benson, O.
A scanning probe-based pick-and-place procedure for assembly of integrated quantum optical hybrid devices
Review of Scientific Instruments 82, 073709 (2011)
This publication is used especially in Section 5.3.

9. **Schell A. W.**, Kewes, G., Hanke, T., Leitenstorfer, A., Bratschitsch, R., Benson, O. and Aichele, T.
Single defect centers in diamond nanocrystals as quantum probes for plasmonic nanostructures
Optics Express 19, 7914-7920 (2011)
This publication is used especially in Sections 8.2 and 9.2.

10. Schröder, T., **Schell A. W.**, Kewes, G., Aichele, T., and Benson, O.
Fiber-Integrated Diamond-Based Single Photon Source
Nano Letters 11, 198-202 (2011)
This publication is used especially in Section 6.2.

11. Wolters, J., **Schell A. W.**, Kewes, G., Nuesse, N., Schoengen, M., Doescher, H., Hannappel, T., Loechel, B., Barth, M. and Benson, O.
Enhancement of the zero phonon line emission from a single nitrogen vacancy center in a nanodiamond via coupling to a photonic crystal cavity
Applied Physics Letters 97, 141108 (2010)
This publication is used especially in Section 6.1.

Other Publications

12. **Schell, A. W.**, Takshima, H., Kamioka, S., Oe, Y., Fujiwara, M., Benson, O., Takeuchi, S.
Ultra-Wide Tunable Nanoibre Cavity With Large Emitter Coupling Effciency for Integrated Quantum Optics and Photonics
submitted (2014)

13. Albrecht, R., Bommer, A., Pauly, C., Mücklich, F., **Schell, A. W.**, Engel, P., Schröder, T., Benson, O., Reichel, J., Becher, C.
Narrow-band single photon emission at room temperature based on a single nitrogen-vacancy center coupled to an all-fiber-cavity
Applied Physics Letters 105, 073113 (2014)

14. Kuhlicke, A., **Schell, A. W.**, Zoll, J., Benson, O.
Nitrogen vacancy center fluorescence from a submicron diamond cluster levitated in a linear quadrupole ion trap
Applied Physics Letters 105, 073101 (2014)

15. Liebermeister, L., Petersen, F., Münchow, A. v., Burchardt, D., Hermelbracht, J., Tashima, T., **Schell, A. W.**, Benson, O., Meinhardt, T., Krueger, A., Stiebeiner, A., Rauschenbeutel, A., Weinfurter, H., Weber, M.
Tapered fiber coupling of single photons emitted by a deterministically positioned single nitrogen vacancy centers
Applied Physics Letters 104, 031101 (2014)

16. Wolters, J., Nikolay, N., Schoengen, M., **Schell, A. W.**, Probst, J., Löchel, B., Benson, O.
Thermo-optical response of photonic crystal cavities operating in the visible spectral range
Nanotechnology 24, 315204 (2013)

17. Wahl, M., Rohlicke, T., Rahn, H. J., Erdmann, R., Kell, G., Ahlrichs, A., Kernbach, M., **Schell A. W.**, Benson, O.
Integrated multichannel photon timing instrument with very short dead time and high throughput
Review of Scientific Instruments 84, 043102 (2013)

18. Wu, S., **Schell A. W.**, Lublow, M., Kaiser, J., Aichele, T., Schietinger, S., Polzer, F., Kühn, S., Guo, X., Benson, O., Ballauff, M., Lu, Y.
Silica coated Au/Ag Nanorods with Tunable Surface Plasmon Bands for Nanoplasmonics with Single Particles
Colloid and Polymer Science 291, 585-594 (2013)

19. Benyoucef, M., Zuerbig, V., Reithmaier J.P., Kroh, T., **Schell A. W.**, Aichele, T., Benson, O.
Single-photon emission from single InGaAs/GaAs quantum dots grown by droplet epitaxy at high substrate temperature
Nanoscale Research Letters 7, 493 (2012)

20. Wissert, M. D., **Schell A. W.**, Ilin, K. S., Siegel, M. and Eisler, H.-J.
Nanoengineering and characterization of gold dipole nanoantennas with enhanced integrated scattering properties
Nanotechnology 20, 425203 (2009)

Book Chapters

21. **Schell, A. W.**, Wolters, J., Schröder, T., Benson, O., Using defect centres in diamonds to build photonic and quantum optical devices
in Quantum Information Processing with Diamond: Principles and Applications
edited by Steven Prawer, Igor Aharonovich 2014

Patent Applications

1. undisclosed application
Year: 2013

2. **Schell, A.**, Henze, R., Benson, O., Kewes G.
Photon-to-plasmon coupler
Application numbeR: US 13/770,157, Date of filing: Feb 19, 2013

3. Schröder, T., Benson, O., **Schell, A.**, Engel, P., Bahnholzer M. J., Gädeke, F., Birkl, G.
SINGLE PHOTON EMISSION SYSTEM
Application number: PCT/EP2011/064223, Date of filing: 18.08.2011

4. Eisler, H.-J., **Schell, A.**, Wissert, M
Beam transformation module with an axicon in a double-pass mode
Application number: EP20080022404, Date of filing: 23.12.2008

Conference Contributions

Conference Proceedings

1. **Schell, A. W.**, Neumer, T., Qiang, S., Kaschke, J., Fischer, J., Wegener, M., Benson, O.
   Laser-Written Microstructures for Enhanced Single-Photon Collection Efficiency
   CLEO: QELS Fundamental Science (CLEO QELS) 2014, JW2A.122

2. **Schell, A. W.**, Neumer, T., Qiang, S., Kaschke, J., Fischer, J., Henze, R., Wolters, J., Wegener, M., Benson, O.
   On-Chip Integration of NV Centers in Three-Dimensional Laser-Written Microstructures for Single Photon Applications
   Quantum Information and Measurement (QIM) 2014, QTu3B.5

3. **Schell, A. W.**, Engel, P., Benson, O.
   Scanning Quantum Emitter Fluorescence Lifetime Imaging in Three Dimensions Using a Single NV Center
   Frontiers in Optics (FiO) 2013, FTu1C.2

4. **Schell, A. W.**, Neumer, T., Qiang, S., Kaschke, J., Fischer, J., Henze, R., Wolters, J., Wegener, M., Benson, O.
   Nanophotonics with Single Photons from NV Centers in Three-Dimensional Laser-Written Microstructures
   Frontiers in Optics (FiO) 2013, FW1C.2

5. **Schell, A. W.**, Kaschke, J., Fischer, J., Henze, R., Wolters, J., Wegener, M., Benson, O.
   Single Photon Nanophotonics Using NV Centers in Three-Dimensional Laser-Written Microstructures
   The European Conference on Lasers and Electro-Optics (CLEO_Europe) 2013, CK_7_1

6. **Schell, A. W.**, Engel, P., Benson, O.
   Single NV Centers in Nanodiamond as Three Dimensional Scanning Lifetime Probe
   International Quantum Electronics Conference (IQEC) 2013, IH_1_3

7. **Schell, A. W.**, Wolters, J., Kewes, G,. Schröder, T,. Aichele, T., Benson, O.
   Assembly of Quantum Optical Hybrid Devices via a Scanning Probe Pick-and-Place Technique
   Quantum Electronics and Laser Science Conference (QELS) 2012, QW3H.2

8. Schröder, T., Fujiwara, M., Noda, T., Zhao, H.-Q., **Schell, A. W.**, Kewes, G., Benson, O., Takeuchi, S.
Near-field coupling of a single NV center to a tapered fibers
Published in Proceedings Volume 8272, 2012, Advances in Photonics of Quantum Computing, Memory, and Communication V, 827209

9. Wolters, J., **Schell, A. W.**, Sadzak, N., Schröder, T., Schoengen, M., Probst, J., Löchel, B., Benson, O. J.
Nanodiamonds for Integrated Quantum Technology: Charm and Challenge
Quantum Information and Measurement (QIM) 2012, QW1B.3

10. Schröder, T., **Schell, A. W.**, Gädeke, F., Kewes, G., Aichele, T., Benson, O.
Ultra-bright and efficient single photon generation based on integrated nanodiamonds containing single defect centers
Quantum Electronics and Laser Science Conference (QELS) 2011, QFG1

11. Schröder, T., **Schell, A. W.**, Kewes, G., Barth, M., Aichele, T., Benson, O.
Integrated photonic quantum technologies with fiber-integrated single photon emitters
Published in Proceedings Volume 7943, 2011, Silicon Photonics VI, 79431

12. Aichele, T., **Schell, A.**, Barth, M., Schröder, T., Wolters, J., Benson, O., Nüsse, N., Löchel, B.
Assembly of fundamental photonic elements from single nanodiamonds
IEEE Photonics Society, 2010 23rd Annual Meeting of the, 2010, 142 - 143

Own Talks Without Proceedings

13. **Schell, A. W.** (stand in for Benson, O.)
Prospects of diamond defect centers as quantum light sources
Photonics West 2014, 8994-17 **(invited)**

14. **Schell, A. W.**, Engel, P., Benson, O.
Scanning single-emitter fluorescence lifetime imaging
Photonics West 2014, 8993-86

15. **Schell, A. W.**
Scanning probes based on single quantum emitters for lifetime imaging and nanomagnetometry
Adlershofer Forschungsforum 2013 **(invited)**

16. **Schell, A. W.**
Three dimensional scanning lifetime microscopy using single NV centers in nanodiamond
538. WE-Heraeus-Seminar, 2013

17. **Schell, A. W.**, Kaschke, J., Fischer, J., Henze, R., Wolters, J., Wegener, M., Benson, O.
NV-centers as single-photon emitters integrated into three-dimensional laser-written micro-structures
DPG Tagung Hannover 2013, Q 9.5

18. **Schell, A. W.**, Engel, P., Benson, O.
Scanning probe techniques in quantum plasmonics
DPG Tagung Regensburg 2013, Q 86.4

19. **Schell, A. W.**, Kaschke, J., Fischer, J., Henze, R., Wolters, J., Wegener, M., Benson, O.
Three-dimensional quantum photonic elements based on nanodiamonds in laser-written 3D microstructures
Photonics West 2013, 8635-15

20. **Schell, A. W.**, Kewes G., Wolters, J., Schröder, T., Aichele, T., Benson, O.
A pick-and-place technique for the assembly of integrated quantum optical hybrid devices
DPG Tagung Stuttgart 2012, Q 23.8

21. **Schell, A. W.**, Kewes G., Wolters, J., Schröder, T., Aichele, T., Benson, O.
A pick-and-place technique for the assembly of integrated quantum optical hybrid devices
DPG Tagung Berlin 2012, Q 19.6

22. **Schell, A. W.**, Aichele, T., Benson, O.
Assembly and coupling of diamond nanocrytsals to photonic- and plasmonic nanostructures
DPG Tagung Hannover 2010, Q 60.8

Own Posters Without Proceedings

23. **Schell, A. W.**, Neumer, T., Engel, P., Kewes G., Wolters, J., Benson, O.
Hybrid integration of nanodiamonds containing single NV centers
KAKENHI Quantum Cybernetic Winter Meeting 2013

24. **Schell, A. W.**, Neumer, T., Engel, P., Kewes G., Wolters, J., Benson, O.
Building hybrid quantum systems using nanodiamonds
Quantum Information Processing and communication, Florence, 2013

25. **Schell, A. W.**, Engel, P., Kewes G., Wolters, J., Benson, O.
Coupling of NV-centres to photonic and plasmonic structures
519th WE-Heraeus-Seminar - Hybrid Quantum Systems 2012

26. **Schell, A. W.**, Kewes G., Wolters, J., Schoengen, M., Schröder, T., Aichele, T., Benson, O.
Hybrid Quantum Nanostructures and Plasmonics
491. Wilhelm und Else Heraeus-Seminar - Quantum and Nano Plasmonics 2011

27. **Schell, A. W.**, Kewes G., Wolters, J., Schoengen, M., Schröder, T., Aichele, T., Benson, O.
Hybrid Quantum Nanostructures and Plasmonics
KOSMOS summer school 2011

Student Supervision

Diploma and Master Students

1. Tanja Neumer
Thesis title: *Design and Characterisation of Light Collecting Microstructures Fabricated by Direct Laser-Writing* (2014)

2. Philip Engel
Thesis title: *Ein 3D-Raster-Lebensdauer-Mikroskop mit einer Einzelphotonenquelle als nanoskopische Sonde* (2013)

3. Tim Kroh
Thesis title: *Charakterisierung von Quantenpunkt-Einzelphotonen für Quantenrepeater-Anwendungen* (2012)
Co-supervision with Otto Dietz.

4. Günter Kewes
Thesis title: *Wechselwirkung von NV-Zentren in Nanodiamanten mit plasmonischen Strukturen* (2011)
Co-supervision with Thomas Aichele.

Bachelor Students

5. Robert Koslowski
   Thesis title: *Wellenleitung von Oberflächenplasmonen entlang lithographischer Goldstrukturen* (2011)
   Co-supervision with Thomas Aichele.

6. Stephan Scholz
   Thesis title: *Wellenleitung von Oberflächenplasmonen entlang Nanodrähten* (2010)
   Co-supervision with Thomas Aichele.

List of Figures

Acknowledgement

In danke allen, die mich bei der Erstellung dieser Arbeit (auf welche Weise auch immer) unterstützt haben.

Danke.

Selbständigkeitserklärung

Ich erkläre hiermit, die vorliegende Arbeit selbständig und nur unter Verwendung der angegebenen Quellen und Hilfsmittel angefertigt zu haben. Ich habe mich nicht anderweitig um einen Doktorgrad beworben und besitze einen solchen auch nicht. Die dem Verfahren zugrunde liegende Promotionsordnung der Mathematisch-Naturwissenschaftlichen Fakultät der Humboldt-Universität zu Berlin habe ich zur Kenntnis genommen.

Berlin, den Andreas Wolfgang Schell